AXISYMMETRIC CONTROL IN TOKAMAKS

by

DAVID ALLAN HUMPHREYS

S.B., Electrical Engineering
Massachusetts Institute of Technology (1982)
and
S.B., Physics
Massachusetts Institute of Technology (1982)

Submitted to the Department of Physics
in partial fulfillment of the requirements for the degree of

DOCTOR OF PHILOSOPHY

at the

MASSACHUSETTS INSTITUTE OF TECHNOLOGY

February 1991

Signature of Author.....
Department of Physics
February 25, 1991

Certified by.....
Ian H. Hutchinson
Thesis Supervisor

Accepted by.....
George F. Koster
Chairman, Departmental Committee on Graduate Students

AXISYMMETRIC CONTROL IN TOKAMAKS

by

DAVID ALLAN HUMPHREYS

Submitted to the Department of Physics
on February 25, 1991, in partial fulfillment of the
requirements for the degree of Doctor of Philosophy
in Physics

ABSTRACT

Vertically elongated tokamak plasmas are intrinsically susceptible to vertical axisymmetric instabilities as a result of the quadrupole field which must be applied to produce the elongation. The present work analyzes the axisymmetric control necessary to stabilize elongated equilibria, with special application to the Alcator C-MOD tokamak. A rigid current-conserving filamentary plasma model is applied to Alcator C-MOD stability analysis, and limitations of the model are addressed. A more physically accurate nonrigid plasma model is developed using a perturbed equilibrium approach to estimate linearized plasma response to conductor current variations. This model includes novel flux conservation and vacuum vessel stabilization effects. It is found that the nonrigid model predicts significantly higher growth rates than predicted by the rigid model applied to the same equilibria.

The nonrigid model is then applied to active control system design. Multivariable pole placement techniques are used to determine performance optimized control laws. Formalisms are developed for implementing and improving nominal feedback laws using the C-MOD digital-analog hybrid control system architecture. A proportional-derivative output observer which does not require solution of the nonlinear Ricatti equation is developed to help accomplish this implementation.

The nonrigid flux conserving perturbed equilibrium plasma model indicates that equilibria with separatrix elongation of at least $\kappa_{sep} = 1.85$ can be stabilized robustly with the present control architecture and conductor/sensor configuration.

Thesis Supervisor: Ian H. Hutchinson
Title: Professor of Nuclear Engineering

Acknowledgments

I would like to thank the many people who have made my graduate years at MIT so rewarding and enjoyable. While graduate school is fraught with many trials, the people with whom we work can transform these trials into positive experiences. In this regard I have been very fortunate. My supervisor, Prof. Ian Hutchinson, has always been generous with both his time and his support. It has been a true privilege to be able to work with him during my time at Alcator, and I will always be grateful for that opportunity. He is the finest teacher I have ever known.

I would also like to thank my thesis readers, Prof. Jeffrey Freidberg and Prof. Miklos Porkolab, for their encouragement and helpful suggestions. Special thanks are also due Dr. Steven Horne and Dr. George Johnston, for their generous sharing of wisdom and spirit.

I am also grateful to my fellow graduate students and friends at the Plasma Fusion Center who have helped me in one way or another to survive the ordeals and remain human throughout. In particular, I would like to extend my appreciation to Scott Haney, Warren Krueger, Frank Wong, Pat Stewart, Tom Luke, Paul Stek, Gerry Tinios, and Chi-Wa Tsui.

Finally, I would like to thank my family for their love and support throughout the long years. To my brother, Steve, now as always, gratitude beyond words. To my parents, past and present, I dedicate whatever good may come of my work. My thanks will never be enough, yet will always be beyond measure. To my sister, Heather, my thanks for open arms and open heart.

Most importantly of all, my deepest gratitude goes to Sharon, Jessica, and Jared, who have perservered throughout, and have always provided the color, the flavor, and the music to make life ever more beautiful each day.

Contents

List of Figures

List of Tables

Chapter 1

Introduction

It has long been recognized that tokamak plasmas with noncircular poloidal cross–sections can exhibit significant performance improvements over plasmas with circular cross–sections. Vertical elongation allows higher plasma betas and higher toroidal current densities to be stably achieved than would be possible in a circular poloidal geometry [1]. For this reason, present generation tokamaks built by fusion programs around the world are typically highly shaped and often possess very complex coil and vacuum vessel geometries which do not lend themselves readily to exact analysis. In particular, most machines confine highly elongated D-shaped plasmas using a relatively small number of equilibrium field (EF) coils in order to reduce cost and afford diagnostic access to the machine. The highly discrete nature of EF coil arrays strongly constrains the number of control degrees of freedom in shaping, and significantly complicates the stability analysis. EF coils cannot be located arbitrarily, in areas which are convenient for analytic modeling, for they must satisfy engineering and diagnostic access constraints while still providing sufficient shaping and stabilizing influence to produce the desired range of plasmas. Vacuum vessels as well cannot be configured so as to oblige the stability analyst, for example in such a way as to be conformal to all plasmas. Moreover, walls and EF coils are

typically highly conductive and closely coupled to the plasma, thus strongly influencing plasma stability. In addition, modern tokamaks such as these tend to be high performance devices, supporting very high currents at high temperatures [2].

All of these characteristics make the problem of control of axisymmetric plasma properties a challenging one. Evolving and maintaining plasma shape throughout a shot while controlling axisymmetric instabilities becomes much more demanding under such conditions than with less strongly shaped devices. The passive growth rate of the well known vertical instability, intrinsic to vertically elongated tokamaks, can become very large for some otherwise desirable plasmas [3]. In this case, the technical and economic feasibility of fast power supplies can be stretched to the limit. Furthermore, due to the energies involved, insufficiency or failure of the equilibrium control system can result in significant damage to a machine [4].

The problem of analysis of magnetohydrodynamic (MHD) stability also becomes much more difficult in such complex machine geometries. Vacuum vessels are frequently allowed to provide significantly conductive toroidal current paths, precisely because such currents can aid in the passive stabilization of MHD instabilities. This significant vacuum vessel contribution to plasma dynamic response makes an accurate vessel model necessary for a realistic stability analysis. Unfortunately, irregularities in vacuum vessel shape can make analytic calculations difficult or impossible. The toroidally conductive structures surrounding a plasma, including discrete EF coils, necessary coil support structures, and the often irregular vacuum vessel itself, are unlikely to be conformal to flux surfaces, or possess any otherwise fortuitous configuration with regard to analytic calculation of plasma modes.

Experimental devices must also perform a great deal of equilibrium modification (e.g. with pellet injection or RF heating), often changing plasma characteristics in unpredictable ways. So called "soft disruptions" can also change the plasma current profile dramatically, while not destroying plasma confinement. It would be unacceptable for the shaping and stability control system not to be tolerant of such

strong but not intrinsically destructive perturbations.

It is therefore critical to have a sophisticated control system which can extract as much performance as possible from a highly shaped tokamak, while providing some measure of safety in the presence of significant equilibrium modification. Ideally such a system would be generally robust, tolerant of some variation in plasma characteristics, and able to compensate as much as possible for the lack of passive stability margin with some degree of active control margin.

One of the most limiting aspects of plasma control analysis is the difficulty in deriving a satisfactory plasma model. In the regime of interest for most equilibrium and stability control of tokamaks, the plasma equilibrium is well described by the MHD model. In particular, plasma equilibrium in a tokamak is well described by the Grad-Shafranov equation, a nonlinear, elliptic partial differential equation requiring the specification of two free functions to allow solution. The difficulty of solving this equation for realistic geometries has frequently caused tokamak control designers to use simpler plasma models of various types. Arguably the simplest and most popular model for the analysis of axisymmetric modes has been the filament–circuit model [5,6].

1.1 Rigid Filament–Circuit Model

The filament-circuit model comes in many varieties, but in general includes a filamentary model of the plasma and a toroidal conductor model (including the vacuum vessel and EF coils) consisting of an array of conducting loops. The geometry and resistances of these loops are chosen to preserve general circuit characteristics of the vacuum vessel. That is, such things as the local resistance and overall mutual inductive coupling between regions are accurately preserved. Self inductances are typically calculated from the geometry of the loop cross–sections chosen. Such a

model has the virtue of extendability to convergence: in principle the array can be made as fine as desired until the dominant mode decay rates converge sufficiently. It can therefore provide a good estimate of vessel modes and decay rates in the absence of a plasma.

While this approach provides a good vacuum vessel model, the corresponding plasma model is relatively inaccurate. Several simplifying assumptions are commonly made. An array of filaments or even a single filament alone is used to represent the plasma, and mutual couplings with the vacuum vessel elements are calculated from this abstraction of the plasma. The plasma mass is usually taken to be negligible, and plasma motion is taken to be rigid and purely vertical, although sometimes radial motion is included as well [7]. Because it is a natural assumption for a circuit approach and is consistent with a single-filament plasma model, plasma current is usually kept constant, rather than the flux linkage which would be fixed in an ideal MHD fluid.

For a truly filamentary plasma, the self inductance is infinite, and in such a case the assumption of conserved flux is equivalent to conserved current. In addition, owing to the purely vertical field on the midplane, vertical motion of a single filament does not cut any field lines. But neither of these is *a priori* justified in a multifilament plasma model. In principle, a multifilament plasma can compress flux significantly enough to affect the instability, even when free to move only vertically, mostly along the primarily vertical field lines. A multifilament model is attractive despite the inconsistency in the way flux conservation is treated. Most importantly, it allows sampling of the field curvature across the entire plasma, and thus a more accurate calculation of the destabilizing force.

Fortunately it has been demonstrated that the growth rate associated with a current conserving rigid perturbation is closer to the true MHD value than that due to a rigid flux conserving perturbation [8]. In this reference, "rigid flux conserving perturbation" means rigid vertical motion of the internal plasma flux surfaces, to

be distinguished from rigid motion of the plasma current. Furthermore, for purely elliptical plasmas the two models are the same [12]. There is also evidence to suggest that current conservation is roughly obeyed experimentally in vertical instabilities [9].

For vertical motion alone, the complete system of plasma and conducting coils is described by a coupled set of Kirchoff's voltage law equations along with a force balance equation for rigid motion. These can then be cast in the form of an ordinary eigenvalue problem ($\mathbf{A}\underline{x} = \lambda\underline{x}$) if the plasma is taken to be massless. If plasma mass is included, a generalized eigenvalue problem ($\mathbf{A}_1\underline{x} = \lambda\mathbf{A}_2\underline{x}$) will result. Solution of these eigenvalue problems yields "passive" growth rates for the vertical instability, by which we mean growth rates in the absence of "active" feedback.

With the realization that elongated plasmas could provide significant improvement in performance over circular cross-section machines came a serious effort to understand the vertical axisymmetric instability which accompanies vertical elongation. Many different rigid plasma displacement models have been used since the beginning of this effort in order to better understand the fundamentals of the vertical instability.

Analytic models using simplified plasma geometries, typically including a distributed continuous current profile and flux conserving rigid plasma displacement, have revealed much about the essential nature of the mode [10,11,12]. Key results of such studies include the observations that elongation is generally destabilizing, more peaked current profiles (corresponding to higher internal inductance, l_i) are less stable than flat current profiles, and that the proximity, conformality, and resistivity of surrounding conductors determine whether an elongated plasma is stable, unstable on an ideal MHD timescale, or unstable on a resistive wall diffusive timescale.

Rigid filamentary plasma models have been used primarily to emphasize detailed aspects of a conductor model, typically at the expense of accuracy in plasma

dynamics [7,6]. Many of these analyses have proved to model the instability and the plasma-conductor interaction sufficiently well to allow design of experimentally satisfactory control systems for elongated plasmas [7,13]. The success of such a simple, easily implemented and understood model has made it an almost universal method for designing vertical stability control systems [14,15]. However, the design resulting from the simple model is usually checked with a more complicated simulation before implementation.

The rigid filament–circuit approach is, of course, fundamentally inaccurate in many ways. For example, a physical plasma does not conserve current, and the correct energy minimizing perturbation does not in general consist of rigid vertical motion. This is not necessarily a fatal problem, since there are distinct advantages to using an inaccurate model whose inaccuracies are relatively easy to understand, instead of a potentially highly accurate model whose internal complexities are great and mysterious. But abuse of the simple model can lead to grossly incorrect results. For example, a single filament placed at the magnetic axis may yield a very different growth rate from one placed at the current centroid. Furthermore, growth rate predictions of a rigid single filament or multifilament model applied in regimes of marginal MHD stability are highly suspect, particularly if plasma mass is taken to be zero. However, this approach possesses the virtues of physical simplicity and relative ease of calculation. Even in the most elaborate of such models, only a single equilibrium need be calculated for each equilibrium to be analyzed, and only the resulting current profile need be used in the analysis. The same function can be performed by elaborate time–dependent simulation codes, but the cost in complexity and execution time can make these approaches very unattractive for the design process.

What is needed is an approach which provides a middle ground between analyses which are highly accurate although complex and costly, and approaches which are relatively inaccurate although simple, readily understood, and fast. One such

approach, due to Haney and Freidberg [16] and now being applied to the design of ITER (the International Thermonuclear Experimental Reactor), is that of a variational equilibrium coupled with somewhat general perturbation trial functions. This method is extremely fast and provides a better plasma model than that assumed in a rigid filament-circuit analysis, but falls slightly short of an exact MHD solution due to the variational nature of the equilibrium.

1.2 Perturbed Equilibrium Model

The approach of the present work, which seeks to come closer to true MHD–consistent plasma behavior, uses equilibrium perturbation to determine the plasma response to toroidal currents. This technique depends on the validity of the massless plasma approximation. Because the modes under analysis are assumed to be strongly affected by the presence of resistive structures, the growth times are considered to be much longer than characteristic ideal MHD times (typically of the order of microseconds). The inertial term in the ideal momentum equation can then be neglected, and the plasma can be taken to be in quasi-equilibrium at all times. This is equivalent to the massless plasma approximation frequently assumed in the expression of force balance in the rigid filament–circuit model. Given the assumption of quasi-equilibrium, the plasma response can be estimated in a linear sense by perturbing a base equilibrium with sufficiently small coil current variations.

This approach is similar to that taken by Albanese et al [17], addressing the simple case of vertical motion due to EF coil current variation alone, while keeping all plasma profile shapes and total plasma current constant. These analyses neglect the stabilizing effects of the vacuum vessel as well as internal dynamic variation in toroidal current, pressure, and poloidal current profiles. These models therefore cannot even approximately conserve magnetic flux. Moreover, they have lacked a practical method for evaluating vacuum vessel effects.

Another similar approach has been taken by Hoffmann et al [18], who used an equilibrium code in flux-conserving mode to model plasma response with a quasi-equilibrium assumption and determine stability boundaries. However, no attempt was made to couple plasma dynamics to conducting structures in order to calculate growth rates for resistive wall modes.

The present work introduces a mapping of vacuum vessel effect to approximately equivalent EF coil effect, allowing determination of the stabilizing influence of a vacuum vessel. The presence of vacuum vessel stabilization is often crucial in maintaining plasma stability on an MHD timescale. We further allow plasma profiles to vary, providing sufficient internal degrees of freedom to approximately conserve flux in the plasma. Ideally, a perturbational approach using an equilibrium solver which exactly conserves flux everywhere would be preferred. However, the lack of ready availability of a free boundary flux–conserving equilibrium solver was prohibitive. As will be seen, the approximate approach provides quite a reasonable measure of flux conservation, and preserves many degrees of freedom in plasma shape variation, consistent with the degree of control and influence afforded by the EF coil configuration.

Once a satisfactory plasma model has been obtained, the difficult problem of determining a sufficiently robust control algorithm remains. Tokamaks with highly elongated plasmas can possess vacuum vessel and EF coil configurations which do not provide sufficient stabilization to passively increase vertical instability growth times to much greater than 2 ms. In such an instance, it is desirable to maximize the efficiency of the active system to extract as much performance and disturbance tolerance from the system as possible. In the present work we apply a variety of novel control analysis and design techniques to the problem of shaping and stability control in high performance tokamaks with a relatively low degree of passive stabilization. In particular, the analysis is applied to the Alcator C–MOD tokamak, now under construction at MIT, for a range of equilibria expected to be

achievable when the machine begins operation in 1991.

1.3 The Alcator C–MOD Tokamak

Alcator C–MOD [22] is a high performance, high field, compact tokamak which was designed to be somewhat prototypical of the Compact Ignition Tokamak, (CIT). This latter is an igniting design currently (1990) under consideration as a possible intermediate step before the construction of ITER (referred to above). It is then envisioned that ITER will provide the physics knowledge and proof-of-principle to allow the construction of a true power reactor sometime in the next century.

Alcator C–MOD is the latest in a series of machines in the toroidal confinement program of the MIT Plasma Fusion Center. The name given to the devices, Alcator, is an acronym for the Italian terms *"ALto CAmpo TORus"*, meaning High Field Torus. This reflects a fundamental approach common to toroidal confinement devices in this series built at MIT, all of them being compact, high field tokamaks. As a test bed for technologies and physics issues expected to be critical to an ignition machine, Alcator C–MOD provides a highly shaped plasma with a high toroidal field ($B_t \simeq 9\ T$) in a low aspect ratio geometry, requiring great structural integrity. As the EF coils are located within the toroidal field (TF) coil structure, much of the EF coil magnetic stress is supported by a thick vacuum vessel. Such a vacuum vessel requires a relatively long time for magnetic field penetration at startup, but by virtue of its low resistance can provide a great deal of passive stabilization of MHD instabilities. The machine also provides a high degree of diagnostic access, resulting in many interruptions in the toroidal current paths at top and bottom as well as around the outboard wall. The poloidal cross-section of the C–MOD vacuum vessel is to a large extent a rectangular picture frame, chosen in order to reduce machining and construction costs, with some distortion to provide for stabilization and increased diagnostic access.

Because of this highly nonconformal wall shape, the degree of passive stabilization afforded by the C–MOD vacuum vessel is relatively low. To some extent this is compensated for by the location of EF coils within the TF coil structure. This design brings the highly conductive copper equilibrium field coils quite close to the plasma, allowing their stabilizing properties to strongly influence axisymmetric stability. However, if the nearest conducting surfaces in the form of the vacuum vessel are not sufficient to stabilize the plasma on an MHD timescale, then no amount of added conductor further away can make up for this lack [12]. The vacuum vessel and internal conductors therefore provide a fundamental limit to achievable, ideal MHD stable equilibria. Nevertheless, the nearness of the EF coils can serve to significantly slow modes which are already MHD stabilized by the vacuum vessel, and this will prove to be of great benefit in achieving machine goals.

1.4 Axisymmetric Control in Tokamaks

This thesis will address the problem of axisymmetric control analysis and design in tokamaks using several approaches, and discuss the limitations and advantages of such methods. These techniques are then applied to the design of the Alcator C-MOD analog-digital hybrid integrated equilibrium and stability control system.

Chapter 2 presents an overview of tokamak physics. Topics covered include basic tokamak geometry, equilibrium principles, and stability physics. Chapter 3 describes the rigid filament plasma model and its application to passive vertical stability analysis. Advantages and disadvantages are elucidated, and results of its application to C–MOD equilibria are presented. Chapter 4 develops the perturbed equilibrium approach to passive analysis of plasma–vessel modes. The general algorithm is described, and methods for mapping vessel effects through coil effects and conserving flux are derived. Passive results for C–MOD equilibria are presented and the approach is compared with the rigid model. Chapter 5 deals with the

use of the rigid and perturbed equilibrium models in the analysis of equilibrium and stability control. The basic nature of and issues involved in this active analysis are addressed. Chapter 6 presents methods for designing and evaluating the performance of equilibrium control systems. Pole placement algorithms with full state feedback, proportional–derivative (PD) output feedback, and involving several forms of observer are derived. Multivariable root–locus analysis and "Bode plots" are employed in the design process. Time domain performance criteria are also used, along with systematic error robustness analyses. Specific application is made to the Alcator C–MOD analog–digital hybrid control system architecture. Chapter 7 consists of conclusions and suggestions for further work.

Chapter 2

Tokamak Physics

Two general approaches are available for terrestrial confinement of the extremely high temperature plasmas necessary for commercial production of fusion energy. The first of these, inertial confinement, involves the use of lasers or particle beams to compress and heat a fuel capsule to high density and temperature. The goal in this approach is to produce enough fusion reactions before the plasma flies apart to yield a sufficient gain in energy and satisfy economic constraints. The plasma in this case is thus "confined" by its own inertia.

The second approach to plasma confinement involves the use of magnetic fields to impede energy and particle loss. Charged particles in a magnetic field tend to gyrate in closed orbits about field lines, thereby experiencing greatly restricted motion perpendicular to the field. However, motion parallel to field lines is not restricted in this way. In fact, the parallel thermal conductivity is calculated (classically, ignoring "neoclassical" transport due to toroidal effects and "anomalous" transport enhancement due to plasma microinstabilities) to be on the order of 10^{12} times greater than the perpendicular thermal conductivity [1]. It is therefore extremely desirable to cause field lines to close upon themselves entirely inside a fusion reactor. A cylindrical device with field lines which stream out of the ends of the machine

loses energy at a rate dominated by transport along field lines. By contrast, a toroidal device with field lines which close upon themselves inside the machine will lose energy only through the much slower transport perpendicular to field lines.

The most promising device of this latter type has been the tokamak. This chapter will review the geometry and essential physics of tokamak operation. Important features of tokamak equilibrium and stability will be described, leading up to the axisymmetric instabilities which are the central focus of the remainder of this work.

2.1 Basic Description and Terms

The tokamak is a toroidal device which confines high temperature plasmas with a magnetic field [35]. The geometry of a tokamak is shown in Fig. 2.1. By convention the $\hat{\phi}$ direction is termed the "toroidal" direction, and the $\hat{\theta}$ direction is referred to as the "poloidal" direction. The cylindrical coordinates are (R,ϕ,Z), and the toroidal coordinate system is usually defined to be (r,θ,ϕ). Note that with this convention the toroidal coordinates define a "left-hand" system. Tokamak equilibrium geometry is essentially axisymmetric, by which we mean that equilibrium plasma quantities are independent of the toroidal angle, ϕ.

The magnetic field of a tokamak can be separated into two orthogonal components. The toroidal field, B_t, is the stronger of these two. It is typically primarily responsible for providing stability. The poloidal field, B_p, although weaker than the toroidal field, is primarily responsible for equilibrium maintenance. The sum of these two fields produces total magnetic field lines which wrap helically around the tokamak.

The vacuum toroidal field is produced by current flowing in the poloidal direction through a set of toroidal field (TF) coils which link the plasma column.

Integrating Ampere's law along a circular path in the toroidal direction and exploiting the axisymmetry of the toroidal field, we find

$$\vec{B}_t = B_0 \left(\frac{R_0}{R}\right) \hat{\phi}, \tag{2.1}$$

where B_0 is the toroidal field at $R = R_0$, the machine major radius. The region defined by $R < R_0$ is known as the "inboard" side of the plasma or machine, and $R > R_0$ defines the "outboard" side.

The poloidal field arises from toroidal current flowing within the plasma and from toroidal currents in axisymmetric coils external to the plasma. These axisymmetric coils are known as "equilibrium field" (EF) coils. The toroidal plasma current serves to ohmically heat the plasma, as well as to help confine it through the poloidal field. The plasma current is driven inductively by varying the current in an "ohmic heating" (OH) coil whose flux is linked by the plasma.

Several quantities are conventionally used to characterize a tokamak plasma. The "aspect ratio" is the ratio of machine (or plasma) major radius, R_0, to plasma minor radius, a. The "inverse aspect ratio", ϵ, defined by

$$\epsilon \equiv \frac{a}{R_0}, \tag{2.2}$$

is a more commonly used quantity. The inverse aspect ratio is a measure of the effect of toroidicity on tokamak physics. A value of ϵ much less than unity means that the local plasma physics is described well by a cylindrical model. Conversely, an ϵ value comparable to unity indicates that in general toroidal effects cannot be ignored.

The plasma "β" is the ratio of kinetic pressure, p, to magnetic pressure:

$$\beta \equiv \frac{2\mu_0 p}{B^2}. \tag{2.3}$$

The toroidal and poloidal β-values, β_t and β_p, are calculated using the toroidal and poloidal magnetic fields respectively. Plasma β is a measure of confinement efficiency and economic efficiency.

The "safety factor", q, is the change in toroidal angle of a field line as it makes one poloidal circuit:

$$q \equiv \frac{\Delta\phi}{\Delta\theta} = \frac{\Delta\phi}{2\pi}. \tag{2.4}$$

A sufficiently high q-value at the plasma edge confers a measure of "safety" from a class of instabilities known as "kinks", to be discussed later. For a high aspect ratio plasma, the edge safety factor is the same as a quantity known as the "kink safety factor", q_*, and is given by

$$q_* \equiv \frac{aB_0}{R_0 B_\theta}, \tag{2.5}$$

where B_0 is the toroidal field at $R = R_0$, and B_θ is the edge poloidal field. The value of q_* at which a machine can operate stably is an important figure of merit, since high current (and consequently low q_*) is important for high ohmic heating and confinement, yet stability requirements establish a lower limit on q_*. Machines typically operate with $q_* > 2$.

For an ohmically heated conventional (low β) tokamak, the following general scalings are used: $B_p/B_t \sim \varepsilon$, $\beta_t \sim \varepsilon^2$, $\beta_p \sim 1$, and $q \sim 1$ [1]. In actual operation, present ohmic tokamak experiments do not generally achieve such large β values as this. More typical values are $\beta_t \sim \varepsilon^4$ and $\beta_p \sim \varepsilon^2$ [2].

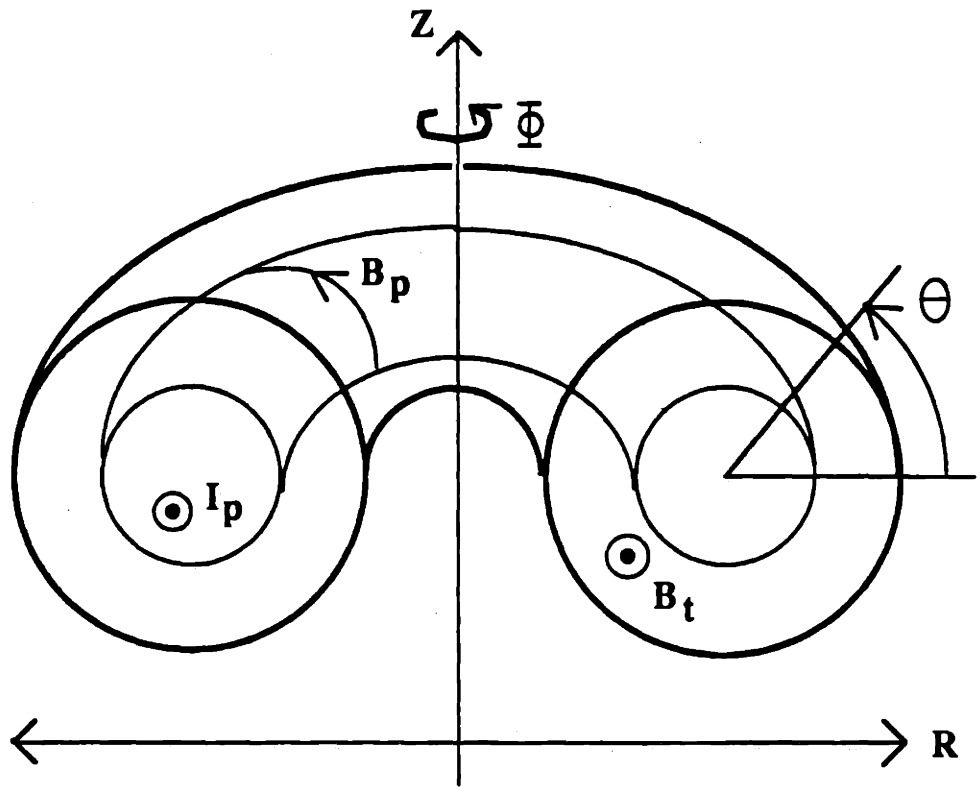

I_p = (toroidal) plasma current

B_t = toroidal B-field

B_p = poloidal B-field

Φ = toroidal angle

Θ = poloidal angle

Figure 2.1: Basic tokamak geometry.

2.2 Tokamak Equilibrium

2.2.1 Ideal Magnetohydrodynamics

Many aspects of the equilibrium and stability of a high temperature tokamak plasma are well described by the equations of ideal magnetohydrodynamics (MHD) [1]. These consist of 7 equations describing the dynamics of a perfectly conducting fluid in the presence of electromagnetic fields. The first two equations are the continuity and state equations for an unmagnetized fluid:

$$\frac{\partial \rho}{\partial t} + \nabla \cdot (\rho \underline{v}) = 0, \tag{2.6}$$

and

$$\frac{d}{dt}(p\rho^{-\Gamma}) = 0. \tag{2.7}$$

Three of Maxwell's equations are included, Faraday's law

$$\nabla \times \underline{E} = -\frac{\partial \underline{B}}{\partial t}, \tag{2.8}$$

Ampère's law

$$\nabla \times \underline{B} = \mu_0 \underline{J}, \tag{2.9}$$

and Gauss' law of magnetism

$$\nabla \cdot \underline{B} = 0. \tag{2.10}$$

The last two equations connect the two unmagnetized fluid equations with Maxwell's equations. These are the conservation of momentum equation

$$\rho \frac{d\underline{v}}{dt} = -\nabla p + \underline{J} \times \underline{B}, \tag{2.11}$$

and the ideal Ohm's law

$$\underline{E} + \underline{v} \times \underline{B} = 0. \tag{2.12}$$

The latter reflects the fact that in a perfectly conducting ideal MHD fluid, the magnetic field lines are tied to or "frozen-in" to the fluid elements. This equation

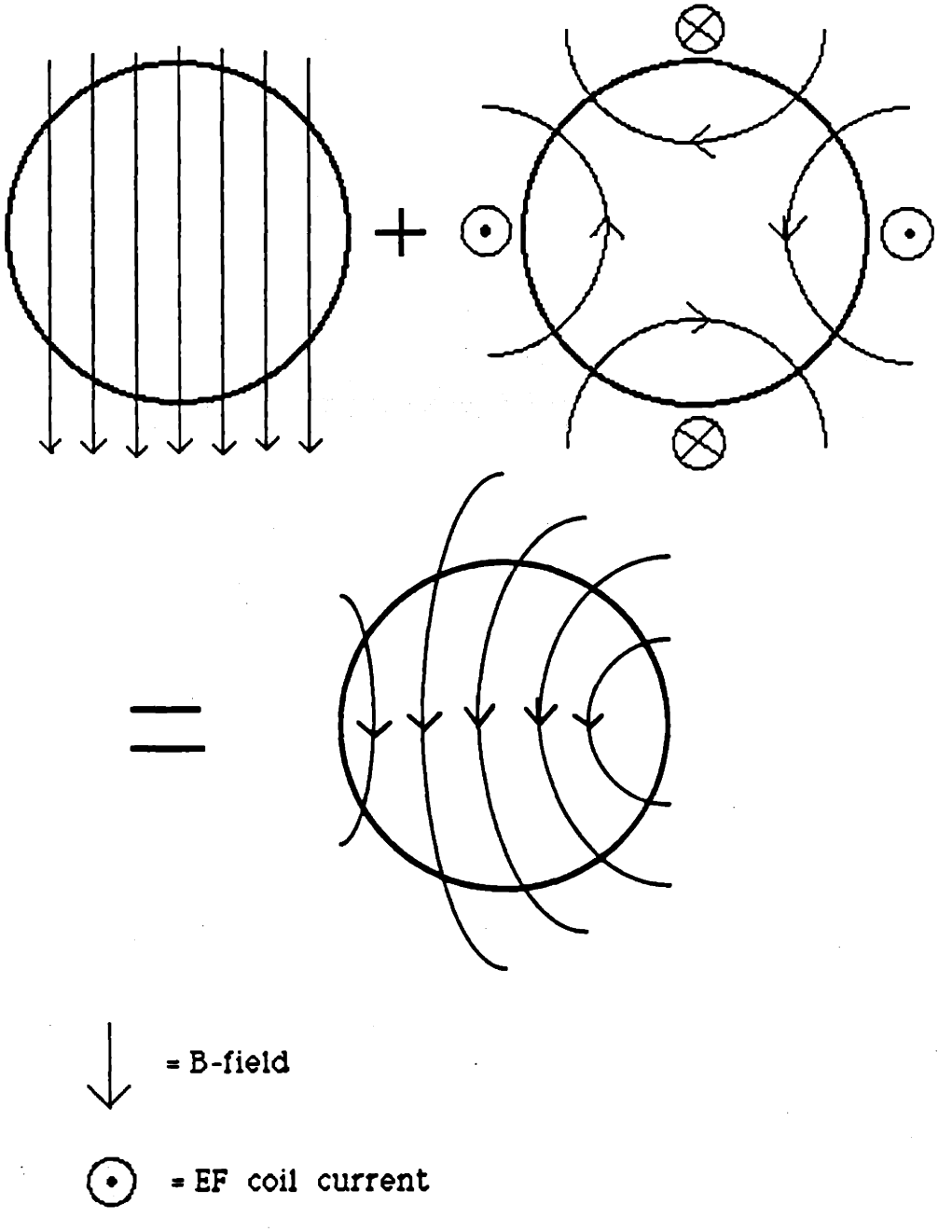

Figure 2.2: Quadrupole field addition for plasma elongation.

is therefore also known as the "frozen-in" law. The conservation of momentum equation, Eq. 2.11, shows that in an MHD fluid, forces arise either from pressure gradients or magnetic $\underline{J} \times \underline{B}$ effects.

In these equations, ρ is the fluid mass density, $\underline{v}$ is the fluid velocity, p is the pressure, $\Gamma = 5/3$ is the ratio of specific heats, E is the electric field, B is the magnetic field, J is the current density, and $d/dt = \partial/\partial t + \underline{v} \cdot \nabla$ is the convective derivative.

2.2.2 Equilibrium

The static equilibrium condition is obtained by setting $d/dt = 0$ in the momentum conservation equation, Eq. 2.11, and choosing zero flow velocity, $\underline{v} = 0$. This results in

$$\nabla p = \underline{J} \times \underline{B}, \tag{2.13}$$

$$\nabla \times \underline{B} = \mu_0 \underline{J}, \tag{2.14}$$

and

$$\nabla \cdot \underline{B} = 0. \tag{2.15}$$

The force balance equation, Eq. 2.13, implies several important physical features of MHD equilibria. Dotting this equation with $\underline{B}$, we obtain

$$\underline{B} \cdot \nabla p = 0. \tag{2.16}$$

It follows that magnetic field lines lie in surfaces of constant pressure, and these surfaces comprise a set of closed nested tori. Similarly, dotting Eq. 2.13 with $\underline{J}$, we find

$$\underline{J} \cdot \nabla p = 0, \tag{2.17}$$

indicating that current density lines also lie in surfaces of constant pressure.

The poloidal field can be written as [1]

$$\underline{B}_p = \frac{1}{R}\nabla\psi \times \hat{\phi} \tag{2.18}$$

where the stream function, ψ, is related to the toroidal component of the vector potential, A_ϕ, through

$$\psi = RA_\phi. \tag{2.19}$$

The stream function is simply related to the poloidal magnetic flux, ψ_p, through

$$\psi_p = 2\pi\psi \tag{2.20}$$

and the terms are sometimes used interchangeably. We shall define the poloidal flux after examining the surfaces of constant pressure somewhat further.

Dotting the poloidal field with Eq. 2.13, we find

$$\underline{B}_p \cdot \nabla p = \frac{1}{R}(\nabla\psi \times \hat{\phi}) \cdot \nabla p = 0. \tag{2.21}$$

This is satisfied if $p = p(\psi)$, so that

$$(\nabla\psi \times \hat{\phi}) \cdot \nabla p = (\nabla\psi \times \hat{\phi}) \cdot (\nabla\psi)\frac{dp}{d\psi} = 0. \tag{2.22}$$

The poloidal flux and stream function are thus constant on a constant pressure surface. The flux function is usually taken to be the independent variable in equilibrium descriptions, and the constant flux and pressure surfaces in which the magnetic field lines and current stream lines lie are known as "flux surfaces". Any quantity which is constant on a flux surface is termed a "surface quantity". The poloidal flux on a flux surface can now be defined to be the total magnetic flux passing through a disk-shaped surface, S_p, lying in the $Z = 0$ plane and extending out to the flux surface in question:

$$\psi_p \equiv \int \underline{B}_p \cdot \hat{n}\, dS_p. \tag{2.23}$$

The point near the center of the plasma where pressure and flux reach extrema is termed the "magnetic axis". The horizontal plane cutting through the magnetic

axis is referred to as the "plasma midplane". Usually this plane coincides with the machine midplane, defined by $Z = 0$, and we shall use the term "midplane" to refer to both except where necessary to distinguish between them.

2.2.3 The Grad-Shafranov Equation

For toroidal geometry, the static equilibrium equation, Eq. 2.13, can be expressed in terms of the magnetic stream function. The resulting form is known as the Grad-Shafranov equation:

$$\Delta^* \psi = -\mu_0 R^2 p' - FF', \tag{2.24}$$

where

$$\mu_0 R J_\phi = -\Delta^* \psi, \tag{2.25}$$

and

$$\Delta^* \psi \equiv R^2 \nabla \cdot \left(\frac{\nabla \psi}{R^2} \right), \tag{2.26}$$

$$p' \equiv \frac{dp}{d\psi},$$

$$F' \equiv \frac{dF}{d\psi}.$$

The function $F(\psi)$ is related to the poloidal plasma current, I_{pol}, and the magnitude of the toroidal field through

$$F(\psi) = RB_t = -\frac{I_{pol}}{2\pi}. \tag{2.27}$$

The poloidal current is evidently a surface quantity, and is defined in a manner similar to the poloidal magnetic flux:

$$I_{pol} \equiv \int \underline{J}_p \cdot \hat{n} \, dS_p. \tag{2.28}$$

Two free functions must be specified to permit solution of the Grad-Shafranov equation. Typically $p(\psi)$ and $F(\psi)$ are given, and the flux function is solved for.

For a circular tokamak, the force balance is of two general types: minor radial force balance (in the $\hat{r}$ direction), and major radial force balance (in the $\hat{R}$ direction). For the usual ohmic tokamak scaling (in particular $\beta_p \sim 1$), equilibrium of the minor radial forces essentially represents a balance between the pressure gradient and the $\underline{J}_\phi \times \underline{B}_p$ force. For $\beta_p \sim 1$ the $\underline{J}_p \times \underline{B}_\phi$ force is negligible.

The plasma β-values provide a measure of plasma diamagnetism. In fact, for $\beta_p < 1$, an ohmic tokamak plasma is paramagnetic. Thus, the actual toroidal B-field across the plasma is greater than the vacuum toroidal B-field. This is the usual case for present tokamak experimental devices. For $\beta_p > 1$, an ohmic tokamak plasma is diamagnetic. The actual toroidal B-field across the plasma is less than the vacuum toroidal B-field in this case.

A tokamak plasma experiences three different mechanisms which give rise to expansion forces in the major radial direction. Because they arise as a result of the toroidal geometry, these are often referred to as "toroidal forces". They include the "hoop" force, the "tire-tube" force, and the "1/R" force. The hoop force is present in any current carrying loop. The poloidal field lines on the inboard side created by the toroidal current are of a higher density due to the bend than those on the outboard side. The field strength is therefore higher on the inboard side. Since the magnetic field pressure on the plasma is proportional to B^2, the magnetic pressure is also greater on the inboard side. Although the inboard surface area is somewhat smaller than the outboard surface area, the quadratic dependence on field strength dominates, and the net effect is to produce an expansion force in the outward radial direction.

The tire-tube force is similar to the force which causes a bicycle tire inner tube to hold its shape as a result of the kinetic pressure of the gas confined within. The kinetic pressure can be viewed as approximately uniform around the edge of the plasma, but the surface area on the outboard side is greater than that on the inboard side. The net force due to kinetic pressure is therefore also in the outward

radial direction.

The 1/R force arises from the toroidal field's 1/R dependence. Since the toroidal field is higher on the inboard side of the plasma than the outboard, the magnetic field pressure is higher as well. By the same argument used in the case of the hoop force, the net force is in the outward radial direction.

One method of countering this net expansive toroidal force is to surround the plasma with a highly conductive wall. The image currents induced in such a wall would keep the plasma confined within the conducting shell. This approach fails if the lifetime of the plasma discharge is expected to be longer than the magnetic field diffusion time through the wall. For such plasmas the net toroidal expansive force must be balanced by an externally applied uniform vertical field.

2.2.4 Shaped Plasmas

Plasmas whose poloidal cross-sections are significantly different from a circle are known as "shaped" plasmas. Extreme variations from a circular cross-section are described as "highly shaped". To produce such a plasma requires the addition of fields with higher order variation in poloidal angle. In particular, to produce a vertically elongated plasma such as that shown in Fig. 2.3 requires the addition of a quadrupole field. The simplest realization of a quadrupole field arises from coils placed above and below the plasma carrying current in the same direction as the plasma current, as well as coils inboard and outboard, each carrying current opposite to the plasma current. This coil configuration, the form of the quadrupole field, and the result of adding it to the vertical field is shown in Fig. 2.2. Physically, the upper and lower coils attract the plasma, stretching it vertically, while the inboard and outboard coils repel the plasma, compressing it horizontally. The net effect is to create vertical elongation. The definition of plasma elongation, $\kappa \equiv b/a$, is demonstrated in Fig. 2.3.

2.3 Tokamak Stability

The sources of energy to drive MHD instabilities in a tokamak plasma are pressure gradients and current/field gradients. In the present section we shall only address current driven instabilities. These are typically the most destructive, and we shall be principally concerned with one particular kind of current driven instability in the remainder of this work.

There are three principal physical effects which tend to stabilize MHD modes. The first of these is magnetic field compression. This consists of motion of magnetic field lines towards each other in directions perpendicular to the B-field, corresponding to a field perturbation which is parallel to the equilibrium field. The second stabilizing effect is magnetic field line bending, corresponding to the appearance of a perturbed field perpendicular to the equilibrium field. Finally, magnetic field curvature which is convex toward increasing plasma pressure is stabilizing. This kind of field configuration relative to the pressure gradient is known as "good field curvature".

For the toroidal geometry of a tokamak, the MHD modes are taken to consist of a plasma displacement function of the form:

$$\underline{\xi}(t,\underline{r}) \equiv \int \underline{v}\, dt = \underline{\xi}(r) e^{i(m\theta - n\phi - \omega t)}, \tag{2.29}$$

where m and n are the poloidal and toroidal mode numbers, and ω is the mode frequency. Flux surfaces on which $q = m/n$ are known as "mode rational" surfaces. Line bending stabilization is minimized on these surfaces, so that an m/n instability can grow when localized to the corresponding mode rational surface. The physical origin of this minimization of line bending stabilization is that the helical pitch of the magnetic field matches the pitch of the mode.

2.3.1 Kink Modes

Low mode number modes are in general not localized, but rather consist of unstable displacement of the bulk of the plasma. An important class of low m-number mode is referred to as "external kink" modes. These result in a helical perturbation or "kink" of the entire plasma, including the plasma surface. The physical driving force of the instability is readily understood by considering a single bend of the helical kink. Just as in the case of the toroidally expansive hoop force, the inside of the bend will experience an increase in field line density and therefore an increase in the magnetic pressure. This tends to increase the severity of the bend, thus continuing the growth of the instability.

The stability of an m/n external kink mode constrains safety factor values at the edge and magnetic axis. Roughly, stability requires that (for low β) $q_e > 1$ and $q_e/q_0 > 2-3$. Here q_e is the edge q (usually denoted q_a), and q_0 is the magnetic axis q. These limits correspond to a sufficiently peaked current profile being required for stability. It is of interest to note that the stability of internal kink modes (kink modes causing displacement inside the plasma without disturbing the plasma surface) further constrains safety factors. In particular, the stability of the m=1 internal kink requires that $q_0 > 1$.

The satisfaction of such safety factor constraints is sufficient to provide stability to the kink modes described only when the plasma β is sufficiently low. At some higher value of β the plasma will suddenly become unstable to a class of instabilities known as "ballooning" modes. The value of β for which ballooning modes are marginally stable (with the $q(r)$ profile adjusted to provide marginal kink stability) is the "Troyon β limit", β_{lim}. This quantity is given approximately by [1]

$$\beta_{lim} \simeq 2.8 \left(\frac{I_p}{a B_t} \right). \tag{2.30}$$

Here the quantities are defined in MKS units, and β_{lim} is expressed in %.

2.3.2 MHD Growth Rates

The typical growth rate of ideal MHD instabilities (in the absence of stabilizing conductors) can be estimated with a simple scaling argument using the momentum conservation equation, Eq. 2.11, and the continuity equation, Eq. 2.6. We choose the zero β limit so that pressure can be ignored, and focus on magnetic forces alone. The characteristic scale distance of plasma density and field variation is the minor radius, a. The dominant current-field interaction, as indicated in the equilibrium description above, is that of the poloidal field with toroidal current. With these physical considerations, we find the following scaling of the momentum equation:

$$\rho\frac{d\underline{v}}{dt} \sim \underline{J}\times\underline{B} = \frac{1}{\mu_0}(\nabla\times\underline{B})\times\underline{B} \sim \frac{B_p^2}{\mu_0 a}. \tag{2.31}$$

The inertial term is scaled as

$$\rho\frac{d\underline{v}}{dt} \sim \rho\frac{v}{\tau_A} \sim \rho\frac{a}{\tau_A^2} \tag{2.32}$$

where τ_A is the characteristic time scale of the instability, known as the "Alfvén time". We have therefore that

$$\tau_A^2 \sim \frac{a^2}{v_A^2} \tag{2.33}$$

where $v_A \equiv \frac{B_p}{(\rho\mu_0)^{1/2}}$ is the poloidal Alfvén velocity. The Alfvén time is on the order of 0.1-1.0 μsec for a typical tokamak.

When there are conducting structures in proximity to the plasma the growth rate of ideal MHD modes can be significantly reduced. This principle allows the active control of certain unavoidable instabilities with feedback systems having response times significantly longer than a microsecond.

The most potentially damaging of these unavoidable unstable modes is an m=1, n=0 axisymmetric mode [4]. For a vertically elongated plasma, this mode consists essentially of an unstable bulk plasma motion in the vertical direction. For this reason it is often referred to as the "vertical instability". The succeeding chapters

of this work will be primarily concerned with this mode in noncircular tokamaks. It is intrinsic to vertically elongated plasmas, but can be actively controlled when surrounding conductors are able to slow its growth rate sufficiently.

2.4 The Vertical Instability

The Troyon β limit discussed above can be expressed in a different form which shows its dependence on elongation [1]:

$$\beta_{lim} \simeq 14 \left(\frac{\varepsilon \kappa}{q_*} \right), \tag{2.34}$$

where

$$q_* \equiv \frac{2\pi a^2 \kappa B_t}{\mu_0 R_0 I_p}. \tag{2.35}$$

An elongated plasma can therefore be expected to have a higher β-limit than a circular plasma with the same aspect ratio and q_*. Higher plasma current densities can also be achieved stably with elongated plasmas [35]. Because economic efficiency is directly related to the plasma β, and heating and confinement depend on plasma current, the advantages of producing stable elongated plasmas are significant.

2.4.1 Physical Origin: Decay Index

The necessity of a quadrupole field in order to produce an elongated plasma equilibrium was demonstrated above. Now we examine the consequences of such a field. Consider a plasma model consisting of a toroidal, current-carrying, filamentary loop located on the midplane. When this plasma is displaced upward by a small amount z, it will experience a vertical force, F_z, given by

$$F_z = -2\pi R_p I_p \frac{\partial B_R}{\partial z} z \tag{2.36}$$

where R_p is the major radius of the filament, I_p is the toroidal plasma current, and B_R is the vacuum radial field. The gradient of B_R is taken at the location of the

filament. The signs are chosen so that in equilibrium, $I_p > 0$, $B_z < 0$, and thus $\frac{\partial B_R}{\partial z} < 0$. Therefore $F_z > 0$ for a positive z displacement of the plasma, and the motion is unstable. This unstable mode is known as the "vertical axisymmetric instability". It consists of an unstable n=0, m=1 bulk motion of the plasma in the vertical direction.

The criterion for stability can be expressed in terms of field curvature. As shown in Fig. 2.2, when the vacuum field curvature is concave on the outboard side and the vertical field has the correct sign to provide toroidal equilibrium, the plasma is unstable to vertical perturbations. Conversely, a vacuum field concave to the inboard side is stabilizing. This field curvature is described by the "decay index", n, which is related to the destabilizing force, F_z. Consider Eq. 2.36 rewritten in the following form:

$$F_z = 2\pi I_p n B_{z0} z, \tag{2.37}$$

where the decay index, n, is defined as

$$n \equiv -\frac{R}{B_{z0}}\frac{\partial B_z}{\partial R} = -\frac{R}{B_{z0}}\frac{\partial B_R}{\partial z}. \tag{2.38}$$

Here the vertical field B_{z0} is evaluated at the filament location, and we have made use of Ampère's law to determine that for a vacuum field

$$\frac{\partial B_z}{\partial R} = \frac{\partial B_R}{\partial z}. \tag{2.39}$$

A positive decay index corresponds to a concave outboard field, and a negative decay index corresponds to a concave inboard field. The general condition for stability in the absence of conducting structures is therefore given by:

$$n > 0. \tag{2.40}$$

Since producing an elongated plasma requires the application of a quadrupole field as in Fig. 2.2, some regions of negative decay index must necessarily be formed. For a realistic plasma equilibrium, the decay index will vary widely across the

plasma, and the net destabilizing effect is a result of the destabilizing force sampled by the current profile over the entire plasma. It should be emphasized that decay index is only a measure of curvature, not of destabilizing force. To compare net destabilizing forces in different equilibria, care must be taken to sum over the appropriate local field gradient force quantities, not over the local decay indices (see Section 3.1). The local decay index is effectively the gradient force term normalized by the local B_z, so the "average" (current density weighted) destabilizing force cannot be simply related to the "average" (current density weighted) decay index.

2.4.2 Conductor Effects

In the absence of stabilizing conductors, an equilibrium with net destabilizing decay index will be unstable on a poloidal Alfvén time, as described above for general MHD instabilities. In the presence of a conducting wall which is sufficiently close to the plasma in some average sense (implying some degree of conformality), the mode will grow much more slowly, roughly on the wall L/R time scale. By "L/R", we mean the inductive/resistive decay time of the conducting wall. It is then said to be "stable on the ideal (MHD) time scale". Insufficiently close or insufficiently surrounding conductors will fail to slow the mode from the ideal MHD growth rate [12]. A perfectly conducting wall which satisfies proximity and conformality conditions would completely stabilize the mode.

The wall L/R time is the same as the penetration time for magnetic diffusion through the wall. For a circular wall of radius a_w and thickness δ, this characteristic time is given by

$$\tau_D = \frac{\mu_0 a \delta}{\eta}, \tag{2.41}$$

where η is the resistivity of the wall. Thus, a thick, highly conductive wall which is very close to the plasma provides the best stability. However, vacuum vessels are limited in their allowable proximity to the plasma by such requirements as the need

to minimize impurity contamination of the plasma. Furthermore, a very thick wall makes it difficult to drive flux through the vessel during startup.

For a tokamak surrounded by a stainless steel vacuum vessel, the field penetration time is typically much greater than the ideal MHD growth time by at least 3 orders of magnitude. More accurate calculation depends on the actual geometry.

2.5 Remarks

In this chapter we have presented the salient physical principles of tokamaks as necessary preparation for the rather specialized stability analysis to follow. The basic geometry and figures of merit for high temperature plasmas which obey ideal MHD in general, and tokamak plasmas in particular, were described. Essential results from ideal MHD theory were presented or derived. Tokamak equilibrium characteristics and requirements were described in detail, and the particular nature of elongated equilibria was addressed. The physical mechanisms of tokamak MHD instabilities were then described, with particular emphasis on the physics of the vertical axisymmetric mode.

The vertical instability will be the primary focus of the remainder of this work. Because elongated plasmas are intrinsically unstable to vertical modes of the type described here, some degree of stabilization must be applied to prevent disruption of the plasma and damage to the machine. Since conducting walls can at best slow the mode down, an active feedback system must be used to provide the necessary control.

In order to better understand the nature of this mode and its interaction with conductors such as the vacuum vessel, a tractable model of the plasma-conductor system must be derived. An acceptable model must retain the important physics aspects of the system, while still being simple enough to understand and to allow

reasonably swift calculation of solutions.

In the next chapter, we shall derive and apply a simple rigid filament plasma model to the analysis of axisymmetric plasma-conductor mode physics. Forms of this model have been used with great success in the analysis of vertical instability for many tokamak experiments. However, several important aspects of the plasma physics are treated incorrectly in the rigid filament model. For this reason, a more physically accurate model is developed in later chapters of this work and applied to the problem of Alcator C-MOD vertical stability analysis.

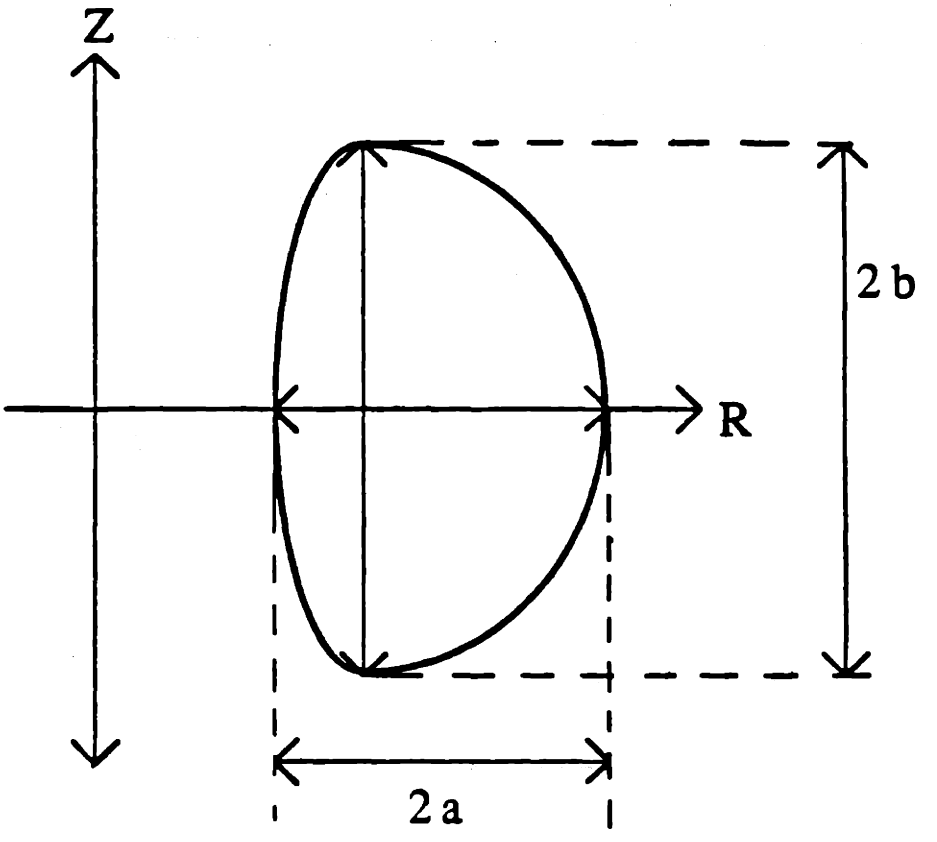

Elongation $K \equiv b/a$

Figure 2.3: Definition of elongation, $\kappa \equiv b/a$.

Chapter 3

Rigid Plasma Modeling for Vertical Stability Analysis

The simplest and historically most common plasma model used in the analysis of vertical stability is the rigid filament–circuit model. Already mentioned in Chapter 1, the rigid filamentary plasma model has certain advantages over more accurate but more complex models. Because the plasma is assumed to move rigidly, the field influence of plasma to conductors is extremely easy to calculate. Dynamic plasma response is reduced to one or two degrees of freedom of motion (in Z and R), although it may sometimes also include artificial inductance variation to approximately model flux conservation. For vertical motion, the plasma is usually taken to be current–conserving, a limit which is consistent with a plasma made up of infinite–inductance filaments, but which breaks down when plasma motion must be in a direction perpendicular to field lines. In particular, for an air-core tokamak radial motion is incorrectly described by a current–conserving model. In fact, in a current–conserving plasma the radial "hoop force" acts in a direction opposite to that in which it acts in a flux–conserving one. One must therefore choose the mix of representations carefully in order to describe plasma response in an approximately

physical way when using the rigid filamentary approach.

This chapter deals with the general vertical stability problem and the simple models traditionally used to assess passive growth rates in a resistive walled tokamak. Despite its physical limitations, the rigid model provides an excellent tool for understanding the qualitative nature of the vertical mode, and for roughly determining stability characteristics for actual machines.

3.1 Rigid Filament Plasma Model

The rigid filament–circuit approach combines physical simplicity and rapid computation of solutions with the potential for a high degree of accuracy in the conductor model. Unfortunately, an inherent weakness of the model is that the plasma itself is not treated correctly. In this model, the plasma is represented by a set of discrete filaments, which are only allowed to move rigidly in the vertical direction.

A plasma model consisting of a single filament alone will lose current profile effects, except as they are reflected in the equilibrium field gradient at the chosen location for the filament. Even if many filaments are used, the rigid shift is not necessarily the correct energy minimizing displacement. At best, without allowing filament currents to vary, a multifilament plasma model will simply give a better estimate of the net destabilizing field gradient force across the entire plasma. However, this is reason enough to use a multifilament rather than single filament model, since *a priori* it is far from clear where a single filament should be located to produce the most accurate results.

In the following we shall describe the circuit model form which is appropriate for a uniform rigid vertical shift. We shall retain finite plasma mass [5,6], and modify the model to include a multifilament plasma specification. The coils representing stabilizing conductors can be driven according to control laws modeling a feedback

response due to plasma motion, but in the present chapter we will only address passive results. Plasma filament currents are kept fixed, so that all plasma-coil induction is due to the motion of the plasma. The filament self inductances are thus effectively infinite.

This circuit model yields a set of NC voltage equations for the NC resistive loops representing the conductors external to the plasma. These are of the form:

$$L_j \frac{d\tilde{I}_j}{dt} + r_j \tilde{I}_j + \sum_{j' \neq j} M_{jj'} \frac{d\tilde{I}_{j'}}{dt} + \sum_{i}^{NF} Ip_i \frac{\partial M_{ij}}{\partial z} \frac{\partial z}{\partial t} = V_j^{applied} \tag{3.1}$$

- Where:
  - $\tilde{I}_j$ are the perturbed coil currents $(j = 1, NC)$,
  - $M_{jj'}$ is the inter-coil mutual inductance matrix,
  - M_{ij} is the coil-filament mutual inductance matrix,
  - r_j is the resistance of coil j,
  - L_j is the inductance of coil j,
  - NF is the number of plasma filaments,
  - $V_j^{applied}$ is the voltage applied to coil j.
  - NC is the number of conducting loops.

If the coil in question is a driven control coil, the applied voltage is given by a control law depending on the plasma displacement. For passive (undriven) coils this voltage is simply zero.

The system of equations is closed by including the equation of motion of the plasma for vertical displacements. This is simply the force balance including the force due to non-zero decay index and the damping force due to eddy currents induced in surrounding conductors. These are denoted F_z^{DI} and F_z^{Eddy} respectively,

and the resulting force equation is:

$$m\frac{d^2z}{dt^2} = F_z^{Eddy} + F_z^{DI} \tag{3.2}$$

$$F_z^{Eddy} = \sum_j^{NC}\sum_i^{NF} I_{p_i}\frac{\partial M_{ij}}{\partial z}\tilde{I}_j \equiv \sum_j^{NC} S_j\tilde{I}_j \tag{3.3}$$

$$F_z^{DI} = -\sum_i^{NF} 2\pi R I_{p_i}\frac{\partial B_{Ri}}{\partial z}z \equiv S_B z \tag{3.4}$$

- Where:
  - Ip_i are the plasma filament currents $(i = 1, NF)$,
  - B_{Ri} is the radial vacuum field at filament i,

We now look for normal mode solutions of the form:

$$z \rightarrow ze^{\gamma t}, \qquad \tilde{I}_j \rightarrow \tilde{I}_j e^{\gamma t} \qquad \text{(etc...)}$$

Arranging Eqs. 3.1 and 3.2 in matrix form, a generalized eigenvalue problem is obtained:

$$\mathbf{A}_1\vec{x} = \gamma\mathbf{A}_2\vec{x} \tag{3.5}$$

where the state vector $\vec{x}$ contains the perturbed quantities z, $\zeta \equiv \dot{z}$, and the $\tilde{I}_j$. The rows of the matrices $\mathbf{A}_1$ and $\mathbf{A}_2$ consist of the circuit and force equations, along with the definition of ζ. This definition allows the expression of the second order force equation in terms of two first order differential equations. The solution of the system thus gives us the normal modes and associated growth or damping rates. This collection of normal modes includes many modes which do not contribute to plasma motions of interest. These represent decay modes of the conductor array with essentially no plasma motion. In addition, if the plasma mass is non-zero, two high frequency oscillatory roots appear which are highly damped on the slow time scale of the instability. These therefore represent transients which can be ignored

given sufficient wall stabilization. This is accomplished by assuming the plasma to be in quasi-equilibrium at all times, effectively setting the mass to zero. In this case, the components of the state vector are only the perturbed coil currents, and the system can be expressed as an ordinary eigenvalue problem:

$$\mathbf{A}\vec{x} = \gamma\vec{x}. \tag{3.6}$$

3.2 Analysis of Simplifying Approaches

Once one has chosen the rigid filament–circuit model approach to analyze the vertical stability problem, there are still many possible model variations from which to choose. A single filament (or many filaments) can be used to represent the plasma. The plasma mass can be included or neglected. The plasma can be taken to be current conserving or flux conserving. Many considerations contribute to the validity and desirability of such assumptions, and we shall discuss some of these in detail.

3.2.1 Massless Approximation

To address the massless approximation, consider the case of a single resistive coil in the vicinity of a plasma represented by an array of filaments which are taken to conserve current, so that the circuit equations given in the previous section are applicable:

$$m\ddot{z} = S_c I_c + S_B z \tag{3.7}$$

$$L_c\dot{I}_c + S_c\dot{z} + r_c I_c = 0 \tag{3.8}$$

After Laplace transforming, we obtain a third order characteristic equation

$$s^3 + \nu_c s^2 + (\nu_w^2 - \nu_B^2)s - \nu_B^2\nu_c = 0 \tag{3.9}$$

where $\nu_c \equiv r_c/L_c$, $\nu_w^2 \equiv S_c^2/L_c m$, $\nu_B^2 \equiv S_B/m$. ν_c is thus the characteristic decay time of the coil, ν_B^2 is proportional to the destabilizing field gradient force term,

and ν_w^2 reflects the eddy current stabilization effect.

The zero-mass limit of this equation yields one root, which is unstable and consists of the characteristic decay frequency with a modification due to eddy current stabilization.

$$s = +\frac{\nu_c}{(\nu_w^2/\nu_B^2) - 1}. \tag{3.10}$$

In this limit the divergence corresponding to the ideal MHD stability boundary occurs when $\nu_w^2 = \nu_B^2$. This also defines the "critical decay index", n_c:

$$n_c \equiv \frac{I_p M_{pc}'^2}{2\pi B_{z0} L_c}, \tag{3.11}$$

describing the limit to curvature which can be stabilized on an ideal timescale. Since $n_c < 0$, decay indexes below this value will be unstable on an Alfvén timescale.

In general when mass is retained the roots of Eq. 3.9 consist of a stable complex conjugate pair with imaginary parts on the order of the Alfvén frequency, and one real unstable root whose magnitude depends on the degree of stabilization. In this case the ideal stability boundary is somewhat more difficult to define. If we transform the characteristic equation into a dimensionless form by dividing through by ν_B, defining $x \equiv s/\nu_B$, $\varepsilon \equiv \nu_c/\nu_B$, $\eta \equiv \nu_w^2/\nu_B^2$, we obtain

$$x^3 + \varepsilon x^2 + (\eta - 1)x - \varepsilon = 0 \tag{3.12}$$

ε is the normalized natural decay frequency, and η can be thought of as a measure of wall stabilization. If we now plot the unstable real root as a function of η, we find a family of curves as ε varies (Fig. 3.1). The figure shows growth rates normalized to the characteristic Alfvén frequency ($x \equiv s/\nu_B$, where s is the actual growth rate), as a function of the stabilization factor, $\eta \equiv \nu_w^2/\nu_B^2$. The curves represent: a) $\epsilon = 10^{-3}$, b) $\epsilon = 0.1$, c) $\epsilon = 0.55$, where $\epsilon \equiv \nu_c/\nu_b$. ϵ is typically less than 10^{-4}.

The figure shows that although $\eta \geq 1$ is no longer such a hard ideal stability boundary as in the massless case, it is still a good approximate boundary for typical cases of interest ($10^{-6} \leq \varepsilon \leq 10^{-4}$). In such a case we see the growth rate change

from resistive frequencies ($x \ll 1$) for $\eta \gtrsim 1$ to Alfven frequencies ($x \sim 1$) for $\eta \lesssim 1$. $\eta \geq 1$ is thus also the approximate boundary for validity of the massless approximation. That is, if η is sufficiently greater than 1, the system is significantly well stabilized on the Alfven timescale, and the massless approximation will be quite good. Of course, if it should become important to follow the transition to ideal instability, for example in analyzing highly elongated equilibria, mass must be retained. The numerical consequence of neglecting plasma mass is that for ideal unstable cases, the eigenvalue corresponding to the previously unstable eigenmode becomes negative. When restricting the study to passive cases this is fine, since such a result is unphysical and immediately recognizable. However, active cases which are driven into ideal instability will masquerade as stable cases. Care must therefore be taken to sweep gains from zero across the gain in question for near-MHD unstable cases. The growth rate divergence and discontinuity will then be apparent.

3.2.2 Plasma Filaments

Now consider the case of a number of filaments representing the plasma. Historically, the most common form of rigid filament plasma model has used a single filament to represent the plasma current, and much success has been ascribed to such an approach [13]. The reasoning is that although a true plasma has a current profile with a characteristic width comparable to the width of the vacuum vessel itself, the magnetic flux at the wall due to the plasma is not significantly different from that due to a single judiciously placed filament. Thus the coupling of the plasma to the wall is thought to be modeled satisfactorily by a single filament. There are several difficulties with this approach. The first is that the accuracy with which a filament approximates the plasma coupling to the wall is dependent on the shape of the wall, and to a lesser extent on the shape of the plasma current profile. This is primarily

due to the form of the "coupling". In both the force balance and circuit equations (Eqs. 3.2 and 3.1), the wall coupling terms are proportional to B_R, a quantity which can differ significantly over crucially stabilizing regions of the vacuum vessel, even though the flux pattern may appear to be qualitatively close in the two cases.

Figures 3.2 and 3.3 show the difference between actual plasma flux and that simulated by a filament at the magnetic axis for a typical C–MOD equilibrium along with the C–MOD vacuum vessel. Although the flux patterns *appear* to be quite similar, the resulting calculated growth rates are very different.

To illustrate, consider the single filament growth rate results summarized in Table 3.1 for two example equilibria, denoted ex1 and ex2. Notation for this table is as follows: MF = multifilament, F_{av} = current weighted destabilizing force gradient averaged over plasma, F_{ma} = local destabilizing force gradient evaluated at magnetic axis, F_{cc} = local destabilizing force gradient evaluated at current centroid, (MA) = plasma-vessel coupling calculated with filament at magnetic axis, (CC) = plasma-vessel coupling calculated with filament at current centroid.

The first case, ex1, is that shown in Figs. 3.2 and 3.3, a fairly well stabilized equilibrium despite its rather high elongation ($\kappa = 1.6$, $\delta_{av} = .35$): its multifilament growth rate is only 147 $\sec^{-1}$. Applying a force gradient equal to the current weighted average over the entire plasma to the single filament located at the magnetic axis for coupling purposes, we find a growth rate of 117 $\sec^{-1}$. Placing the filament at the current centroid for calculation of plasma–vessel coupling yields 135 $\sec^{-1}$, a growth rate much closer to the multifilament value. Using the local force gradient measured at the filament location, both magnetic axis and current centroid give values quite different from the multifilament result.

From these results one might be tempted to conclude that a single filament located at the current centroid is sufficient to calculate the effective plasma–vessel coupling. However, the case just examined represents a quite well–stabilized equi-

Quantity	ex1	ex2
κ_{95}	1.6	1.7
δ_{95}	.35	.38
$MF\ \gamma_+$	147.	751.
$F_{av}(MA)\gamma_+$	117.	419.
$F_{av}(CC)\gamma_+$	135.	426.
$F_{ma}(MA)\gamma_+$	56.	41.
$F_{cc}(CC)\gamma_+$	98.	43.

Table 3.1: Summary of single filament growth rate comparisons for 2 example equilibria. See text for notation.

librium. The situation is worse for highly elongated equilibria with growth rates significantly greater than the conductor L/R time (which we shall refer to as "highly unstable"). Consider the second example shown in the table, ex2, an equilibrium with $\kappa_{95} = 1.7$, we note in particular the difference between the multifilament growth rate of 751 $\sec^{-1}$ and the two single filament results using the average force gradient while located at the magnetic axis (419 $\sec^{-1}$) or current centroid (426 $\sec^{-1}$). This clearly constitutes an unacceptable discrepancy.

Thus, despite the use of the "correct" destabilizing force, the growth rate can be significantly different, even when the flux pattern due to the plasma appears to be approximately the same. We must emphasize that the only difference in these cases described above is in the plasma–vacuum vessel inductive coupling.

Table 3.1 has also demonstrated the serious difficulty involving the effects of vacuum fields on the plasma. There is no guarantee that a filament placed at an arbitrary location (such as the magnetic axis or current centroid) for purposes of calculating the decay index will see the correct net destabilizing force, and will thus find the correct growth rate. This problem is illustrated dramatically in Figs. 3.4 and 3.5, which show growth rates as a function of radial position of a single filament along the plane at the Z–position of the current centroids for two highly unstable example C–MOD equilibria. Current centroids are denoted by R_0 in the figures,

and in both cases the magnetic axis is located at 66.0 cm. Fig. 3.4 corresponds to a typical example equilibrium with $\kappa_{sep} = 1.8$, $\delta = .35$, and multifilament rigid growth rate of 390. sec^{-1}. and Fig. 3.5 corresponds to a typical example equilibrium with $\kappa_{sep} = 2.0$, $\delta = .32$, and multifilament rigid growth rate of 950. sec^{-1}.

In the case shown in Fig. 3.4, the major radial position which would yield the correct (multifilament) growth rate is quite distant from both the current centroid and the magnetic axis. The situation is particularly bad for equilibria such as that represented by Fig. 3.5, since in this case there is no apparent location for which a single filament will yield the same growth rate as the multifilament model.

We note in passing that active analyses also tend to be very sensitive to choice of filament model, since using a single filament is essentially the same as drastically increasing the peakedness of an equilibrium which may not originally have been highly peaked. In particular, this can significantly decrease the coupling between control coil and plasma, even when the vacuum vessel coupling may not be as strongly affected (since the vacuum vessel effectively surrounds the plasma).

Having argued that some degree of spatial distribution is important in a filamentary model of a plasma used in rigid models, it is reasonable to ask how many filaments are sufficient. Figs. 3.6 and 3.7 show convergence of growth rate values calculated with increasing numbers of filaments modeling the plasma for the equilibria used in Figs. 3.4 and 3.5 respectively.

The figures show that for both of these typical C–MOD cases, only about 5 filaments need be used for the calculated growth rate to come within 10%, and roughly 20 filaments or more should be used to come within 1% of the converged growth rate. To perform this convergence study, for each choice of filament number the plasma was divided into a rectangular grid having the desired number of elements, and the filament corresponding to each grid element was located at the current centroid of that element.

That roughly 5 filaments are so effective reflects both the low order of significant multipole moments in the vacuum magnetic field, and the low order of significant toroidal current moments in the plasma current distribution.

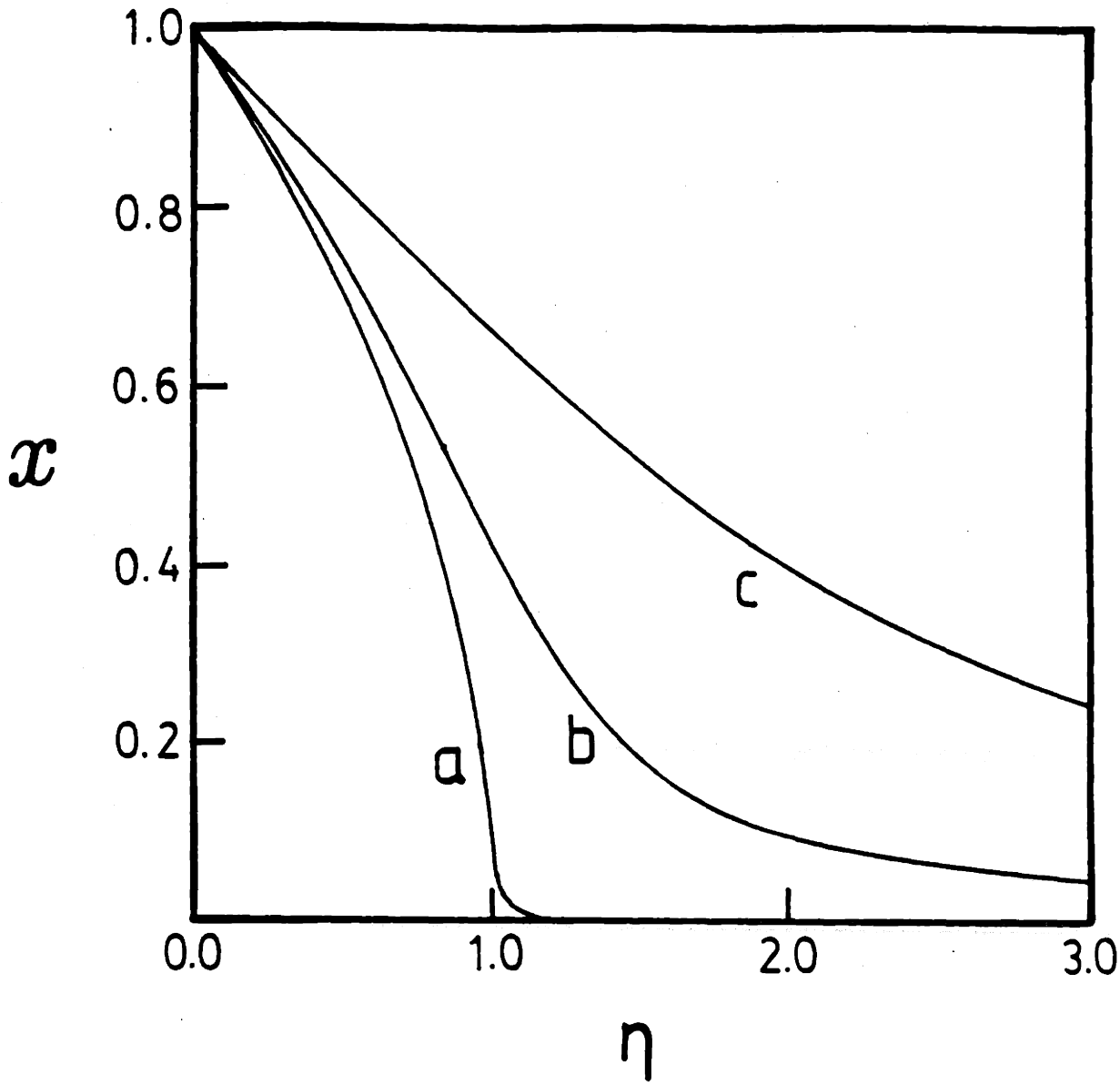

Figure 3.1: Growth rates normalized to the characteristic Alfvén frequency ($x \equiv s/\nu_B$, where s is the actual growth rate), as a function of the stabilization factor, $\eta \equiv \nu_w^2/\nu_B^2$.

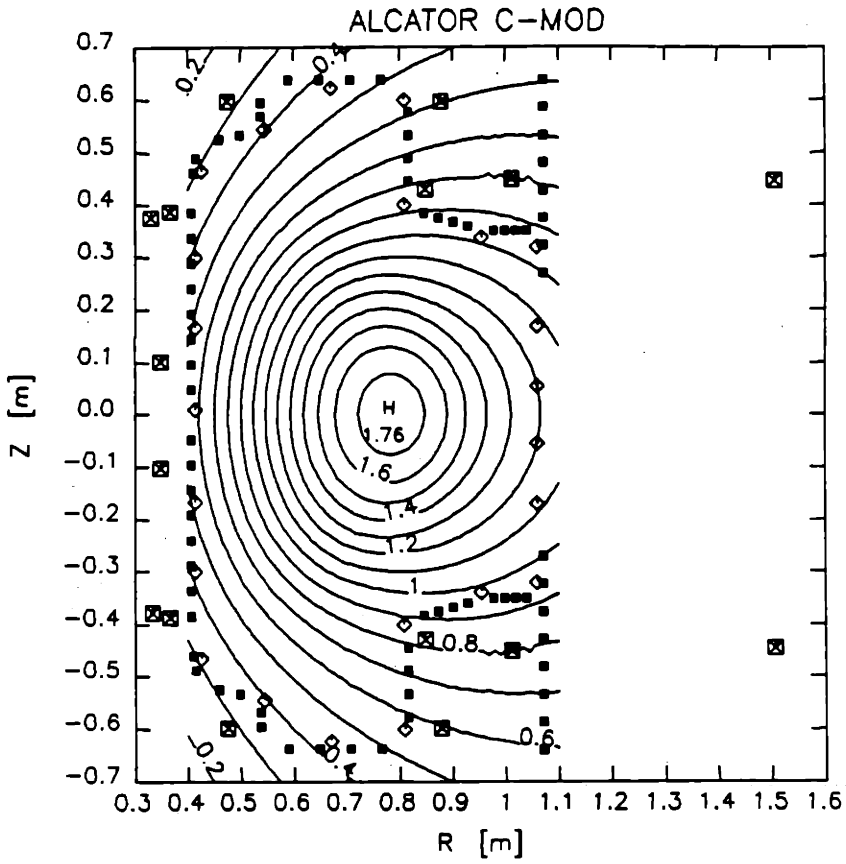

Figure 3.2: Flux due to actual plasma current distribution for equilibrium ex1.

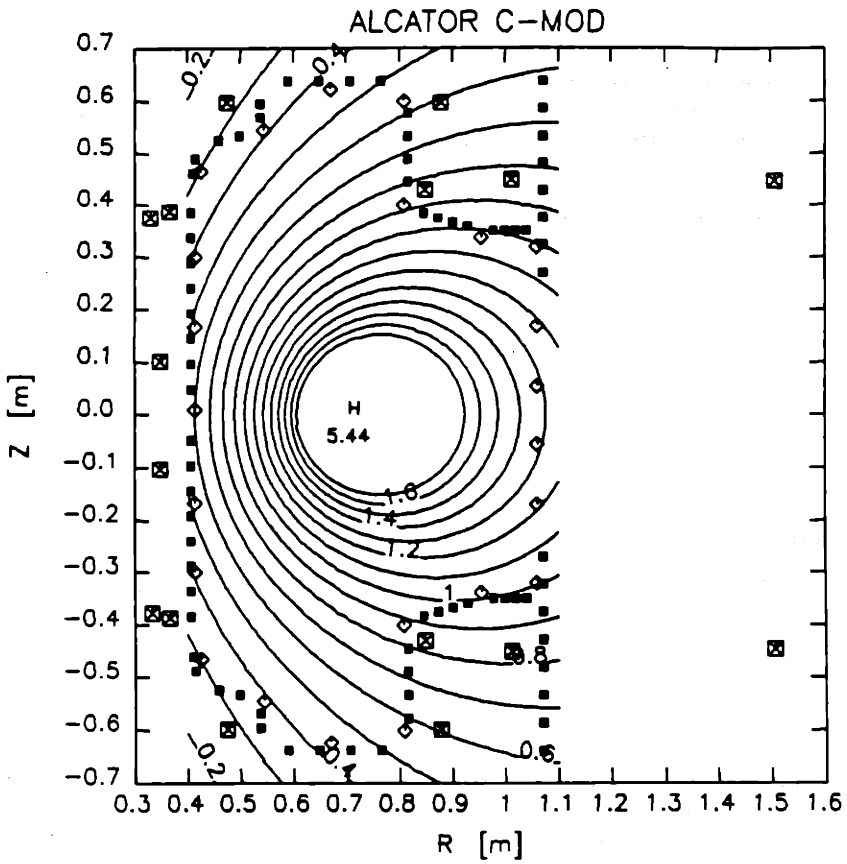

Figure 3.3: Flux due to a single filament modeling equilibrium ex1, located at the ex1 current centroid.

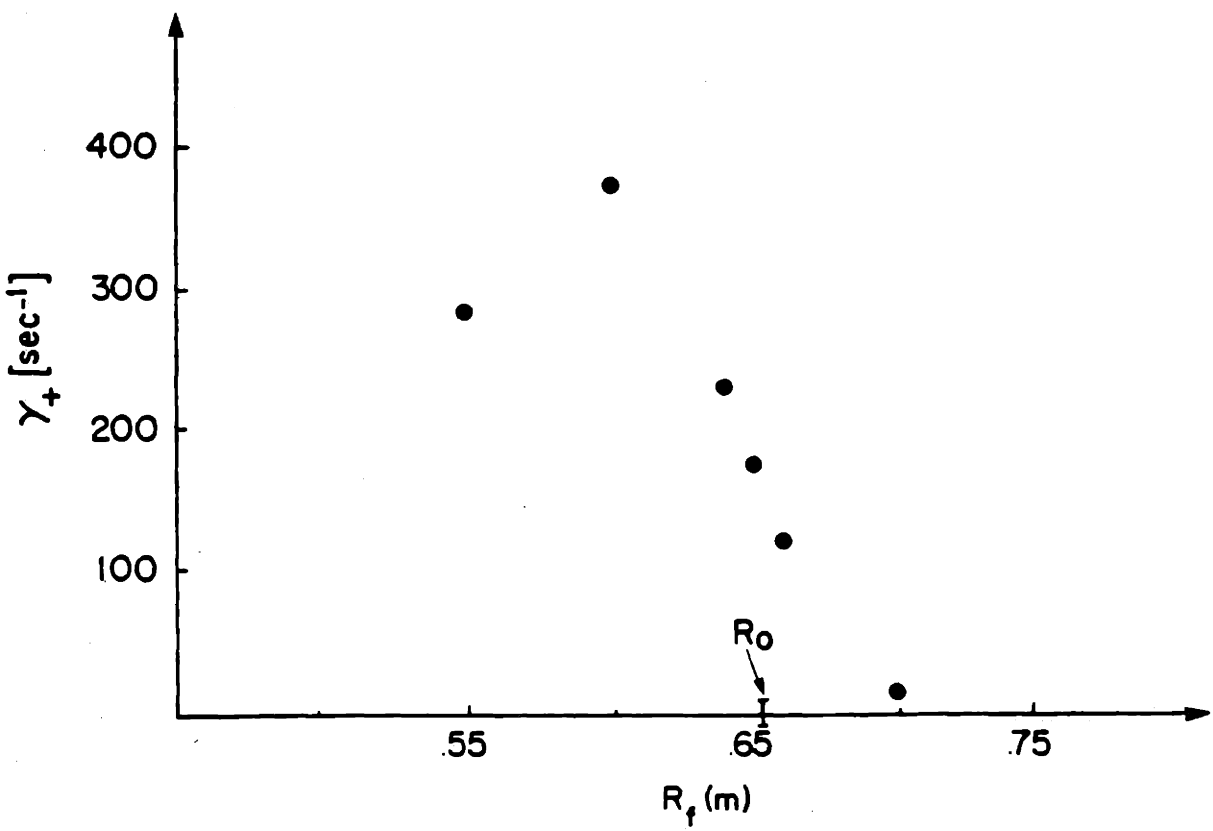

Figure 3.4: Growth rates for single filament plasma as a function of filament radial position on the midplane (eq6). R_0 denotes the current centroid, at $R = 0.65m$, while the magnetic axis is located at $R = 0.665m$.

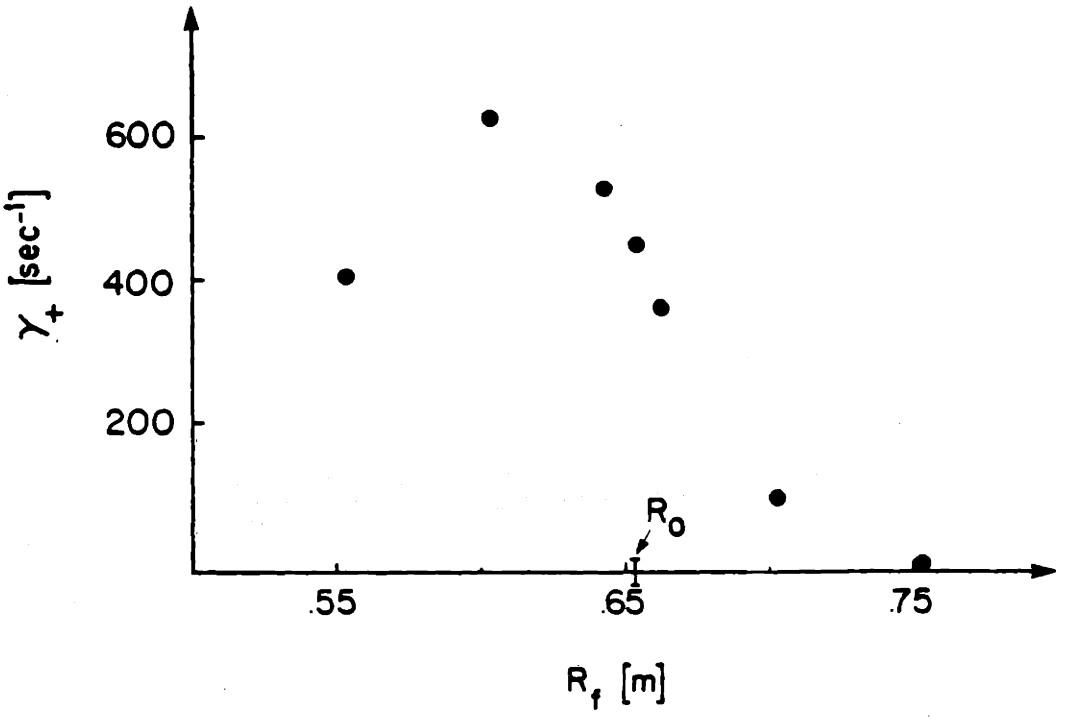

Figure 3.5: Growth rates for single filament plasma as a function of filament radial position on the midplane (eq7). R_0 denotes the current centroid, at $R = 0.65m$, while the magnetic axis is located at $R = 0.665m$.

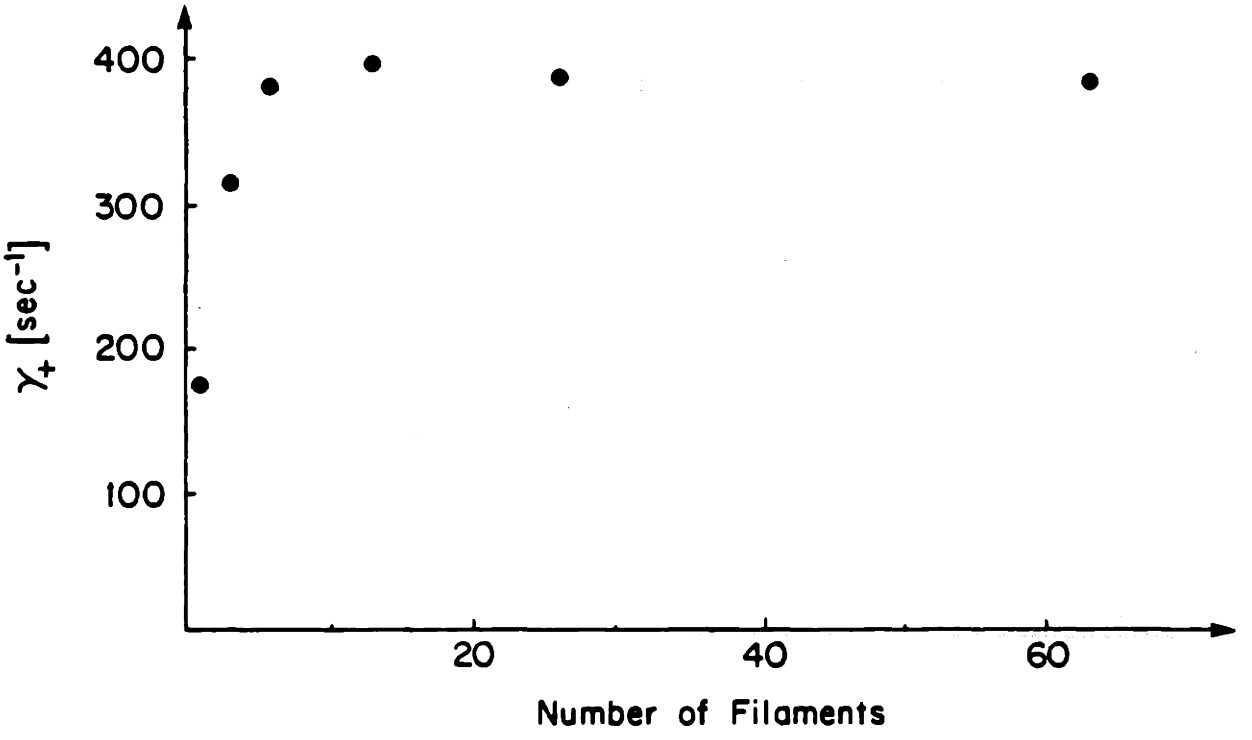

Figure 3.6: Growth rate as a function of number of plasma filaments for example $\kappa = 1.8$, $\delta = .35$ equilibrium.

3.3 Marginal Wall Position Studies

Several alternative methods of analysis are available with which to benchmark the rigid plasma–circuit model. Analytic solutions exist for simplified geometries, in particular for marginal wall positions. Full MHD analysis codes (such as GATO) can provide marginal wall positions with more realistic geometries and complex displacement profiles. To benchmark resistive growth rates, either actual machine data or a more detailed tokamak simulation must be used. Here we shall consider marginal wall position comparisons with analytic cases for rough qualitative benchmarking.

Haas [12] has demonstrated that there is a maximum distance at which a perfectly conducting wall will stabilize the vertical mode for an elliptical plasma. This provides a rough test of the general reliability of the rigid model: if a resistive wall is used we would expect to see a similar critical distance manifest itself. This would be the point at which the mode becomes ideal MHD unstable rather than unstable on the slow resistive time scale. For low β cases to be stable on the ideal timescale this criterion requires that:

$$\left(\frac{r_p}{r_w}\right) \gtrsim \left(\frac{\kappa - 1}{\kappa + 1}\right)^{1/2} \tag{3.13}$$

Here r_p is the characteristic plasma minor radius, r_w is the characteristic conducting wall minor radius, both measured from the magnetic axis along the midplane in the outboard direction, and $\kappa \equiv b/a$ is the plasma elongation. For an elliptical equilibrium with κ of 1.8, this criterion for ideal MHD stability is:

$$\left(\frac{r_w}{r_p}\right) \lesssim 1.97 \tag{3.14}$$

Expecting rough agreement even for the unusual case of an Alcator C-MOD equilibrium, the rigid filament plasma–circuit model was used to predict the critical distance for onset of ideal MHD instability for two vacuum vessel wall shapes.

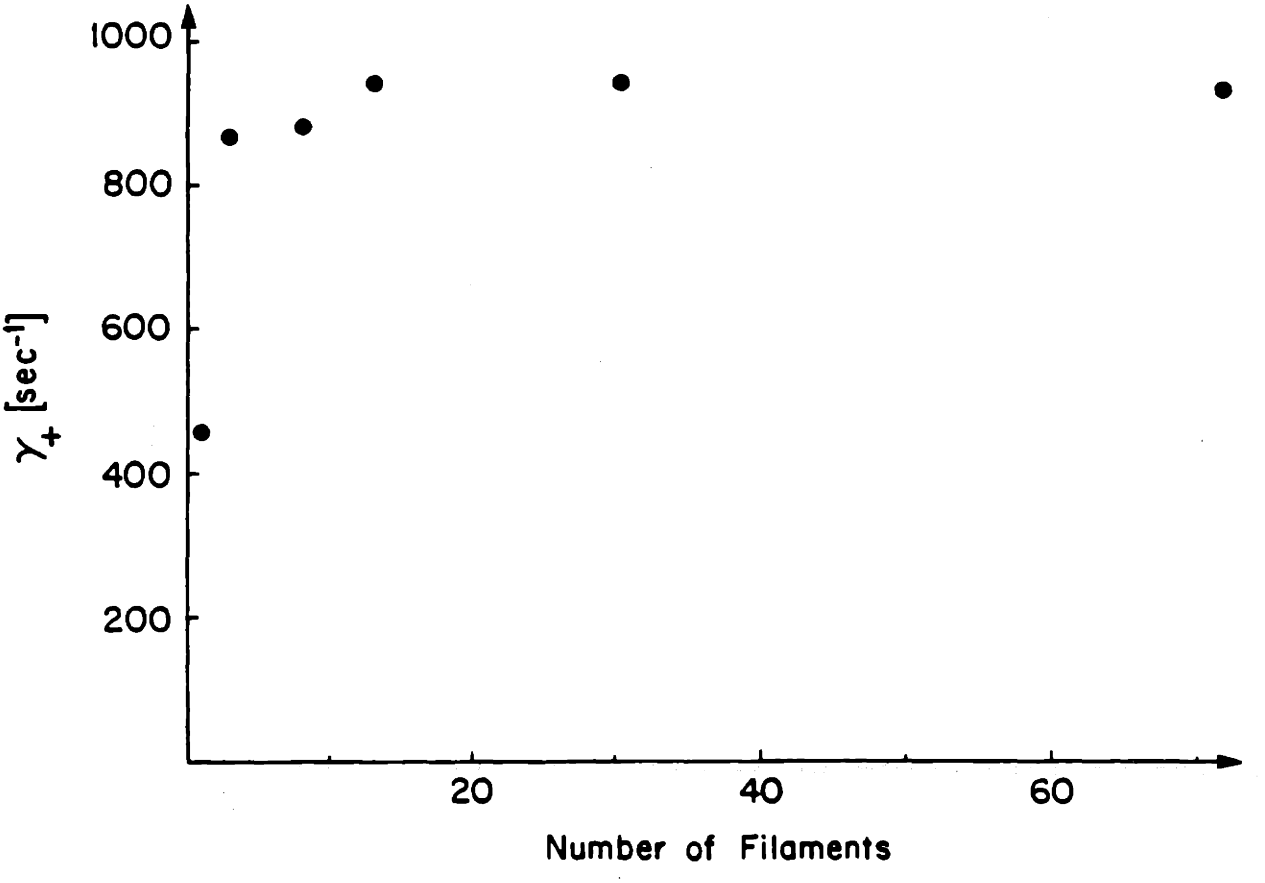

Figure 3.7: Growth rate as a function of number of plasma filaments for example $\kappa = 2.0$, $\delta = .32$ equilibrium.

Figures 3.8, 3.9, and 3.10 show the real parts of all of the system eigenvalues, plotted on an Alfven-like frequency scale to reveal the transition to ideal instability. An array of conductors modeling a given wall shape is enlarged conformally from an initial position at the plasma surface. At a critical value of r_w/r_p, the real parts of two of the modes go rapidly from the resistive frequency regime to an Alfven growth/damping rate. One of these is the unstable root, and this is the critical point we wish to compare with the Haas result.

Because the Haas criterion was calculated for a conformal (elliptical) wall, the first vacuum vessel shape chosen was a D-shaped array of conductors approximately conformal to the plasma surface for a typical Alcator C-MOD equilibrium. Using the multifilament plasma model, this array was enlarged from an initial configuration lying on the plasma surface (Fig. 3.8). The ideal instability onset point was found to occur at:

$$\left(\frac{r_w}{r_p}\right) = 2.00. \tag{3.15}$$

Still using a multifilamentary plasma, the critical distance was also determined for the actual C-Mod vessel, sweeping its size using the same algorithm as in the conformal case (Fig. 3.9). As expected, the resulting value,

$$\left(\frac{r_w}{r_p}\right) = 1.80, \tag{3.16}$$

indicates that such a highly non-conformal wall must be closer to the plasma than the conformal wall must be. Nevertheless, even this critical distance is encouragingly close to the Haas prediction.

The conformal shell case was repeated using a single filament located at the current profile centroid (Fig. 3.10). In this case the result is significantly more optimistic, yielding a critical distance of

$$\left(\frac{r_w}{r_p}\right) = 2.28 \tag{3.17}$$

This greater optimism for the case of a single filament at the current centroid is consistently observed and emphasizes the need for a multifilament model. Note that as the magnetic axis is further out than the current profile centroid, placing the single filament on the magnetic axis yields even more optimistic results (due to the more favorable decay index with increasing major radius).

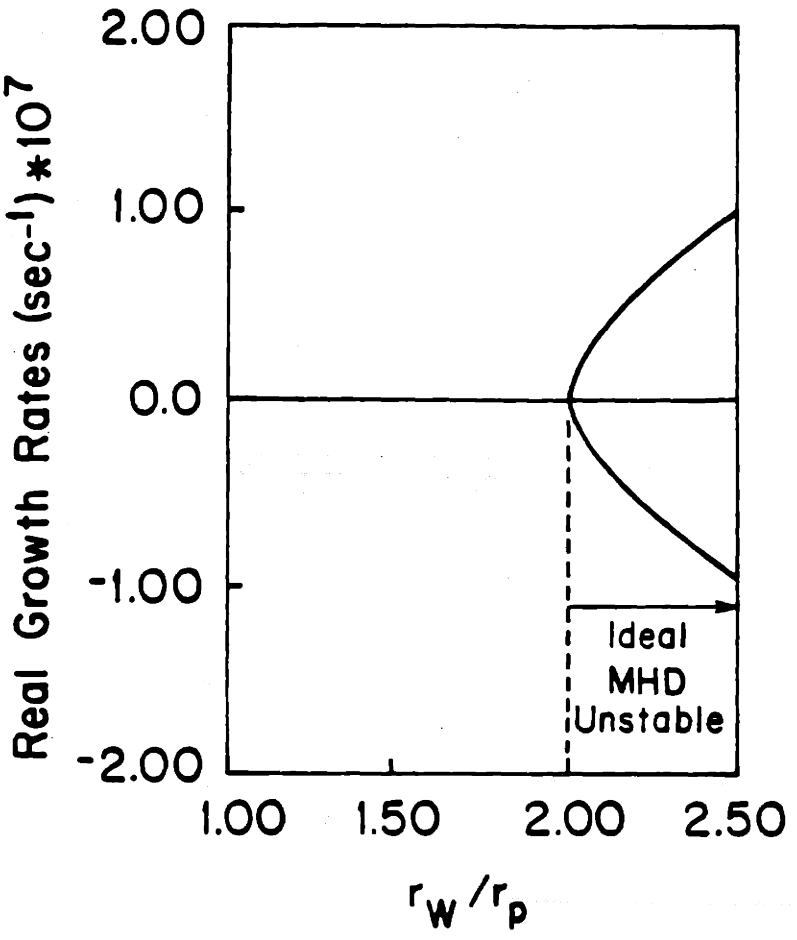

Figure 3.8: Growth rates as a function of wall distance, illustrating the critical distance for onset of ideal instability for a conformal D-shaped wall and a multifilament rigid plasma model.

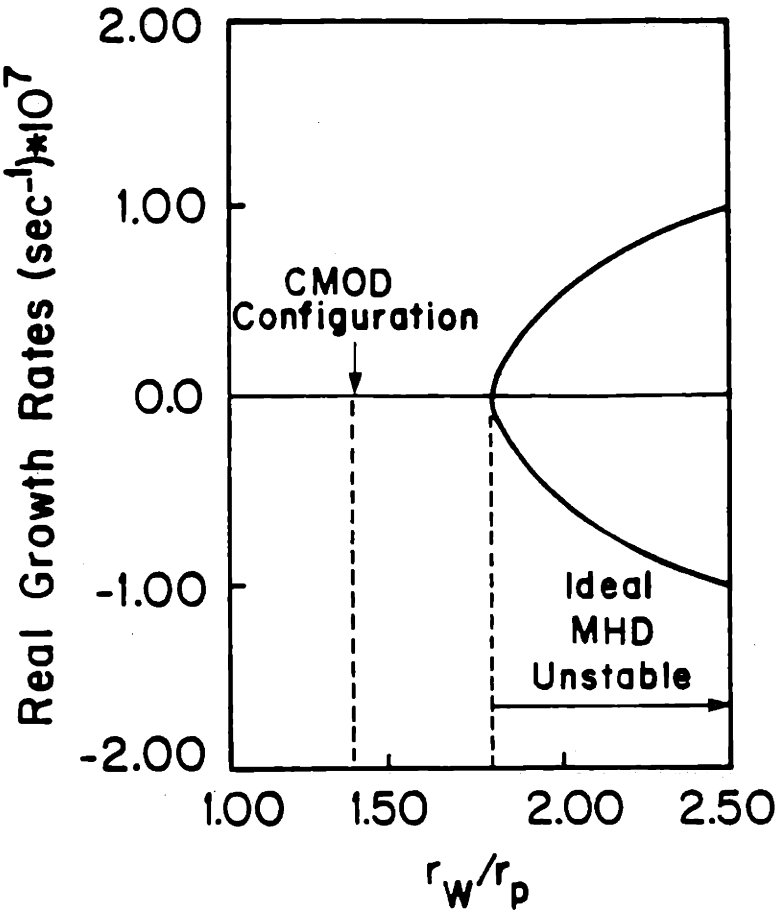

Figure 3.9: Growth rates as a function of wall distance, illustrating the critical distance for onset of ideal instability for a C-MOD vacuum vessel model and a multifilament rigid plasma model.

Major Radius	R_0	.665 m
Minor Radius	a	0.21 m
Toroidal Field	B_T	9 T
Plasma Current	I_p	3 MA
Elongation	κ	1.8 (typ)
Triangularity	δ	0.4 (typ)
Flat-top Duration	(@ 9 T)	1 sec
Flat-top Duration	(@ 5 T)	7 sec

Table 3.2: Essential Machine Parameters for Alcator C–MOD.

3.4 Alcator C–MOD Vertical Stability Analysis Using the Rigid Model

3.4.1 Machine Description and General Discussion

Alcator C–MOD is a high performance tokamak intended to be somewhat prototypical of the Compact Ignition Tokamak (CIT). As such it will provide a test bed for many of the critical issues to be faced in the design and operation of CIT. The essential machine parameters are summarized in Table 3.2.

Figure 3.11 shows the physical geometry of the Alcator C–MOD poloidal cross-section, while Fig. 3.12 shows the vacuum vessel and EF coil discretization for stability analysis. Referring to the physical drawing, Fig. 3.11, notice that there is a total of 13 EF coils. These include a novel "notched" OH stack, consisting of 3 separate current-carrying elements. OH1 extends the entire height of the vacuum vessel and typically carries the bulk of the induction current which produces the loop voltage and thus drives the ohmic current in the plasma. OH2–Upper and OH2–Lower (which we denote by OH2U/L) carry independently controllable currents to assist in producing up–down nonsymmetric plasmas. The vertical control coils, labeled EFC in Fig. 3.11, are driven by a fast, chopping power supply with response time of less than 1 ms. All of the other coils are driven by slower 12 phase supplies.

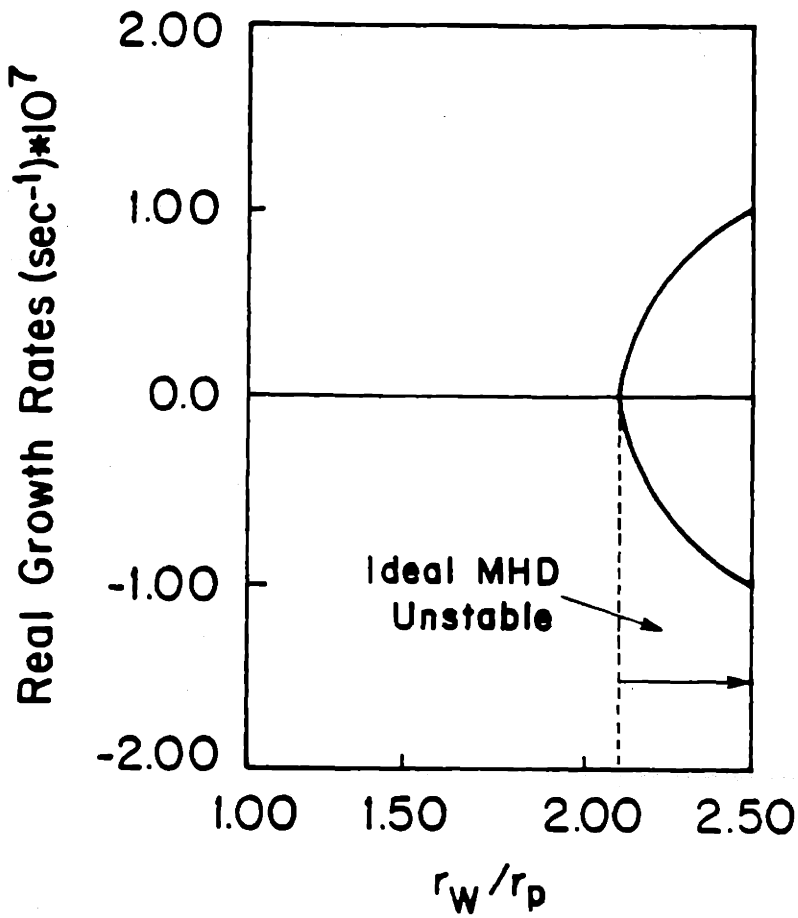

Figure 3.10: Growth rates as a function of wall distance, illustrating the critical distance for onset of ideal instability for a conformal D-shaped wall and a single filament rigid plasma model.

C–MOD will confine a strongly shaped, diverted plasma, with maximum elongation $\kappa \gtrsim 1.8$. It is the great complexity of the resulting system geometry which originally motivated intense study of the vertical control problem in C–MOD. These complex features include D-shaped single and double null plasmas and a roughly rectangular vacuum vessel with a high degree of diagnostic access, producing many interruptions in toroidal current paths, In particular, the poor stabilization resulting from this combination of characteristics necessitates a highly sophisticated control system. To gain some feel for the stabilization effects of the resistive elements, it is of interest to examine some characteristic resistive decay times of the system.

The diffusive penetration time of the vacuum vessel, τ_D [1], is defined as:

$$\tau_D \equiv \frac{\mu_0 a d}{\eta} \tag{3.18}$$

where a is a rough equivalent radius for a circular model of the vacuum vessel wall, d is the thickness of the vacuum vessel wall, and η is the resistivity of the vacuum vessel. For Alcator C-MOD, we take $a = 50$ cm, $d = 1.27$ cm (.5 in), and $\eta = 70$ $\mu\Omega$-cm (the resistivity of stainless steel at room temperature), and we obtain $\tau_D \simeq 11$ ms. For the EFC control coils, characteristic of copper elements in the system in general, the L/R time (coil inductance over coil resistance at room temperature) is

$$\left(\frac{L}{R}\right)_{Cu} = 90 \text{ ms.} \tag{3.19}$$

The vacuum vessel model itself has many possible decay modes due to the large number of coils used to represent it. The dominant stable midplane–antisymmetric mode of the vacuum vessel alone (i.e. with no plasma and no EF coils included) is of particular interest. This is the lowest order mode which couples to vertical plasma motion. The current distribution in surrounding conductors for this mode is shown in Fig. 3.13. The radius of each circle in the figure is proportional to the current in that element, and positive or negative currents are denoted by "+" or "." symbols respectively. As one would expect, the dominant antisymmetric mode has a roughly

$\sin\theta$ dependence of current distribution on poloidal angle. The corresponding decay time is

$$\left(\frac{L}{R}\right)_{Antisym} = 8.9 \text{ ms.} \tag{3.20}$$

For completeness we include the dominant midplane–symmetric mode, which is the slowest eigenmode of the vacuum vessel. The current distribution of this mode is shown in Fig. 3.14, and its decay time is

$$\left(\frac{L}{R}\right)_{Sym} = 15 \text{ ms.} \tag{3.21}$$

If we now include EFCU/L together with the vacuum vessel and examine the resulting dominant asymmetric and symmetric modes, we find the current distributions shown in Figs. 3.15 and 3.16 respectively. Their corresponding decay times are

$$\left(\frac{L}{R}\right)^{VV+EFC}_{Antisym} = 85 \text{ ms,} \tag{3.22}$$

and

$$\left(\frac{L}{R}\right)^{VV+EFC}_{Sym} = 100 \text{ ms.} \tag{3.23}$$

Notice the strong current component in the EFC coils for these modes. Note also that for illustrative purposes the EFC coils have been allowed to assume independent currents in this example. In operation these coils are connected in antiseries and are driven by the same power supply ("antiseries" connnected coils carry the same magnitude of current, but the current flowing in one coil is oppositely directed from the current flowing in the other).

Considering these modes and their decay times, it is clear that despite the discreteness of the EF coils, they can in fact contribute quite significantly to stabilization.

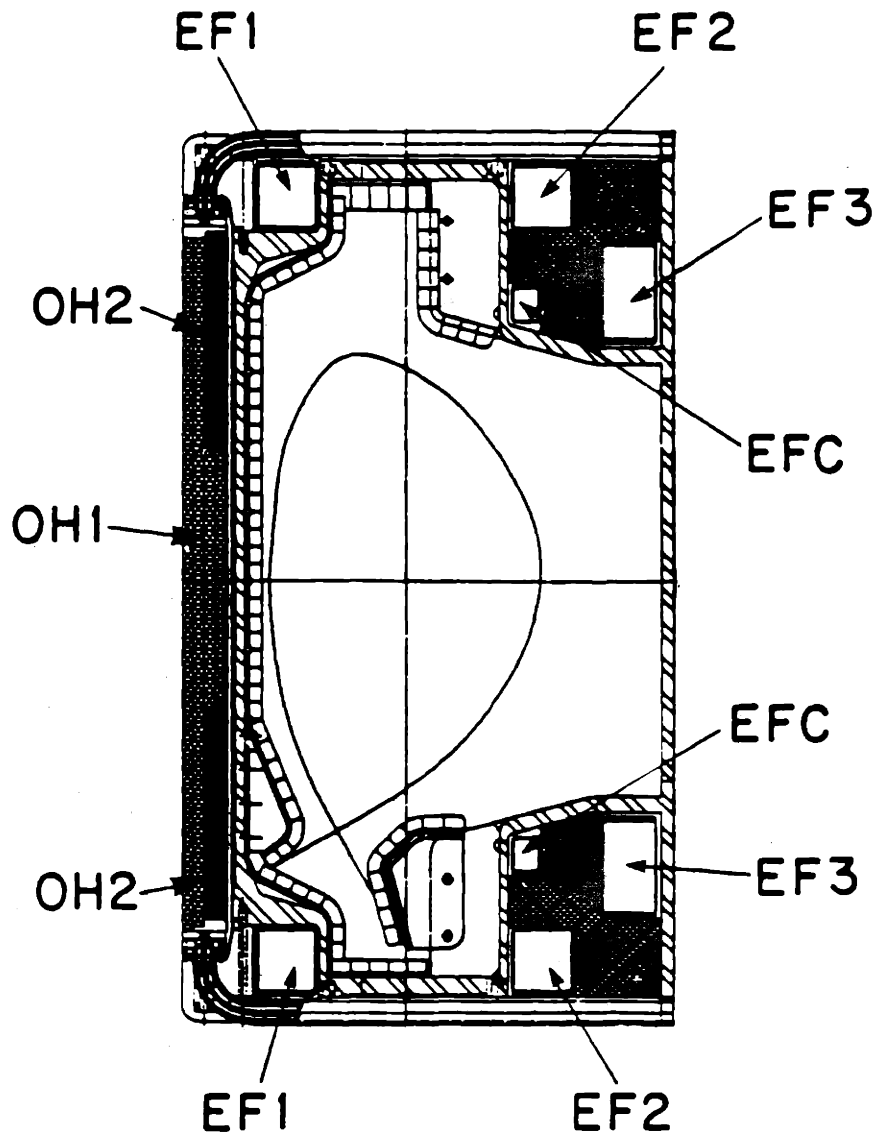

Figure 3.11: Alcator C-MOD machine geometry. Arrows indicate EF coils and the OH stack. EFC denotes the vertical control coil pair. Note the "notched" OH coil design, consisting of the single large OH1 segment and two independently driven OH2 coils.

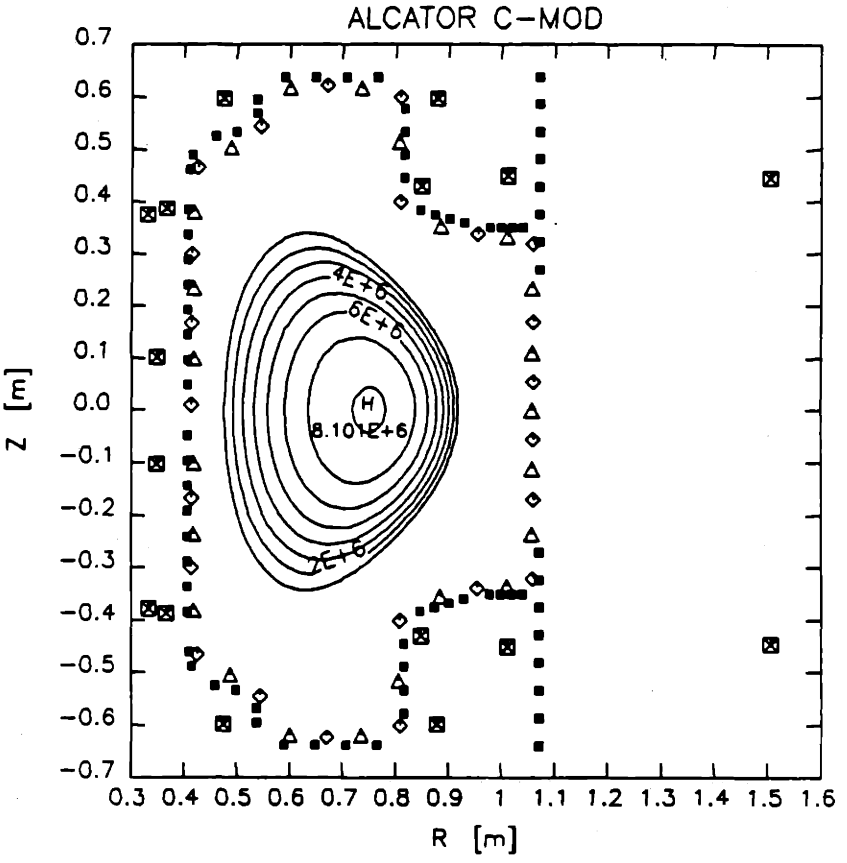

Figure 3.12: Discretized conductor model of the Alcator C–MOD machine geometry. Solid squares denote vacuum vessel elements, and EF coils are represented by open squares marked with "X". Diamonds denote flux loops, and triangles, B_p coils. Current contours of a typical equilibrium are shown.

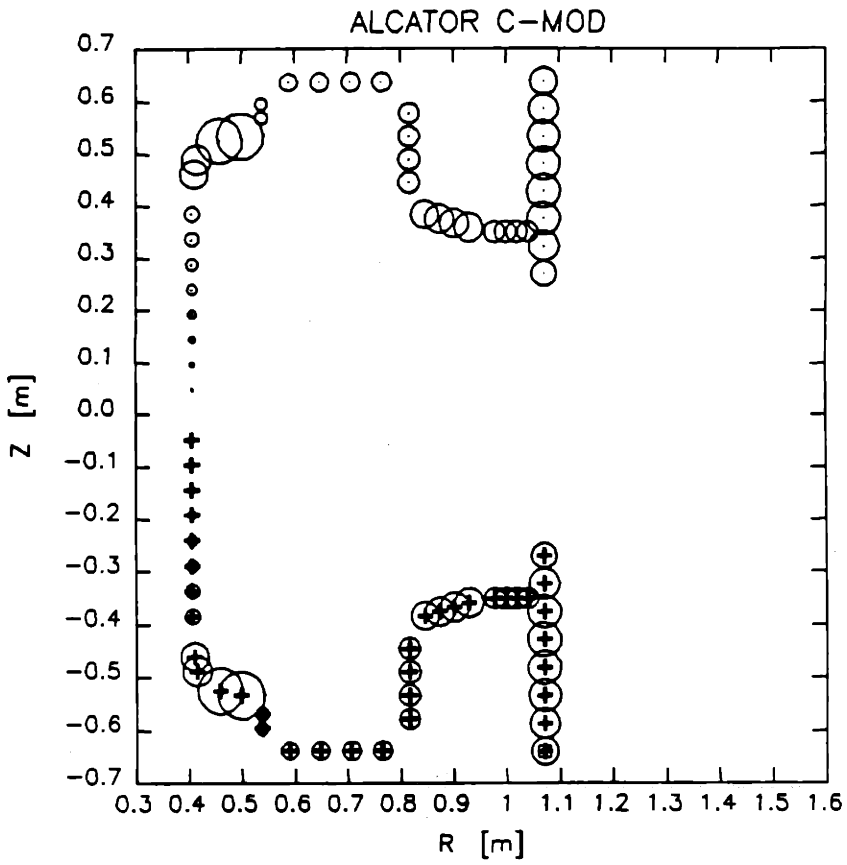

Figure 3.13: Current distribution for the dominant asymmetric pure vacuum vessel mode; the plasma and EF coils are absent.

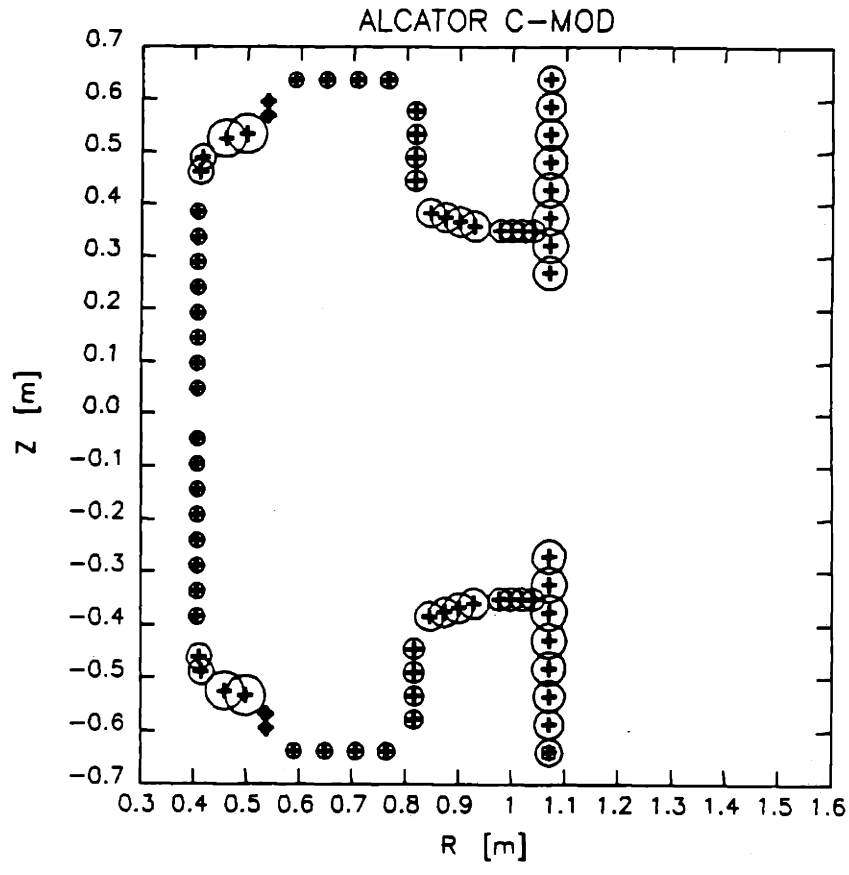

Figure 3.14: Current distribution for the dominant symmetric pure vacuum vessel mode; the plasma and EF coils are absent.

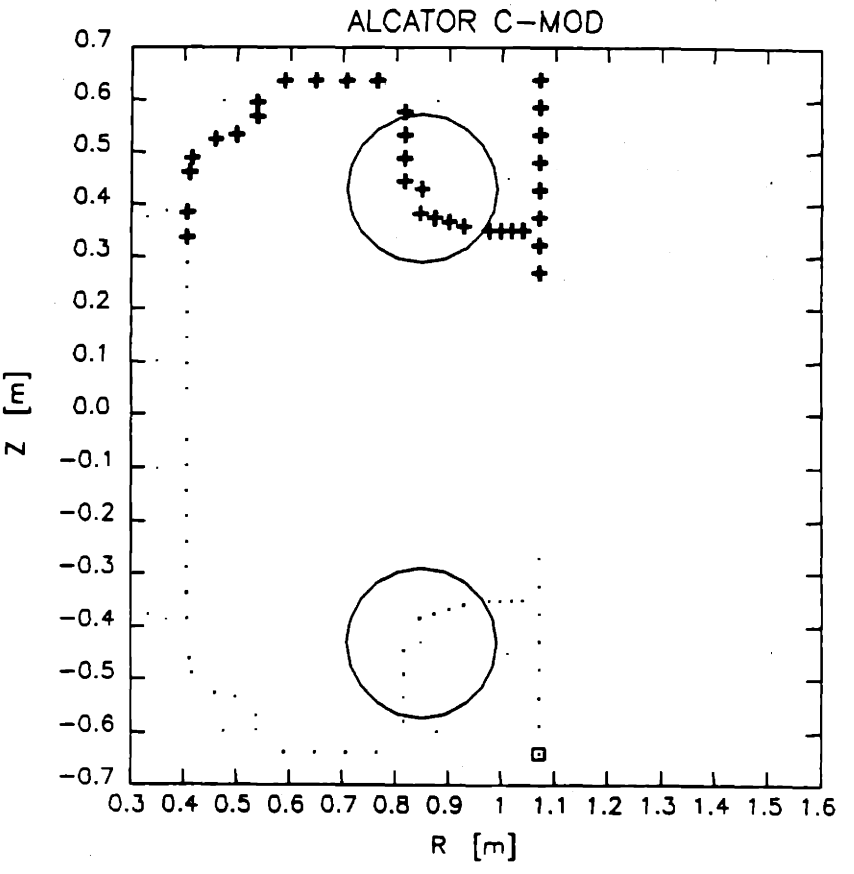

Figure 3.15: Current distribution for the dominant asymmetric mode with vacuum vessel and EFCU/L included; the plasma is absent.

3.5 Passive Results

Calculation of passive growth rates alone for the vertical instability can provide a great deal of valuable information to the control designer. Comparison of the instability growth rates calculated under various conditions can serve as a "zero–order" test of the possibility of stabilization under those circumstances. Comparing the growth rates for different stabilizer geometries, for example, provides a method for discriminating between candidate conductor configurations. Comparing the typical response time of feedback power supplies to the growth rate aids in the rough estimation of the achievability of equilibria. Identifying the point of onset of ideal MHD instability supplies an important limit in machine operation.

In this section we shall explore the application of passive analysis with rigid filament models to tokamak design. We describe a set of sample equilibria, and discuss the actual design process for Alcator C–MOD. In this regard, we examine the appropriate use of passive data in the analysis of wall and EF coil design, and discuss other aspects of the stability analysis which are well addressed by the simple model.

3.5.1 C–MOD Equilibria

To illustrate the use of the rigid filament model in passive stability evaluation studies, we present a set of typical Alcator C–MOD equilibria, which represent a range of elongations and triangularities. This set comprises a range of theoretically achievable equilibria used in the early design of the machine, and yielded results which had a major impact on the final vacuum vessel and EF coil configurations. All of these equilibria are characterized by $q_0 \simeq 1$, $R_{ma} \simeq 67$ cm, and $Z_{ma} = 0$. Here the subscript "ma" denotes magnetic axis quantities. The corresponding *separatrix* elongations and triangularities of this "original design set" are summarized in Table

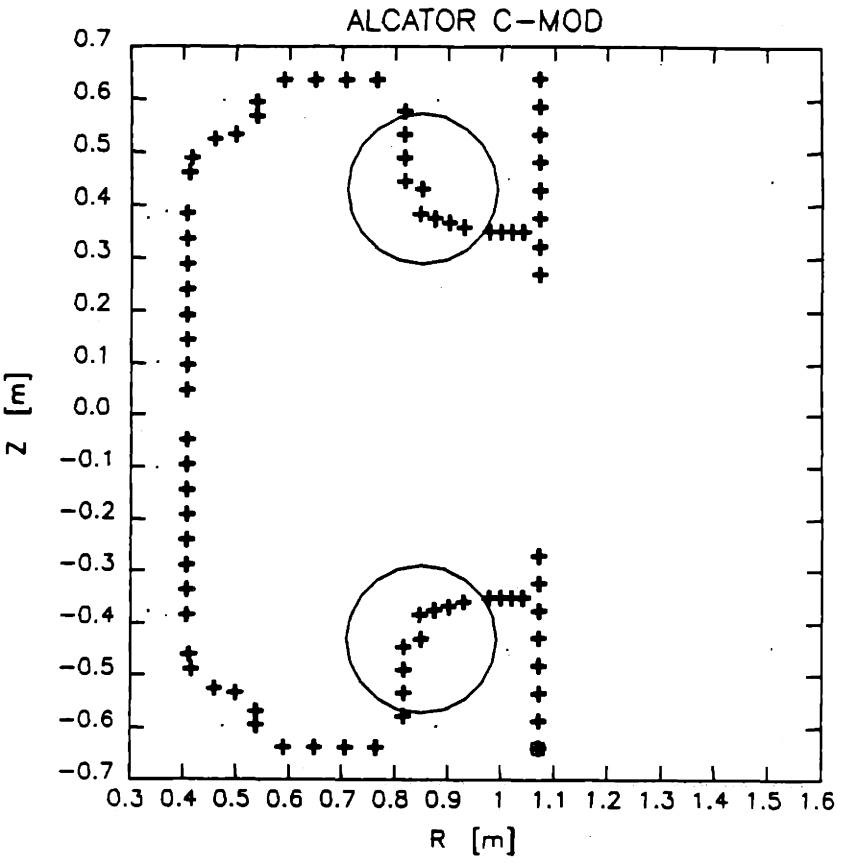

Figure 3.16: Current distribution for the dominant symmetric mode with vacuum vessel and EFCU/L included; the plasma is absent.

Equilibrium	κ_s	δ_s	γ_{efc}	γ_{oh2}
eq1	1.65	.33	25.	57.
eq2	1.81	.33	466.	484.
eq3	1.97	.30	894.	902.
eq4	1.80	.56	446.	463.
eq5	1.80	.28	424.	442.
eq6	1.80	.35	388.	–
eq7	2.00	.32	945.	–

Table 3.3: Separatrix elongations, and triangularities, and growth rates for the "Original Design Set" of equilibria, used in the early vacuum vessel and EF coil design of Alcator C–MOD. The γ subscripts refer to passively stabilizing EF coil pairs.

3.3. For reference purposes the equilibria are denoted by the labels "eq1" through "eq7".

The Alcator C–MOD experimental mission entails high flexibility of shaping and the stable achievement of maximum elongations on the order of $\kappa_{sep} \sim 1.8 - 2$, hence the range of shaping evident in Table 3.3. An example of the discretized model for one of these (eq7) is shown in Fig. 3.19. Notice the asymmetry in filament distribution arising from the single null plasma configuration, despite the fact that both magnetic axis and current centroid are located on the midplane. The plasma discretization algorithm used here is the same as that described in Sec. 3.2.2.

The original equilibrium data was calculated on a 65×65 grid, so this procedure actually constitutes a "rediscretization" of the equilibrium solution, in order to reduce the number of calculations necessary. The nominal number of elements used is approximately 100 in all the cases shown. Filaments with zero–current resulting from this process are not included in the calculation and are not shown in Fig. 3.19.

Elongation	Rect.VV	Int.Cond.	Ext.VV	Ext.VV/EFC
$\kappa_{sep} = 1.85$	1273.	396.	460.	306.
$\kappa_{sep} = 2.00$	1.4×10^6	2465.	1238.	1076.

Table 3.4: Passive growth rates for stabilizing conductor configuration studies.

3.5.2 Vacuum Vessel Studies

To understand the use and practical impact of this particular rigid filament model implementation, it is of interest to examine the history of the Alcator C–MOD vacuum vessel design. As previously noted, the original vacuum vessel design was essentially a rectangular "picture–frame", a geometry chosen to minimize machining costs, simplifying much of the construction while still maintaining structural strength. This early geometry is schematically illustrated in Fig. 3.17. The discretized vessel (and filament) model used for the vertical stability analysis is shown in Fig. 3.18. A range of highly elongated C–MOD equilibria were tested with this vacuum vessel for a variety of stabilizing conductor configurations. Some selected results of this procedure are shown in Table 3.4 for two highly elongated equilibria. In this table, "Rect.VV" refers to the original rectangular picture frame vacuum vessel design, "Int.Cond." refers to a Cu conductor inside the rectangular vacuum vessel, "Ext.VV" refers to an extended vacuum vessel wall in the upper and lower outboard region (see Fig. 3.11), and "EFC" refers as always to the EFC coil pair (also as shown in Fig. 3.11). Hence "Ext.VV/EFC" represents the actual final design.

Note that because for many of the configurations studied the plasma was MHD unstable, the mass was retained in the calculations according to the procedure described in Section 3.1. This results in calculated growth rates in excess of 10^6 sec^{-1} with the onset of ideal MHD instability.

From these passive results alone, it is clear that the rectangular vessel could not satisfactorily stabilize the kinds of equilibria desired for C–MOD. A variety

of alternative configurations which attempted to minimize the modification of the basic rectangular shape of the vacuum vessel were analyzed. These included several different designs of additional stabilizer suspended within the original vessel, passive conductors mounted on already existing hardware within the original vessel, and the somewhat extensive redesign of the vessel wall indicated in Table 3.4 as the final design. Some of the results of these comparisons are shown in the table. These passive results, along with active simulation confirming the feasibility of feedback stabilization, led to the decision to undertake a major modification of the vacuum vessel design. This modification changed the vessel design from the original rectangular picture frame to that shown in Fig. 3.11. Rigid analysis thus predicts that the final design configuration will succeed in passively stabilizing the nominal $\kappa_{sep} = 2$ case sufficiently well to allow stable control of the vertical instability with the available power supplies.

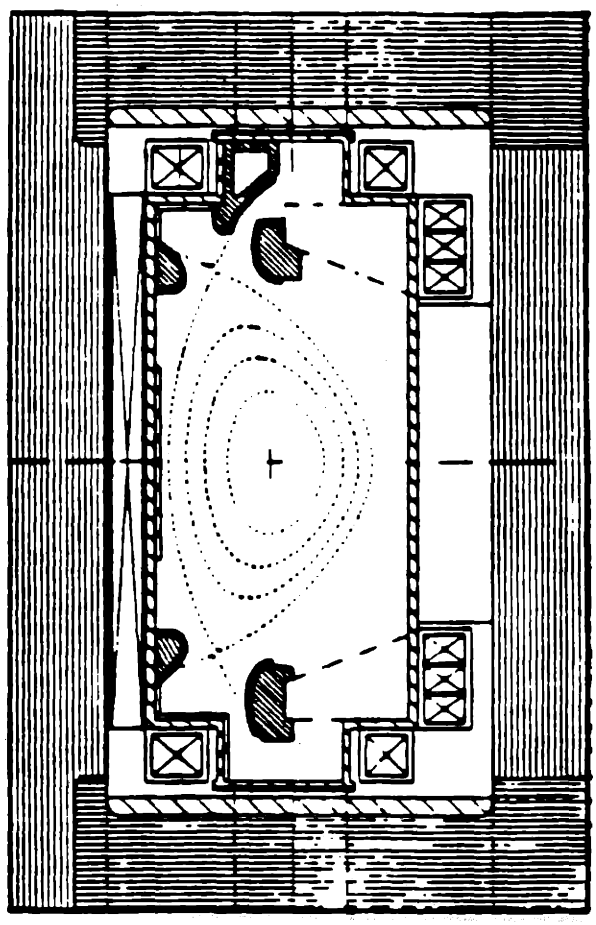

Figure 3.17: Original rectangular "picture-frame" vacuum vessel configuration.

3.5.3 Stabilizing EF Coils

A fast circuit model code is ideal for studying the relative passive stabilization effects of various control coil placements during the design process. The coils can be repositioned easily in the model, and the effect of the new configuration on stability can be rapidly assessed. These coils will typically be the closest copper coils which are well-coupled to the plasma vertical motion, and should therefore have a strong influence on passive stability properties.

In discussing the vacuum vessel redesign we have alluded to the addition of the EFC control coils, but the competing EF coil stabilization analysis also deserves brief mention. In fact, many control coil positioning options were investigated during the design of C–MOD, but we shall address the passive stability for two cases alone. They correspond to control on the OH2 portions of the "notched" OH stack, or on the EFC coils.

Passive growth rates corresponding to these cases were shown in Table 3.3 for the original design set of equilibria. Comparing the growth rate columns, it is clear that for passive purposes the stabilizing effects of these two choices for control coil are in general comparable for C–MOD. This reflects a similar coupling to the plasma for the two coil sets. In light of this, the EFC coils were in fact added to the design to be used for active control and contribute to passive stabilization. This modification was done as part of the vacuum vessel redesign mentioned above. The decision to add the EFC coils also took into account active results to be considered in Chapter 5, and acknowledged the difficulty of engineering a fast control power supply operating in parallel with the OH2 equilibrium supplies.

3.6 Remarks

Passive analysis can provide a sense of the difficulty of stabilizing given equilibria, and to some extent provide a measure of the relative quality of various stabilizing configurations. Indeed, primarily as a result of the passive growth rate analysis, an assemblage of alternative conductor configurations could be readily compared in the design of Alcator C–MOD, allowing swift optimization. However, on the basis of passive growth rate data alone nothing reliable can be said about such active details as power supply response time and power requirements. Active simulations are required to determine actual limits on the control system. In particular, while the passive growth rate may not be very sensitive to exact control coil location, the calculated tolerable delay time may depend more strongly on it.

The use of the rigid filament model itself is intrinsically limitation in the analysis of fusion plasmas. It fails to conserve flux, keeping plasma current constant everywhere instead. What is desired, even in performing passive stability calculations, is a plasma model which provides a more realistic account of the degrees of freedom available to the plasma, and provides some approximation to ideal MHD flux conservation. Therefore, before addressing the active control issues in Chapter 5, we first turn our attention to passive analysis using the equilibrium perturbation plasma response model.

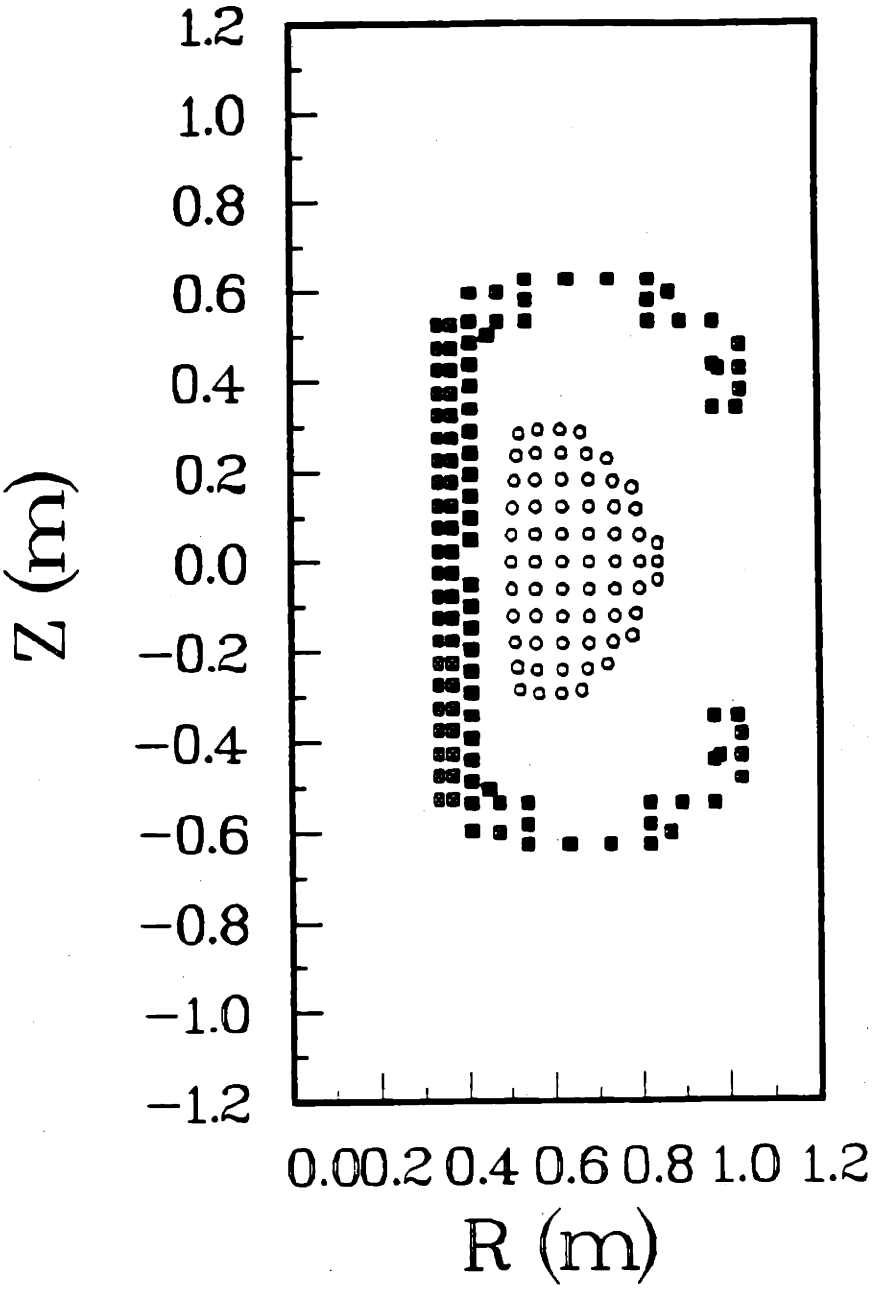

Figure 3.18: Discretized model of rectangular "picture–frame" vacuum vessel.

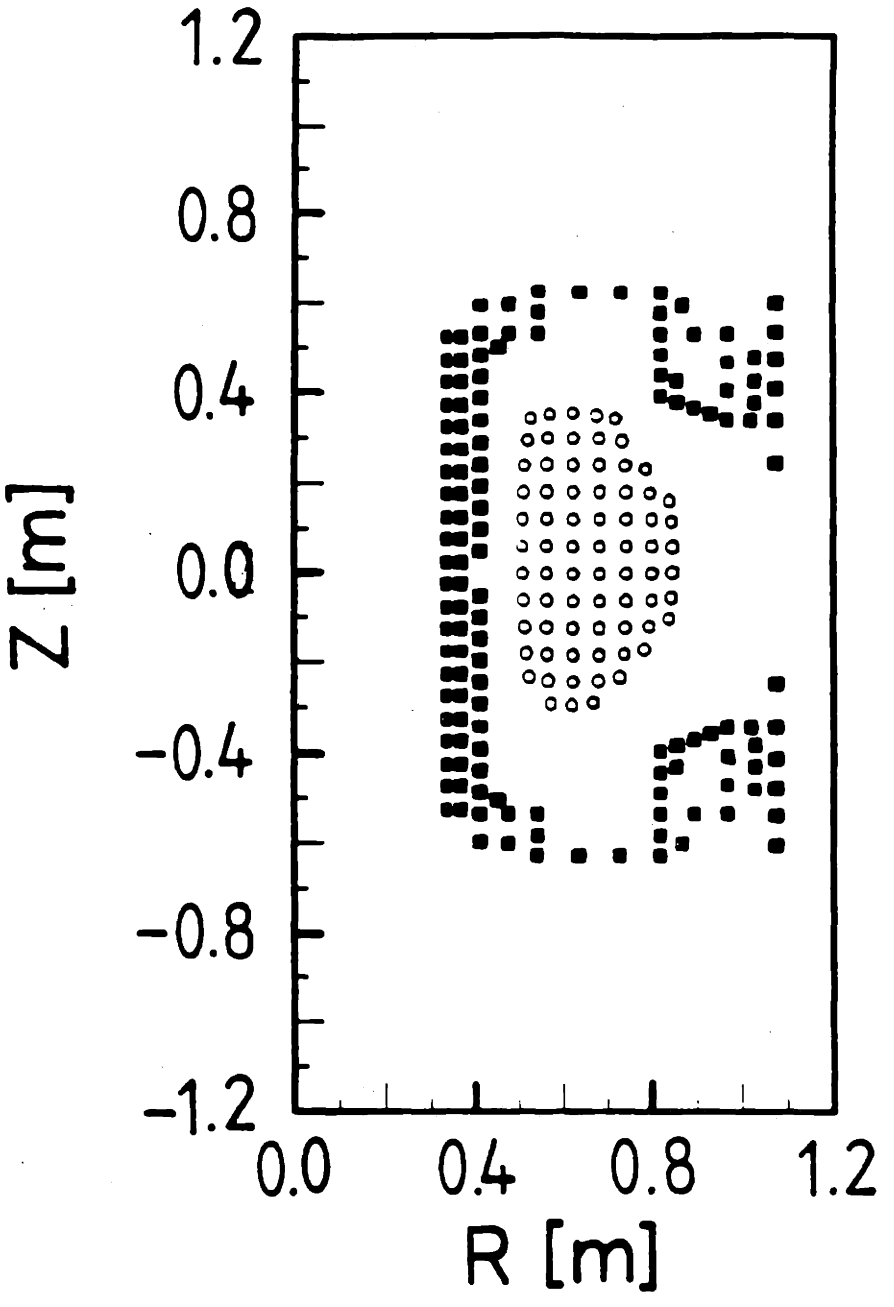

Figure 3.19: Example of discretization of "Original Design Set" equilibria. Shown here is equilibrium eq7, a single null, $\kappa = 2$, $\delta_{av} = .32$ case.

Chapter 4

Perturbational Equilibrium Plasma Response Model

As we have seen, the rigid filament plasma approach to vertical stability analysis has several drawbacks, all related to the inaccuracy of the plasma model. In particular, it fails to account properly for flux conservation, and it cannot in general exhibit the correct energy minimizing eigenmode. What is needed is a method for calculating approximate plasma responses to coil and vacuum vessel current perturbations, while conserving flux and allowing sufficient degrees of freedom to the plasma itself so that a reasonable approximation of the energy minimizing perturbation can be found. Several algorithms which accomplish this were briefly discussed in Chapter 1. In the present work we explore a method based on perturbing coil currents from those currents which yield a given base equilibrium, thereby determining a complete basis for linearized plasma response (while maintaining equilibrium) due to coil current variations. The general approach is similar to that of Albanese et al [17], but we take a unique approach to the method in two important ways. First, the effect of a resistive vacuum vessel is estimated by mapping the effect of vessel element current variations through approximately equivalent EF coil current

variations. Second, by allowing plasma internal dynamics to vary, we approximately conserve flux. While this falls slightly short of an actual flux conserving perturbation calculation, it does manage to conserve to a high degree of accuracy the poloidal flux profile as a function of toroidal flux.

In this chapter we shall examine the perturbational equilibrium approach to plasma modeling for vertical stability analysis, and apply it to passive studies. Active control analysis and design will be addressed in Chapters 5 and 6.

4.1 Modeling Plasma Response with Perturbed Equilibria

4.1.1 Quasi-equilibrium Assumption

As described previously, we exploit the quasi-equilibrium assumption, which allows us to use perturbed equilibrium solutions to determine the linearized plasma response to axisymmetric currents. The first step in this procedure is to assume stability on the ideal time scale. If the resistive stabilization of all instabilities (and in particular the vertical instability) is sufficient to slow the growth rate of the mode to a value significantly below the Alfvén frequency, then the inertial term can be neglected in the MHD momentum equation (see Chapter 2):

$$\rho \frac{d\underline{v}}{dt} = -\nabla p + \underline{J} \times \underline{B}. \tag{4.1}$$

This is easily seen by comparing the scaling of the inertial term with the $\underline{J} \times \underline{B}$ driving term:

$$\frac{1}{\rho a} \underline{J} \times \underline{B} \sim \frac{B^2}{\mu_0 \rho} \frac{1}{a^2} \sim \frac{v_A^2}{a^2} \sim \omega_A^2, \tag{4.2}$$

where v_A is the familiar Alfvén velocity, a is a characteristic scale length of the plasma, and ω_A is thus a corresponding Alfvén frequency. This is to be compared

with the corresponding scaling of the inertial term:

$$\frac{1}{a}\frac{d\mathbf{v}}{dt} \sim \gamma^2_{instab}, \tag{4.3}$$

the characteristic instability growth rate. For Alcator C–MOD, this characteristic Alfvén frequency is $\omega_A \sim 6 \times 10^6 \text{sec}^{-1}$, while the vertical instability growth rate is typically less than 1000 sec^{-1}. In fact, a growth rate much above this value would exceed safety margins on the fast power supply response capability, thus rendering the mode uncontrollable regardless of plasma inertia effects.

From the above argument we can see that stability on the ideal MHD time scale is equivalent to setting the plasma mass to zero. The momentum equation thus becomes the equilibrium equation (Eq. 2.13). For the purposes of plasma response, then, the plasma can be assumed to satisfy the Grad–Shafranov equation (Eq. 2.24) at all times. We next choose a base equilibrium about which to determine the linearized response to perturbed EF coil currents. Perturbing each EF coil current in turn from its base equilibrium value produces a new equilibrium, with one caveat concerning numerical stability. Because the equilibria of interest are intrinsically unstable (to vertical displacements), a separate coil current must be allowed to vary in order to allow stable numerical convergence. This means that each perturbed equilibrium has folded into it both the effects of the "primary" perturbed coil as well as the vertically stabilizing effect of the chosen numerical feedback coil(s). This complicating additional perturbation on each perturbed equilibrium can be unfolded by performing another perturbation for each feedback coil. For these cases, the plasma is moved vertically by a small amount using only the current of the numerical feedback coil(s), while keeping all other EF coil currents fixed at the base equilibrium values. This procedure evaluates the effect of the feedback coil current(s) separately. This effect can then be removed from the other perturbed equilibrium results.

4.1.2 Alternative Approaches

Before continuing with the description of the approach taken in the present work, certain alternative approaches deserve mention. As described above, the equilibrium solutions in this process are necessarily free boundary, since the plasma response must be determined from the fixed set of coil currents (and the varying numerical feedback coils), and not the other way around. However, one can imagine performing a similar operation with a fixed boundary approach, by perturbing in turn each of a set of properly chosen plasma shape and position parameters. The correct perturbed EF coil currents for each resulting perturbed equilibrium must then be calculated self consistently, in such a way as to accurately reflect the small perturbation from the base which each equilibrium should represent. This is rather difficult, since the set of coil currents which produce a given equilibrium (to within a chosen accuracy) is not unique. The fixed boundary perturbed equilibrium approach thus requires an additional degree of sophistication in calculating coil currents. Many of the tools required for this method already exist. In particular, the variational equilibrium algorithm [16] mentioned in Chapter 1 holds the promise of providing an extremely swift alternative to the relatively laborious calculations required by the free boundary approach. However, as yet the algorithms needed to calculate correct perturbed coil currents have not been developed.

Another possible approach is that of time-dependent, combined MHD and transport models such as the Tokamak Simulation Code (TSC) [19] or DINA [20]. These methods evolve a plasma through an entire shot, including full resistive effects of walls and PF coils, while performing self–consistent transport calculations. This provides a great deal of detail in the modeling of a plasma discharge, and allows investigation of almost every aspect of tokamak operation. However, although TSC, for example, is an extremely powerful tokamak analysis tool and represents a major achievement in numerical modeling of plasma phenomena, its use in control studies

is hampered by complexity and execution time. The process of design for any control system necessarily involves the testing of candidate control laws and some degree of iteration in order to arrive at acceptable performance. With present supercomputer technology, a single tokamak shot simulation to this high degree of detail and completeness can easily consume 4 hours of cpu time. This makes iteration extremely difficult.

Moreover, the necessary complexity of the various models incorporated in such a simulation means that uncertainty always remains regarding the nature and accuracy of those models for a given machine. When a machine is in operation and producing experimental data against which to benchmark the code, the free parameters of the transport, heating, fueling, and other models can be modified appropriately to reproduce the behavior of the actual experiment. In the absence of such a running experiment, for example during the initial design process, the number of assumptions which must be made can cast doubt on the reliability of conclusions drawn from the computer simulation. To be sure, this can be equally applied to any theoretical model and computer simulation of a physical system, but the usefulness of a model increases when the complexity of assumptions made is minimized.

Although TSC is generally too slow to be an ideal iterating tool for control design, it must be said that it has certainly been employed successfully for such design by researchers who have become expert in its use. The code has in fact taken on a crucial role as a tool for the confirmation of control laws derived through other methods, and as a means of demonstrating feasibility of stabilization in various scenarios. In modern tokamak stability analysis, it has no peer in this role. Later in this chapter we shall use a TSC simulation carried out by Ramos [21] to help benchmark the predictions of the perturbational equilibrium approach.

Given the difficulty of iterating with a large system such as TSC, and the presently unsolved problem of using a fixed–boundary approach to estimate plasma response, the free–boundary equilibrium perturbation method seems to fall into a

useful middle ground. It shares many of the good aspects of the rigid filament approach, while improving on the deficits of that method. While we must pay a penalty in the time required to calculate several equilibria in order to analyze only one, once this initial calculation is completed the iteration process is essentially as fast as that used for a rigid filamentary plasma model. It is thus of great interest in solving the control design problem.

4.2 Current–Conserving Algorithm

What results from the free boundary analysis is a set of perturbed equilibria equal in number to the number of EF coils. These provide a complete description of the possible variation in plasma shape and position which can arise (in a linearized sense) from perturbational changes in any EF coil currents. Ideally these perturbations would be performed using a flux conserving model. That is, to obey ideal MHD, the plasma must conserve poloidal and toroidal flux at every corresponding fluid element from the base equilibrium to each perturbed equilibrium. If each of the perturbed equilibria conserved flux throughout the plasma, a flux conserving plasma response would automatically result.

The present study made use of a variant of the PEST (Princeton Equilibrium, Stability and Transport) code [23], called ASEQ, for free boundary equilibrium solution. Although PEST does not include any transport, the original intent of the designers to do so seems to have persisted in the name of the code [24]. While a flux conserving operating mode apparently exists in some of the progeny of PEST, this option was not available in the present work. The perturbed equilibria are therefore calculated at constant plasma current, and an algorithm for achieving approximate flux conservation must be used.

The circuit equation, expressing plasma–conductor coupling, appears much the

same as for the rigid formulation (Eq. 3.1):

$$\mathbf{M}_{ss}\dot{I}_s + \mathbf{R}_s I_s + \mathbf{X}_{ss}\dot{I}_s = \vec{V}_s \tag{4.4}$$

where we now and henceforth express the problem in matrix rather than tensor terms, in preparation for the state space formulation we shall exploit in succeeding chapters. In general, we shall use bold face upper case Roman letters to signify matrices, and plain letters to signify vectors. An explicit vector symbol may, however, be used sometimes to disambiguate. In this equation, the subscripts "s" and "ss" refer to generic stabilizing conductors, which we will understand to mean such objects as PF coils, circuits consisting of coupled PF coils, or vacuum vessel elements. They are not to be construed as tensor indices. In future, subscripts "c" and "v" will specifically refer to PF coils and vacuum vessel elements respectively. $\mathbf{M}_{ss}$ is the inductance matrix (including mutual and self inductances), $\mathbf{R}_s$ is the diagonal resistance matrix for the conductors, and V_s is the vector of voltages applied to conductors. $\mathbf{X}_{ss}$ represents the plasma response and coupling from plasma to conductors for constant plasma current, defined as the partial derivative of the flux at the conductors due to plasma alone with respect to conductor currents:

$$\mathbf{X}_{ss} \equiv \frac{\partial \vec{\psi}_{s(p)}}{\partial \vec{I}_s} \tag{4.5}$$

Calculation of this matrix using the perturbation data is relatively straightforward. Constructing the perturbed coil current matrix $\mathbf{I}_{EF}$, whose columns are the vectors of EF coil currents for each of the perturbed equilibria, $\vec{I}^1_{EF}$, minus the base equilibrium EF coil vector, $\vec{I}^0_{EF}$, we obtain:

$$\mathbf{I}_{EF} \equiv \left[\; (\vec{I}^1_{EF} - \vec{I}^0_{EF}) \;\; (\vec{I}^2_{EF} - \vec{I}^0_{EF}) \;\; \ldots \;\; (\vec{I}^{NEQ}_{EF} - \vec{I}^0_{EF}) \; \right]. \tag{4.6}$$

NEQ is the number of perturbed equilibria. The inverse of the perturbed equilibrium coil current matrix, $\mathbf{I}^{-1}_{EF}$, can now operate on equilibrium data (from the right, in the convention used here) to provide a predictor for that data given perturbed

EF currents. We ensure conventional invertibility by creating NEQ=13 perturbed equilibria for the 11 shaping coils plus 2 small vertical displacement cases in which EFCU/L are fed back upon separately to move the equilibrium to the perturbed vertical position demanded. In this way the influence of EFCU/L in the shaping perturbations is evaluated and can be unfolded from the total response. We illustrate with the predictor needed to complete Eq. 4.5.

The current conserving plasma response matrix for EF coil currents, $\mathbf{X}_{cc}$, maps EF coil currents to flux changes due to the plasma current alone measured at EF coils. Constructing the corresponding equilibrium data set matrix, whose columns are these perturbed fluxes at the EF coils:

$$\Psi_{EF} \equiv \left[\; (\vec{\psi}^{1}_{EF} - \vec{\psi}^{0}_{EF}) \;\; (\vec{\psi}^{2}_{EF} - \vec{\psi}^{0}_{EF}) \;\; \ldots \;\; (\vec{\psi}^{NEQ}_{EF} - \vec{\psi}^{0}_{EF}) \; \right] \tag{4.7}$$

the plasma response matrix is easily found to be

$$\mathbf{X}_{cc} \equiv \Psi_{EF} \mathbf{I}^{-1}_{EF} \tag{4.8}$$

Note that this is the sense in which "operating from the right" with $\mathbf{I}^{-1}_{EF}$ yields the predictor of interest.

Provided we are only concerned with the effect of EF coils on plasma stability, the matrix just calculated completes the circuit equation. This was the extent of the analysis of Albanese et al [17]. However, for the case of Alcator C–MOD, the vacuum vessel provides a significant amount of stabilization. In fact, most plasmas of interest for the intended mission of C–MOD would be ideal unstable in the absence of the vacuum vessel. The influence of this large and highly conductive structure close and well–coupled to the plasma must therefore be assessed in the formalism of the perturbed equilibrium algorithm. Unfortunately, the obvious approach of calculating equilibrium solutions for individually perturbed vacuum vessel element currents (effectively treating vessel elements like EF coils) is not reasonable with the ASEQ implementation considered here. Significant modification of the code would

be necessary in order to operate in this mode. Moreover, since there are nearly 100 discrete conductors in the vacuum vessel model and EF coil set, the number of perturbed equilibria needed would require a significantly longer amount of time to calculate.

Instead, we choose to approximate the influence of the vacuum vessel on the plasma in terms of the influence of the EF coil set. Since the only data available through the EF coil current perturbation approach reflects only these degrees of freedom, this represents no change in information. It does, however, mean that any vacuum vessel current distributions whose effect on the plasma cannot be sufficiently well approximated with EF coil currents will not be accurately dealt with. There is a vast nullspace consisting of NV-NC $\sim$ 63 vessel current vectors for which the plasma will be largely unaffected. This is not unreasonable, however, since the number of modes which essentially do not couple to plasma motion in the passive problem is in fact greater than this. This issue will be addressed later in the chapter. First, however, we describe the method for assessing the influence of the vacuum vessel on the plasma.

4.3 Vacuum Vessel Effects

The influence of any set of conductor currents on the plasma is determined by the vacuum field over the plasma region due to those currents. Since the vacuum magnetic flux satisfies Laplace's equation and the system is axisymmetric, specifying the flux everywhere on a closed contour determines its value everywhere within that contour. Thus, if a contour is circumscribed around the plasma in the poloidal plane and the flux on this surface is determined, the vacuum field over the plasma region will also be determined. The approximation of EF coil current influence using vessel element currents is therefore equivalent to approximating the flux pattern on such a contour due to vessel currents by using coil currents. Operationally, we choose

some sufficiently large number NE of grid points which are those NE points with flux values nearest to the edge flux, defining a locus, $\mathcal{E}$, which roughly surrounds the plasma.

The flux at $\mathcal{E}$ due to an arbitrary set of EF coil currents, $\vec{I}_c$, is given by

$$\vec{\psi}_{\mathcal{E}(c)} = M_{\mathcal{E}c}\vec{I}_c \tag{4.9}$$

Similarly, the flux due to a vector of vessel currents, $\vec{I}_v$, is

$$\vec{\psi}_{\mathcal{E}(v)} = M_{\mathcal{E}v}\vec{I}_v \tag{4.10}$$

where $\mathbf{M}_{\mathcal{E}c}$ and $\mathbf{M}_{\mathcal{E}v}$ are the appropriate mutual inductance matrices. We now attempt to set these two flux vectors equal to each other. This can only be accomplished approximately, minimizing some norm of choice in the $\mathcal{E}$ space:

$$M_{\mathcal{E}v}\vec{I}_v = M_{\mathcal{E}c}\vec{I}_c \tag{4.11}$$

Choosing a least-squares norm, the problem can be solved directly with a singular value decomposition (SVD) inverse [25]. For the usual least-squares problem

$$\mathbf{A}\vec{x} = \vec{b} \tag{4.12}$$

an SVD inversion of A, yielding the solution

$$\vec{x} = \mathbf{A}^{-1}\vec{b} \tag{4.13}$$

minimizes the quantity

$$(\vec{x} - \mathbf{A}^{-1}\vec{b})^T(\vec{x} - \mathbf{A}^{-1}\vec{b}). \tag{4.14}$$

Defining the SVD of a matrix A as

$$\mathbf{A} = \mathbf{U}\mathbf{\Sigma}\mathbf{V}^T, \tag{4.15}$$

the SVD inverse is given by

$$\mathbf{A}^{-1} = \mathbf{V}\mathbf{\Sigma}^{-1}\mathbf{U}^T. \tag{4.16}$$

As a matter of notation, whenever a rectangular matrix is being inverted in the present work, the superscript "-1" will be understood to indicate the SVD (generalized) inverse.

Before performing the simple operation to produce the least-squares solution, the question of which vector is being solved for must be addressed. At first glance, it may appear that what is needed is an approximation to the coil current vector, $\vec{I}_c$, in terms of the vessel current vector, $\vec{I}_v$. One might therefore suppose that the correct solution to be found is

$$\vec{I}_v = \mathbf{M}_{\mathcal{E}v}^{-1}\mathbf{M}_{\mathcal{E}c}\vec{I}_c. \tag{4.17}$$

However, since the number of vessel elements, NV, greatly exceeds the number of coil elements, NC, determining $\vec{I}_v$ in this way from $\vec{I}_c$ represents an ill-posed problem.

The correct problem to be solved is to find the coil current vector which best approximates the effect of vessel element currents. Posed in this way the problem is overdetermined, and can thus be appropriately solved in least-squares as described. The result is the current mapping matrix

$$\mathbf{D}_{cv} \equiv \mathbf{M}_{\mathcal{E}c}^{-1}\mathbf{M}_{\mathcal{E}v}, \tag{4.18}$$

which maps $\vec{I}_v$ vectors to $\vec{I}_c$ vectors which have an approximately equivalent effect on the plasma. This operation, of course, makes explicit the existence of the large vessel current nullspace mentioned above.

The circuit equation can now be modified to express the plasma-vessel inductive coupling alone, using a different plasma response matrix $\mathbf{X}_{vc}$, defined by

$$\mathbf{X}_{vc} \equiv \Psi_{vv}\mathbf{I}_{EF}^{-1}. \tag{4.19}$$

This matrix describes the flux change at vessel elements due to plasma response to EF coil currents. Ψ_{vv} here is the equilibrium set of flux vectors due to plasma

current alone at the vessel elements. $\mathbf{X}_{vc}$ is then operated upon from the right by the current mapping matrix, $\mathbf{D}_{cv}$, to give the new vessel-vessel plasma response matrix,

$$\mathbf{X}_{vv} \equiv \mathbf{X}_{vc}\mathbf{D}_{cv} = \frac{\partial \vec{\psi}_{v(p)}}{\partial \vec{I}_v}, \tag{4.20}$$

and the complete vessel circuit equation,

$$\mathbf{M}_{vv}\dot{\underline{I}}_v + \mathbf{R}_v\underline{I}_v + \mathbf{X}_{vv}\dot{\underline{I}}_v = \underline{V}_v. \tag{4.21}$$

From Eqs. 4.20 and 4.21 it is now clear that the indicated inversion for the solution of Eq. 4.11 is the correct one. The adequacy of this mapping will be addressed in Sec. 4.7.

The extension of these equations for combined sets of conductors, including both EF coils and vacuum vessel elements, is immediate once the various plasma response matrices, $\mathbf{X}_{cc}$, $\mathbf{X}_{cv}$, $\mathbf{X}_{vc}$, and $\mathbf{X}_{vv}$, have been calculated. We emphasize that these matrices have been calculated with the constraint that plasma current and profile shape parameters have been kept constant. In order to approximately conserve flux in the plasma, these parameters must be allowed to vary. In the next section we introduce the current/profile-varying plasma response matrix and the additional constraint equation needed to accomplish approximate flux conservation.

4.4 Flux Conservation

Equilibria calculated with the form of ASEQ used here cannot be forced to conserve q profile or poloidal and toroidal flux throughout the plasma from one run to the next. Although it is in principle possible to iterate over the equilibrium code itself in order to obtain, say, a set of q profile conserving cases, such an iteration would require prohibitively large amounts of computation. However, since the code requires the specification of total plasma current, it is natural to keep the toroidal current constant from one run to the next. Varying the plasma current provides

one control degree of freedom for approximately conserving flux. The effect on the plasma and surrounding conductors due to changing plasma current can then be determined by finding the solution for a current value slightly perturbed from the base equilibrium value, while keeping all coil currents (again excepting the EFC pair) fixed.

As must be done in all methods of Grad–Shafranov equation solution, ASEQ must make some assumptions regarding the form of two of the three unknowns in that equation. As part of this procedure, the form of the P' and FF' profiles as functions of normalized flux are specified. For all of the solutions in the present work, P' and FF' are taken to be proportional to the "Strickler profile" shape function, given by:

$$h'(\bar{\psi},\alpha) = \frac{e^{-\alpha\bar{\psi}} - e^{-\alpha}}{e^{-\alpha} - 1} \tag{4.22}$$

where the normalized flux is

$$\bar{\psi} \equiv \frac{\psi - \psi_{axis}}{\psi_{edge} - \psi_{axis}}, \tag{4.23}$$

and α is a shape parameter related to the profile width. P' and FF' depend on two different shape parameters, α_p and α_f:

$$P' \propto h'(\bar{\psi},\alpha_p) \quad \text{and} \quad FF' \propto h'(\bar{\psi},\alpha_f). \tag{4.24}$$

Greater positive values of these profile parameters corresponds to more peaked profiles, and more negative values, to flatter profiles. Varying one or both of these shape parameters for the two profiles provides one or two more degrees of freedom for flux conservation.

Allowing plasma current and a profile shape parameter such as α_f to vary adds another matrix term to the circuit equation. If we define a parameter vector, $\vec{p}$, as a vector containing the perturbed plasma current and perturbed shape parameter, the new term is

$$\left.\frac{\partial\vec{\psi}_{s(p)}}{\partial\vec{p}}\right|_{I_c} \dot{\vec{p}} \equiv \mathbf{Y}_{ss}\dot{\vec{I}}_s \tag{4.25}$$

We must now find constraint equations to specify the parameter vector, $\vec{p}$, in terms of coil currents, permitting the definition of $\mathbf{Y}_{ss}$. Forcing toroidal and poloidal flux to be constant at discrete plasma locations provides the necessary constraints.

The goal is to provide some approximation to overall flux conservation by forcing the flux at certain locations to be constant in the coupled circuit and force problem. A common approach to approximating q profile conservation in theoretical models is to conserve q values at certain discrete locations alone, for example keeping q_0 and q_a constant [1]. However, there is a practical limitation to keeping these particular values constant using the results of ASEQ calculations. The problem arises when one asks where the edge of the plasma is to be found from one equilibrium to the next. Although the equilibrium solution treats the edge as a well–defined locus of points, it establishes this locus by self–consistently defining a particular flux surface as the contour upon which plasma current falls identically to zero. For all of the equilibria dealt with in this study that surface is the "95% surface", the surface having a flux value which is 95% of the separatrix flux value. Attempting to conserve poloidal and toroidal flux on this surface therefore places an unrealistic constraint on the plasma and on the separatrix at the same time. A truly flux-conserving plasma would expand or contract with radial motion in order to conserve flux, but perturbational ASEQ solutions tend to largely conserve poloidal plasma area instead.

A more realistic approximation to flux conservation given the nature of the equilibrium solutions, is to conserve the poloidal flux profile as a function of toroidal flux. If plasma current and one profile shape parameter such as α_f are allowed to vary, two values can be constrained. The magnetic axis is one endpoint of the profile which is especially easy to constrain. Toroidal flux is, by definition, zero on axis, but the poloidal flux varies among the perturbation set of equilibria. The constraint equation for the perturbed axis flux which relates the set of perturbed coil currents, $\vec{I}_c$, to the internal parameter vector, $\vec{p}$ (whose elements are taken to

be the perturbed plasma current and the change in α_f), is simply

$$\Delta\psi_a = \frac{\partial\psi_a}{\partial\vec{I}_c}\vec{I}_c + \frac{\partial\psi_a}{\partial\vec{p}}\vec{p} = 0. \tag{4.26}$$

Throughout this section we use the subscript "a" to refer to the magnetic axis, "e" to refer to the plasma edge, "0" to refer to the unperturbed base equilibrium, and "1" to refer to an equilibrium perturbed from the base.

Flux conservation at the edge requires a slightly more subtle argument. Referring to Fig. 4.1, consider the $\psi_p(\psi_t)$ profile for the base equilibrium (ψ_{e0}, ψ_{a0}), and that of an equilibrium perturbed from this base (ψ_{e1}, ψ_{a1}). Since the 95% surface toroidal flux calculated for the perturbed solution is different from that of the base, the perturbed edge cannot be identified with the base edge. Instead, in order to constrain the $\psi_p(\psi_t)$ profile to be as unchanged as possible, the edge poloidal flux is forced to be the appropriate value which will extrapolate to a fixed $\psi_{pe}(\psi_{te})$. Fig. 4.1 illustrates this more clearly. We therefore require

$$\psi_{e1} = \psi_{e0} + \left(\frac{\partial\psi_p}{\partial\psi_t}\right)(\psi_{t1} - \psi_{t0}). \tag{4.27}$$

Since the sign convention used in ASEQ requires that

$$\left(\frac{\partial\psi_p}{\partial\psi_t}\right) = -\frac{1}{q_{e0}}, \tag{4.28}$$

we find that

$$\Delta\psi_e = -\frac{1}{q_{e0}}\Delta\psi_t. \tag{4.29}$$

The edge constraint equation is therefore

$$\frac{\partial\psi_{ex}}{\partial\vec{I}_c}\vec{I}_c + \frac{\partial\psi_{ex}}{\partial\vec{p}}\vec{p} = 0, \tag{4.30}$$

where

$$\frac{\partial\psi_{ex}}{\partial\vec{I}_c} \equiv \left(\frac{\partial\psi_e}{\partial\vec{I}_c} + \frac{1}{q_{e0}}\frac{\partial\psi_t}{\partial\vec{I}_c}\right), \tag{4.31}$$

and

$$\frac{\partial\psi_{ex}}{\partial\vec{p}} \equiv \left(\frac{\partial\psi_e}{\partial\vec{p}} + \frac{1}{q_{e0}}\frac{\partial\psi_t}{\partial\vec{p}}\right). \tag{4.32}$$

The quantity ψ_e is the total change in poloidal flux from the base equilibrium edge to the perturbed equilibrium edge. The quantity ψ_{ex} has the meaning indicated in Fig. 4.1.

The expanded form of the constraint appears as:

$$\left(\frac{\partial \psi_e}{\partial \vec{I}_c} + \frac{1}{q_{e0}} \frac{\partial \psi_t}{\partial \vec{I}_c}\right) \vec{I}_c + \left(\frac{\partial \psi_e}{\partial \vec{p}} + \frac{1}{q_{e0}} \frac{\partial \psi_t}{\partial \vec{p}}\right) \vec{p} = 0. \tag{4.33}$$

We now construct the plasma flux vector:

$$\vec{\psi}_x \equiv \begin{bmatrix} \psi_{ex} \\ \psi_a \end{bmatrix}. \tag{4.34}$$

Recalling the definition of the internal plasma parameter vector

$$\vec{p} \equiv \begin{bmatrix} I_p \\ \alpha_f \end{bmatrix}, \tag{4.35}$$

Eqs. 4.26 and 4.33 combine to yield the desired relation between $\vec{p}$ and $\vec{\psi}_x$

$$\frac{\partial \vec{p}}{\partial \vec{I}_c} = -\left(\frac{\partial \vec{\psi}_x}{\partial \vec{p}}\right)^{-1} \left(\frac{\partial \vec{\psi}_x}{\partial \vec{I}_c}\right). \tag{4.36}$$

$\left(\frac{\partial \vec{\psi}_x}{\partial \vec{p}}\right)$ and $\left(\frac{\partial \vec{\psi}_x}{\partial \vec{I}_c}\right)$ are calculated according to the definitions in Eqs. 4.31 and 4.32 above, and by applying the same kind of inversion of the equilibrium dataset internal parameter and current matrices respectively. A modified perturbed equilibrium dataset matrix similar to Ψ_x must be constructed which includes the ψ_{ex} entries as well as the ψ_a. This is then operated upon from the right with the inverted dataset internal parameter and current matrices to produce Eq. 4.36.

Inserting Eq. 4.36 into Eq. 4.25 yields the flux conserving circuit equation:

$$\mathbf{M}_{ss}\dot{I}_s + \mathbf{R}_s I_s + \mathbf{X}_{ss}\dot{I}_s + \mathbf{Y}_{ss}\dot{I}_s = \vec{V}_s, \tag{4.37}$$

where

$$\mathbf{Y}_{ss} \equiv -\left.\frac{\partial \vec{\psi}_{s(p)}}{\partial \vec{p}}\right|_{I_c} \left(\frac{\partial \vec{\psi}_x}{\partial \vec{p}}\right)^{-1} \left(\frac{\partial \vec{\psi}_x}{\partial \vec{I}_s}\right). \tag{4.38}$$

4.5 Computational Tools and Accuracy

Before describing the passive results from stability analysis using the perturbational equilibrium plasma response, it is worth noting some accuracy limitations intrinsic in the calculation and the sources of these limitations.

The principal constraint on the accuracy implied by the equilibrium perturbation procedure as implemented in the present work is that of data significant figure limitation. One of the tools evolved for the Alcator C–MOD MHD effort is the C–MOD Relational Database (RDB). This system allows the storage and referencing of equilibrium data, found by the running of an equilibrium code such as ASEQ, or by actual reconstruction of machine operating data. Once the tokamak is in operation, it is envisioned that actual shot data can be stored in RDB and readily accessed for analysis and use in achieving desirable equilibria in later shots. This database is the medium through which the perturbed equilibrium solutions used in this work are stored and extracted. It provides an extremely broad range of MHD data, and a means of constructing "streams" of information for a sequence of equilibria. As of this writing, more than 4000 C–MOD equilibria have been created with ASEQ and stored in RDB, encompassing a very large range of shapes, currents, β-values, etc...

At present, equilibrium data stored in RDB is limited to 5 significant figures (4 decimal places) by virtue of the data writing formats of ASEQ. Thus database quantities are only safely reliable to about one part in 10^4. This was chosen as a reasonable limit to the accuracy of the equilibrium solutions themselves. Although machine precision for the VAX computer used for the equilibrium calculations is $\epsilon_m \sim 2 \times 10^{-7}$, the large number of grid points and arithmetic operations required results in a significant amplification of this intrinsic error appearing in the final solution [25]. If we choose the number of grid points, (65×65), as a rough conservative estimate of the number of independent operations, N, then the cumulative error,

given by $\sqrt{N}\varepsilon_m$, is $\varepsilon_{cum} \sim 1 \times 10^{-5}$. The 4 decimal place format of the database data storage was therefore roughly appropriate.

Unfortunately, this degree of accuracy severely constrains the size of perturbation for which equilibrium solutions will reliably reflect that perturbation. We expect this accuracy limit to mask the perturbation for quantities perturbed to roughly $1 - 5 \times 10^{-4}$ or less.

As perturbation size decreases in the perturbed equilibrium calculation, the growth rate is observed to decrease, eventually converging to the linear value for sufficiently small perturbation. The procedure for determining convergence of plasma response is simply to reduce the perturbation sizes until succeeding passive growth rates converge to within 5% or less of each other (see Sec. 4.7.1).

4.6 Passive Analysis

A set of three equilibria is examined now using the equilibrium perturbation approach just described. These cases consist of a range of elongations and degrees of vertical instability which are of interest to the mission of Alcator C-MOD. Their essential characteristics are shown in Table 4.1. In the table, "ma" refers to magnetic axis, "95" refers to values at the 95% flux surface, and "av" refers to the average of upper and lower values. The minor radius "a" is defined here as the midplane half width of the plasma. All 3 equilibria are 9 T toroidal field, and lower single null diverted. These equilibria range in elongation from $\kappa_{95} = 1.4$ to $\kappa_{95} = 1.7$, $\kappa_{sep} = 1.5$ to $\kappa_{sep} = 1.8$. Various growth rates are shown in Table 4.2. The first row of this table shows rigid model growth rates with vacuum vessel alone for passive stabilization, as a standard for comparison. Rows 2, 3, and 4 use the perturbational flux conserving approach. Rows 1 and 2 show the growth rate for vacuum vessel stabilization alone, row 3 shows the growth rate for

Quantity	eq8	eq9	eq10	units
I_p	1.30	3.01	3.01	MA
R_{ma}	67.8	67.5	67.9	cm
z_{ma}	-2.00	0.00	2.00	cm
a	21.1	21.1	21.3	cm
κ_{95}	1.41	1.58	1.70	
κ_{sep}	1.55	1.69	1.85	
$\delta_{95(av)}$	.300	.271	.379	
q_0	1.05	1.01	.973	
q_{95}	4.16	2.08	2.53	
β_p	.313	.197	.101	

Table 4.1: Essential characteristics of the perturbed equilibrium example set. See text for notation details.

Case	eq8	eq9	eq10
VV(Rigid)	277.	464.	745.
VV(pert)	372.	622.	1390.
VV+EFC	281.	512.	1170.
VV+EFC+OH2	170.	349.	1050.

Table 4.2: Dominant unstable mode growth rates for the perturbed equilibrium example set of equilibria. Growth rates are given in $\sec^{-1}$.

vacuum vessel + EFCU/L(antiseries), and row 4 shows the rate for vacuum vessel + EFCU/L(antiseries) + OH2U/L(independent). For all of these cases the vacuum vessel is present as a passive stabilizer at room temperature. In actual operation the vacuum vessel will be at an average temperature of approximately 213 Kelvin ($-60°$ C) due to the cryogenic cooling of the machine with liquid nitrogen (LN). The EF coils will experience an average temperature closer to the LN temperature of 77 Kelvin, but this is likely to fluctuate rather widely over the shot-to-shot cycle. The room temperature assumption for the conductor array is therefore a pessimistic one.

Flux contours for the base equilibria are shown in Figs. 4.2, 4.3, and 4.4. Note that they are all diverted plasmas with a single lower X-point (single null). The initial construction of Alcator C–MOD will be equipped with divertor hardware on

the bottom of the machine alone, and thus will run lower single null discharges when diverted. The design will be upgraded at a later date to allow double null operation as well.

From the passive data alone, we would expect to be able to control the two lower elongation cases satisfactorily, since the growth rates for these cases are well below a kilohertz. They should therefore be readily controllable with the EFC power supply, which has a response time below 0.25 ms. The highest elongation/growth rate case, denoted eq10, reveals a minimum growth rate of about 1300 sec^{-1}. Active analysis is necessary to establish the controllability of this equilibrium, and of course to confirm the intuitive expectations regarding the controllability of eq8 and eq9 as well. Such active modeling will be addressed in the succeeding chapters.

The modes corresponding to the unstable roots for eq8–eq10 are shown in Figs. 4.5 through 4.10. These are the vacuum vessel + EFC modes, showing conductor current distributions and vacuum flux due to the conductor currents. The plasma contours shown represent toroidal current density contours, and are included only to indicate the plasma equilibrium location and shape. The current contours are labeled in units of $Amperes/m^2$. In these figures, the "+" symbol stands for positive current (in the same direction as the plasma toroidal current), and "." represents negative current. The radius of circles drawn around conductor elements represents the magnitude of the corresponding currents. Refer to Fig. 3.12 for locations of EF coils and vacuum vessel elements.

The general midplane antisymmetry of the current modes reflects the bulk vertical motion of the plasma. This is clearly the dominant motion involved in the modes. The flux patterns generated by the current distribution confirm this intuition. Primarily horizontal flux lines correspond to a radial field, which acts to resist the vertical plasma motion. Although for all of these cases the unstable mode is essentially vertical and midplane symmetric (antisymmetric wall currents; symmetric displacement vector), the force is not purely vertical across the plasma.

There are regions where the force due to the modal conductor currents has a radial component. These regions tend to be primarily localized near the plasma edge, an area which it has been speculated may play an important role in experimental axisymmetric instability. Notice also the pronounced midplane asymmetry (especially in the cases of eq8 and eq10) which arises from the magnetic axis being displaced slightly from the midplane in those equilibria (see Table 4.1). Asymmetry in the base equilibrium results in asymmetry in the mode.

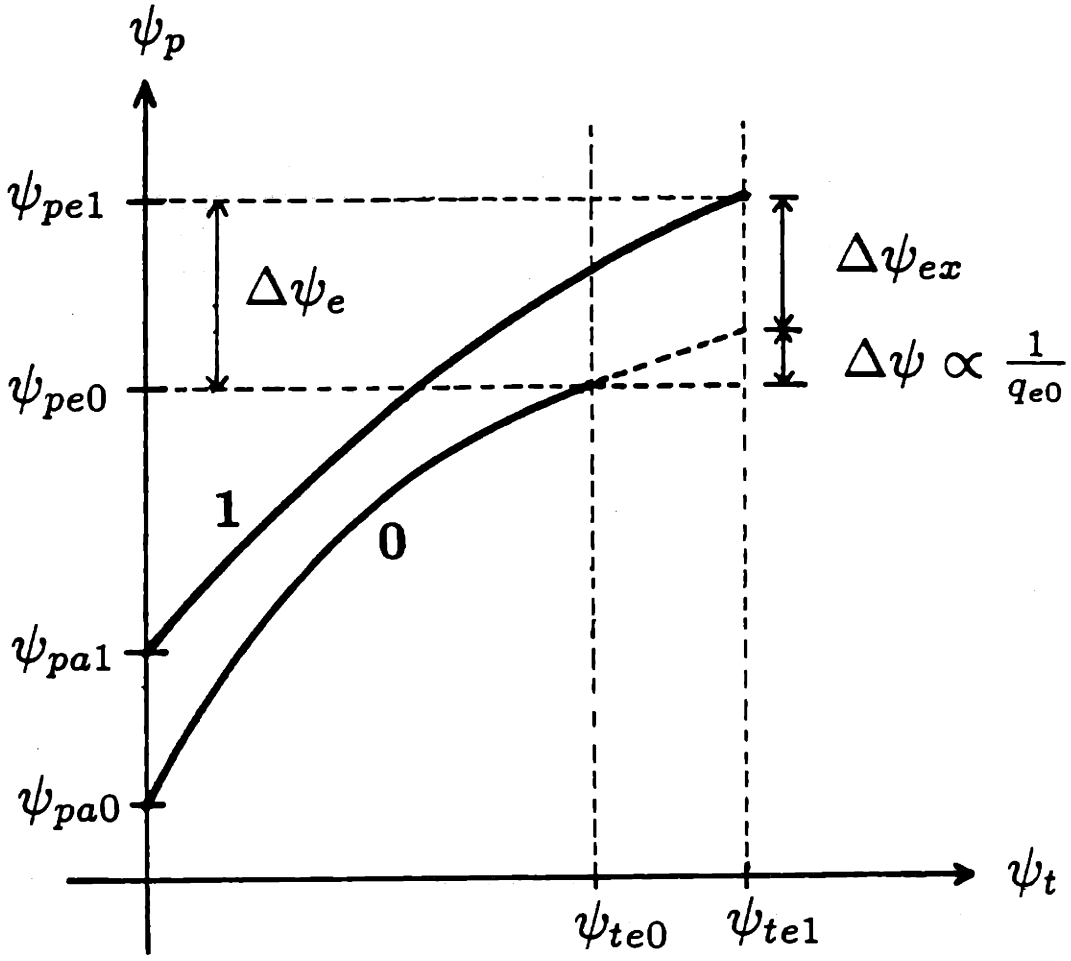

Figure 4.1: Illustration of approximate edge flux conservation.

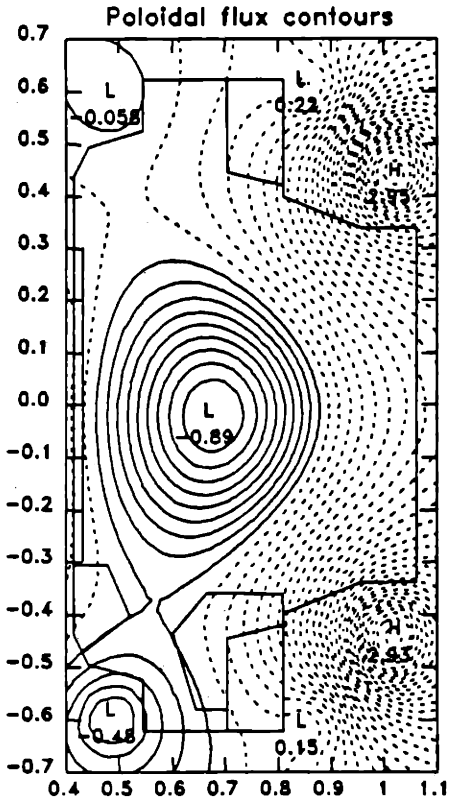

Figure 4.2: Poloidal flux contours for base equilibrium eq8.

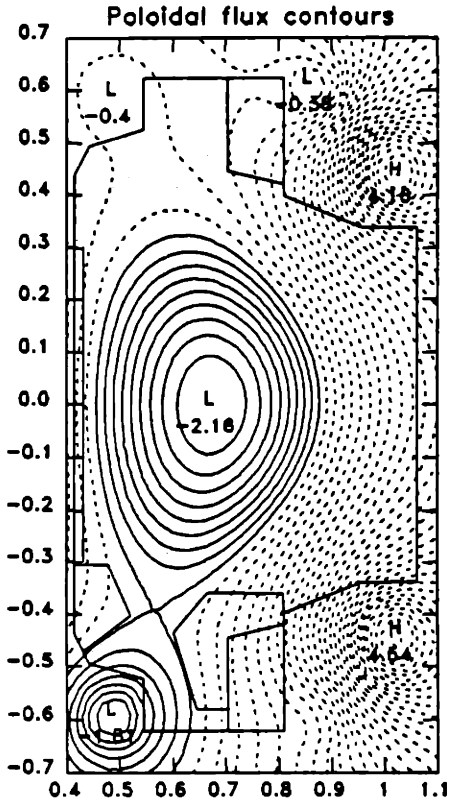

3368

6744aa

Figure 4.3: Poloidal flux contours for base equilibrium eq9.

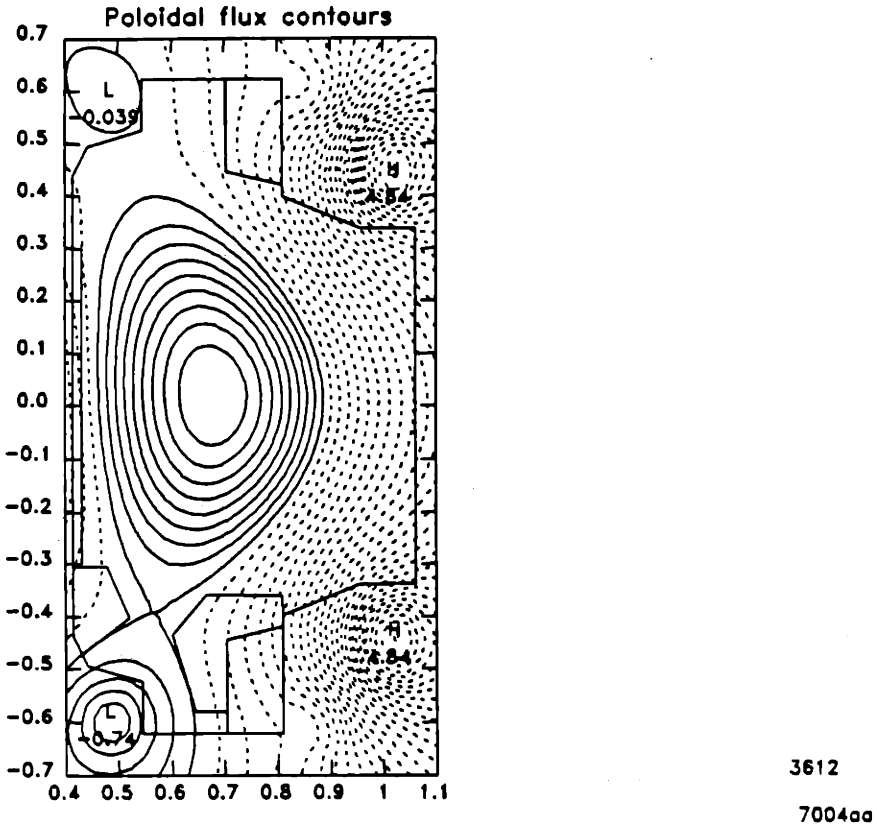

Figure 4.4: Poloidal flux contours for base equilibrium eq10.

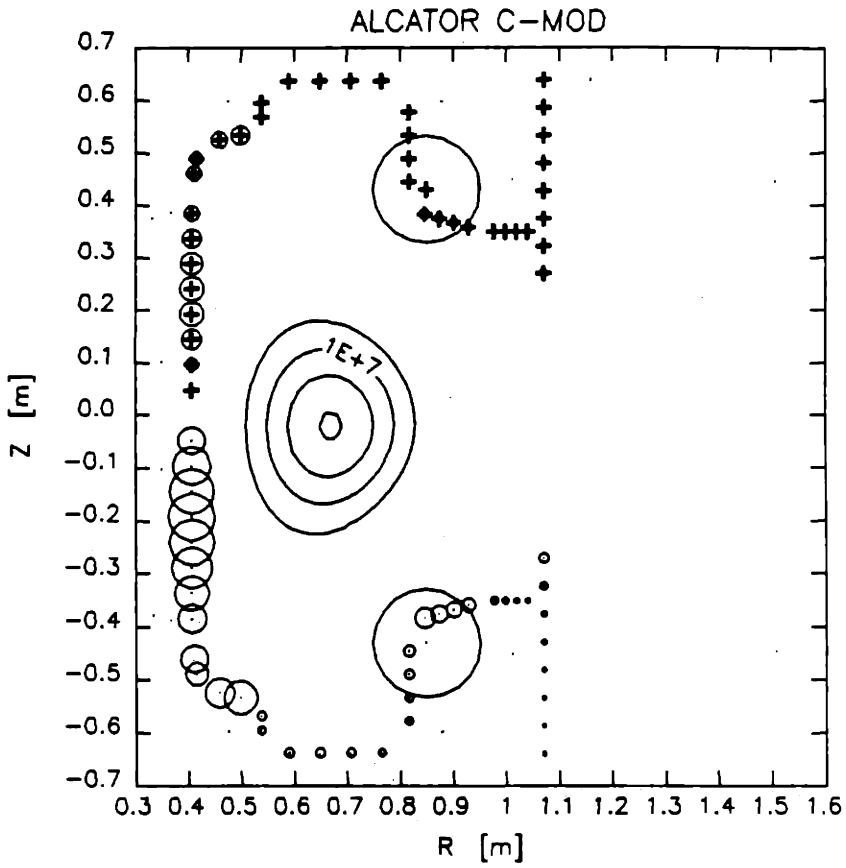

Figure 4.5: Unstable vertical mode conductor current distribution for equilibrium eq8 with vacuum vessel + EFCU/L(antiseries) stabilization. See text for symbol interpretation.

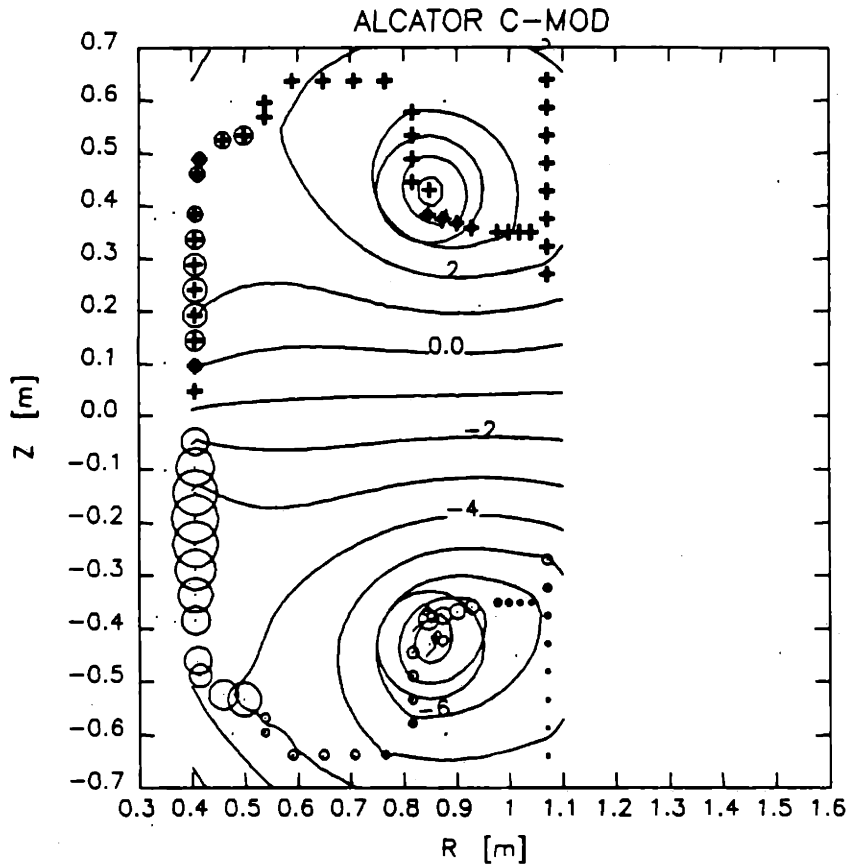

Figure 4.6: Unstable vertical mode vacuum flux distribution for equilibrium eq8 with vacuum vessel + EFCU/L(antiseries) stabilization. See text for symbol interpretation.

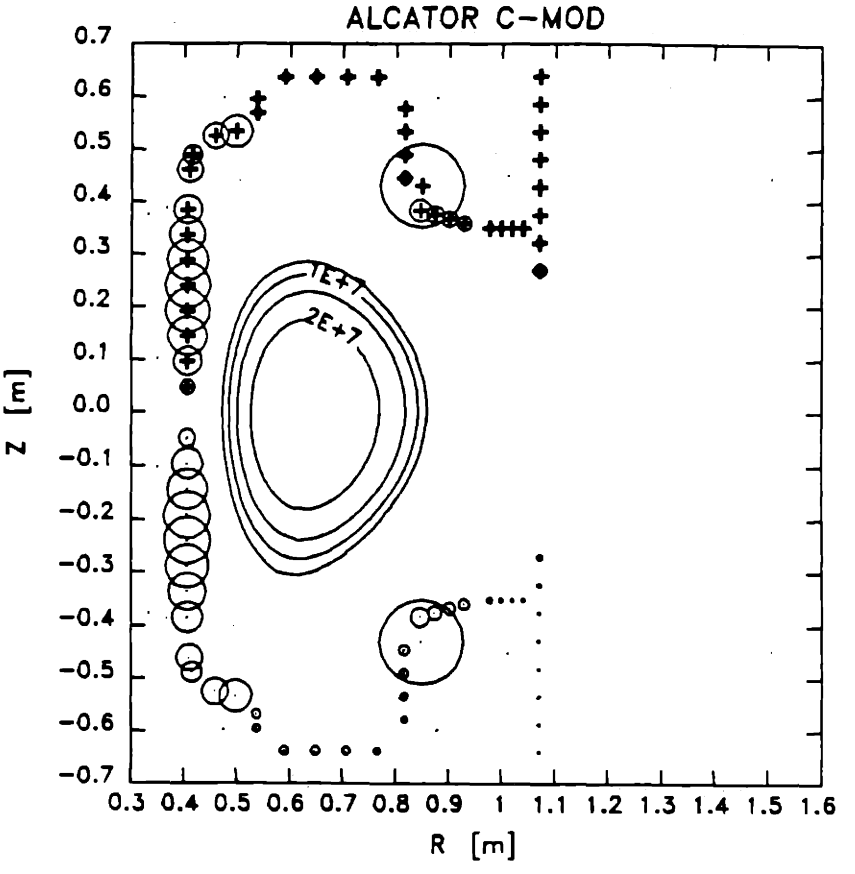

Figure 4.7: Unstable vertical mode conductor current distribution for equilibrium eq9 with vacuum vessel + EFCU/L(antiseries) stabilization. See text for symbol interpretation.

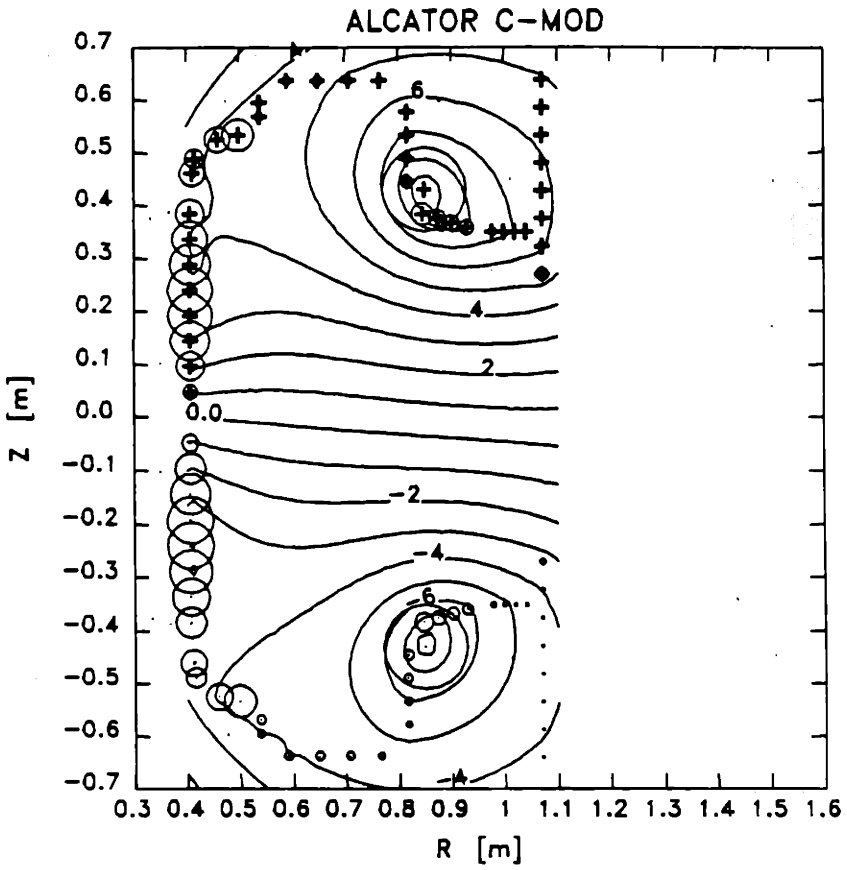

Figure 4.8: Unstable vertical mode vacuum flux distribution for equilibrium eq9 with vacuum vessel + EFCU/L(antiseries) stabilization. See text for symbol interpretation.

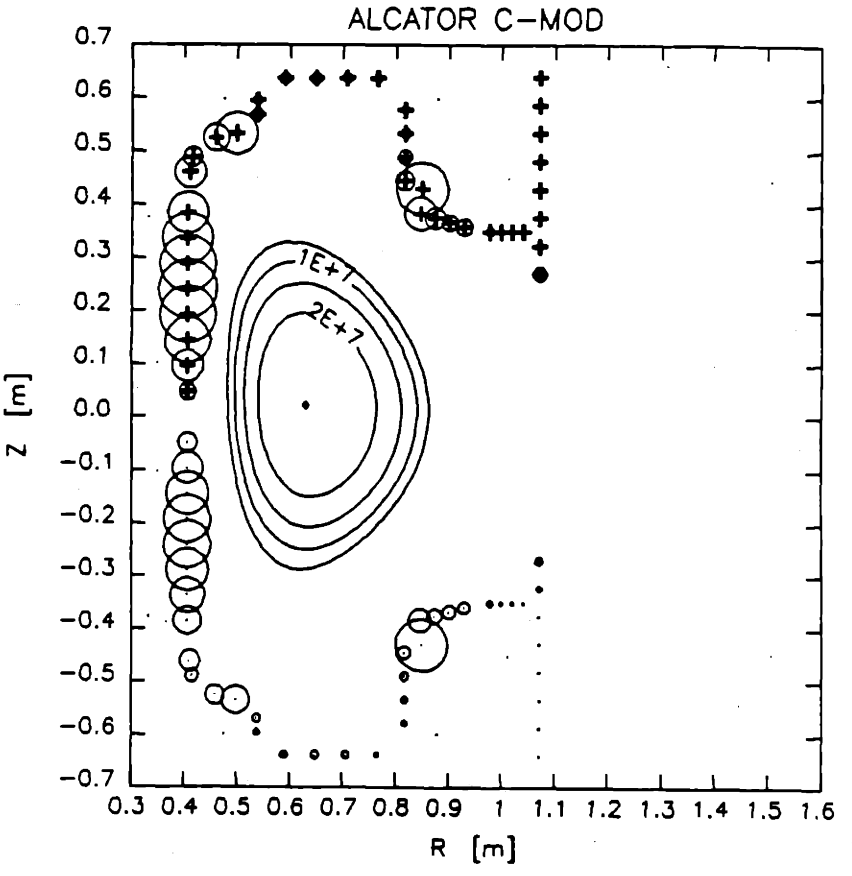

Figure 4.9: Unstable vertical mode conductor current distribution for equilibrium eq10 with vacuum vessel + EFCU/L(antiseries) stabilization. See text for symbol interpretation.

4.7 Testing of the Model

In this section we investigate the nature and reliability of the equilibrium perturbation plasma response model. It must be shown that the model converges properly and adequately describes vacuum vessel modes with the EF current mapping algorithm. It is important to demonstrate the convergence of growth rate results with decreasing perturbation amplitude in order to establish that the linear growth rate region has been found. The fundamental number of degrees of freedom in the perturbation set and the accuracy of the vacuum vessel to EF coil current mapping is also addressed. Finally, we benchmark the algorithm with a comparison between the perturbation result and a TSC simulation of the axisymmetric instability for a C–MOD equilibrium. We begin by examining the convergence of growth rates for varying perturbations.

4.7.1 Passive Growth Rate Convergence Studies

As the size of the perturbation is reduced, the passive growth rate predicted by the equilibrium perturbation algorithm tends to decrease as well. This is consistent with the increasing decay index encountered by the plasma as it moves away from the midplane, as shown in Figs. 4.11 and 4.12. For the purposes of the present study, we consider two perturbations which differ by a factor of 2 to be converged if the growth rates resulting from the two cases differ by no more than 5%. Table 4.3 shows the last three steps of the convergence sequence for eq8–10. The current perturbation shown ("ΔI_c") is the fixed amount of current added to the base equilibrum EF coil currents to produce the 11 perturbed current cases, and the vertical displacement perturbation ("ΔZ_{ma}") is the amount by which the magnetic axis is moved vertically for the 2 cases which assess the influence of the EFCU/L coils.

A current perturbation on the order of 1–2 kA and a vertical displacement of

		ΔI_c	ΔZ_{ma}	γ	% Diff
	step 1	.02	.5	391.	-
eq8	step 2	.01	.25	387.	1.0
	step 3	.002	.05	372.	3.9
	step 1	.01	.25	845.	-
eq9	step 2	.005	.10	637.	25.
	step 3	.002	.05	622.	2.4
	step 1	.005	.10	2111.	-
eq10	step 2	.002	.05	1338.	37.
	step 3	.001	.02	1388.	3.7
Units		MA	cm	sec^{-1}	%

Table 4.3: Convergence sequence for eq8–10. Last 3 steps in convergence process. Step 3 represents the converged growth rate. "% Diff" is the difference from the previous step.

about .02–.05 cm are typically sufficiently small to achieve convergence to the linear growth rate region. These current and displacement perturbations correspond to roughly the same average flux change at vacuum vessel elements, $\Delta\psi \simeq 10^{-3}$ Wb.

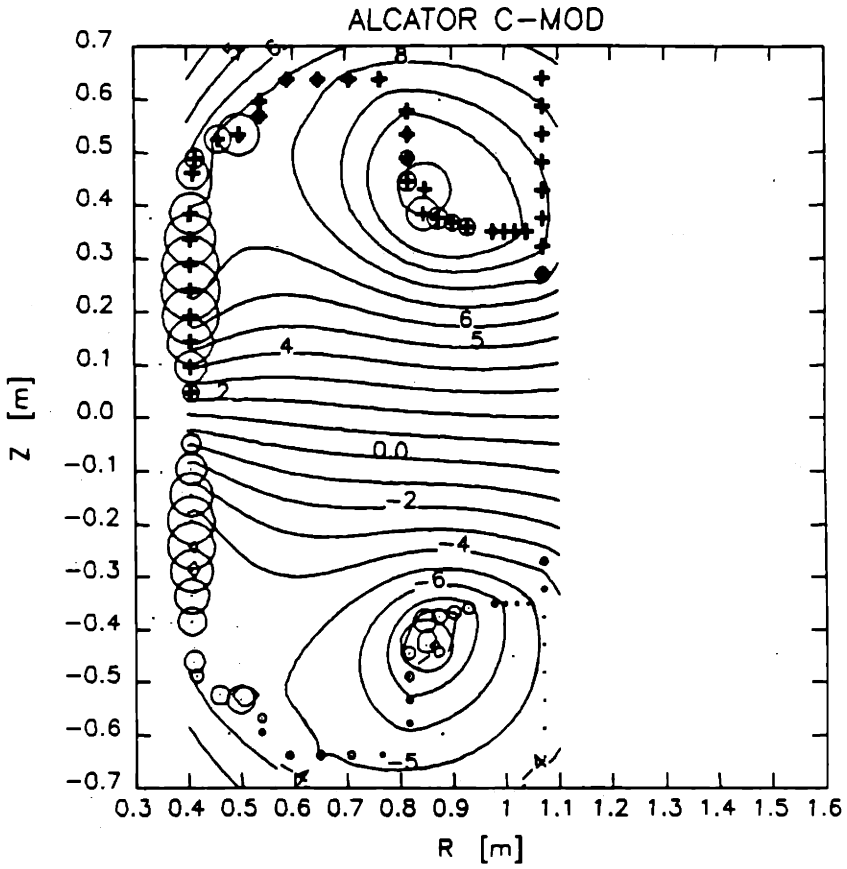

Figure 4.10: Unstable vertical mode vacuum flux distribution for equilibrium eq10 with vacuum vessel + EFCU/L(antiseries) stabilization. See text for symbol interpretation.

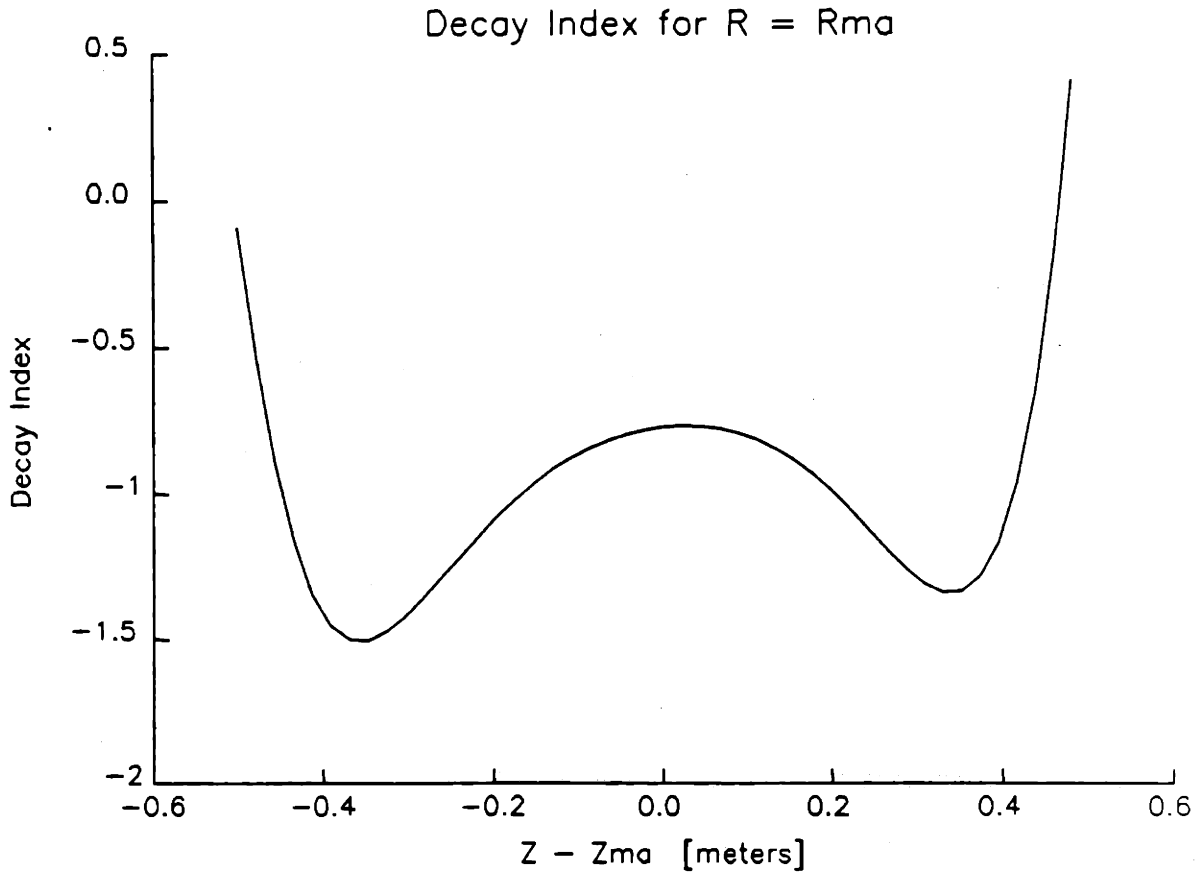

Figure 4.11: Decay index as a function of $\Delta Z \equiv Z - Z_{ma}$ along the line $R = R_{ma}$. The decay index becomes increasingly destabilizing as $|\Delta Z|$ increases.

4.7.2 EF Coil to Vessel Current Mapping

As described previously, the effect of vacuum vessel currents on the plasma is estimated by approximating flux values on a contour, $\mathcal{E}$, due to vessel currents, by using currents in the EF coil set. Clearly this approximation cannot be very good for high order vacuum vessel modes (i.e. with high frequency of variation with poloidal angle). Indeed, since the vessel model used in this work contains 76 elements, and there are 13 independent elements in the EF coil model, there exists a large null space of 63 vessel modes whose influence on the plasma cannot be modeled at all by EF currents.

However, the value of the approach depends on the space of vessel current vectors which strongly affect the plasma being well approximated by EF current vectors. If it can be demonstrated that the number of degrees of freedom in plasma variation is significantly lower than the number of EF coils, this can be satisfied. It is also important that the space of flux modes due to plasma current alone be of low rank, so that plasma modes which affect the vessel are also well approximated by less than 13 vectors. This does indeed turn out to be the case.

The actual degrees of freedom, the number of basis vectors needed to span the significant subspace of a multivariate system, can be determined by finding the SVD of the appropriate mapping matrices [25]. In particular, the coupling between plasma degrees of freedom and the vessel is described by the equilibrium perturbation set matrix Ψ_{vv} (defined in Sec. 4.3). Performing the decomposition on Ψ_{vv} we obtain

$$\Psi_{vv} = \mathbf{U}_v \mathbf{\Sigma}_v \mathbf{V}_v^T. \tag{4.39}$$

For the coil and vessel configurations we have defined throughout, these matrices have dimensions: $\Psi_{vv}(76 \times 15)$, $\mathbf{U}_v(76 \times 76)$, $\mathbf{\Sigma}_v(76 \times 15)$, and $\mathbf{V}_v(15 \times 15)$. The 15 non-zero singular values of Ψ_{vv} are plotted in Fig. 4.13 for case eq9. Notice that the singular values are plotted on a logarithmic scale. The figure shows that the fifth

singular value is down by a factor of about 10^{-3} from the maximum, indicating that 4 or 5 flux modes should be quite sufficient to describe the influence of the plasma on the vessel, and that the attendent plasma variation consists of far fewer than 13 degrees of freedom. It is therefore to be expected that the vessel to EF coil current mapping will be sufficient to describe the plasma response for the significant modes of the system.

We now turn our attention to the plasma surface mapping locus, $\mathcal{E}$, defined in Sec. 4.3. This is the locus of points at which the difference between fluxes due to EF currents and fluxes due to vessel currents is minimized. The resulting locus for the case of eq9 is plotted in Fig. 4.14. The dense contours surrounding the current density contours represent the mapping locus, which in this case consists of the NE=76 points which are closest in flux value to the edge flux (i.e. the flux at the 95% surface). Although there are gaps in the set which are noticeable on the scale of this contour plot, this set of mapping points surrounds the plasma very effectively. A single large gap here subtends a poloidal angle of about 25 deg (.44 radian), but the largest gap below this subtends only a few degrees.

The proof of the mapping lies in the error between flux measurements at these mapping points due to vessel currents and due to "equivalent" EF coil currents. Figures 4.15 through 4.18 show various cases of the vessel current-derived flux values plotted against the EF coil current-derived fluxes calculated using the mapping matrix, $\mathbf{D}_{cv}$, defined in Eq. 4.18. For each of these cases, the vessel mode vectors have been normalized to unity. Figure 4.15 shows the result for the unstable mode with the vessel alone acting as passive stabilizer. For this case the root difference squared (RDS) between the two predicted flux vectors, is

$$\text{RDS} \equiv \sqrt{\sum_{i}^{NE}(\psi_{xv(i)} - \psi_{xc(i)})^2/NE} = .051 \text{ Wb}, \tag{4.40}$$

while the mean value of the vessel current derived fluxes is .065 Wb, and the root mean squared (RMS) deviation from this mean is 1.36 Wb. Here we use $\psi_{xv,c(i)}$

to refer to the flux value at element i of the mapping locus due to the vessel and EF coil currents respectively. These statistical quantities provide a measure of the quality of the mapping. For a good approximation of the vessel current derived fluxes using the EF coil currents, the RDS should be a small fraction of the RMS deviation. For the unstable mode, this ratio is about 4%.

For comparison, we show two pathological modes of relatively high order which are not well modelled by this procedure. Figure 4.16 shows the result for a randomly generated mode, with current values uniformly distributed between -1 and 1. The resulting mode, shown in Fig. 4.17, is normalized before mapping to the approximately equivalent EF coil current set. For this case the RDS is .015 Wb, the mean value of the vessel current derived fluxes is .092, and the RMS deviation of the vessel derived fluxes is .270. Thus the RDS is only about 6% of the RMS deviation. The overall effect of this mode, although of very high order in poloidal angle variation, is therefore fairly well modeled by the EF current representation.

Figure 4.18 shows the result for a worst case vessel mode, shown in Fig. 4.19, in which each element is the opposite of its adjacent elements. Thus the variation in poloidal angle (more properly, in distance traveled along the vacuum vessel) is close to the maximum possible for our vessel discretization model. In this case the RDS is 4.36×10^{-3} Wb, the mean of the vessel current derived fluxes is .0186, and the RMS deviation is .030. The RDS is only about 15% of the RMS deviation even for this outlandish case.

We see, therefore, that the low order modes which dominate the behavior of the plasma are quite well modeled by the mapping algorithm. The quality of the mapping drops off with increasing current variation with poloidal angle, but remains remarkably good even for the worst possible case. This is a reflection of the distance from the conductors to the plasma. High order flux variation due to higher order vessel modes decays more rapidly than lower order variation. Since we measure the mapping effect at a plasma surface removed from the current locations,

the quality of the mapping effect at this surface is actually better than one would expect considering the rank deficiency of the EF coil set alone. This is a fortuitous result similar to that observed in approximating a distributed plasma with a small number of filaments (discussed in Chapter 3).

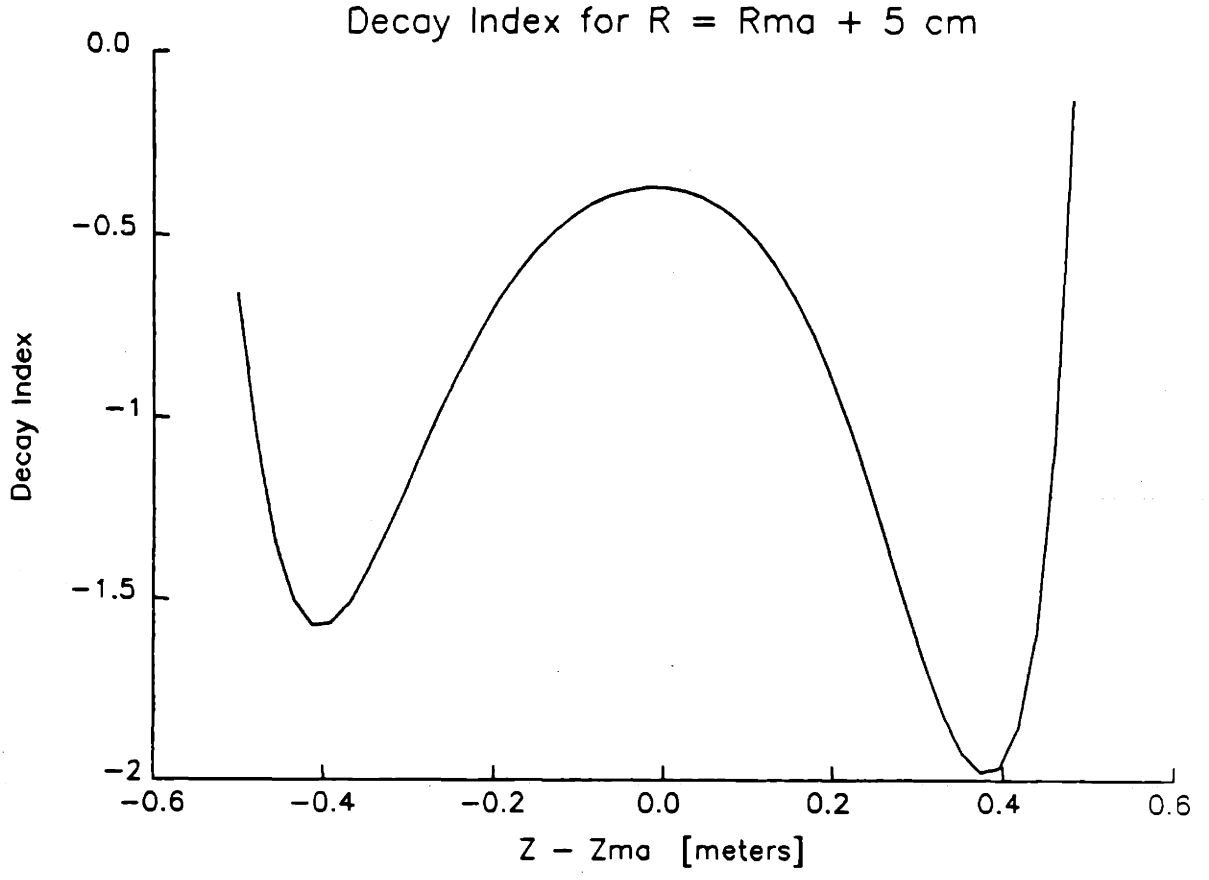

Figure 4.12: Decay index as a function of $\Delta Z \equiv Z - Z_{ma}$ along the line $R = R_{ma} + 5\text{cm}$. The decay index becomes increasingly destabilizing as $|\Delta Z|$ increases.

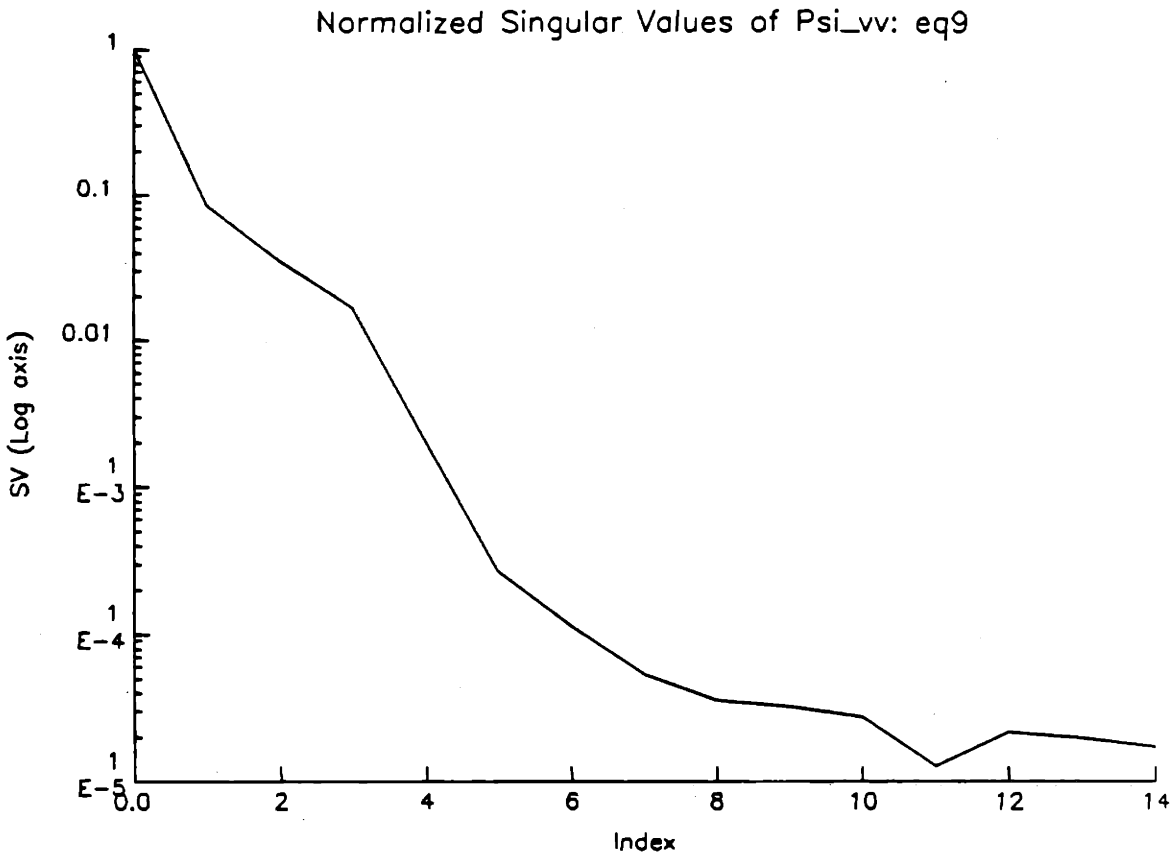

Figure 4.13: The singular values of Ψ_{vv} for equilibrium eq9.

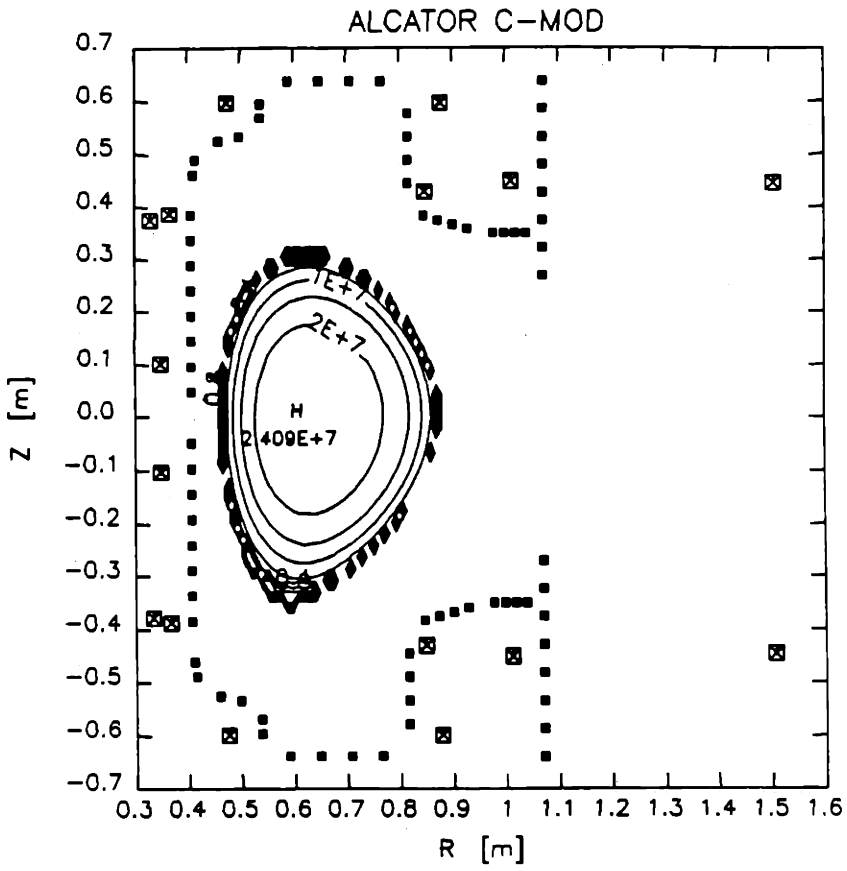

Figure 4.14: Plasma surface flux mapping locus, $\mathcal{E}$, for equilibrium eq9. Dark regions surrounding the current contours represent the mapping locus.

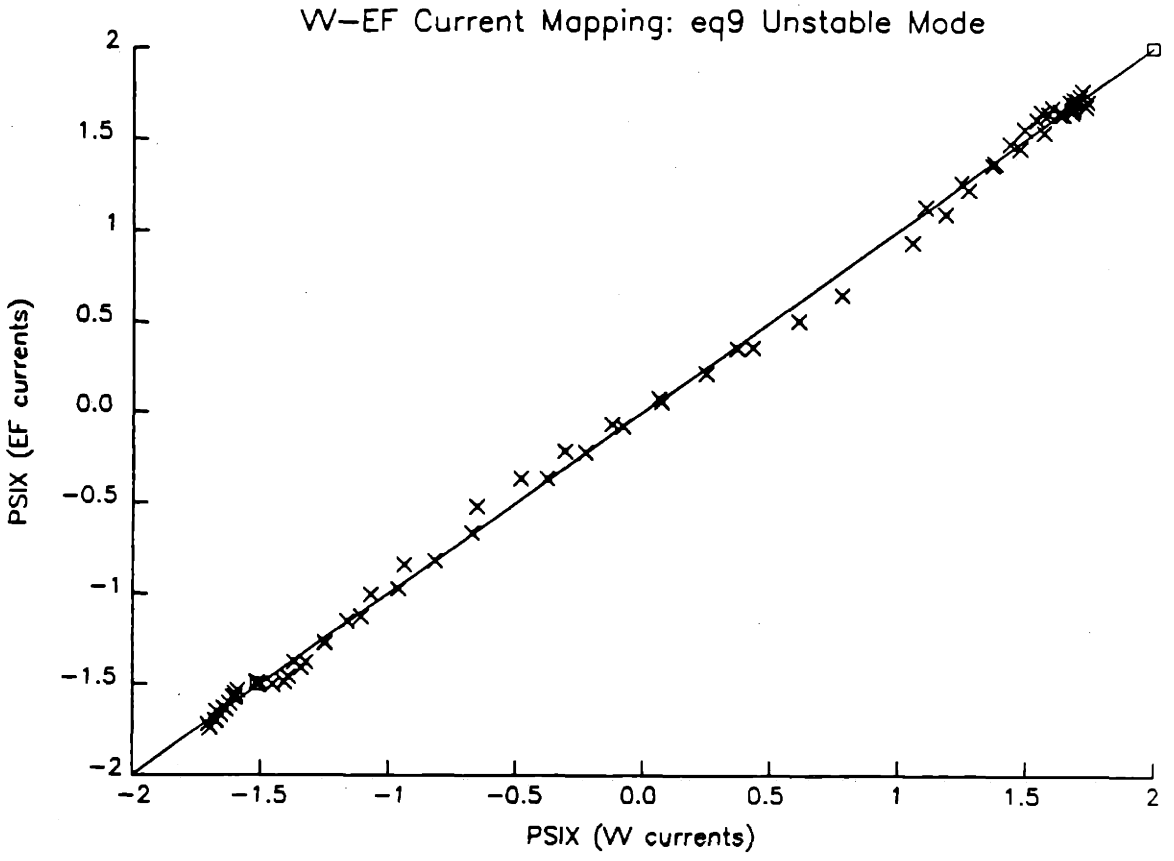

Figure 4.15: Vacuum vessel current derived fluxes at the mapping locus $\mathcal{E}$ vs. flux due to "equivalent" EF coil currents for the passive unstable mode of equilibrium eq9 (stabilized by vessel only).

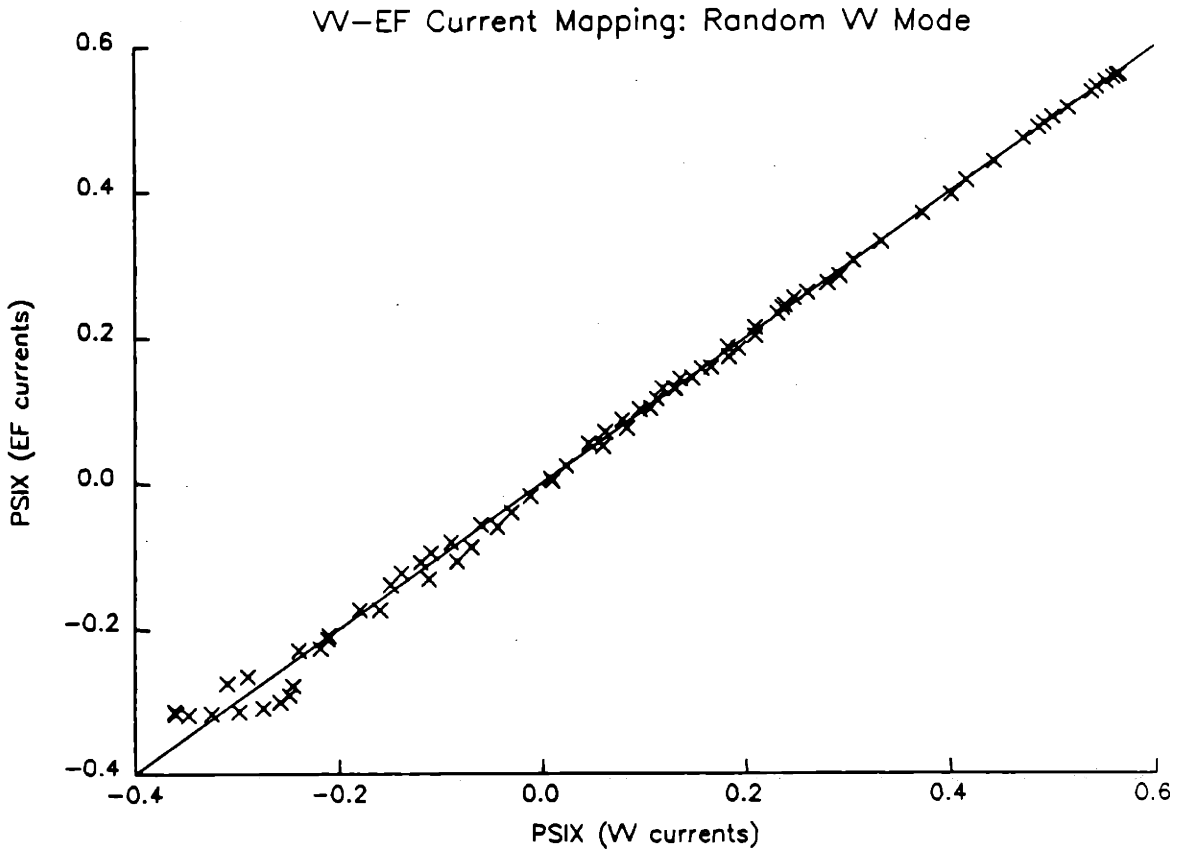

Figure 4.16: Vacuum vessel current derived fluxes at the mapping locus $\mathcal{E}$ vs. flux due to "equivalent" EF coil currents for a random distribution of vessel currents.

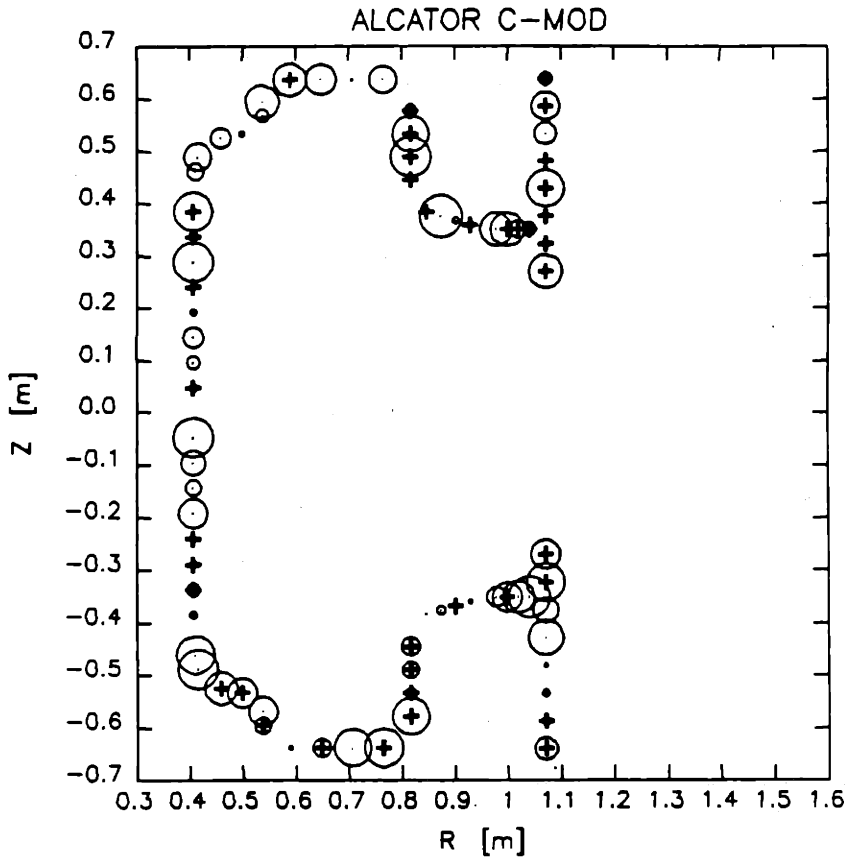

Figure 4.17: A random distribution of vessel currents used as an example for assessment of the accuracy of the mapping from vessel currents to "equivalent" EF coil currents.

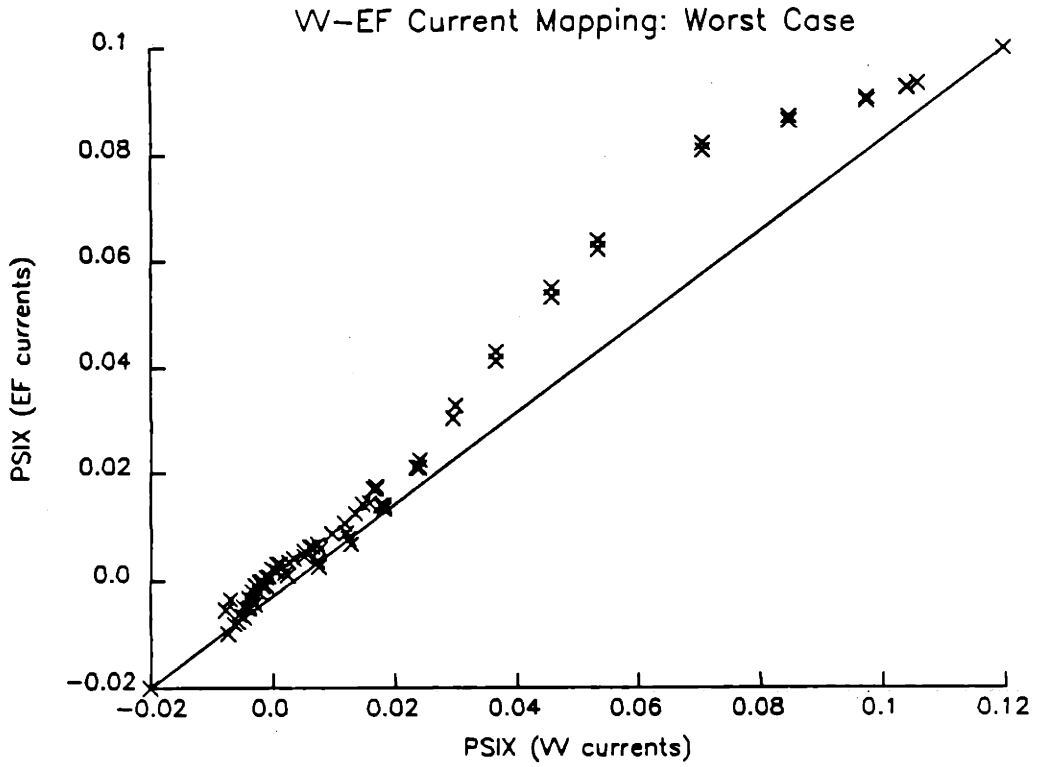

Figure 4.18: Vacuum vessel current derived fluxes at the mapping locus $\mathcal{E}$ vs. flux due to "equivalent" EF coil currents for a "worst case" distribution of vessel currents.

4.7.3 Comparison with TSC

After a tokamak has been designed and constructed, the designers are in the enviable position of being able to benchmark their systems analyses against the actual operating device. This allows control designers, for example, to determine such things as the actual time constants of coils and vessels, and the true effectiveness of their control law predictions. This in turn allows the control theories to be modified and improved. In this way, an actual machine is the ultimate arbiter of the correctness of a stability approach.

Before the machine begins operation, however, there are essentially two avenues of comparison available: other tokamaks already in operation, and other computer simulations. Because of the highly machine-specific nature of the stability and control analysis evolved in the present work, a very large additional effort would be required in order to compare predictions for other tokamak geometries and equilibria to available experimental data. However, the Tokamak Simulation Code, TSC [19], provides an ideal computer simulation benchmarking tool for design comparison. As already described, it possesses certain limitations for actual design, but admirably fills the need to check the predictions of a simpler model such as the perturbational equilibrium approach.

Fortunately, Alcator C–MOD has been extensively simulated with TSC in the work of Ramos [21]. This work includes a study of axisymmetric stability and control for a plasma representative of a flattop point in the middle of a shot. It is strictly incorrect to describe this point as an "equilibrium", since it was arrived at in the TSC run by evolving the plasma through a time–dependent shot simulation. The code run was then interrupted at some point mid-shot, and the resulting plasma studied for axisymmetric stability. That said, however, we shall continue to refer to this case as an equlibrium, since for the purposes of this comparison, the results of Ramos' study treats the initial plasma in the same way that the per-

Quantity	Value	units
I_p	3.00	MA
B_0	9.0	T
R_{ma}	67.5	cm
R_0	66.5	cm
z_{ma}	0.00	cm
a	21.0	cm
κ_{95}	1.6	
κ_{sep}	1.75	
$\delta_{95(av)}$	.30	
δ_{sep}	.40	

Table 4.4: Essential characteristics of TSC simulation benchmarking equilibrium to be compared with eq9.

turbational approach treats the base equilibrium. Essential characteristics of this initial "equilibrium" state are given in Table 4.4. Notice that all of the fundamental features are well matched by equilibrium eq9 (see Table 4.1). Case eq9 was in fact chosen to match the available TSC benchmarking case, since this equilibrium represents a standard $\kappa_{95} = 1.6$ single null scenario for C–MOD operation. The primary differences between the two cases are the triangularity, a difference which is small enough not to have an important effect on the vertical instability in this case [26], and the profile forms, a potentially large difference. Since TSC uses an actual transport simulation to evolve plasma current and pressure profiles, it would be the most fortuitous of events for the Strickler profiles of ASEQ and the TSC profiles to resemble one another at all. In fact, the profiles of eq9 are qualitatively rather peaked compared to those of the TSC case [27]. But details regarding the profiles would require a more involved examination of the TSC data, which was not readily available from [21].

After the shot evolution is interrupted in the TSC simulation, there follows a brief transient phase, during which vacuum vessel currents are allowed to decay and provide the perturbation needed to initiate the growth of the unstable "vertical" axisymmetric mode. With feedback disabled and EF coil currents maintained at

their original equilibrium values, the plasma is allowed to evolve in accordance with the growth of the instability.

The operation of TSC requires the specification of several non-physical, but computationally required quantities which contribute to the interpretation of results. The two quantities which affect the growth rate results in the present work are the artificial Alfvén speed scaling factor, FFAC, and the artificial "viscosity", ν_{num}, a numerical damping introduced to provide for iterative computational stability.

Since TSC models both MHD and transport phenomena simultaneously, and the characteristic timescales of these phenomena differ by a factor of about 10^6, practical numerical solution of the fluid equations requires an artificial scaling of one of these timescales. For a typical shot simulation, the fast MHD phenomena do not significantly affect the plasma, so ions can be taken to have very large mass, effectively lengthening the MHD timescale to be nearer to that of diffusive transport phenomena. TSC therefore takes the ion mass to be $\mathrm{FFAC}^2 m_i$, resulting in an Alfvén speed of $\mathrm{FFAC}^{-1} v_A$. By running a shot with a large FFAC, fast MHD physics is suppressed, with the compensation that the time-dependent problem is computationally tractable. However, while these effects are unimportant in a plasma being successfully maintained in equilibrium, they must be restored in order to correctly simulate the axisymmetric instability. FFAC must be reduced to 1, or at least enough points must be calculated with decreasing FFAC to establish a convincing extrapolation to FFAC=1. In addition to FFAC, the numerical viscosity, ν_{num}, must also be varied to establish its effect on results. The relative magnitude of the influence of varied ν_{num} decreases with decreasing FFAC.

In the work of Ramos, both FFAC and ν_{num} were varied sufficiently to achieve reasonable extrapolation to FFAC=1 and demonstrate the approximate uncertainty introduced by the use of numerical viscosity. For the equilibrium described in Table 4.4, comparable to eq9, a careful reanalysis of the data given in [21] yields an

FFAC=1 extrapolated growth rate of $\gamma = 940 \pm 60$ sec^{-1}. The error bars are estimated from the extrapolations for the two values of ν_{num} used (an ad hoc value ν_0, and $2\nu_0$). This is to be compared with the perturbed equilibrium growth rate prediction of 622 ± 32 sec^{-1}, where a 5% error bar has been used to reflect the convergence criterion for that procedure. While the respective error bars exclude agreement between the two predictions, the perturbed equilibrium result is significantly closer to the TSC result than is the rigid model (see Table 4.2). While the perturbational result differs from the TSC result by 50%, the rigid growth rate is more than 100% off. Considering the great difference in vacuum vessel models and plasma profiles between the two cases, the agreement is relatively good.

4.8 Discussion

This chapter has developed and demonstrated the perturbational equilibrium approach to estimating an approximately flux conserving plasma response in the presence of conductors other than those used to perform the original perturbations. Using this algorithm, the inductive coupling between the plasma and both EF coil set and vacuum vessel elements can be modeled, and a plasma response to currents induced in these arrays can be approximated. The resulting plasma model, although lacking some degrees of freedom present in a physical plasma, contains the most important degrees of freedom controllable by the given coil set with which the initial perturbations were performed. The number of modes of the plasma which significantly couple to a conductor array such as the vessel model used here is actually quite small, on the order of 4 or 5. The 13-dimensional space spanned by the EF coil current perturbations (and the vertical displacement perturbations) thus provides more than enough information to allow the approximate modeling of the plasma response under these conditions.

Comparison has been made with a full nonlinear simulation of the growth of the

axisymmetric instability for a typical Alcator C–MOD equilibrium using the Tokamak Simulation Code. This comparison demonstrates that while the perturbational approach does not exactly match the predictions of TSC, it comes significantly closer to the TSC result than does the rigid plasma model. The perturbational method differs from the TSC result by about 50% in passive growth rate, while the rigid model prediction differs by more than 100%.

Passive growth rates for a set of typical C–MOD equilibria of varying elongations and degree of vertical stability were calculated using both the perturbational and rigid models. While the rigid model indicates that the growth time for the most unstable equilibrium (eq10, $\kappa_{sep} = 1.85$) is significantly longer than the response time of the C–MOD fast power supplies, the perturbational model finds the instability growth time comparable to the nominal 1 ms limit for marginal power supply response. However, to properly assess the controllability of these cases, a full active simulation is necessary. The fundamental active control predictions of the rigid and perturbational equilibrium models must be compared, and the implications for power supply sufficiency and equilibrium achievability determined. Of course, the rigid vertical simulation cannot model radial or shape plasma perturbations, which are implicitly included in the perturbational model. Only the latter approach allows integrated analysis of the entire equilibrium and stability control problem.

In the next chapter we therefore turn our attention to the issues both of basic active control for the comparison of rigid and perturbational predictions, and analysis of the integrated control problem using perturbed equilibria.

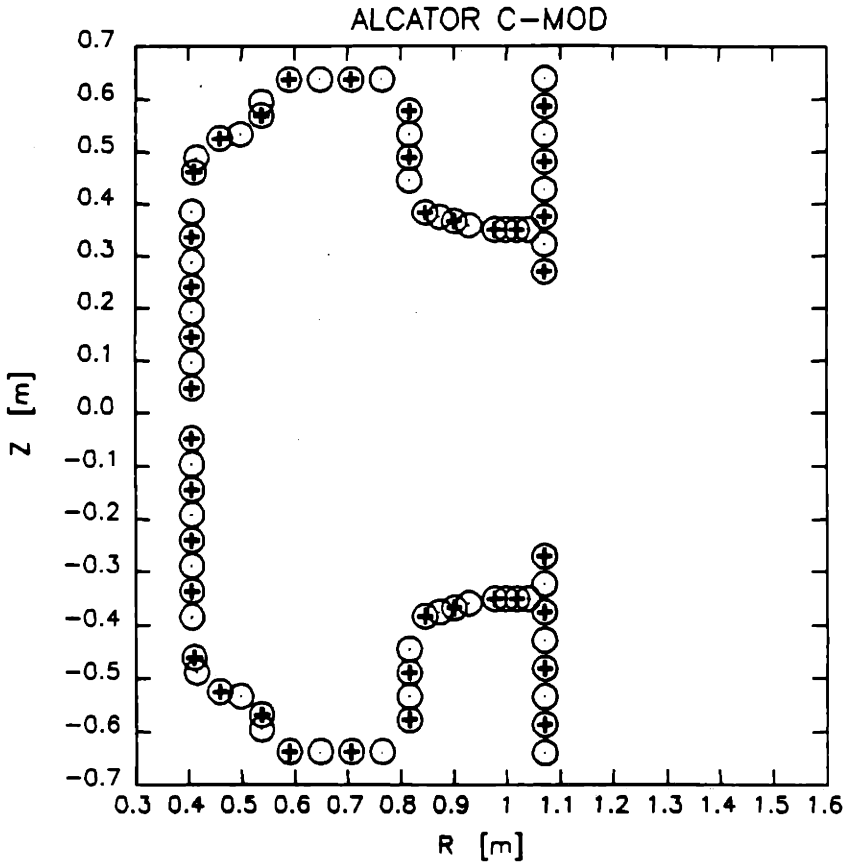

Figure 4.19: A "worst case" distribution of vessel currents used as an example for assessment of the accuracy of the mapping from vessel currents to "equivalent" EF coil currents.

Chapter 5

Stability Control Analysis

As a tokamak plasma is evolved through a typical discharge, it passes through several broadly different kinds of equilibria. It may begin as a small, cold, circular plasma carrying little current and lying at the bottom of the vacuum vessel, before becoming more elongated and beginning to fill the machine's poloidal cross-section. As the shot progresses, the PF coil currents follow their preprogrammed trajectories to develop the plasma into the shape planned for the flattop portion of the current evolution. During the current flattop, when in general the plasma is intended to be held in some particular shape, it may still experience a variety of changes and disturbances. For example, heating experiments may change temperature and current profiles, pellet injection may strongly perturb the plasma density as well, and internal plasma modes can cyclically alter the nature of the equilibrium. It is crucial that the nominal evolution of the plasma be controlled to follow the preprogrammed path of the shot, and highly desirable for the resulting control to be robust enough to tolerate a certain degree of perturbation along the way.

With this chapter we begin the examination of the axisymmetric control problem. We shall examine the general features of the active control problem for equilibrium and vertical stability maintainance. We shall also construct the state space

formalism for this problem and describe the accomodation of power supply dynamics using that formalism. This will provide the necessary preparation for the control design description of the next chapter.

5.1 General Characteristics of Vertical Active Control

The passive modes of a rigid model describing vertical motion consist of a set of highly damped modes which do not significantly couple to plasma motion, and a few modes which do include plasma response, one of which is unstable for elongated equilibria. The modes which do not involve plasma motion are termed "quasiconstant roots" (QR) in this work, since as feedback gain is increased, these roots are not strongly affected. Their eigenvalues do not change significantly compared to those which do couple to plasma motion. Roots such as these latter, which do vary significantly as gain is swept, are termed "feedback roots" (FR). We shall also use this terminology in discussing other plasma models. The number and behavior of FR's will differ depending on such factors as whether or not mass is included, the order of power supply models used, and the relative coupling of the control coils and the vacuum vessel to the plasma.

In the case of a massless plasma model, the FR's typically include the (dominant) vertical instability mode and one or more passively stable modes which couple to this one through the driven coil current. If a power supply model containing internal dynamics is used, the poles representing a demand on the power supply may also couple to the vertical mode when the control loop is closed. Varying the closed loop gain will then modify the eigenvalues of all of these modes.

When finite plasma mass is retained, a complex pole pair of highly damped oscillatory modes is introduced in the passive system. These can be affected by

sufficiently high gain or driving frequency, and so for these limits are also "feedback roots". Under such circumstances, this pole pair can be driven unstable even as the vertical mode is stabilized. However, since these modes depend on plasma inertia, the power supply driving frequency required to destabilize them approaches the Alfvén frequency. Since this is well beyond any reasonable power supply capability, this limit can be discounted. Later sections of this chapter will discuss appropriate poles in a power supply model reflecting the frequency response limit.

Many of the general principles of active control can be found in simplified second order models. We begin by investigating some of the limits to controllability which are intrinsic to the tokamak stabilization problem. We employ a massless plasma model with two stabilizing coils, one of which is considered to be actively driven.

5.2 Simple Analytic Limits to Controllability

Consider a system consisting of two stabilizing resistive coils and a massless plasma free to move rigidly in the Z–direction only. This system is represented schematically in Fig. 5.1. The equation of motion from Chapter 3, Eq. 3.2, is then a force balance equation:

$$0 = S_1 I_1 + S_2 I_2 + S_B z. \tag{5.1}$$

The corresponding circuit equations are

$$L_1 \dot{I}_1 + M_{12} \dot{I}_2 + r_1 I_1 + S_1 \dot{z} = V_1 \tag{5.2}$$

$$L_2 \dot{I}_2 + M_{12} \dot{I}_1 + r_2 I_2 + S_2 \dot{z} = 0 \tag{5.3}$$

where coil 1 is the active control coil, to which control voltage V_1 is applied, I_1 is the current in coil 1, I_2 is the current in coil 2, and z is the plasma vertical displacement. S_1, S_2, and S_B are defined as in Eqs. 3.3 and 3.4. The remaining terms are defined

as in Eq. 3.1. S_1 and S_2 are measures of plasma-coil coupling and S_B is a measure of destabilizing force due to unfavorable decay index.

Laplace transforming the circuit equations and expressing the plasma displacement, z, in terms of the voltage, V_1, applied to coil 1, we obtain:

$$z(s) = \frac{\tau_z s + 1}{As^2 + Bs + C} V_1(s), \tag{5.4}$$

where the exact forms of the non-zero quantities A, B, and C are not important for the purposes of the present investigation. We shall extract physical insight without addressing the details of these quantities. The variable s is the Laplace transform frequency variable defined by $s \equiv \sigma + i\omega$, where σ and ω are the real and imaginary components of the frequency.

We define the "transfer function", G(s), as:

$$G(s) \equiv \frac{z(s)}{V_1(s)} = \frac{\tau_z s + 1}{As^2 + Bs + C}, \tag{5.5}$$

which describes the frequency domain response of the plasma displacement, z, to input voltage, V_1. This is referred to as the "passive" transfer function, since it describes the plasma response in the absence of any "active" feedback. Inspection reveals that there exists one driving frequency s for which the plasma displacement is not affected, and two frequencies for which the plasma displacement becomes infinite. That is, it contains one zero and two poles. As in the single coil case studied in Chapter 3, one of these poles is unstable. We describe this as a "right half-plane" pole, referring to the complex s-plane. The other pole is a stable, or "left half-plane" pole [5]. We shall address the location of the zero presently.

We now express the passive transfer function in a more physically suggestive form:

$$G(s) \equiv \frac{G_0(\tau_z s + 1)}{(\tau_1 s + 1)(\tau_2 s - 1)} \tag{5.6}$$

where τ_2^{-1} is the unstable pole. We can now create a feedback law causing a voltage to be applied to coil 1 which is proportional to a sum containing the vertical

displacement, z, and the vertical velocity, $\dot{z}$. The voltage is then described by a differential equation:

$$V_1(t) = -K_0(\tau_a \frac{dz(t)}{dt} + z(t)), \tag{5.7}$$

where K_0 is the feedback gain and τ_a is the derivative feedback time constant. Laplace transforming this equation we obtain

$$V_1(s) = -K_0(\tau_a s + 1)z(s). \tag{5.8}$$

This form of feedback is known as proportional-derivative (PD) feedback. The system now appears as in Fig. 5.2, in which $H(s) = K_0(\tau_a s + 1)$. Applying this feedback law as illustrated in the figure, the displacement is related to the driving voltage through

$$\frac{z(s)}{V_1(s)} = \frac{G(s)}{1 + G(s)H(s)}. \tag{5.9}$$

The poles of this equation are the solutions of the equation:

$$G(s)H(s) = \frac{\alpha(\tau_z s + 1)(\tau_a s + 1)}{(\tau_1 s + 1)(\tau_2 s - 1)} = -1, \tag{5.10}$$

where $\alpha \equiv G_0 K_0$.

The corresponding root-locus equation whose solution gives the location of system poles as the gain, α, varies is

$$(\alpha\tau_z\tau_a + \tau_1\tau_2)s^2 + (\alpha[\tau_a + \tau_z] - \tau_1 + \tau_2)s + (\alpha - 1) = 0 \tag{5.11}$$

For typical values of the various time constants, the solutions for s will have no positive real part if α is made sufficiently large, even if $\tau_a = 0$. The system will thus be stabilizable without derivative feedback. The necessary condition for stability is $\alpha > 1$ and $\alpha[\tau_a + \tau_z] > \tau_1 - \tau_2$, assuming that the system zero, $-1/\tau_z$, is a left-half plane zero (i.e. $\tau_z > 0$). However, this is not necessarily the case. Expansion of the full solution shows that the intrinsic system zero is given by

$$-\frac{1}{\tau_z} = -\frac{\tau_2}{L_2 - \frac{S_2}{S_1}M} \tag{5.12}$$

Now, since $S_i \equiv I_p \frac{\partial M_{ip}}{\partial z}$, we have

$$\frac{S_2}{S_1} = \frac{M'_{2p}}{M'_{1p}} = \frac{R_2 B_{R2}}{R_1 B_{R1}} \tag{5.13}$$

where " ' " has been used to indicate the derivative with respect to z, and B_{Ri} is the radial B-field at coil i due to the plasma. Clearly this can be arbitrarily large as the B_R-coupling between coil 1 (the control coil) and the plasma is reduced. An extreme example is placement of coil 1 near the same z-location as the plasma filament, where B_R is equal to or nearly zero. In particular, if the coupling between the passive stabilizing structure (represented here by coil 2) and the plasma sufficiently exceeds that between the control coil and the plasma, a right-half plane system zero will result. For the case of $\tau_z < 0$, defining $t_z \equiv |\tau_z|$, we find for the new characteristic equation

$$(-\alpha t_z \tau_a + \tau_1 \tau_2)s^2 + (\alpha[\tau_a - t_z] - \tau_1 + \tau_2)s + (\alpha - 1) = 0 \tag{5.14}$$

Then, for $\tau_1 > \tau_2$, true for a system which is not extremely well passively stabilized, this system cannot now be stabilized without derivative feedback (i.e. if $\tau_a = 0$). Since vacuum vessels are in general better coupled to the plasma than control coils are, there is usually a maximum elongation which a given machine can stabilize without derivative feedback. This phenomenon is seen in Alcator C–MOD, and has also been demonstrated with a more involved second order model for the case of D-IIID [13].

5.3 Rigid Model with Displacement Feedback

The simplest form of control for the vertical instability is perfect displacement feedback. In this case, the actual vertical displacement of the plasma, z, is assumed to be directly available to the feedback loop. This is especially appropriate for the rigid model, in which the vertical displacement provides an exact description of the

unstable mode. Voltage signals which are functions of time integrals and derivatives of z can then be applied to the control coils. In this section we shall use a simple single zero, single pole control law:

$$V_i + t_b \frac{dV_i}{dt} = -\alpha_i (z + t_a \frac{dz}{dt}) \tag{5.15}$$

describing the voltage V_i applied to coil i as a function of displacement z and velocity $\dot{z}$. This yields a transfer function of the form:

$$\frac{V_i(s)}{Z(s)} = \frac{-\alpha_i(1 + t_a s)}{(1 + t_b s)}. \tag{5.16}$$

This form is especially useful in analyzing the constraints of a realistic pulsed power supply. Such supplies possess an inherent time delay in their response to a control signal. For a finite time period following the application of a demand signal, the power supply output will be completely unchanged. After the delay time interval has passed, the power supply begins to respond to the demand signal. If this response delay time is too long relative to the growth time of the phenomenon being controlled, the power supply will not be able to stabilize that mode.

The control law form above allows us to model this intrinsic delay with a single pole, t_b, and then to determine the maximum possible t_b for which the system can be stabilized. The physical nature of this model is illustrated in Fig. 5.3. The figure shows the actual step demand input to the power supply, the exponential rise associated with the single pole model, and the time delayed response of a realistic power supply. The single pole is necessarily an optimistic model, since it exhibits a finite response for an arbitrarily small time interval following excitation, whereas a true delay has no response until after the delay time. A single pole represents a linear phase lag, rather than the highly nonlinear pure delay. Nevertheless, a mere phase lag is sufficient to exhibit the phenomenon of uncontrollability if the "delay time", t_b, is too great.

In general, elongated C-MOD equilibria have been found to require derivative feedback in order to be stabilized at all, even with zero delay. This is the same

Equilibrium	Min. t_a	Max. t_b	Max. t_b	Units
	($t_b = 0$;mf)	($t_a = 50$;mf)	($t_a = 50$;sf)	msec
eq6	$0.1 < t_a < 0.5$	3.0	5.0	msec
eq7	$0.1 < t_a < 0.5$	1.0	3.0	msec

Table 5.1: Maximum tolerable "delay time", t_b, for equilibria eq6 and eq7.

phenomenon as that illustrated in the discussion of analytical models above, and has been noted by other authors [13]. Figure 5.4 for example, shows the result of sweeping gain in eq6 of the original design set (see Chapter 3) using direct displacement feedback with no derivative term. The unstable root has a growth rate of 388 sec^{-1} at zero gain, but becomes more and more stable as gain is increased. In the absence of derivative feedback, however, this root never becomes stable. Figure 5.5 shows the result of adding derivative feedback. For this case the modes are stabilized.

As one would expect, addition of a single pole modeling power supply delay makes the system more difficult to stabilize, and in fact a given equilibrium will exhibit a maximum tolerable delay for which stability can be achieved at all. Stability boundary results showing maximum tolerable delays and necessary zero values for eq6 and eq7 are shown in Table 5.1. In the table, "Min. t_a" refers to the minimum required lead (derivative feedback) time constant for zero delay, "Max. t_b" refers to the maximum tolerable delay time constant, and "mf","sf" refer to multifilament and single filament plasma models respectively. The optimal lead time constant, t_a, allowing achievement of the maximum delay, is shown in the second row of the table. Using this crude delay model, the maximum tolerable delay time for the maximum elongation equilibrium (eq7; passive growth rate = 945) is found to be approximately $t_b^{max} \simeq 1$ msec using a lead value of 50 msec.

The actual fast power supply will have a response time on the order of 0.2 msec, providing a significant safety margin for this result. It is of interest to note that a previous EFC location yielded a passive growth rate for this equilibrium of

980 sec^{-1} and maximum tolerable delay of approximately $t_\delta^{max} \simeq 0.4$ msec with the same lead value. Thus the passive growth rate was affected relatively little by this design change, but the acceptable delay was roughly doubled.

The table also includes tolerable delay predictions resulting from a single filament plasma model located at the current centroid. From these two comparisons, it is clear that a single filament model can differ significantly from a multifilament model in its maximum tolerable delay time prediction. For the case of the highly unstable eq7, this difference amounts to a factor of three in tolerable delay time prediction. This could represent the difference between accepting a 12-phase power supply as adequate for vertical stability control or not. As suggested in Chapter 3, active as well as passive results are unreliable when only a single filament is used to represent the plasma.

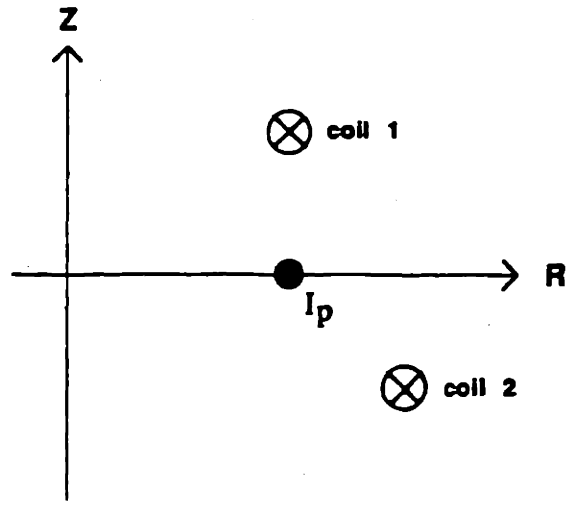

Figure 5.1: Schematic of 2-coil system for studying controllability.

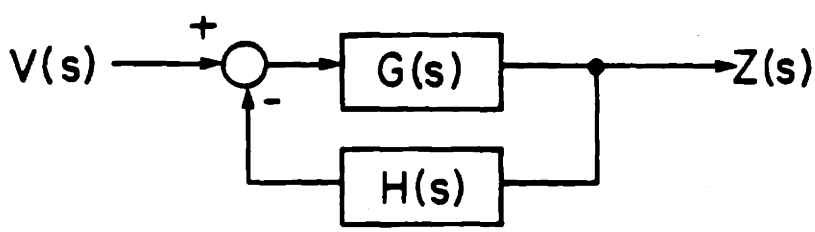

Figure 5.2: Block diagram of closed loop feedback system.

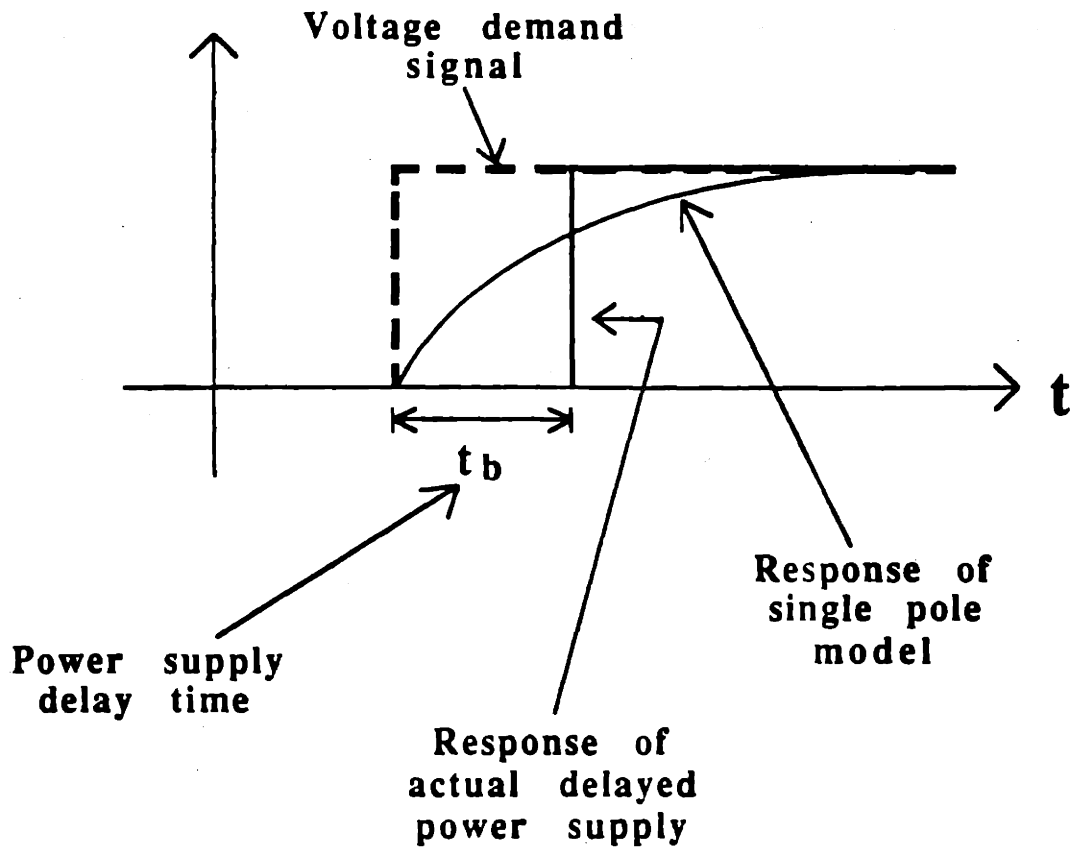

Figure 5.3: Time responses of realistic power supply and single pole model to step input voltage demand signal.

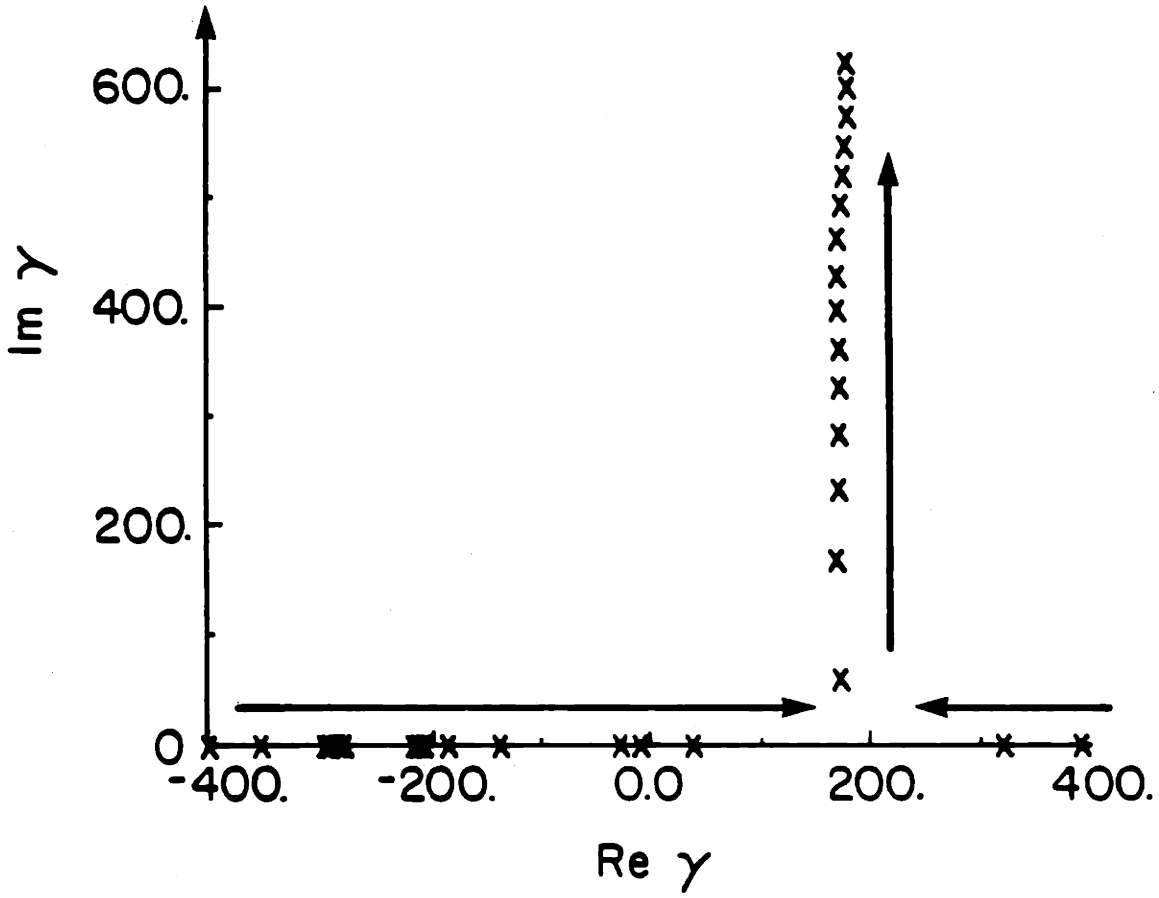

Figure 5.4: Root-locus plot for eq6 with no derivative feedback ($t_a = 0$). Arrows indicate direction of motion of FR as gain increases.

5.4 State Space Formalism

Multivariable dynamic systems do not lend themselves readily to description and analysis in terms of single-input single-output Laplace transform transfer function. It is more appropriate to exploit the vector nature of the multivariable dynamics, and employ linear algebra methods to represent the system using the "state space" formalism. This approach, pioneered by the Soviet Union during the 1960's, has become the standard method for analyzing multivariable control systems, and defines the so-called "modern" era of control. This formalism has proven extremely powerful, and has given rise to entire subfields of study in multivariable control theory, including the areas of linear quadratic optimal control and observer design [28,29]. In this section we shall describe the state space equations, and show how the tokamak axisymmetric control problem is cast into that form.

5.4.1 State Space Equations and Terminology

In general, multivariable linear dynamic system equations of arbitrary order can be written in the form of two first order linear differential matrix equations. The first of these equations is known as the "state equation":

$$\dot{\underline{x}} = \mathbf{A}\underline{x} + \mathbf{B}\underline{u}. \tag{5.17}$$

This describes the time evolution of the state vector, $\underline{x}$, as a function of the present state and control inputs, $\underline{u}$. The second equation, known as the "output equation":

$$\underline{y} = \mathbf{C}\underline{x} + \mathbf{D}\underline{u}, \tag{5.18}$$

gives the sensor signals, $\underline{y}$, as a function of the state and control variables. It is most often the case that the control-to-sensor matrix, $\mathbf{D}$, is zero, and this matrix is usually neglected in derivations [29].

By convention we refer to the "system matrix", A, the "control", or "input matrix", B, and the "sensor", or "output matrix", C.

Feedback in a state space system is described by

$$\underline{u} = f(\underline{x}, \underline{y}), \tag{5.19}$$

where f() represents a differential matrix function of the state and output variables. The control vector can thus be a function of the state and output vectors and their higher order derivatives. "Full state feedback" refers to the case where $\underline{u}$ is a function of $\underline{x}$ alone, and "output feedback" refers to the case where $\underline{u}$ is a function of $\underline{y}$ alone.

From the structure of the state equation, it is apparent that the passive eigenvalues and eigenvectors are the eigenvalues and eigenvectors of the state matrix, A. Denoting the eigenvalues by λ_i and the eigenvectors by $\underline{v}_i$, we can construct the usual (right) eigenvector matrix, V, whose columns consist of the $\underline{v}_i$ vectors, and the diagonal eigenvalue matrix, Λ, whose diagonal entries are the eigenvalues. Hence the usual (left) eigenmode equation:

$$\mathbf{AV} = \mathbf{V}\Lambda. \tag{5.20}$$

The left eigenvector matrix, W, is similarly defined by

$$\mathbf{WA} = \Lambda\mathbf{W}, \tag{5.21}$$

whose i^{th} row we denote by $\underline{w}_i$. It is also common to denote the i^{th} column of the control matrix by $\underline{b}_i$.

Using the above notation, the general time response of the state vector for a given initial state vector $\underline{x}(0) \equiv \underline{\xi}$, and a given control vector as a function of time, $\underline{u}(t)$, is described by [28]:

$$\underline{x}(t) = \sum_{i=1}^{NX} (\underline{w}_i^T \underline{\xi}) \underline{v}_i e^{\lambda_i t} + \sum_{i=1}^{NX} \sum_{k=1}^{NU} (\underline{w}_i^T \underline{b}_k) \underline{v}_i \int_0^t e^{\lambda_i (t-\tau)} u_k(\tau) d\tau. \tag{5.22}$$

The inner product, $(\underline{w}_i^T \underline{b}_k)$, is a measure of the controllability of mode i using control k. If any of these pairs of vectors are orthogonal, this quantity will be zero, and the corresponding mode will be uncontrollable with that control. This controllability measure can be used to compare competing control coil configurations to aid in the optimization of EF coil placement during the early design of a tokamak.

The output time response is simply the state time response operated on by the sensor matrix, C. We denote the l^{th} row vector of C by $\underline{c}_l^T$. Because of the appearance of the right eigenvector, $\underline{v}_i$, in the state vector time response, the quantity $(\underline{c}_l^T \underline{v}_i)$ is a measure of the observability of mode i using sensor l. As in the case of controllability, if any of these pairs of vectors are orthogonal, this quantity will be zero, and the corresponding mode will be unobservable using that sensor. In the same way as described above for controllability, this observability measure can be used to compare competing sensor configurations to aid in the optimization of sensor design.

The state space approach has been used to evolve a large array of techniques for control system analysis and design. We shall use some of these methods and extensions of them in the design of the C-MOD control system, described in the next chapter.

5.4.2 Tokamak Axisymmetric Control Problem

The discretized conductor model we have described to analyze plasma response in the presence of resistive walls and EF coils lends itself readily to a state space formulation. The perturbed equilibrium plasma model itself reveals several degrees of freedom, and thus also requires a multivariable representation of some form in order to correctly describe the dynamics of the system. Since the plasma response has been mapped to conductor currents, and the number of degrees of freedom available in the conductor array far exceeds those of the plasma alone, the natural

state variables for the system are either conductor element currents or fluxes at those conductors. The state space can be formulated in either way. We choose currents to be the state variables somewhat arbitrarily, although with the belief that currents allow a more intuitive grasp of a mode. A current mode also possesses the virtue of allowing easy separation of flux due to currents and flux due to plasma alone.

The axisymmetric control problem is straightforward to cast into state space form. The circuit equation including flux conserving plasma response, expressed in terms of the stabilizing conductor current vector, $\underline{I}_s$, is given by (see Eq. 4.37)

$$\mathbf{M}_{ss}\dot{\underline{I}}_s + \mathbf{D}_{ss}\dot{\underline{I}}_s + \mathbf{R}_s\underline{I}_s = \underline{V}_s \tag{5.23}$$

where the matrix $\mathbf{D}_{ss}$ contains the complete plasma response.

Only certain EF coil circuits are actively driven, leaving the vessel elements and undriven EF circuits with zero applied voltage. The applied voltage vector, $\underline{V}_s$, can therefore be expressed as

$$\underline{V}_s \equiv \mathbf{B}_1\underline{v} \tag{5.24}$$

where the new control vector, $\underline{v}$, contains entries for only the actual driven coils, and $\mathbf{B}_1$ contains ones in the appropriate entries to influence only the driven coils, and zeros elsewhere. $\mathbf{B}_1$ is thus in general a rectangular matrix.

Manipulating the circuit equation, we obtain

$$\dot{\underline{I}}_s = -(\mathbf{M}_{ss} + \mathbf{D}_{ss})^{-1}\mathbf{R}_s\underline{I}_s + (\mathbf{M}_{ss} + \mathbf{D}_{ss})^{-1}\mathbf{B}_1\underline{v} \tag{5.25}$$

which has the desired form,

$$\dot{\underline{x}} = \mathbf{A}\underline{x} + \mathbf{B}\underline{u}. \tag{5.26}$$

The following identifications result:

$$\mathbf{A} \equiv -(\mathbf{M}_{ss} + \mathbf{D}_{ss})^{-1}\mathbf{R}_s \tag{5.27}$$

$$\mathbf{B} \equiv (\mathbf{M}_{ss} + \mathbf{D}_{ss})^{-1}\mathbf{B}_1 \tag{5.28}$$

and of course the state vector, $\underline{x}$, is identified with I_s, and the input vector, $\underline{u}$, is identified with the driven coil applied voltage vector, $\underline{v}$.

The sensor signals available to the control system include poloidal fluxes at flux loops, poloidal field values at B_p coils, and possibly EF coil currents from Rogowski coils. Clearly this system represents one of the cases in which the output vector does not depend on the controls. Thus the **D** matrix is zero. The sensor matrix is simply constructed from the appropriate Green's functions and plasma response matrices, using the perturbed equilibrium data and vessel-coil mapping matrix as demonstrated in Chapter 4. All of the sensor data available expressed in an output vector yields

$$\underline{y} = \begin{bmatrix} \underline{\psi}_{FL} \\ \underline{B}_p \\ \underline{I}_{EF} \end{bmatrix} \tag{5.29}$$

5.5 Modeling Power Supply Dynamics

The state space formalism makes it particularly easy to extend the number of dynamic variables in order to accomodate subsystems not included in the original state equation. This provides a way of incorporating the power supply dynamics without recalculating the basic state matrices. Consider a set of power supplies, each of which receives one input demand signal, and drives one EF circuit with an actual output voltage signal. The internal dynamics of the i^{th} power supply is assumed to be reasonably well approximated by a single-input-single-output (SISO) transfer function of order n_i (that is, with n_i poles). By inverse Laplace transforming these transfer functions, the differential equations describing the power supply models can be recovered, and a state space representation can be constructed. Let this space be described by the state equation

$$\dot{\underline{x}}' = \mathbf{A}'\underline{x}' + \mathbf{B}'\underline{u}, \tag{5.30}$$

and output equation

$$\underline{v} = \mathbf{C}'\underline{x}'. \tag{5.31}$$

The output vector, $\underline{v}$, for this space is the actual driving voltage for the active EF circuits, and the input vector, $\underline{u}$, is the set of demand voltages fed to the power supplies. This will become the input vector for the combined state space including the conductors, plasma, and power supply models (hence the unprimed $\underline{u}$).

For reference purposes, let a subscript "1" denote the state space matrices before the power supply dynamics addition. Thus we take

$$\dot{\underline{x}}_1 = \mathbf{A}_1\underline{x}_1 + \mathbf{B}_1\underline{v}_1 \tag{5.32}$$

and

$$\underline{y}_1 = \mathbf{C}_1\underline{x}_1 + \mathbf{D}_1\underline{v}_1. \tag{5.33}$$

to describe the state space of Eqs. 5.25 through 5.29.

Construction of the new, combined state space is relatively straightforward. The combined state vector is defined by

$$\underline{x} \equiv \begin{bmatrix} \underline{x}_1 \\ \underline{x}' \end{bmatrix} \tag{5.34}$$

while the output vector is unchanged: $\underline{y} = \underline{y}_1$. As mentioned above, the new input vector, $\underline{u}$, represents demand signals applied to the power supply. The new, combined state matrix is defined by

$$\mathbf{A} \equiv \begin{bmatrix} \mathbf{A}_1 & \mathbf{B}_1\mathbf{C}' \\ \mathbf{0} & \mathbf{A}' \end{bmatrix}, \tag{5.35}$$

the new, combined control matrix is defined by

$$\mathbf{B} \equiv \begin{bmatrix} \mathbf{B}_1\mathbf{D}' \\ \mathbf{B}' \end{bmatrix}, \tag{5.36}$$

and the new output matrix is given by

$$\mathbf{C} \equiv \left[\begin{array}{cc} \mathbf{C}_1 & \mathbf{0} \end{array} \right]. \tag{5.37}$$

If the dimension of the power supply state space is NPS, so that $\mathbf{A}'$ is [NPS $\times$ NPS], and the lengths of the original state space vectors are NX, NY, and NU, then the dimensions of the new, combined state space vectors are: $\underline{x}$(NX+NPS), $\underline{y}$(NY), and $\underline{u}$(NU).

5.6 Discussion

This chapter has addressed the general analysis and formulation of the equilibrium and stability control problem. General characteristics and limitations to this control were discussed and results of simple rigid model control with direct displacement feedback were presented.

The application of proportional-derivative feedback to vertical stability was discussed in the context of a rigid plasma model. Stabilization of Alcator C-MOD equilibria was shown to require derivative feedback control in addition to proportional gain feedback. This requirement is common to all systems in which the plasma is better coupled to the vacuum vessel than to the driven conductors.

A single-pole transfer function was used to simulate power supply delay in order to investigate the maximum tolerable delay and corresponding derivative feedback necessary for stabilization. For the highest elongation example equilibrium in the Original Design Set (eq7; $\kappa_{sep} = 2.0$), having a passive rigid vertical growth time of about 1.0 msec, the maximum tolerable power supply delay time was found to be about the same as the growth time, 1.0 msec. Similarly, the growth time for eq6 of the Original Design Set ($\kappa_{sep} = 1.8$) was roughly the same as the maximum tolerable delay time for this case, about 3 msec. To achieve stability with these delays, a derivative feedback time constant of about 50 msec was required. This is

in contrast to a derivative feedback time constant of only about 0.3 msec required for stabilization in the absence of any power supply delay model.

It was also noted that the maximum tolerable delay time constant for a single filament plasma model was found to be 2 to 3 times as long as for the corresponding equilibrium multifilament plasma model. This reinforces our previous argument that single filament models can lead to significantly different results than more accurate multifilament models. Moreover, we have seen that such single filament calculations tend to be optimistic from the point of view of the control design, and thus could result in less safety margin, or even a lack of adequate stability.

Recognizing the intrinsic multivariable nature of the axisymmetric control problem, the state space representation was introduced and the tokamak plasma-conductor system was cast into this form. This formalism naturally accomodates both multivariable internal dynamics, and systems with multivariable input and output arrays. Since the vacuum vessel model consists of a discretized array of conducting loops, the internal state of the system is inherently multivariable. The sensor array, consisting of up to 89 measured quantities, and the driven coil set, in principle a total of 10 independently controlled circuits, together comprise a multivariable input-output system of very large size. Single variable techniques cannot reasonably be used to analyze a system with such large dimensionality. Furthermore, even 2 or 3 degrees of freedom in sensor and control arrays is more efficiently analyzed using multivariable methods.

Following the state space approach, equations describing the internal dynamics of the set of power supplies can be combined with the plasma-conductor circuit equations. The algorithm for combining these two systems was described and the resulting synthesis was constructed.

Casting the system into state space form allows many well-developed techniques to be brought to bear on the problem. In addition, methods developed in

the mature field of multivariate control can be extended to provide solutions appropriate to the unique needs of the C–MOD control system. This, along with the incorporation of power supply models directly into the state space representation, sets the stage for the design analysis of the next chapter.

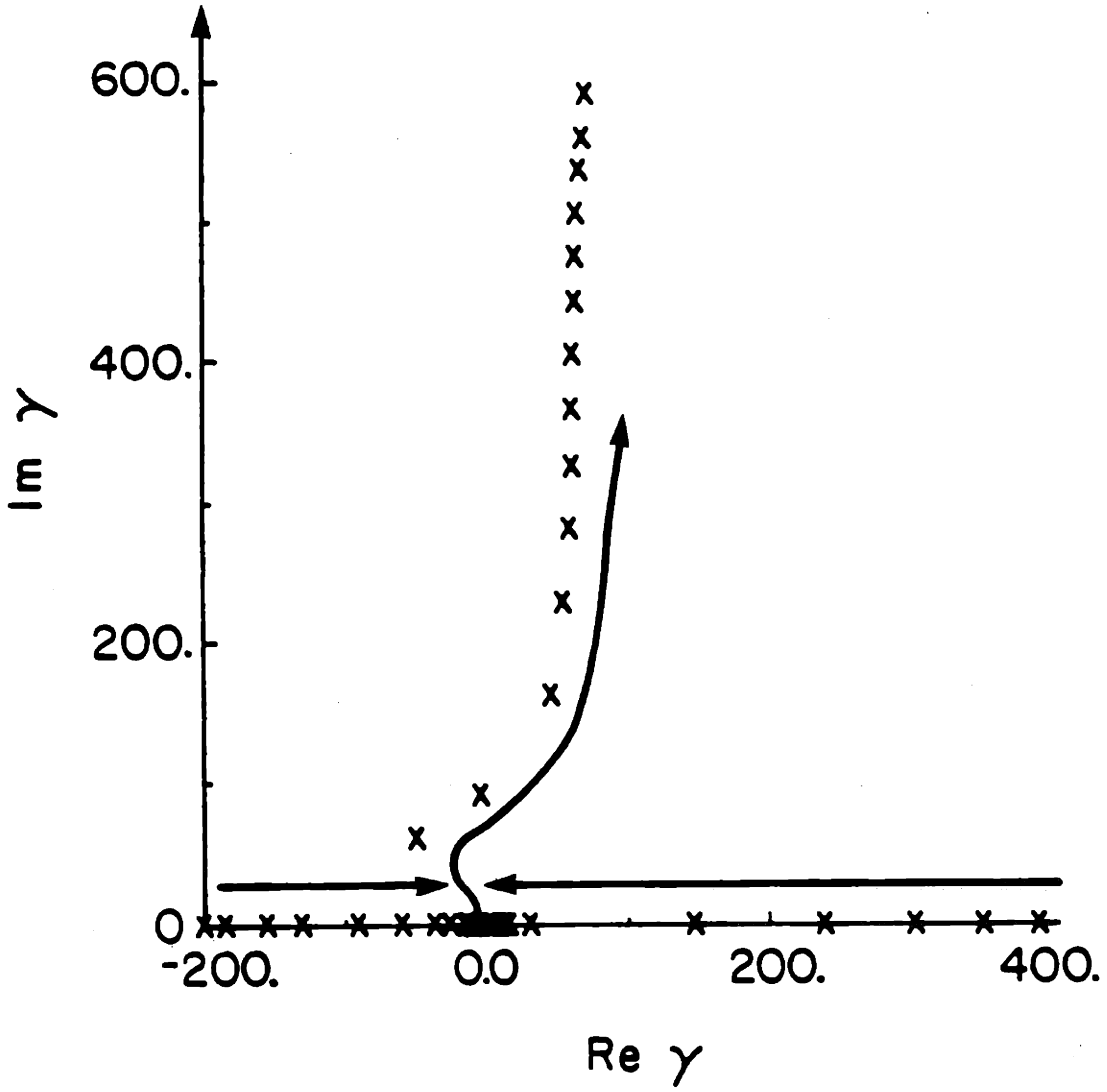

Figure 5.5: Root-locus plot for eq6 with derivative feedback ($t_a \neq 0$). Arrows indicate direction of motion of FR as gain increases.

Chapter 6

Design of Tokamak Equilibrium Control Systems

Once a satisfactory plant model has been derived for a system which must be controlled, several algorithms are available for feedback design. If few degrees of freedom exist in control elements and feedback parameters, an exhaustive approach is frequently both tractable and sufficient to find a satisfactory control law. This was the approach taken in Chapter 5, made possible because only a single feedback variable was used.

When a system exceeds one or two control inputs and sensor outputs, the dimension of the resulting search space makes such an approach completely intractable. Under these circumstances, when the input-output characteristics of a system are inherently multivariable, state space methods provide extremely powerful tools for control design. The natural way in which the state space formalism accomodates not only multivariable input-output systems, but also systems with high order internal dynamics, makes this approach virtually universal in modern control theory [28].

However, multivariable analysis provides many ways of discovering a nominally

acceptable control law. Much of the research of the last 20 years has been directed toward evolving and understanding linear quadratic regulator (LQR) methods, or "optimal" control theory. In its broadest sense, this approach involves the specification of some cost functional which is desirable to minimize in a control design. Such quantities as power, monetary cost, or material stress all lend themselves readily to expression in terms of a quadratic relation among state, control, and sensor variables. Solution of the nonlinear Ricatti equation then typically yields the desired cost minimizing control law [28].

Unfortunately, it is very difficult (or impossible) to build system performance itself into such a formulation. So, while the LQR solution is guaranteed to be stable, it is by no means guaranteed to be robust. An approach which provides somewhat more intuitive access to the performance tradeoffs involved in the nominal design is to move the poles of the system explicitly to more reasonable locations than they are passively found in. Pole placement algorithms which accomplish this have long been studied in the state space formalism. Extensions of these methods comprise the first step in the integrated design process for Alcator C-MOD.

6.1 Pole Placement

In a sense, the ability to control the locations of the poles of a system provides all the power a control designer could ever want. In principle, this is all that is of importance in modifying a system with passively undesirable dynamic characteristics. However, there are practical limits to the usefulness of pole placement, since somewhat sophisticated intuition can be necessary to determine what new locations will yield satisfactory system performance. In certain simple cases, such improved pole placements are clear, but a multivariable system poses intrinsically more difficult dynamics to challenge single variable intuition.

The tokamak control problem we have formulated is fortuitous in this respect, however, because even though the number of multivariate modes in the system is quite large, only a few of these modes are important. Indeed, only a few of these modes are significantly affected by EF coils at all. These are the modes which couple to plasma variation, and which we have termed the "feedback roots" (FR) previously. Furthermore, only one mode among these is unstable to begin with. This is the only pole which must be moved from its passive location to create a satisfactorily stable active system, although performance may be improved by moving certain passively stable poles as well. By identifying the nature of the dominant modes with the corresponding plasma motion, the designer can choose which of these to place along with the unstable root.

6.1.1 Full State Feedback

In order to locate all desired poles reliably at new locations, access to the entire system state is needed. If the vector of state variables is directly available to the feedback system and all of the passive modes of the system are controllable by the specified control–sensor set, then all roots can be placed as desired, within certain basic constraints. For example, complex roots must appear as pole pairs, and in general eigenmode vectors cannot be arbitrarily specified. This form of control is known as "full state feedback" (FSFB) [29].

For many kinds of systems, FSFB is a natural possibility. That is, for such systems the entire state is available, and all passive modes are controllable by design or fortune. Robot manipulators, for example, lend themselves to such control, since by design their positions, orientations, and velocities can be precisely monitored and controlled, and these variables constitute the actual state of the manipulator. If such a manipulator is forced to control another dynamic system with further internal degrees of freedom and dynamics, the additional state variables may not

be directly accessible or controllable. In this case FSFB is impossible, and other strategies must be used.

This latter example is an analog of the tokamak situation. As described in Chapter 5, the state variables for the plasma–conductor system consist of currents induced in the conductor array. Since vacuum vessel currents in particular are not directly measured in tokamaks, that frequently dominant portion of the state is not available. It should be noted that for cases such as that studied by Albanese et al [17], the induced EF coil currents are taken to be both dominant and sufficient to stabilize the vertical mode on an ideal timescale.

Full state feedback is appropriate for this system, but for most tokamaks vessel current information is unavailable for feedback. In fact, the Alcator C–MOD vessel contributes overwhelmingly to stability, making this form of FSFB impossible even in principle. Even in such cases, however, a full state analysis can provide the starting point for a feedback strategy using an "observer" state estimator. If an observer provides a sufficiently accurate estimate of the system state from sensor data alone, this estimate can be used with the full state result to produce an acceptable nominal control law. Performance analysis of the nominal result may then dictate the necessity of further refinement. In preparation for choosing the observer approach for the design of the C–MOD control system, we proceed to construct the FSFB algorithm used here.

6.1.2 Full State Algorithm

The point of departure for the full state feedback approach is to make certain assumptions regarding the nature of control signals. Given the state equation (Eq. 5.17), reproduced here for convenience

$$\dot{\boldsymbol{x}} = \mathbf{A}\boldsymbol{x} + \mathbf{B}\boldsymbol{u} \tag{6.1}$$

we assume controls of the form

$$u = -\mathbf{K}x. \tag{6.2}$$

This results in the closed loop equation

$$\dot{x} = \mathbf{A}_{cl}x \tag{6.3}$$

where $\mathbf{A}_{cl} \equiv \mathbf{A} - \mathbf{BK}$. Denoting the closed loop eigenvectors and control vectors by

$$x_i = p_i e^{\mu_i t} \quad u_i = q_i e^{\mu_i t} \tag{6.4}$$

so that μ_i are the closed loop eigenvalues, and

$$\mathbf{A}_{cl}p_i = \mu_i p_i. \tag{6.5}$$

Equations 6.2 and 6.4 result in

$$q_i = -\mathbf{K}p_i \tag{6.6}$$

and

$$\mu_i p_i = \mathbf{A}p_i + \mathbf{B}q_i. \tag{6.7}$$

Note that $\mathbf{A}$ here is the open loop state matrix. Expressing Eq. 6.6 as the matrix equation

$$\mathbf{Q}_K = -\mathbf{K}\mathbf{P}_K \tag{6.8}$$

where the columns of the $\mathbf{P_K}$ and $\mathbf{Q_K}$ matrices consist of the p_i and q_i vectors respectively, we find

$$\mathbf{K} = -\mathbf{Q}_K\mathbf{P}_K^{-1}. \tag{6.9}$$

Thus, as long as we ensure that the closed loop eigenvectors and control vectors satisfy

$$p_i = (\mu_i\mathbf{I} - \mathbf{A})^{-1}\mathbf{B}q_i, \tag{6.10}$$

then Eq. 6.9 represents the desired solution to place the closed loop poles at the μ_i locations. To perform a FSFB pole placement then, one chooses the desired closed loop poles, μ_i, and control vectors, q_i, such that Eq. 6.10 is satisfied. This determines the closed loop eigenvectors, p_i. Since the eigenvectors can in general be complex, this process must in principle be conducted using full complex vectors and matrices. However, the resulting state feedback matrix, $\mathbf{K}$, must be real. Fortunately, because the plasma–conductor system has no inertia, it will exhibit only pure real passive poles. The pole placement is therefore accomplished by simply taking the real part of the complex $\mathbf{K}$ resulting from Eq. 6.9.

It is worth emphasizing that the closed loop eigenvectors resulting from the full state pole placement algorithm are not chosen freely. They are determined by the choice of control vectors and must satisfy Eq. 6.10. For systems which are not fully controllable, the uncontrollable modes will be unaffected by feedback. Poles which we have previously identified as "quasiconstant roots" will be minimally affected. Thus, in performing a pole placement, only the unstable mode and a small number of feedback-influenced stable modes need be addressed. For the axisymmetric tokamak control problem using a discretized conductor array, almost all of the high order poles in the system are stable and quasiconstant with feedback. It is therefore in general natural to leave these unaffected by the pole placement algorithm. However, modes frequently exist which are quasiconstant and yet are closely coupled to currents driven in control coils. Such modes can be excited by the control system and may limit plasma response speed. It is therefore often desirable to relocate such modes to a higher decay rate in order to achieve an acceptably fast plasma response. This can be accomplished by providing the control system access to information regarding the coil currents which are the dominant components of such modes. Such a case is described in succeeding sections, in which examples of the full state approach and the use of explicit state predictors are described.

6.1.3 Output Feedback

As we have noted, in the case of a tokamak equilibrium control system in which vacuum vessel currents play an important role, the full state is not directly accessible. The sensor signals must therefore be used to estimate the system state of interest. Chapter 5 illustrated the use of estimating plasma vertical position using flux loops in a relatively direct way. That approach assumed that the difference between the signals from two flux loops equidistant from the midplane was close to proportional to the vertical displacement of the plasma. In order for this signal to allow control of an instability, it must reflect the magnitude of the unstable mode sufficiently accurately. It was shown that in some cases that simple form of modal estimation was insufficient to allow control of the vertical mode. Furthermore, the use of only a single flux loop pair is extremely vulnerable to loss of or error in one or both of the signals. There is no significant measure of redundancy in the sensor system.

By comparison, use of a large array of flux loops (and B_p coils) provides a large measure of redundancy, and thus robustness to partial signal loss. The penalty for this approach is the necessity of solving a problem with many more degrees of freedom. Full state feedback provides a method for dealing with the large number of unknowns, but requires the use of a sufficiently accurate estimator for the state of the system, which in this formalism now includes all of the conductor currents. In the following sections we describe the construction of such observers for arbitrary sensor signal vectors. Because the C-MOD control system architecture (discussed in Sec. 6.3 below) includes a proportional-integral-derivative (PID) gain module, the observers derived here will make use of proportional and derivative forms of sensor signals. An integral term is only needed to eliminate bias or long timescale drift in the control loop [30].

6.1.4 Output Observers

For the purposes of the present work, we define an output observer as a linear function, $f(y, \dot{y}, \int y)$, such that

$$\hat{x} \equiv f(y, \dot{y}, \int y) \tag{6.11}$$

is a state vector estimate for a given time-varying sensor signal, and the quantity $(\hat{x} - x)^2$ is sufficiently minimized for modes of interest. Observer designs usually require solution of the nonlinear Ricatti equation, or the calculation of the observability matrix requiring $NX \sim 80$ multiplications of the output matrix, $\mathbf{C}$ [28] (recall from the state space description of Chapter 5 that the output matrix, $\mathbf{C}$, operates on the state vector, $\underline{x}$, to give the output (sensor measurement) vector, $\underline{y}$). To avoid the time-consuming difficulty of such calculations, we propose an alternative observer form requiring relatively few calculations which are, moreover, only linear.

We propose to seek an observer which depends only on the output vector and its derivative (PD output observer):

$$\underline{\hat{x}} = \hat{\mathbf{A}}\underline{y} + \hat{\mathbf{B}}\underline{\dot{y}}. \tag{6.12}$$

Using this equation along with the state equation, Eq. 6.1, and formally setting

$$\underline{\hat{x}} - \underline{x} \equiv \underline{0}, \tag{6.13}$$

results in

$$\hat{\mathbf{B}}\mathbf{C}\mathbf{B}\underline{u} = \underline{0} \tag{6.14}$$

and

$$\hat{\mathbf{A}}\mathbf{C} = \mathbf{I} - \hat{\mathbf{B}}\mathbf{C}\mathbf{A}. \tag{6.15}$$

In order to exactly satisfy Eq. 6.14, we let the rows of $\hat{\mathbf{B}}$ consist of weighted sums of left null vectors of $\mathbf{CB}$. Because some computational implementations of

the SVD will not decompose $\mathbf{CB}$ in the likely event that $\mathbf{B}$ is a column vector, we choose to calculate the SVD of $(\mathbf{CB})^T$:

$$(\mathbf{CB})^T = \mathbf{U}\boldsymbol{\Sigma}\mathbf{V}^T. \tag{6.16}$$

The columns of the row-space matrix $\mathbf{V}$ which correspond to zero (or negligible) singular values define $\mathbf{V}_{null}$, the left nullspace of $\mathbf{CB}$. Therefore defining

$$\hat{\mathbf{B}} \equiv \hat{\mathbf{W}}\mathbf{V}_{null}^T, \tag{6.17}$$

where $\hat{\mathbf{W}}$ is a weighting matrix, Eq. 6.14 is automatically satisfied.

Eq. 6.15 then becomes

$$\mathbf{I} = \hat{\mathbf{A}}\mathbf{C} + \hat{\mathbf{W}}\mathbf{V}_{null}^T\mathbf{C}\mathbf{A} \equiv \hat{\mathbf{A}}\mathbf{C} + \hat{\mathbf{W}}\mathbf{F}, \tag{6.18}$$

and hence

$$[\hat{\mathbf{A}} \;\; \hat{\mathbf{W}}] = \begin{bmatrix} \mathbf{C} \\ \mathbf{F} \end{bmatrix}^{-1}, \tag{6.19}$$

which determines $\hat{\mathbf{A}}$ and $\hat{\mathbf{B}}$. If NN is the rank of the nullspace matrix, $\mathbf{V}_{null}^T$, NX is the usual state vector length, and NY the output vector length, then the solution required is the left inverse of an $([NY + NN] \times NX)$ matrix. For the geometry used in the present work, this can be a well-posed problem if both flux loops and B_p coils are used in the sensor array. In this case NY+NN can be greater than NX (since NY=46, $NN \sim 46$, and $76 < NX < 98$). The estimator is then very accurate in predicting current elements from sensor signals. However, when only flux loop measurements are included in the sensor array, the problem is in general no longer well-posed. The resulting estimator still does quite well for important control modes such as the dominant vertical and radial motions, but higher order modes fall off in accuracy rapidly.

A comparison of typical estimation for the dominant vertical and radial modes using flux loops alone and flux loops and B_p coils is shown in Figs. 6.1 through

6.4. Fig. 6.1 plots the current elements of the predicted mode vs. the actual modal currents for flux loops alone estimating the vertical unstable mode. This is to be compared with Fig. 6.2, illustrating the same prediction for a sensor array consisting of flux loops and B_p coils. Although the flux loop array alone performs satisfactorily, combining flux loop data with signals from the B_p coils results in effectively perfect prediction. Figs. 6.3 and 6.4 show the same comparison for the stable radial plasma mode.

The figures show results for the case of eq9 ($\kappa = 1.6$) passively stabilized by EFCU/L (antiseries) along with the vacuum vessel. As the number of stabilizing EF coils in the model is increased, the quality of the estimator can be expected to degrade when the sensor array becomes "rank deficient". However, the flux loops alone represent a worst case of rank deficiency, and still provide satisfactory state estimation for the most important modes. In addition, explicit inclusion of Rogowski coil EF current information can restore rank sufficiency, if necessary.

These results are another reflection of the intrinsic low order of the tokamak control problem due to the small number of important plasma degrees of freedom. For the purpose of control it is clear that a very small sensor space is sufficient to allow observation of the important control modes. Indeed, most experiments employ single differential flux loop or coil pairs for each control degree of freedom [9,13].

Finally, we note also that a purely proportional observer, defined by

$$\hat{x} = \hat{\mathbf{A}} y, \tag{6.20}$$

results from taking the limit of the PD observer case with $\hat{\mathbf{B}} = 0$. This yields

$$\hat{\mathbf{A}}\mathbf{C} = \mathbf{I} \;\Rightarrow\; \hat{\mathbf{A}} = \mathbf{C}^{-1}, \tag{6.21}$$

which is ill-posed due to the dimensions of $\mathbf{C}$, and yet can provide fairly reasonable results for very low order poles, for the same reason as described above in the PD case.

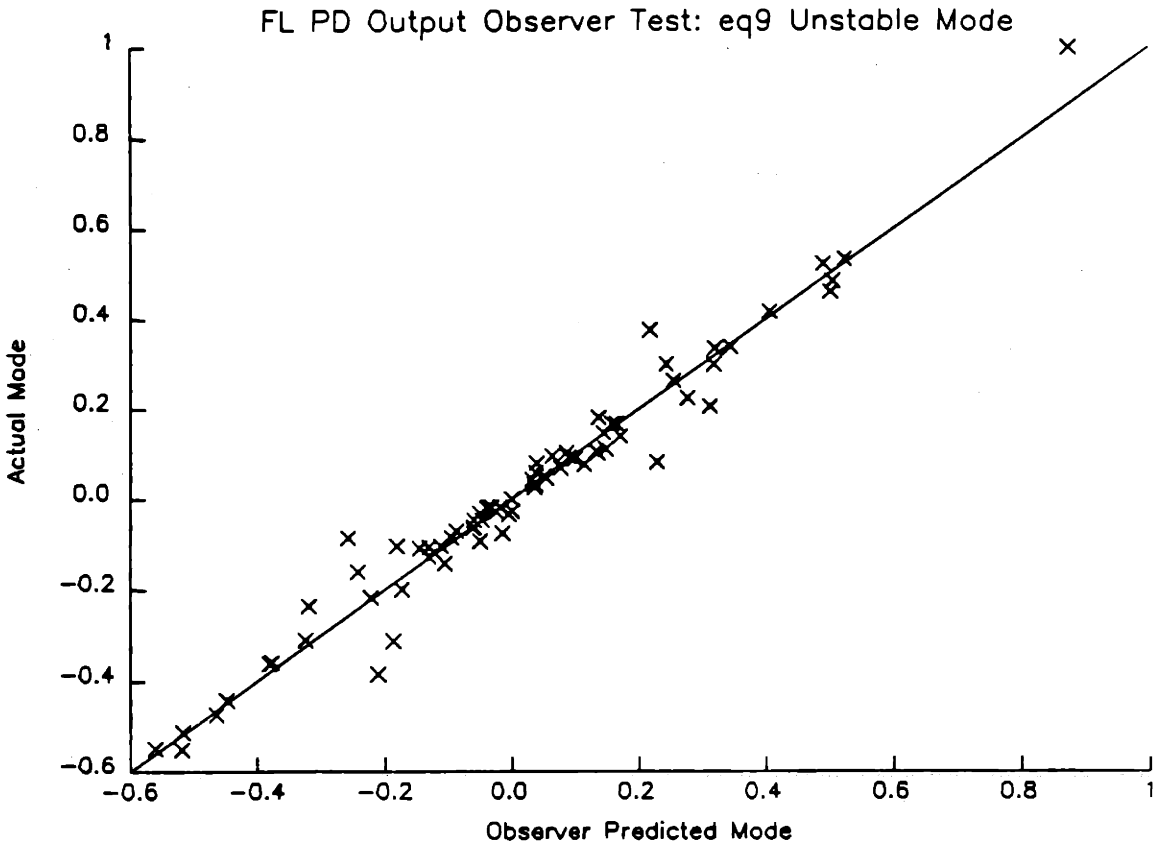

Figure 6.1: Vertical unstable mode current elements for eq9 plotted against modal current elements estimated using flux loop signals alone.

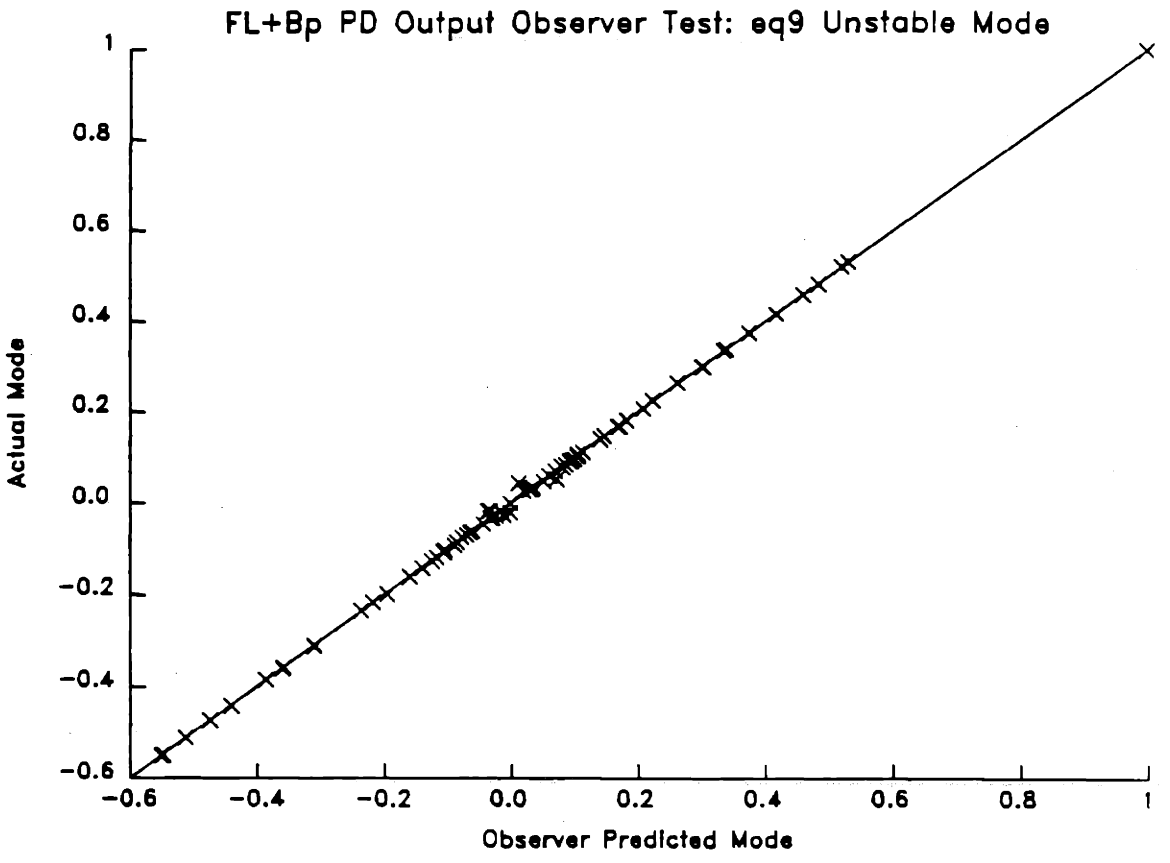

Figure 6.2: Vertical unstable mode current elements for eq9 plotted against modal current elements estimated using flux loop and B_p signals.

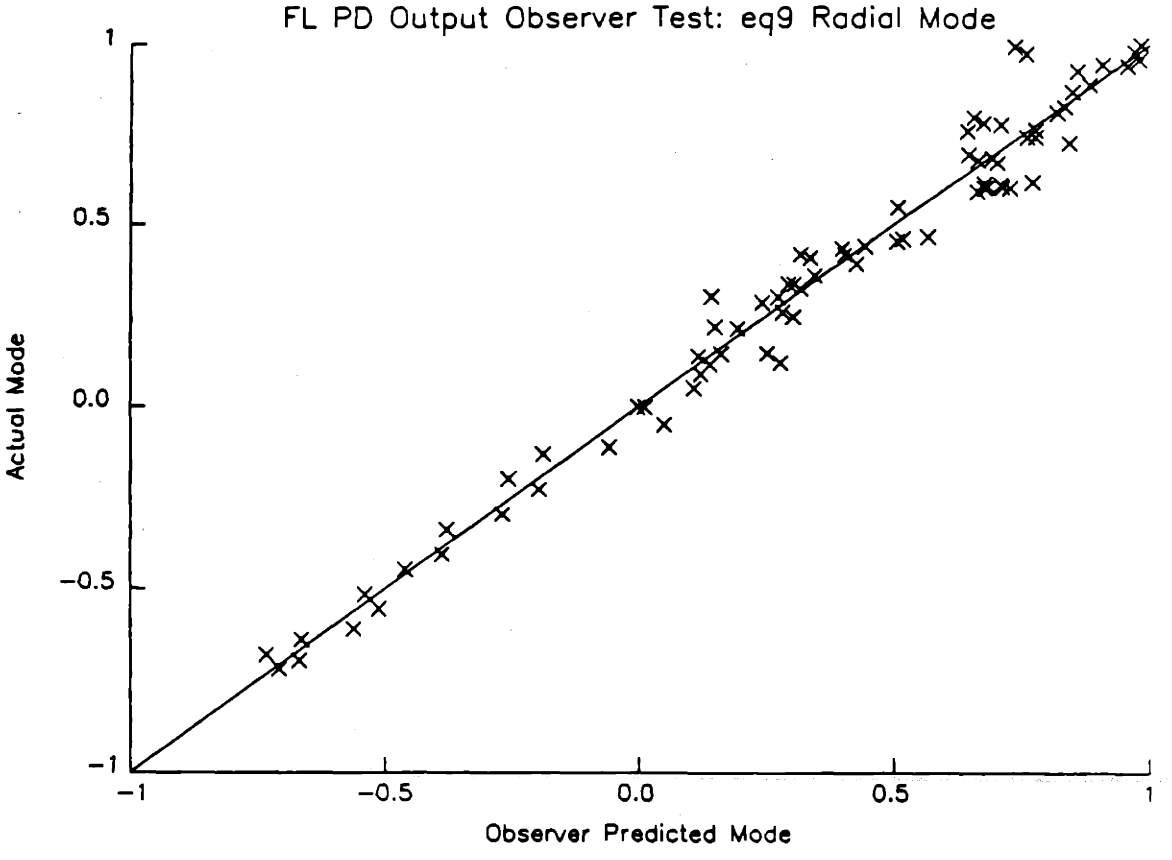

Figure 6.3: Stable radial mode current elements for eq9 plotted against modal current elements estimated using flux loop signals alone.

Eigenvalue	Passive	FSFB	PDOO
1	**512.**	-20.	-20.
2	-20.	-74.	-74.
3	-74.	-193.	-193.
4	-193.	**-198.**	-211.
5	-211.	-211.	-307.
6	-307.	-307.	-341.
7	-341.	-341.	-429.
8	-429.	-429.	-453.
9	-453.	-453.	-497.
10	-497.	-497.	**-545.**
11	-554.	-554.	-566.
12	-639.	-639.	-639.

Table 6.1: Comparison of dominant eigenvalues for passive system, FSFB, and PD Output Observer FB (eq9). Boldface indicates "vertical" mode.

6.2 Applications of Pole Placement

We now apply the full state and PD output observer formalisms developed in the preceding sections to C–MOD equilibria. The second column of Table 6.1 shows the dominant eigenvalues for the case of equilibrium eq9 ($\kappa = 1.6$) passively stabilized by EFCU/L (antiseries) as well as the vacuum vessel. Choosing to stabilize the vertical mode in such a way that its damping time is 5 ms (damping rate of -200 sec^{-1}) for the full state case, we obtain the set of dominant modes shown in the third column of the table. The previously unstable pole has been placed at -198 sec^{-1}. In this case only one pole has been assigned using the single EFCU/L control circuit. Note that no attempt has been made to assign the pole at -20 sec^{-1}, which consists primarily of large EFC current with negligible vessel currents. This pole couples strongly to any current driven in the control circuit, and can therefore limit plasma response if not dealt with. We shall return to this issue presently.

The final column shows the result of using the FSFB **K**-matrix along with the PD output observer described in Sec. 6.1.4. The vertical mode has been moved to a

point even more highly damped than that required by the full state algorithm. This is a consequence of the inexactness of the observer used. Although the poles are placed accurately by FSFB, the observer $[\hat{\mathbf{A}}, \hat{\mathbf{B}}]$ provides inadequate state prediction to yield accurate pole placement.

6.3 Alcator C–MOD Control Architecture

The equilibrium shaping and stability control system architecture chosen for Alcator C–MOD consists of a hybrid analog–digital configuration developed jointly with the CRPP–Lausanne TCV (Tokamak à Configuration Variable) Group [31]. Because in a broad sense the shaping demands and characteristic stability time scales of the two tokamaks are similar, the collaboration is a natural one, and has been extremely fruitful for both groups.

The choice of a hybrid control system is an effort to combine the advantages of both analog and digital architectures while obviating their disadvantages. Purely digital control allows extreme flexibility in algorithm definition, but requires sampling of all signals. This discretization introduces a host of difficulties, including aliasing and intrinsic delays, which must be kept in mind throughout any digital design process. These phenomena can become quite significant and troublesome for a system such as C–MOD, for which a rapid response time and minimized phase lag is very important.

By contrast, completely analog control systems readily provide rapid response and high bandwidth, but are extremely difficult to program. Given the high degree of variation in equilibria to be achieved in both Alcator C–MOD and TCV, such a lack of flexibility is unacceptable.

However, if the number of separate control laws which must be used during a shot is small enough that the gain scheduling intervals are easily accessible by a

digital programmer, then a hybrid system can be used. A hybrid architecture allows an analog feedback system to be programmed digitally by an external controller. In this way, gains can be changed readily as required by a predetermined gain schedule, but all signal-gain multiplication is performed by analog circuitry. This retains all of the speed of an analog controller, as well as the flexibility of a digital one.

6.3.1 The Hybrid Control System

The final realization of the hybrid feedback loop consists of a set of matrices which can be digitally programmed, but perform purely analog multiplications. In addition to pure gain multiplication, a PID array is included for calculation of derivative and integral signals. This allows implementation of the PD algorithms discussed above. The overall architecture showing the principal matrices included in present hardware is given in Fig. 6.5. An interpretation of the architecture showing elements essential for the purposes of this study is shown in Fig. 6.6.

In Fig. 6.5, sensor signals are multiplied by an interpretation matrix, $\mathbf{A}_{pred}$, which in general is intended to consist of "predictors" for estimating various plasma parameters deemed to be important. The PID array then operates on each of these "predicted" signals to produce the signal itself multiplied by a gain, the derivative of the signal multiplied by another gain, and the integral of the signal multiplied by a third gain. As presently implemented, the PID array adds these scaled, PID-operated signals internally, providing only a single output for each input signal.

If the $\mathbf{A}_{pred}$ output parameters have intuitive physical connections to plasma degrees of freedom relating to important control modes, an operator will be able to adjust appropriate PID control gains "by hand" in order to refine the control algorithm between shots. For example, if one output of the $\mathbf{A}_{pred}$ matrix provides a good prediction of the vertical displacement mode, the PID gains multiplying this signal could be varied to improve vertical stability control. The PID output is

then operated on by a mapping matrix, M, whose output in turn drives the power supplies.

The feedback loop as shown in the figure relates the Laplace transforms of the control vector, $\underline{u}$, and the sensor vector, $\underline{y}$, via

$$\underline{u}(s) = \mathbf{M}(\mathbf{G}_p + s\mathbf{G}_d + \frac{1}{s}\mathbf{G}_i)\mathbf{A}_{pred}\underline{y}(s), \tag{6.22}$$

where the G matrices are understood to be diagonal, and s is the usual Laplace transform complex frequency variable.

Figure 6.6 shows a reinterpreted version of the general hybrid architecture shown in Fig. 6.5. The proportional and derivative portions of the control system have been separated into two parallel loops, and the integral portion has been left out. Integral feedback is only needed to eliminate long term drifts and errors. Terms proportional to the integral of the interpreted sensor signals can be added as necessary once satisfactory fast time scale control laws have been determined. In the present work we shall ignore this added capability of the PID array.

Because we wish to approximate the **P** and **Q** matrices from the FSFB/PDOO analysis of Sec. 6.1 using the hybrid architecture, it is natural to completely separate the two loops, creating separate $\mathbf{A}_{pred}$, PID (i.e. $\mathbf{G}_p$ and $\mathbf{G}_d$), and M matrices for the proportional and derivative segments. This allows, for example, the direct implementation of the SVD of the **P** and **Q** matrices with the hybrid. The penalty for this separation of loops is that only 8 channels are available in each of the G matrices representing the gains in the PID (if no integral feedback is used). We expect this to be acceptable, since as indicated before, the typical dimension of the plasma response space is on the order of 4 or 5. Moreover, there is only one unstable mode to be specifically stabilized.

The separated-loop reinterpretation relates the Laplace transforms of the control vector, $\underline{u}$, and the sensor vector, $\underline{y}$, via

$$\underline{u}(s) = (\mathbf{M}_p\mathbf{G}_p\mathbf{A}_p + \mathbf{M}_d s\mathbf{G}_d\mathbf{A}_d)\underline{y}(s). \tag{6.23}$$

The frequency response of the hardware implementing the hybrid system has been measured to provide a bandwidth of approximately 10 kHz with a precision of 1 part in 10^3 of the signal amplitude. This holds for each digitally programmed analog multiplication cell, which provides the gain for a single channel. Because maximum expected instability growth rates for C-MOD are in the 1000-2000 sec^{-1} range, this bandwidth is expected to be sufficient to allow satisfactory control.

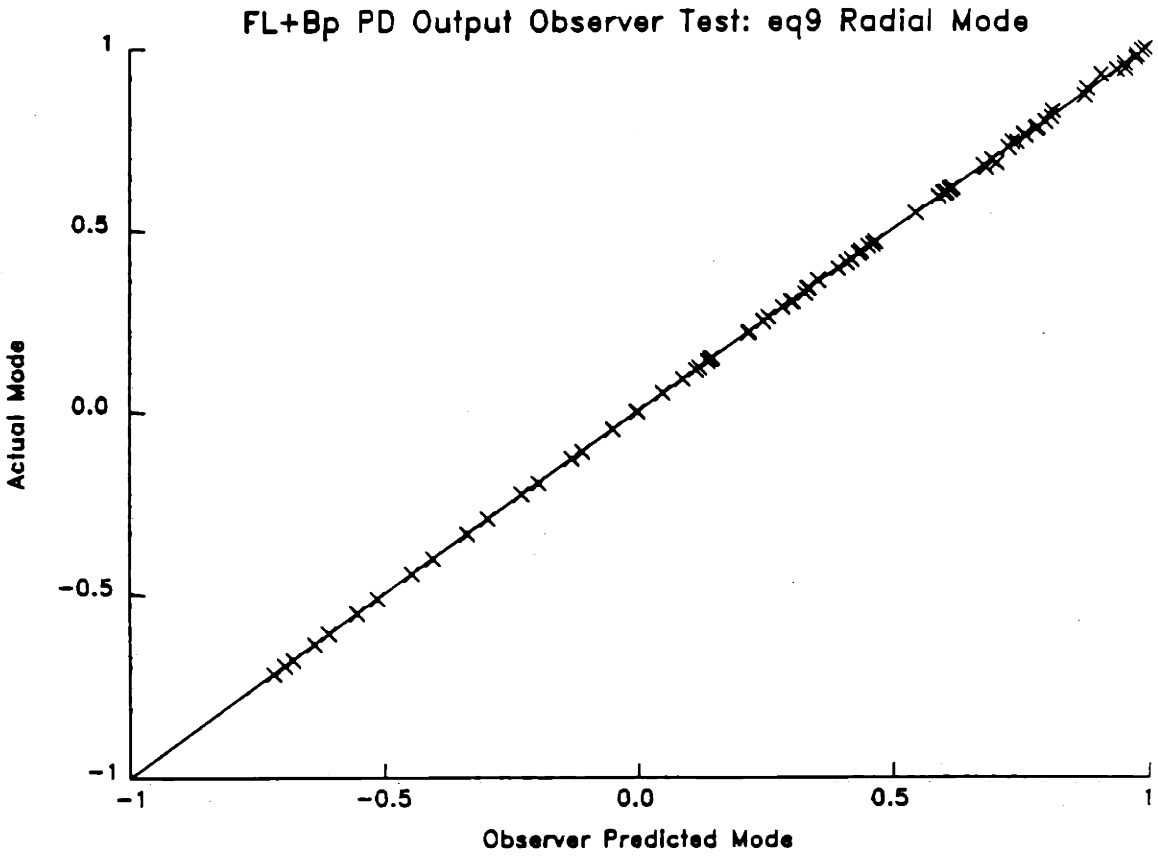

Figure 6.4: Stable radial mode current elements for eq9 plotted against modal current elements estimated using flux loop and B_p signals.

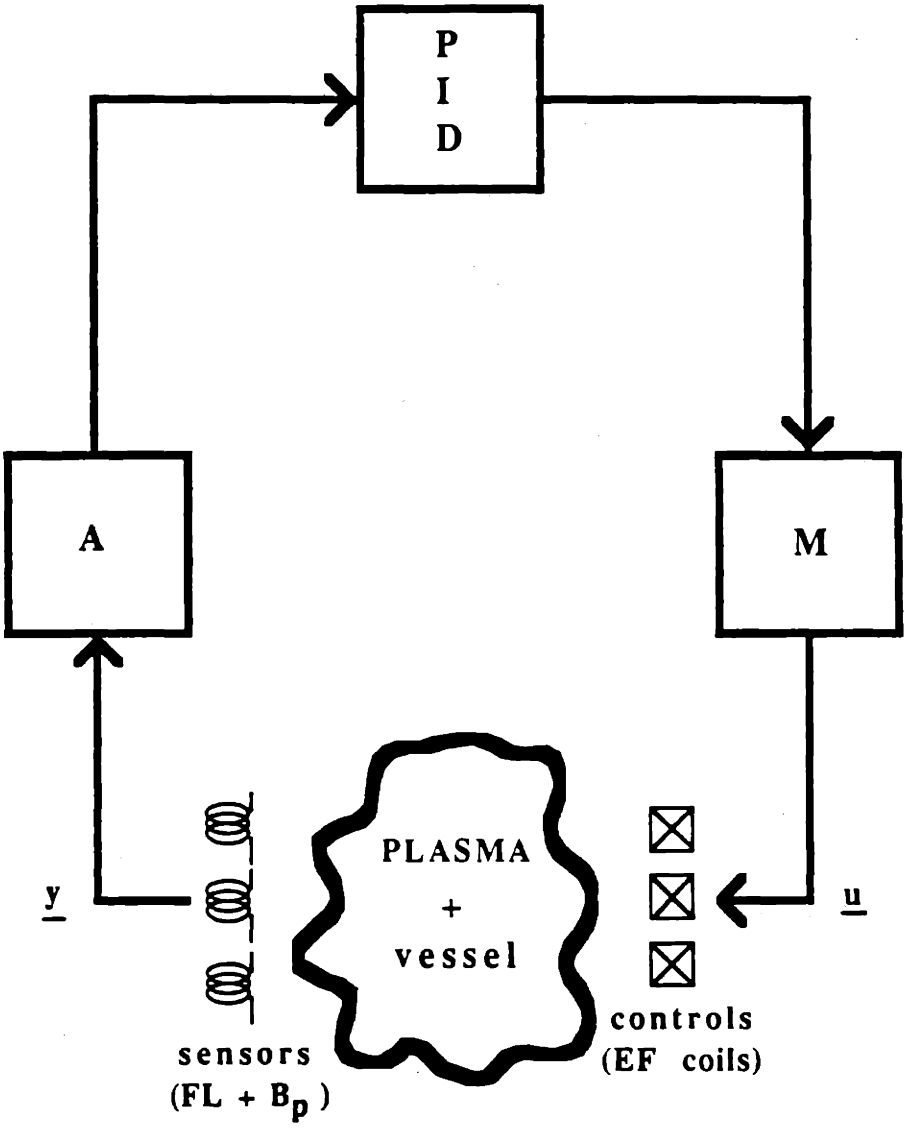

Figure 6.5: Block diagram of general C-MOD hybrid control system architecture.

6.3.2 Modeling PD Results with the Hybrid

The central remaining problem of control law determination for the C–MOD system is that of implementing the "ideal" **P** and **Q** gain matrices calculated with the FSFB and PDOO methods using the hybrid architecture. This implementation must be accurate enough to provide satisfactory stability. One difficulty arises in principle because, as can be seen in the block diagrams previously discussed, in order to directly implement PD feedback the PID array must be divided into two separate sets of gain channels. Each set consists therefore of only 8 channels, which falls short of the 10 EF coil circuits which are to be driven in principle. However, this is not a serious shortcoming in itself, since it has been demonstrated that the plasma response rank is on the order of 4 or 5.

Another difficulty is that for purposes of between shot control diagnostics and feedback law refinement, it is desirable to have the magnetic signal interpretation matrix provide some measure of modal diagonalization within the control loop. By constructing an $\mathbf{A}_{pred}$ whose outputs are recognizable quantities which are physically important for control of the various modes of interest, an operator can actively refine the control law between shots by simply adjusting PID gains. Such a capability may be crucial for achieving satisfactory performance, especially during initial operation of the machine, when a database of actual shots is only beginning to be constructed in order to characterize actual machine geometry and behavior. However, requiring a particular form for $\mathbf{A}_{pred}$ seriously restricts the implementation of a sufficiently accurate approximation to the **P** and **Q** matrices using the remaining elements of the hybrid system.

In the following sections we propose several implementation strategies which address these difficulties, providing experimenters with a broad range of access to and control over the modal physics.

6.3.3 Direct SVD Implementation

The most obvious way to implement the **P** and **Q** matrices using the hybrid architecture is to perform the SVD on each, letting

$$\mathbf{P} = \mathbf{U}_P \mathbf{\Sigma}_P \mathbf{V}_P^T \tag{6.24}$$

$$\mathbf{Q} = \mathbf{U}_Q \mathbf{\Sigma}_Q \mathbf{V}_Q^T, \tag{6.25}$$

and identify each matrix in the SVD with a block of the control system. Thus

$$\mathbf{A}_p \equiv \mathbf{V}_P^T \quad \mathbf{G}_p \equiv \mathbf{\Sigma}_P \quad \mathbf{M}_p \equiv \mathbf{U}_P \tag{6.26}$$

$$\mathbf{A}_d \equiv \mathbf{V}_Q^T \quad \mathbf{G}_d \equiv \mathbf{\Sigma}_Q \quad \mathbf{M}_d \equiv \mathbf{U}_Q. \tag{6.27}$$

$$\tag{6.28}$$

If the ranks of **P** and **Q** are less than 8 (the maximium number of inputs to the $\mathbf{G}_{p,d}$ matrices), then this approach will provide an exact implementation, and the closed loop poles will be located in precisely the locations which the PD output observer afforded. Recall that in general these locations will not be the exact FSFB pole placement locations. One limitation of the direct SVD approach is that because the outputs of the $\mathbf{A}_{p,d}$ matrices are not simply related to obvious, physically identifiable modes in this case, between-shot refinement of the control law is not generally convenient.

Another potential problem with this approach is that of slow decay modes consisting of large currents in EF coils which can limit system response. If slow modes are not explicitly made more stable by pole placement, the only way to improve system response is to include information about the EF currents involved. This is more fully discussed in later sections.

One way of addressing both of these limitations is to define a state interpreter (also called a state "predictor"), $\mathbf{A}_{pred}$, which provides useful physical mode information to the control loop. This allows both between-shot manual operator

refinement and explicit inclusion of driven coil current information in the control loop. With this information available to the system, it is also possible to improve plasma response past the slow decay mode limits.

6.3.4 Implementing General State Interpreters

Before discussing various possible state interpreters ($\mathbf{A}_{pred}$ matrices), we first show the method of implementation of a general estimator in the hybrid architecture. This will turn out to require solution of effectively the same equation as that formulated for the PD output observer problem. The same algorithm can be applied to any chosen state interpretation matrix.

A chosen $\mathbf{A}_{pred}$ matrix in theory consists of a set of "predictors" providing some reasonable interpretation of plasma state parameters which are thought to be useful for control system refinement, and sufficient to control the desired modes. The FSFB result from the pole placement approach is used, and the hybrid control architecture along with the given state interpreter is used to implement an observer. Similar to that formulated in Sec. 6.1.4 above, this observer is defined by

$$\underline{\hat{x}} = \hat{\mathbf{A}}\mathbf{A}_{pred}\underline{y} + \hat{\mathbf{B}}\mathbf{A}_{pred}\underline{\dot{y}}. \tag{6.29}$$

The decision is thus made at the outset to use the same state interpreter for both proportional and derivative loops in the hybrid control implementation. Of course, enough flexibility exists in the architecture to use a separate predictor for each loop, but this complicates the refinement task, since the number of "predicted state" gain channels to be varied would be greater.

By analogy with the Sec. 6.1.4 formulation, the hybrid control observer equations become:

$$\hat{\mathbf{B}}\mathbf{A}_{pred}\mathbf{C}\mathbf{B}\underline{u} = \underline{0} \tag{6.30}$$

and

$$\hat{\mathbf{A}}\mathbf{A}_{pred}\mathbf{C} + \hat{\mathbf{B}}\mathbf{A}_{pred}\mathbf{C}\mathbf{A} = \mathbf{I} = \hat{\mathbf{A}}\mathbf{A}_{pred}\mathbf{C} + \hat{\mathbf{W}}\mathbf{V}_{null}^{T}\mathbf{A}_{pred}\mathbf{C}\mathbf{A}. \tag{6.31}$$

Choosing $\mathbf{G}_p$ and $\mathbf{G}_d$ to be identity matrices, the $\mathbf{M}$ matrices are left to implement the FSFB and observer:

$$\mathbf{M}_p \equiv \mathbf{K}\hat{\mathbf{A}} \tag{6.32}$$

$$\mathbf{M}_d \equiv \mathbf{K}\hat{\mathbf{B}}. \tag{6.33}$$

$$\tag{6.34}$$

The quality of this combined FSFB and hybrid control observer solution clearly depends on the degree to which the state interpreter spans the space of important plasma modes. By allowing the observer implementation no longer to have access to the entire sensor output vector, but only to a set of 8 or less modal interpretations of the sensor signals, the degree of observability is drastically reduced. Again, the small number of plasma modes which are important to control makes such an approach possible. However, the modal interpretation becomes critical to the system performance.

In the following sections, several forms of state interpreter are proposed which are designed to span various different sensor, plasma, and conductor spaces (all interpreted through sensor outputs alone, of course). These interpretation spaces include plasma shape parameters, principal vectors of sensor outputs, sensor modes arising from passive conductor current modes, and toroidal multipole moments of fields due to plasma alone and driven conductors alone.

6.3.5 Shape Predictor $\mathbf{A}_{pred} = \mathbf{A}_s$

The shape predictor state interpreter, $\mathbf{A}_s$, provides predictions of plasma "shape" parameters (R_{ma}, Z_{ma}, κ, etc...) based upon the responses of the set of perturbed

equilibria. It constitutes a "shape predictor" in the same sense that the vessel-vessel plasma response matrix from Sec. 4.3, $\mathbf{X}_{vv}$, constitutes a predictor for flux at the vessel due to plasma current only as a result of changes in vessel currents. $\mathbf{A}_s$ predicts shape variations in the plasma as a function of sensor outputs. It is calculated in much the same way as $\mathbf{X}_{vv}$, using a generalized inverse of the appropriate perturbed equilibrium dataset:

$$\mathbf{A}_s \equiv \mathbf{S}_{EQ}\mathbf{F}_{EQ}^{-1}, \tag{6.35}$$

where $\mathbf{S}_{EQ}$ is the $(NSH \times 15)$ matrix whose columns consist of the NSH shape parameters for each of the 15 perturbed equilibria, and $\mathbf{F}_{EQ}$ is the $(NY \times 15)$ matrix whose columns consist of the NY magnetic signals for each of the 15 perturbed equilibria. Magnetic signals can include flux loop and B_p coil measurements, as well as Rogowski coil measurements of EF coil currents.

Thus, $\mathbf{A}_s$ operating on a sensor signal vector provides a "prediction" of plasma shape parameters, $\underline{S}$:

$$\underline{S} \simeq \mathbf{A}_s \underline{y}. \tag{6.36}$$

6.3.6 Principal Vector $\mathbf{A}_{pred} = \mathbf{A}_{pv}$

As we have seen before, principal component analysis using the SVD provides an extremely powerful way of finding the dominant modes of the input and output space in a matrix mapping. In particular, it can supply a set of sensor signal vectors which represent the "principal modes" of the plasma response. A state interpreter whose rows are the dominant subset of these principal vectors provides a highly efficient measure of the plasma response. If this response is calculated from the SVD of the perturbed equilibria, it is not guaranteed that this space will be weighted in the appropriate way to optimally describe the principal modes of the plasma stability response. However, the principal modes of the perturbed equilibrium plasma response are guaranteed by construction to span the space of

plasma responses allowed by the perturbational formalism. Furthermore, as we have demonstrated previously, the number of significant plasma modes is less than the eight channels provided by the PID array.

If the matrix of sensor signals for the 15 equilibria in the perturbed set is denoted by $\mathbf{F}_{EQ}$, as in Sec. 6.3.5 above, then the principal vectors are found by calculating the SVD,

$$\mathbf{F}_{EQ} = \mathbf{U}_F \mathbf{\Sigma}_F \mathbf{V}_F^T. \tag{6.37}$$

The desired principal sensor signal modes are those columns of $\mathbf{U}_F$ which correspond to the largest singular values. These then make up the rows of $\mathbf{A}_{pv}$.

6.3.7 Toroidal Multipole $\mathbf{A}_{pred} = \mathbf{A}_{tm}$

In recent years much attention has been given to the problem of tokamak equilibrium reconstruction from magnetic measurements. One of the most elegant and direct methods to emerge for solving this problem is the use of toroidal multipolar expansions [32,33]. The toroidal multipole moments are coefficients of expansion of the poloidal flux outside the plasma in terms of toroidal harmonics, solutions to the homogeneous Grad-Shafranov equation in toroidal coordinates. Two sets of multipole moments have been described, "internal" moments due to plasma current alone, and "external" moments due to currents outside the plasma. It has been shown that the internal moments can be related to plasma current moments, which provide a relatively direct measure of physically meaningful objects [32]. The current moments are spatial function-weighted integrals over the plasma current density, and describe such things as vertical and radial displacement of the current centroid, and vertical ellipticity and triangularity of the current distribution.

For the toroidal multipole predictor, we use a state interpretation matrix, $\mathbf{A}_{tm}$, constructed by S. Horne, which operates on the magnetics signals and produces a vector of multipole flux moments [32]. An important feature to note in this

process is the role of coil currents. The calculation is initially done so that the moment amplitudes explicitly exclude the coil contributions to the flux. That is, only plasma current contributions to the moments result from the operation upon magnetics. This places $\mathbf{A}_{tm}$ on the same footing as the shape predictor, $\mathbf{A}_s$. Only plasma state information is derived from the magnetics for the nominal toroidal moment predictor.

6.3.8 Passive Eigenvector $\mathbf{A}_{pred} = \mathbf{A}_{ev}$

Perhaps the most direct way one might imagine interpreting the magnetic measurements so as to provide control over certain plasma modes is to make the interpreted signals proportional to these passive modes. To accomplish this, we create a state interpreter, $\mathbf{A}_{ev}$, whose rows are the magnetic signal vectors corresponding to a set of normalized eigenmodes of interest. The outputs of this predictor are thus the projections of sensor signal vectors onto the signal vectors corresponding to those eigenmodes. If we define a matrix, $\mathbf{V}$, whose NP columns are the NP normalized modes to be "predicted", the state interpreter matrix is defined by

$$\mathbf{A}_{ev} \equiv (\mathbf{CV})^T. \tag{6.38}$$

The passive eigenvectors are not necessarily orthogonal, since the state matrix, $\mathbf{A}$, is not in general Hermitian. The preceding definition of $\mathbf{A}_{ev}$ will therefore yield mixed signals. Each output channel will in general give a nonzero signal when $\mathbf{A}_{ev}$ operates on one of the NP predicted modes. In order for an operator to more easily improve control performance by adjusting the PID gains, it is useful to orthogonalize the outputs of the $\mathbf{A}_{pred}$-matrix, so that operating on any of the NP predicted modes will produce a non-zero signal in only one of the output channels. This can be accomplished by requiring that

$$\mathbf{A}_{ev}\mathbf{CV} = \mathbf{I} \tag{6.39}$$

where **I** is the (NP × NP) identity matrix, so that

$$\mathbf{A}_{ev} \equiv (\mathbf{CV})^{-1}. \tag{6.40}$$

This definition adds no new information to the set of NP interpreted vectors, so the resulting control law is unaffected. It merely reexpresses the set in a basis which simplifies the task of control law refinement by machine operators.

6.3.9 Application of State Interpreters and Hybrid Observer

We turn now to comparison of the control laws resulting from the state interpreters described above. For illustration purposes, we shall address the case of equilibrium eq9, stabilized with only the EFCU/L (antiseries) circuit being driven. The unstable pole was placed at the closed loop value of $\gamma = -100$ for FSFB. A single-pole power supply model with time constant of 0.2 ms is included. Table 6.2 shows the dominant twelve eigenvalues resulting from applying three kinds of state interpreter, as well as the direct SVD implementation of the **P** and **Q** matrices, to this case. The direct SVD implementation is exactly the same as the PDOO result, since in this case only the EFCU/L (antiseries) circuit is used for control. There is therefore only one nonzero singular value, and the hybrid architecture can exactly implement the SVD. Each of the three state interpreters produces five output variables, so as to provide some standard of comparison. The five shape interpreter channels are predicted values of Z_{ma}, R_{ma}, I_p, κ_{95}, and $R_{outer} - R_{inner}$, a measure of the minor radius. The principal vector state interpreter consists of the sensor vectors corresponding to the five largest singular values of the sensor response. The multipole moments used in the toroidal multipole predictor are the first three non-zero odd internal moments, and the first two non-zero even internal moments. The eigenvector predictor uses the top five dominant modes.

Eval	PrincVec	Multipole	Shape	EigMode	SVD
1	**-11.+275i**	**-8.+383i**	**+16.+456i**	**-5.+306i**	-20.
2	**-11.-275i**	**-8.-383i**	**+16.-456i**	**-5.-306i**	-74.
3	-73.	-73.	-73.	-73.	-193.
4	-205.+18i	-199.	-184.	-198.+5i	-211.
5	-205.-18i	-207.	-214.	-198.-5i	-307.
6	-317.	-314.	-297.	-312.	-341.
7	-347.	-342.	-345.	-348.	-429.
8	-429.	-429.	-429.	-429.	-453.
9	-464.	-467.	-463.	-460.	-497.
10	-499.	-502.	-487.+9i	-501.	**-545.**
11	-591.	-505.	-487.-9i	-575.	-566.
12	-618.	-633.	-649.	-640.	-640.

Table 6.2: Comparison of dominant eq9 closed loop eigenvalues for hybrid implementations of PDOO control law: principal vector $\mathbf{A}_{pred}$, multipole moment $\mathbf{A}_{pred}$, shape $\mathbf{A}_{pred}$, eigenmode $\mathbf{A}_{pred}$, and direct SVD.

Comparing the feedback roots for the various cases in Table 6.2 (in bold face), we can identify the best and worst immediately. The shape predictor, $\mathbf{A}_s$, is obviously the worst, as it yields an unstable result. The shape predictor clearly provides some measure of modal observation, since it is much more stable than the passive mode. But the modal interpretation is insufficient, and much refinement will be necessary to find a satisfactory closed loop response, if at all possible. The direct SVD provides the exact solution found by the PD output observer, and as such stabilizes the vertical mode most satisfactorily among the approaches shown. However, note that the slow decay mode at $\gamma = -20.$ is still unaffected. It was, of course, explicitly allowed to remain unaffected by the pole placement process. As we shall see, the continued presence of this pole seriously limits the control system performance for all of the hybrid implementations of the PD control law.

The principal vector, multipole, and eigenvector predictors provide very similar responses. Each of them results in a dominant underdamped mode, with a decay time of 100-200 ms, and a much higher frequency oscillatory component. Each of these bases allow sufficiently good observation of the unstable mode to stabilize it.

However, the nominal result is nowhere near the full state pole placement. This is because the slow decay mode at $\gamma = -20$, representing EFC coil response, limits the control system response. The mode essentially consists of large currents in the EFC circuit with negligible vessel currents, and plasma velocity opposite to the displacement. This motion corresponds to an offset plasma moving slowly back to its equilibrium position, under the stabilizing influence of large EFC currents. The motion is slow enough not to excite significant currents in the vacuum vessel. The conductor currents for this mode are plotted in Fig. 6.7, illustrating the overwhelmingly large EFC component.

The $\gamma = -20.$ mode couples strongly to the unstable mode, and tends to be excited whenever feedback is applied to the driven coils in such a way as to stabilize the plasma. In order to avoid such excitation, and thus coil response limitation, one must provide an observer which discriminates sufficiently between the two modes. We can do this by placing the $\gamma = -20.$ root at a more stable location.

The pole placement technology we have developed provides a way of addressing just such a performance limiting problem as that posed by the slow decay mode. By explicitly placing the pole at a more highly damped location with full state feedback, the driven coil response is enhanced, and the control system will respond more rapidly. The results of placing the unstable pole at a closed loop value of $\gamma = -120.$ and the slow decay root at $\gamma = -100.$ with full state feedback are shown in Table 6.3. In all other respects the system is the same as before. Again, several $\mathbf{A}_{pred}$ matrix examples are compared. While the SVD result shows that the PD output observer (and thus the direct SVD implementation as well) managed to significantly improve the slow decay mode response to a closed loop value of $\gamma = -46$, none of the $\mathbf{A}_{pred}$ implementations were able to improve performance beyond a decay rate of $\gamma = -15$ sec^{-1}. This is because even though the pole placement algorithm implicitly provides sufficient observation of the two modes, the state interpretation matrix implementation of that algorithm in general does

Eval	Shape	Multipole	PrincVec	SVD
1	**-12.+468i**	**-14.+395i**	**-14.+286i**	-46.
2	**-12.-468i**	**-14.-395i**	**-14.-286i**	-74.
3	-73.	-73.	-73.	-193.
4	-184.	-199.	-206.+18i	-211.
5	-214.	-207.	-206.-18i	-307.
6	-297.	-314.	-317.	-341.
7	-345.	-342.	-347.	-429.
8	-429.	-429.	-429.	-453.
9	-463.	-468.	-464.	-498.
10	-486.+8i	-502.+3i	-499.	**-537.**
11	-486.-8i	-502.-3i	-596.	-561.
12	-649.	-633.	-615.	-640.

Table 6.3: Comparison of dominant eq9 closed loop eigenvalues for hybrid implementations of PDOO control law. Unstable and $\gamma = -20$ roots simultaneously placed at -120 and -100 respectively. No EFC current predictor.

not for the $\mathbf{A}_{pred}$ matrices used here. In particular, they don't provide adequate discrimination of the effect of the EFC current. Notice that the shape interpreter $\mathbf{A}_{pred} = \mathbf{A}_{sh}$ now yields a dominant feedback root stabilized comparably to the other predictors.

In the next section we demonstrate the augmentation of a state interpreter to provide improved discrimination of EFC current, and its effect on closed loop plasma response.

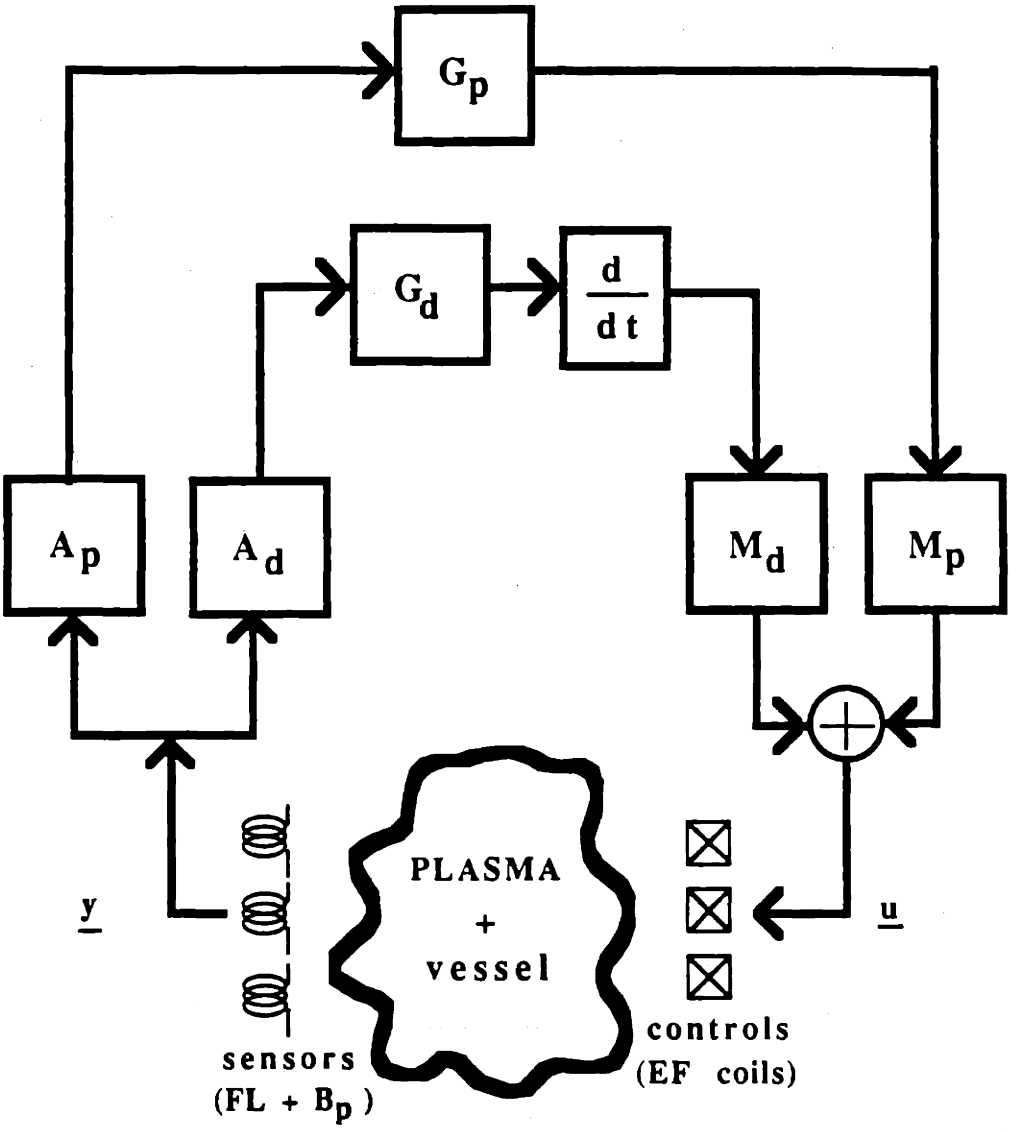

Figure 6.6: Block diagram of interpreted C-MOD hybrid control system architecture showing essential elements for present study.

6.3.10 Improving Coil Response

As is clear from the application results in the preceding section, use of the various state interpreters used proved insufficient to move the unstable root beyond the slow decay root at approximately $\gamma = -20.$ and failed to do even as well as the PD output observer feedback case and its direct SVD implementation when the slow mode was explicitly moved. This is because the $\mathbf{A}_{pred}$ matrices do not provide a sufficient basis for interpreting the *closed loop* modes, and in particular, do not provide sufficient information regarding EFC current.

To correct for this, we can augment a state interpreter so as to provide an explicit channel for interpretation of magnetic signals from plasma and vacuum field response due to EFC current variation alone. Because the toroidal multipole predictor is independent of equilibrium and is known to provide a very good basis for equilibrium representation with very few moments [33], and also allows the complete separation of plasma variation signals from conductor current signals, we choose to test out the theory with that predictor. We replace the fifth row of all of the state interpreter $\mathbf{A}_{pred}$ matrices with a predictor for pure EFC currents from magnetic measurements calculated using toroidal multipoles. The results are shown in Table 6.4. As before, the feedback roots are shown in boldface. The EFC current predictor greatly improves the dominant mode damping rate for the shape and multipole moment state interpreters, and slightly improves the principal vector interpreter result. In both the damping rate and oscillatory component the multipole moment case yields the best result, demonstrating the relative high quality of the plasma state, vessel mode, and EFC current observation of the toroidal multipole approach.

Eval	PrincVec	Multipole	Shape
1	**-18.+276i**	-77.	**-47.+361i**
2	**-18.-276i**	**-95.+179i**	**-47.-361i**
3	-73.	**-95.-179i**	-73.
4	-205.+16i	-146.	-205.+5i
5	-205.-16i	-214.	-205.-5i
6	-318.	-332.+13i	-309.
7	-348.	-332.-13i	-346.
8	-429.	-429.	-429.
9	-465.	-481.+4i	-480.
10	-499.	-481.-4i	-490.+12i
11	-607.+31i	-557.	-490.-12i
12	-607.-31i	-632.	-634.

Table 6.4: Comparison of dominant eq9 closed loop eigenvalues for hybrid implementations of PDOO control law. Both unstable root and $\gamma = -20$ root placed at -100 and -120 respectively. All $\mathbf{A}_{pred}$ augmented by EFC current predictor.

6.4 Time Domain Performance

Time domain performance characteristics are usually described in terms of the general step response form illustrated in Fig. 6.9. The step response parameters which concern us here include the rise time, maximum overshoot and undershoot, settling time, and ring frequency. Rise time, t_r, is usually defined as the time required for a system's step response to go from 10% to 90% of the final value. However, in the presence of undershoot (see below) this must sometimes be modified. If the undershoot consumes an appreciable time, it makes more sense to define the rise time as the time required to reach 90% of the final value from the initial excitation. The maximum overshoot, P_0, is the maximum value of the step response, sometimes expressed as a fraction of the final value. Settling time, t_s, is the time after which the step response stays within 2% of the final value. The ring frequency, ω_r, is related to the rise and settling times in a second order system, and is essentially the frequency of oscillation during settling after the initial overshoot. For a high order system, this can be assessed as the number of oscillations between the initial

crossing of the final value and the "settled" point (at which the settling time is measured) divided by that time interval [30].

Undershoot is a phenomenon which occurs in the presence of a right half-plane or "non-minimum phase" zero [34]. As described in Chapter 5, such zeros can be present in the plasma-conductor system, so this performance criterion must be mentioned. However, the typical behavior of the closed loop systems under examination here will not exhibit undershoot, and are well approximated by pure second order response.

6.4.1 Step Response of Second Order System

The response of a dynamic system can often be approximated by ignoring all the poles outside of a certain radius from the origin. In particular, high order systems are often approximated as second order systems, retaining only the influence of a dominant complex pole pair or a pair of real poles near the origin. As we have seen above, the behavior of the closed loop system is dominated by the fate of the feedback root, perhaps coupled to a slow decay root. The result was a dominant complex pole pair, and a response very close to second order (see Table 6.2, for example). We shall explicitly demonstrate this in the next section by calculating the actual step response. In order to compare the characteristics of the true step response to that of a second order system, it is useful to relate the performance quantities to the complex pole pair directly. Accordingly, this section briefly reviews the usual second order characteristic equation [30] and derives relations between the equation parameters and the pole pair itself.

A second order characteristic equation is usually cast into a standard form involving the *natural frequency*, ω_n, and the *damping ratio*, ζ. The physical relation between these quantities and the real and imaginary parts of a complex pole pair is shown in Fig. 6.8. The figure shows the underdamped case, in which $\zeta < 1$. Two

poles which are separated on the real axis describe an overdamped system ($\zeta > 1$), and a double pole (two poles coinciding) on the real axis constitutes a critically damped system ($\zeta = 1$).

The bandwidth, ω_h, is given by

$$\omega_h = \omega_n(1 - 2\zeta^2 + \sqrt{2 - 4\zeta^2 + 4\zeta^4})^{1/2}, \tag{6.41}$$

and is related approximately to the rise time, t_r, through

$$t_r \simeq \frac{2.2}{\omega_h}. \tag{6.42}$$

For a unit step input, the maximum overshoot, P_0, is given by

$$P_0 = 1 + exp\frac{-\pi\zeta}{\sqrt{1-\zeta^2}}, \tag{6.43}$$

and for completeness we include the time at which the maximum overshoot is achieved, t_p:

$$t_p = \frac{\pi}{\omega_n\sqrt{1-\zeta^2}}. \tag{6.44}$$

The settling time, t_s, is given approximately by

$$t_s \simeq \frac{4}{\zeta\omega_n}, \tag{6.45}$$

and the ring frequency, ω_r, is given by

$$\omega_r = \omega_n\sqrt{1-\zeta^2}. \tag{6.46}$$

Now, since a complex pole pair with poles at $p_1 = -z$ and $p_2 = -z^*$ has the characteristic equation

$$0 = (s + z)(s + z^*) = s^2 + 2\mathrm{Re}zs + |z|^2, \tag{6.47}$$

we can readily identify

$$\omega_n = |z| \quad \text{and} \quad \zeta = \frac{\mathrm{Re}z}{|z|}. \tag{6.48}$$

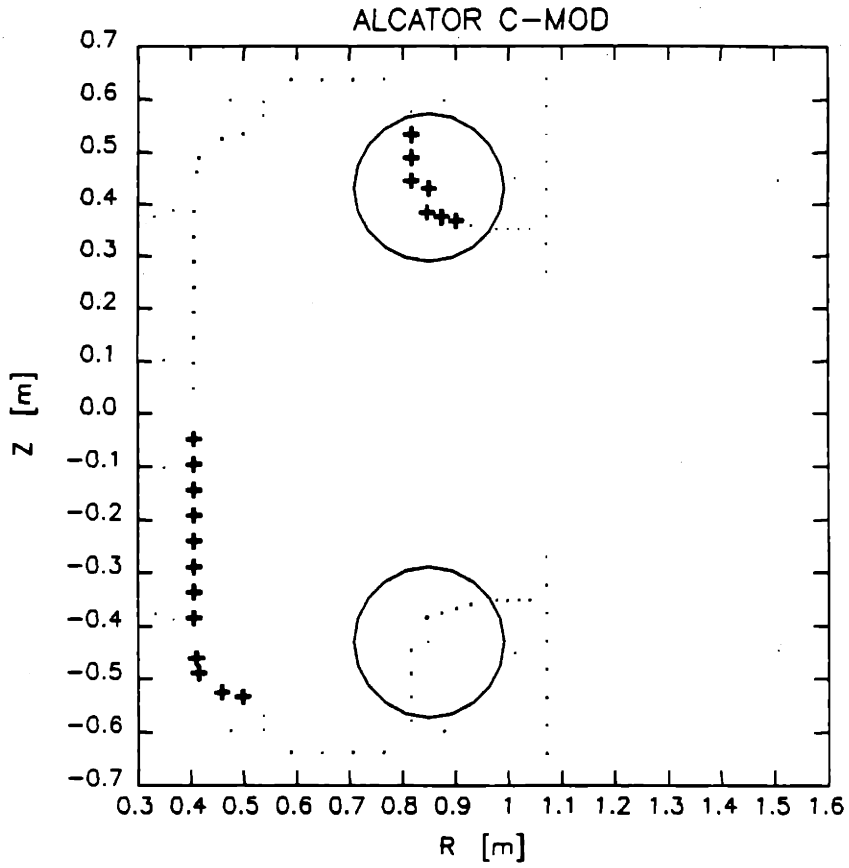

Figure 6.7: Slow decay mode ($\gamma = -20.$) from passive eq9 case with EFCU/L (antiseries) stabilizing.

6.4.2 Time Domain Design

Time domain design is dominated by the tradeoff between the need for sufficiently rapid system response (rise time) and the need for minimizing overshoot. An extremely fast response tends to overshoot more than a slower reponse in a system which is approximately second order. Conversely, a system which is overdamped will not tend to have as fast a rise time as one which is underdamped and overshoots. Settling time, which is connected to both rise time and overshoot, provides another constraint on the two complementary requirements. It is frequently more important to achieve a short settling time than to have merely a fast rise time. The stable nominal closed loop systems achieved in Sec. 6.3.9 in general exhibit extremely underdamped responses with rapid rise time, but slow settling time and some overshoot. This is illustrated in Fig. 6.10, which shows the step response of the closed loop system from Table 6.2 using a principal vector state interpreter, $\mathbf{A}_{pred} = \mathbf{A}_{pv}$.

For the purpose of the step response calculation, a unit step voltage demand is applied to the EFC power supply, and the passive unstable mode or a shape predictor for plasma displacement is used to interpret the state response. Recall that the feedback roots in this case consisted of the pole pair at $\gamma = -11. \pm 275i$. Using the relations from the previous section, this predicts a second order response with natural frequency of $\omega_n = 275$, damping ratio of $\zeta = .04$, bandwidth of $\omega_h = 427$, rise time of $t_r \simeq 5$ ms, overshoot of $P_0 = 1.9$, settling time of $t_s = 364$ ms, ring frequency of $\omega_r = 275$, and a time at which maximum overshoot occurs of $t_p = 11$ ms.

Referring to Fig. 6.10, it is clear that the second order characteristics do not quite match the actual step response, although many of them are close. The rise time is quite accurate (about 5 ms), but the overshoot is much better for the actual step (about 1.13) than for the second order calculation (about 1.9). The difference

is due to the presence of the other modes excited in the system with faster decay rates. It is clearly important, therefore, to calculate the actual step response rather than relying on the second order approximation.

The improved coil response case using the multipole state interpreter resulted in the dominant complex pole pair feedback root $\gamma = -95. \pm 179i$. This can be expected to be significantly better than the unimproved case just studied. The step response for the improved case is shown in Fig. 6.11. The coil response improvement has eliminated the overshoot, lengthened the rise time to about 10 ms, and reduced the settling time to less than 50 ms, where before improvement the settling time was in fact greater than 150 ms. To realistically compare the desirability of the two control laws, decisions must be made regarding the relative importance of rise time, overshoot, and settling time. Or one must consider other criteria to provide additional arbitration. However, in the next two sections, we turn our attention to other performance analysis approaches which may provide further reasons for choosing one control law over another.

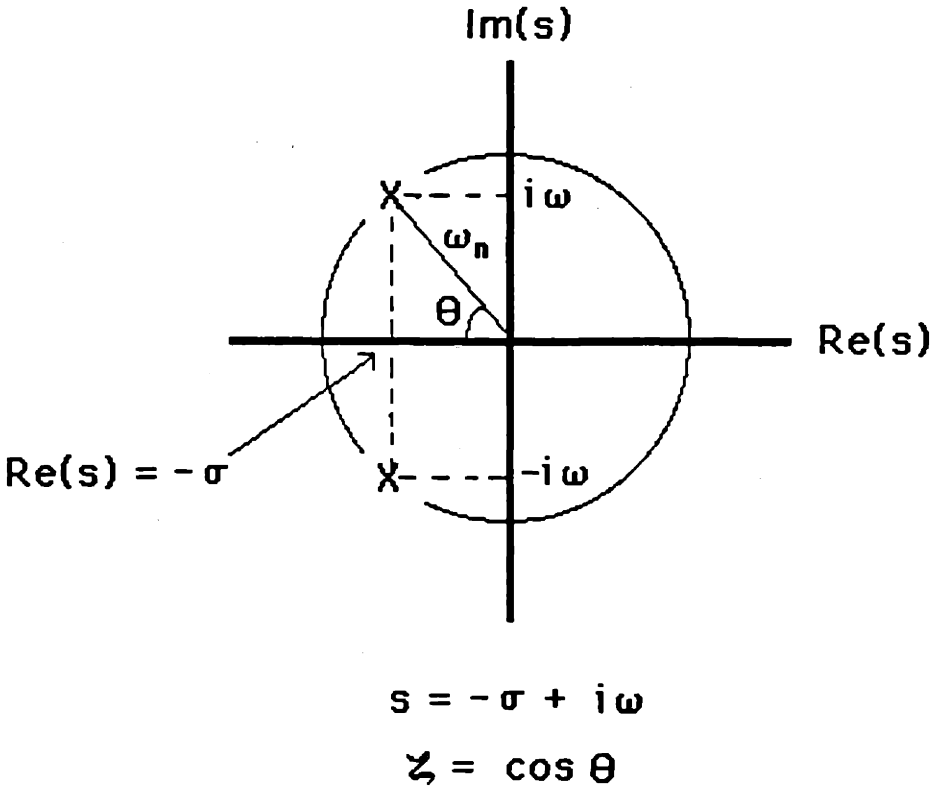

Figure 6.8: Plot of complex pole pair showing relation to ω_n and ζ.

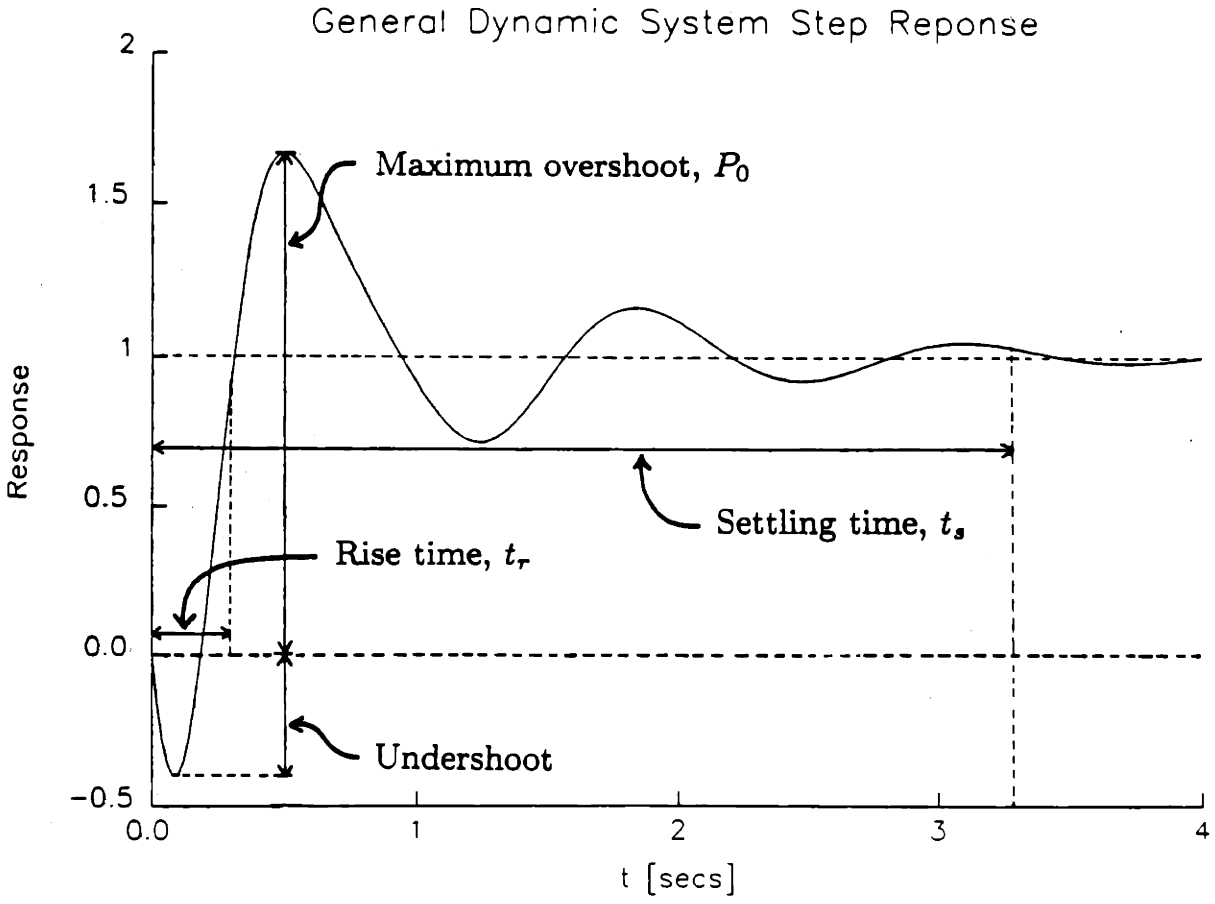

Figure 6.9: Illustration of general dynamic system step response.

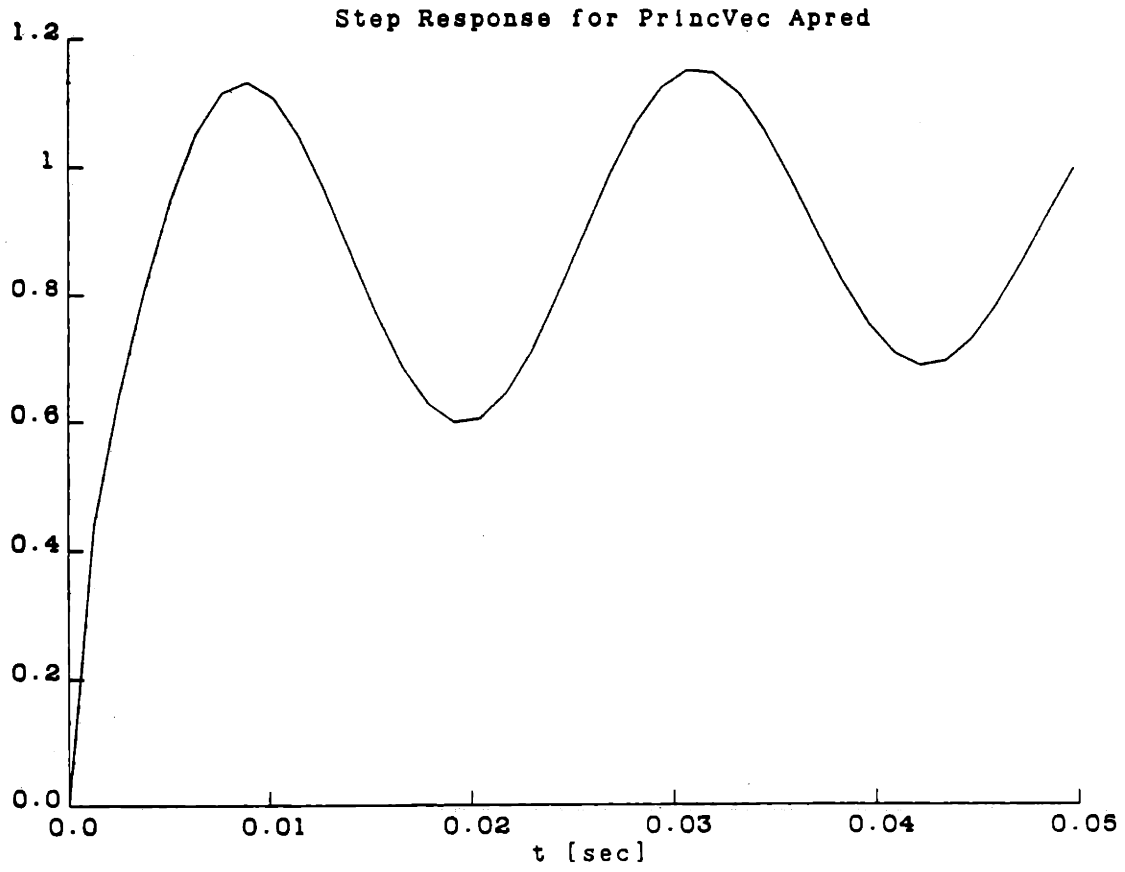

Figure 6.10: Step response of eq9 closed loop case using $\mathbf{A}_{pred} = \mathbf{A}_{pv}$.

6.5 Frequency Domain Performance

Control theory from the time of the pioneering days of servomechanism analysis at the MIT Radiation Laboratory in the mid-20th century has made great use of the frequency domain, primarily via the Laplace transform [28,30]. The power of frequency response methods carries over into the state space approach as well. In this section we shall focus on the Bode Plot and its multivariable analog, which can be used to provide evaluations of relative stability for a given control law. This can also contribute to the ability to refine a nominal control law further by varying PID gains.

6.5.1 Single Variable Bode Plots

To construct a Bode plot for a single input, single output system, we imagine breaking the control loop at some point and injecting a test sinusoidal signal at that point. The single variable Bode Plot is a plot of the magnitude and phase of the output signal arising at the broken location output, as a function of the injected signal frequency. This is illustrated in Fig. 6.13. The figure shows the broken feedback loop block diagram with the input signal labeled V_i and the output labeled V_o. The loop transfer function, **T**, is defined as

$$\mathbf{T}(s) \equiv \frac{V_o(s)}{V_i(s)} = \mathbf{G(s)H(s)} \tag{6.49}$$

where s is the usual Laplace transform complex frequency variable, and for the purposes of the Bode plot, $s = j\omega$. The Bode plot consists of the graphs of $|\mathbf{GH}(j\omega)|$ and $\angle\mathbf{GH}(j\omega)$ as functions of frequency [30].

Aside from describing the bandwidth of a control system, some of the most important kinds of information which can be extracted from the Bode plot are the so-called gain and phase margins. These provide some measure of how far away the system is from instability, and thus reflect the robustness of the control law. The

margins are defined in terms of two frequencies: the "phase crossover" frequency, ω_π, at which the phase plot crosses $\phi = -\pi$, and the "gain crossover" frequency, ω_1, at which the gain plot crosses unity. The gain margin is defined as the inverse of the magnitude of the loop transfer function at the phase crossover frequency:

$$\text{gain margin} = \frac{1}{|\mathbf{GH}(j\omega_\pi)|}. \tag{6.50}$$

The phase margin, often denoted Φ_{pm}, is defined as the phase angle of the loop transfer function at unity gain, ϕ_1, plus π radians (or 180 degrees). These quantities are illustrated in Fig. 6.12, showing a simple generic Bode plot.

The relation between the margins and relative stability can be understood by realizing that to be unstable, a system must undergo phase crossover before the loop gain (magnitude Bode plot) falls below unity. In such a case, a signal injected at V_i in Fig. 6.13 will result in a negative signal with gain greater than unity arising at V_o. When the loop is closed with an inverter at the summation point, as in the top part of Fig. 6.13, this will become unstable positive feedback. Thus, the farther the gain has fallen by the time the system experiences phase crossover, the farther away from instability it is. This relates gain margin to relative stability. The inversion seen in the gain margin formula is so as to make greater gain margin correspond to greater relative stability.

Similarly, the farther away the system is in phase from the unity crossover point by the time it experiences phase crossover, the greater the relative stability. This is the explanation for phase margin. In a sense, perturbations due to model or signal error required to destabilize the system are expected to be greater if the gain and phase margins are large, because a smooth variation in these margins with system error is assumed.

6.5.2 Multivariable Bode Plots

For a multivariable system, the situation is rather different from the single variable case described above. In the case of a multivariable input-output system, the loop signals are in general vectors, and the intermediate matrix multiplications can shrink or expand the spaces represented by those vectors as they travel around the control loop. Furthermore, the signals in each channel will in general cross-couple to other channels during this process. That is, a demand signal applied to one driven coil will result in a response at the other driven coils after the signal has propagated through the loop. It is also difficult to identify a single phase to allow characterization of a phase margin. In the general case, one must use a multivariate analysis which yields information about a multivariable system analogous to the information a Bode plot yields about a single variable system. By taking the SVD of the loop transfer matrix (or a variety of other matrices characterizing the system), one can treat the singular values as one does the magnitude of the single variable loop transfer function. This approach gives up phase information in order to be able to extract some form of useful frequency response from a multidimensional space.

For the moment, we shall address the use of only the "decoupled loop" responses to provide criteria for relative stability. The loop transfer function matrix calculated from the demand inputs to the power supplies, through the loop, and back to the demand vector is given by:

$$\mathbf{T}(j\omega) = (\mathbf{M_p G_p A_p} + j\omega \mathbf{M_d G_d A_d})\mathbf{G}(j\omega) \tag{6.51}$$

where

$$\mathbf{G}(j\omega) \equiv \mathbf{C}(j\omega\mathbf{I} - \mathbf{A})^{-1}\mathbf{B} + \mathbf{D} \tag{6.52}$$

is the plant transfer function matrix.

The multivariable Bode plot for driven circuit i consists of the magnitude and phase of the i^{th} element of the vector resulting from the T matrix operating on the

vector with a one in the i^{th} location and zeros elsewhere, as a function of frequency. Thus we plot the magnitude and phase of the diagonal entries of **T**.

For the case of eq9 controlled and passively stabilized with EFCU/L, the control loop consists of only a single variable, and **T** is a scalar. Figs. 6.14 and 6.15 show the magnitude and phase respectively as a function of frequency for the eq9 closed loop case using the multipole state interpreter along with the EFC current predictor improvement (see Sec. 6.3.10). The figures reflect a system with very large gain and phase margin. The phase margin is about 3.5 radians, or about 200 degrees. The phase crossover point is not shown in Fig. 6.15 since it occurs at such high frequency, so it is impossible to determine the gain margin from these plots. However, it is clear from the magnitude plot that the gain margin is greater than 300 (corresponding to about -50 dB). From these stability margin values, we expect the system to be very robust to model and signal perturbations. As we shall see in the next section, this is indeed the case.

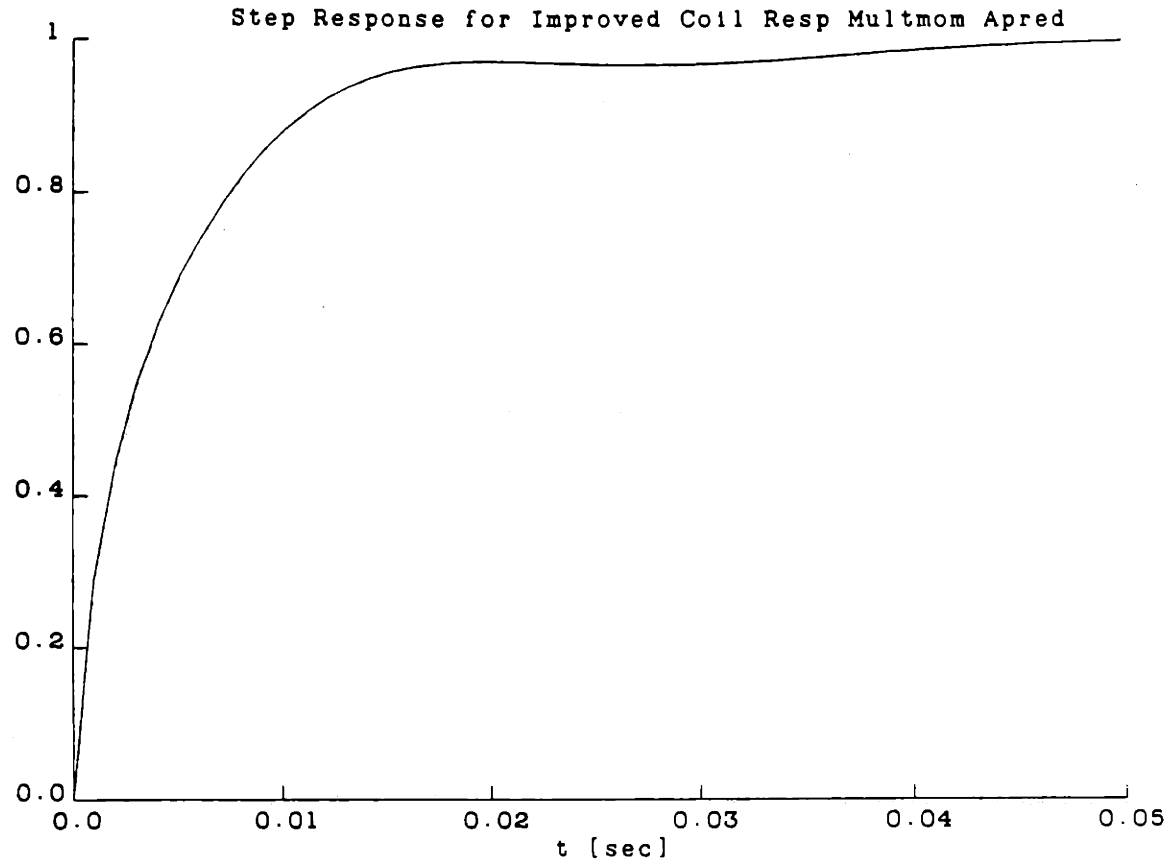

Figure 6.11: Step response of eq9 closed loop case using $A_{pred} = A_{trn}$ augmented with multipole EFC current predictor.

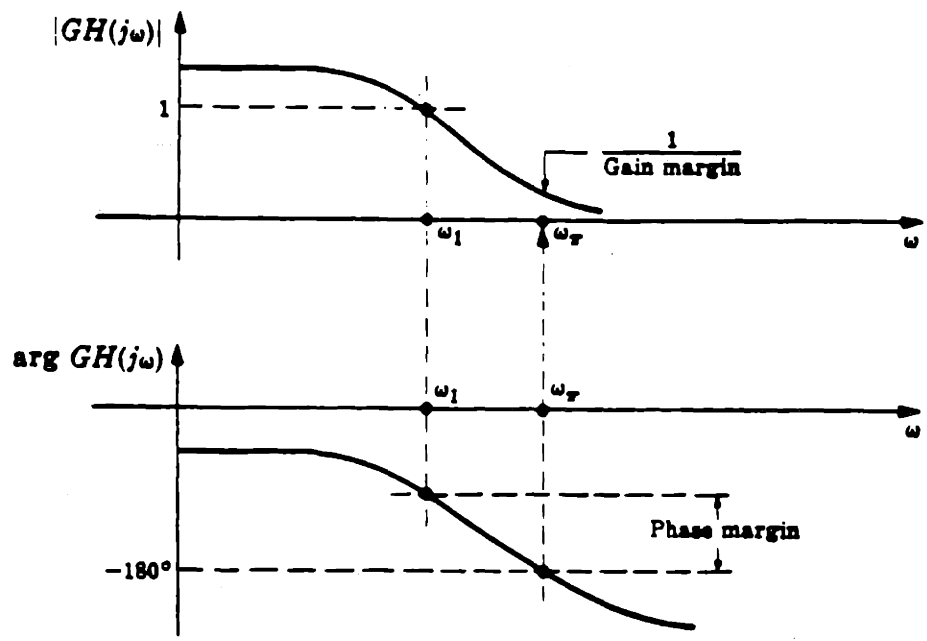

Figure 6.12: Characteristics of the single variable Bode plot.

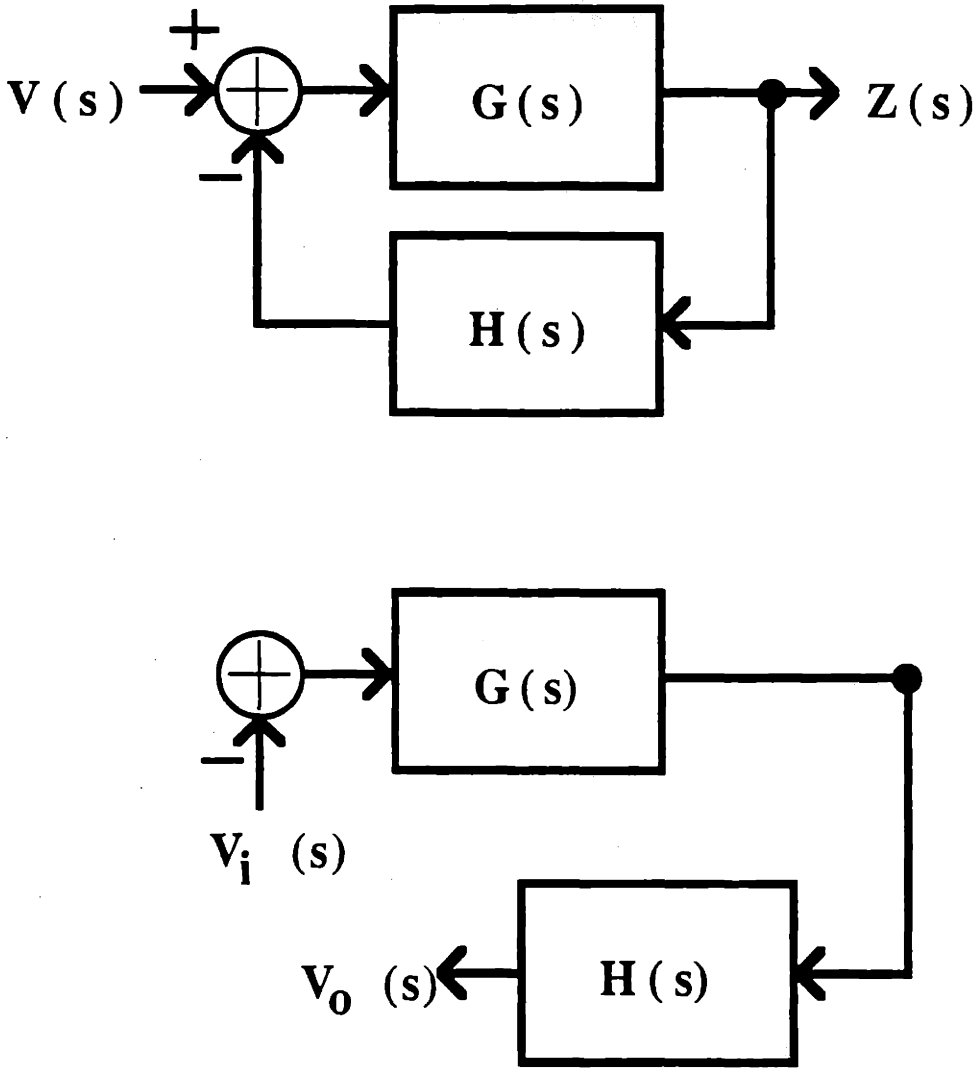

Figure 6.13: Block diagram showing breaking of control loop for Bode plot calculation.

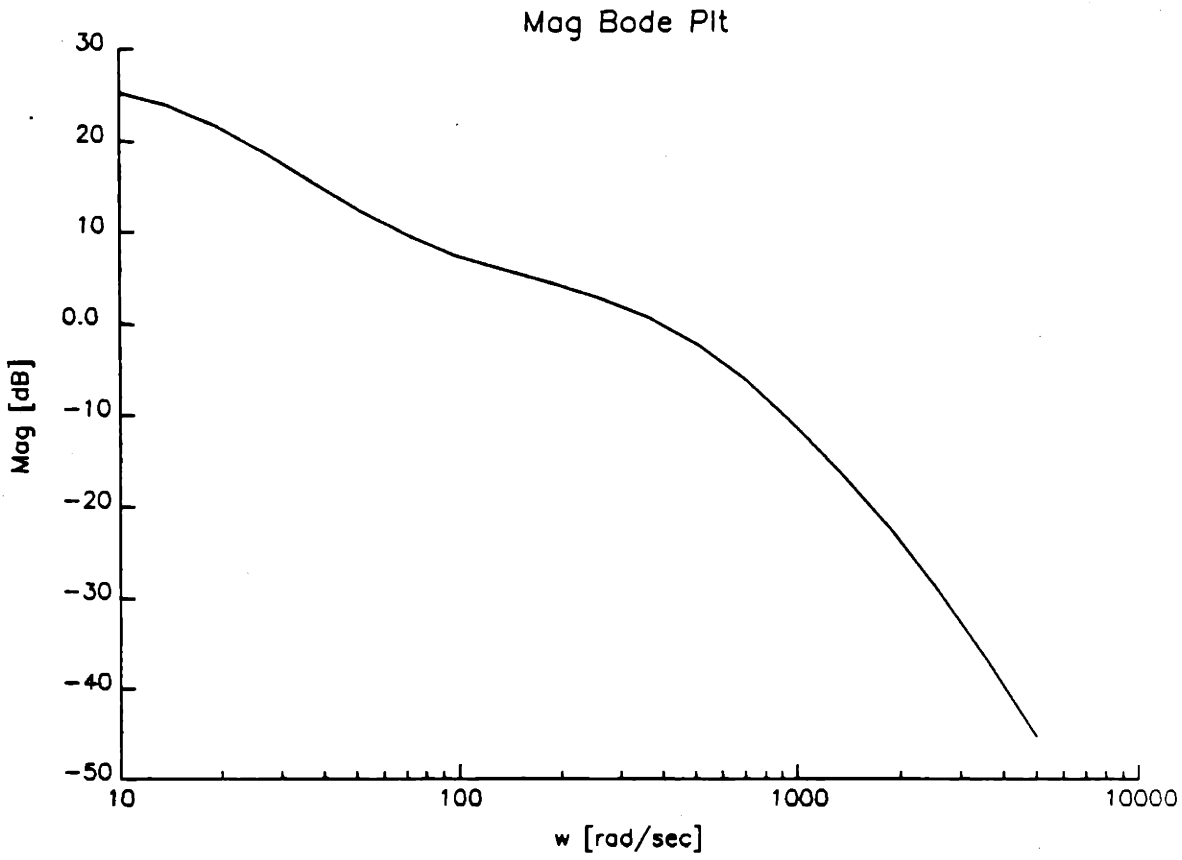

Figure 6.14: Magnitude Bode plot for eq9 with EFCU/L control using multipole moment state interpreter improved by addition of EFC current predictor.

6.6 Error Robustness

One of the most important features which a control system in general may have is error robustness. This is particularly important in the case of the equilibrium control problem, since only a small number of control laws can be used across a shot, yet the plasma can evolve continuously. For this algorithm to work, it is necessary that each control law be robust enough to cover the stability requirements of the full range of evolution between the discrete operating points.

There are two broad areas of robustness which interest us in solving the equilibrium control problem: model error and signal error robustness. Model error robustness refers to how tolerant the stability produced by a control law is to errors in the plant model itself. Signal error robustness refers to how tolerant the stability is to errors in sensor and control signals.

6.6.1 Model Error Robustness

One approach to model error robustness analysis is to perturb aspects of the system randomly, and observe the variation in the closed loop response. This requires a vast number of random matrix perturbations to build up enough statistics to be meaningful. Given the computational constraints of the VAX/VMS system used in this work, this approach is not practical. However, we are still able to examine the impact of systematic error instead.

There are three kinds of matrices which contribute to the initial plant model: the conductor resistance and inductance matrices, and the plasma response matrix. In a general sense, increasing resistance, increasing inductance, and decreasing the plasma response magnitude results in a less stable system. We choose, therefore, to perturb all of the elements in each of these matrices uniformly in those destabilizing directions. This explores a kind of "worst case" systematic error for each kind

Case	Passiveγ_+	Active FR w/ I_{EFC}	Active FR w/out I_{EFC}
R + 5%	537.	$-79. \pm 185i$	$-1.1 \pm 400i$
−5%	486.	$-112. \pm 172i$	$-27. \pm 391i$
M + 5%	624.	$-60. \pm 209i$	$+28. \pm 427i$
−5%	427.	$-124. \pm 151i$	$-44. \pm 367i$
D + 5%	410.	$-119. \pm 172i$	$-40. \pm 352i$
−5%	664.	$-60. \pm 218i$	$+30. \pm 450i$

Table 6.5: Passive and closed loop feedback roots for eq9 standard case with perturbations applied to various matrices describing the basic plant.

of information assumed known about the plant. Note, however, that it is not necessarily *the* worst case with respect to actual eigenvalue calculations or closed loop stability. One would have to calculate the error vectors which maximized variation in passive unstable growth rate, for example, to find the actual worst case.

Table 6.5 shows the passive and closed loop feedback roots for ±5% uniform perturbation of each of the three matrices. The plant case for this study is the same eq9 equilibrium as studied before with EFCU/L stabilization and the same .2 ms single pole lag in the power supply model. For comparison purposes, recall that the nominal passive growth rate for the case with unperturbed matrices was $\gamma_+ = 512$.

In the table, **R**, **M**, and **D** refer to the resistance, inductance, and plasma response matrices respectively. ±5% represents the perturbation applied to these matrices. For example, +5% indicates that the matrix was multiplied by 1.05 before the state space was calculated. The columns entitled "Active FR" list closed loop eigenvalues for the cases indicated. The notation "w/ I_{EFC}" refers to the use of the EFCU/L current predictor along with the multipole moment state interpretor matrix. "w/out I_{EFC}" refers to the use of the multipole moment $\mathbf{A}_{pred}$ alone.

The table shows that the EFC current predictor case provides far greater robustness to this kind of model error than the case without such a predictor. When the predictor is used, all of the plant matrix perturbations still result in quite sat-

isfactory performance. By contrast, in the absence of the current predictor, two of the perturbations result in closed loop instability, and the remaining one results in an insufficiently well damped feedback root. Note that perturbation of each matrix can either increase or decrease stability, depending on the direction of perturbation. While increasing the magnitude of **M** or **R** entries decreases stability, increasing the magnitude of **D** entries increases stability.

This kind of analysis can provide a strong form of arbitration when the time domain performance appears ambiguous. Robustness to model error is very important for the reasons discussed above. However, it is also important to test the resilience of the control system to signal error. It is to this topic we turn our attention next.

6.6.2 Signal Error Robustness

Inaccuracy of sensor or, to a less important degree, control signals, can lead to failure of an insufficiently robust control system. From noise pickup to actual sensor failure, there exists a range of unreliability which can occur. As in the case of model error robustness, we examine a simple kind of "worst case" sensor error in order to understand the degree to which the signals must be reliable for satisfactory stability.

For this performance test, we disable certain sensor array inputs one by one, simulating complete failure of each of these chosen inputs. Referring to the sensors in the geometry plot of Chapter 5, Fig. 3.12, we disable flux loops 0 through 10 individually. The sensors are counted starting from the outboard midplane, and proceeding in a counterclockwise direction. This set therefore constitutes the entire set of flux loops above the midplane. The resulting closed loop feedback root values using the familiar multipole control law with EFCU/L circuit current predictor are shown in Table 6.6.

This data indicates that any one of the flux loops may be lost, or its signal compromised, and the system will be minimally affected. It is, of course, necessary

Flux Loop	Closed Loop FR
0	$-94. \pm 179i$
1	$-95. \pm 181i$
2	$-89. \pm 182i$
3	$-98. \pm 187i$
4	$-86. \pm 198i$
5	$-94. \pm 179i$
6	$-96. \pm 180i$
7	$-93. \pm 180i$
8	$-96. \pm 180i$
9	$-102. \pm 179i$
10	$-102. \pm 178i$

Table 6.6: Closed loop feedback roots for disabled flux loop sensors.

that any spurious signal appearing on the sensor channels be small enough in amplitude for this to be true. An important question to address with this approach is the effect of the set of flux loops on the outboard wall. Since these loops cannot extend all of the way around the vacuum vessel in order to avoid blocking the horizontal ports, they are necessarily saddle loops. Their signal-to-noise ratios are proportionately poorer than those of the continuous loops, and their signals are therefore less reliable.

In fact, for the eq9 case being used here for illustrative purposes, the closed loop feedback root with the four outboard port region flux loops disabled is $\gamma_{FR} = -87. \pm 179i$. Thus, even the total failure of the set of saddle loops will affect the closed loop stability very little.

6.7 The Design Process

Now that the preceding array of tools has been demonstrated, it remains to specify what kinds of performance criteria a tokamak axisymmetric control system should satisfy, and to describe how to go about applying these tools in the design process.

6.7.1 Performance Criteria

We are, in fact, fortunate in that the axisymmetric control problem is not typically very demanding of all aspects of performance. For example, since Alcator C–MOD expects to run plasmas which do not fill the vertical dimension of the vacuum vessel aperture, there is a great deal of room for vertical overshoot. The equilibrium which has been used for illustration throughout this chapter, eq9 ($\kappa_{95} = 1.6$, $z_{ma} = 0$), has its top and bottom limits at about ± 32 cm (see Fig, 4.3, for example). This allows about 15 cm of motion above the plasma, although only 5 cm below before it strikes the divertor hardware. This difference between top and bottom arises as a result of the asymmetric divertor configuration. For initial operation of the machine, only lower divertor hardware will be installed, and only lower single null diverted equilibria will be formed. For an equilibrium such as eq9, the plasma could still tolerate a 50% overshoot for a 2 cm displacement, leaving about a 40% safety margin. A displacement approaching 5 cm would tolerate no overshoot at all.

Of course, in general one wishes to minimize overshoot, but we must consider the other time domain parameters of rise and settling time as well. Typically if overshoot is kept to zero, the rise time is longer than if some amount of overshoot is tolerated. We must therefore determine how fast the plasma should respond. The time scale of a C–MOD shot is several seconds. One would prefer therefore that any control response be much shorter than this time. This requires a response time no longer than a few tens of milliseconds. A reasonable *ad hoc* limit for this kind of consideration we can take to be about 20 msec.

Radial overshoot is another criterion which must be addressed. Since the plasma is generally much closer to the inboard wall in the radial direction than in the vertical, the tolerable radial displacement is much less. For a limited plasma, an inward disturbance displacement can result in current being scraped off, and lead to a disruption [35]. Thus, corrective overshoot must be eliminated for these

equilibria. In the case of a diverted plasma, there is a gap which provides some margin for overshoot, but this gap is typically very small. For eq9, the inner gap is about 1.5 cm, allowing less than 50% overshoot even for a displacement as small as 1 cm. Even in the case of a diverted plasma, therefore, overshoot should be eliminated for radial control. Fortunately, the passive radial mode is already stable with a damping time of about 14 msec, exceeding the 20 msec limit. The mode has no imaginary component, and thus no overshoot. This damping rate is generally the case for the radial modes in C–MOD equilbria, regardless of elongation.

Most large plasma perturbations occur on a timescale much shorter than the *ad hoc* 20 msec limit, in regimes for which no EF coil control system can hope to follow the changes. Pellet injection in Alcator C, for example, typically modified the density profile in less than 500 μsec. The temperature profile adjusted even more quickly, in less than 250 μsec [36,37]. Plasma disruptions also occur on a comparable timescale, about 100 μsec for Alcator C [38]. It must be assumed that such disturbances are not severe enough to result in uncontrollably large instantaneous growth rates or very large displacements. However, extremely fast changes in profiles do occur from such effects as pellet injection and soft disruptions, emphasizing the need for control system robustness if these variations are to be tolerated.

It is instructive to examine the acceptable performance characteristics of already operating tokamaks. Experimental evidence from very demanding elongated devices reveals a fairly large tolerance for poor performance in the equlibrium control system. For example, the D-IIID tokamak operated by General Atomics has achieved record stabilizable elongations of 2.5 as of this writing. Typical D-shaped plasmas run in this machine fill the vessel aperture quite completely with the separatrix often within a few centimeters of the vacuum vessel. Nevertheless, such cases have been achieved with an actual vertical control response overshoot of about 50%, a ring frequency of about 100 sec^{-1}, and a settling time on the order of 50 ms or greater [39].

The JET machine operated by the European Community has achieved full aperture stable elongations in excess of 1.7 with an overshoot of 50%, a ring frequency of about 100 sec^{-1}, and a settling time of greater than 150 ms [9].

From these experimental examples there is clearly a great deal of latitude in acceptable control performance. However, to ensure satisfactory control of highly unstable cases and provide sufficient robustness, the maximum amount of performance should be extracted from a given nominal control solution. In order to further refine the control response, we can iterate within the design loop, adjusting PID gains as needed.

6.7.2 Design Iteration and Refinement

The design process which has been implicit in all of the preceding analysis description up to this point has involved calculation of a nominal control law and testing of its performance. The explicit placement of poles in different locations and the addition of EF coil current predictors in the state interpreter were included as examples of improvement strategies. We have envisioned iterating with techniques such as these until the system exhibits acceptable step response, frequency response, and robustness behavior. However, there is a more detailed refinement scheme which is allowed by the hybrid geometry.

Because the individual channels of the PID do not cross-couple, one can sweep the gain for each channel corresponding to an interpreted state variable (received as an output of the A_{pred} matrix), and set the gains at their optimal values. To reduce the search space to a tractably small number of sweeps, we order the interpreted state variables in a hierarchy of expected importance, and optimize each one in turn following this ordering. After each gain sweeping optimization, frequency and step response performance can be tested and the iteration repeated. The general design procedure is illustrated in the next section with the high elongation, high passive

growth rate equilibrium, eq10.

6.8 Control Design for Example Equilibrium

We now apply the design procedure described above to the equilibrium eq10. Recall that this case is an equilibrium with $\kappa_{95} = 1.7$ and $\kappa_{sep} = 1.85$. It exhibits a passive growth rate in the presence of the vacuum vessel alone of 1388 sec^{-1}. By comparison, the rigid vertical growth rate is calculated to be 745 sec^{-1} for vacuum vessel alone. We consider the active case in which OH2U and OH2L are driven independently and EFCU/L are connected as usual in antiseries. There are thus three independently driven control circuits. The unstable passive mode in this case has a growth rate of 1052 sec^{-1}. The corresponding rigid result is 600 sec^{-1}.

The conductor current distribution for this (nonrigid, flux-conserving) mode is shown in Fig. 6.16 and the flux contours arising from these currents are shown in Fig. 6.17. It is particularly important to note that the net effect of the plasma's unstable motion on the closely coupled inboard wall and OH2 coils is so as to result in a positively induced current in the upper inboard wall and EFCU, but a negatively induced current in OH2U. Roughly the opposite occurs in the conductors below the midplane. This is entirely due to induction from the EFC coils. If only OH2U/L were present, the sign of the OH2 currents would be the same as that of the adjacent vessel wall. This will prove important in determining the form of the control signal weighting vector for pole placement.

A more complete list of the passive eigenvalues in the presence of the three stabilizing EF coil circuits is given in Table 6.7. The modes corresponding to the three dominant stable modes are shown in Figs. 6.18 through 6.20 (modes numbered 2 through 4 in column 2 under "Passive"). These modes clearly couple strongly to the driven coil currents, consisting as they do primarily of these currents. We shall

Eigenvalue	Passive	FSFB	PDOO
1	**1052.**	-5.6	-5.6
2	-5.6	-7.0	-7.1
3	-7.0	-22.	-22.
4	-22.	-80.	-80.
5	-80.	**-100.**	**-140.+763i**
6	-200.	-200.	**-140.-763i**

Table 6.7: Comparison of dominant eigenvalues for passive system, FSFB, and PD Output Observer FB (eq10). Boldface indicates "vertical" mode.

therefore expect the system performance to be limited by their presence as the eq9 case above was.

We begin by using the full state feedback (FSFB) algorithm to place the unstable pole alone at $\gamma = -100$. The control signal weighting vector for full state pole placement, denoted q_i in Sec. 6.1, is defined to be $q_i = [V_{EFCU}, V_{OH2U}, V_{OH2L}] = [1, -1, 1]$, so that the unstable mode, having the same relative sign among coil currents, can be affected. This results in the the set of closed loop stable poles listed in Table 6.7. The corresponding proportional-derivative output observer (PDOO) result is also shown in the table. Notice that the feedback root (FR) has become a pole pair with a very high frequency imaginary component and a real part which is more damped than the FSFB result, just as in the eq9 PDOO case. As predicted, the slow decay modes remain behind.

Before attempting to deal with the slow decay modes, it is interesting to examine the effects of the various hybrid control implementation schemes. We expect the multipole moment $\mathbf{A}_{pred}$, which gave the best result in the case of eq9, to perform much less well for eq10. This is because the coordinate origin used for calculation of the multipole predictor was taken to be the machine centroid, at $R_{cent} = 66.5$ cm on the midplane, $Z = 0$. The magnetic axis of the eq10 equilibrium is shifted vertically by 2 cm, resulting in a less accurate modal reconstruction from the multipole state interpreter. In fact, all of the state interpreters used in the eq9 case

Eigenvalue	PDOO/SVD
1	-7.0.
2	-9.8
3	-22.
4	-80.
5	-136.+830i
6	-136.-830i

Table 6.8: Dominant closed loop eigenvalues for PDOO FB and SVD implementation of PDOO (eq10).

result in highly unstable closed loop systems. The multipole $\mathbf{A}_{pred}$ yields an unstable roots of $\gamma = +149 \pm 859i$. The principal vector $\mathbf{A}_{pred}$ results in unstable roots of $\gamma = +109 \pm 849i$. The shape $\mathbf{A}_{pred}$ yields the worst of all, unstable roots of $\gamma = +393 \pm 981i$. Of course, the direct SVD implementation results in exactly the same roots as the PDOO case. We focus on this implementation.

The step response for the direct SVD implementation of PDOO FB is shown in Fig. 6.21, and clearly shows the characteristic response time of the slow decay mode at $\gamma = -5$. More specific pole placement is called for. Returning to the pole placement step in the precedure, we place the $\gamma = -5$ passive pole at -75, and the unstable mode at -100. After PDOO calculation and direct SVD implementation, we find the set of dominant closed loop poles shown in Table 6.8.

As the table shows, both poles were successfully moved. The step response for this case is given in Fig. 6.22. The figure shows that the system responds much more swiftly now, with a roughly 65% rise time of about 20 ms, but a settling time dominated by the slow decay mode at $\gamma = -7$. Sweeping of $\mathbf{G}_p$ and $\mathbf{G}_d$ gains can improve performance somewhat beyond this. Fig. 6.23 shows the result of sweeping the gain corresponding to the largest singular value in both $\mathbf{G}_p$ and $\mathbf{G}_d$ simultaneously. Thus the time constant for derivative feedback is kept fixed. The plot shows that the feedback root becomes more and more stable with increasing gain, but the slow decay mode at $\gamma = -7$ is a quasiconstant mode for this form of

Case	Passiveγ_+	Active FR	Active Dom. Root
R + 5%	1105.	$-167. \pm 897i$	-13.
M + 5%	1518.	$-92. \pm 1020i$	-13.
D − 5%	1632.	$-152. \pm 1212i$	-13.

Table 6.9: Closed loop roots (FR and dominant stable root) for eq10 case with perturbations applied to various matrices describing the basic plant.

gain variation. Next we sweep the gains corresponding to the second singular value. This produces the plot shown in Fig. 6.24. In this case, an optimum point is found at a gain value of about 12000. The resulting dominant closed loop root is then $\gamma = -13$. The gain sweep of the third singular value is shown in Fig. 6.25 to yield no improvement of the dominant mode.

The step response for the control law optimized by gain sweeping is shown in Fig. 6.26. Clearly the performance has been significantly improved by removing the performance limiting poles.

It remains to examine the robustness of this control law to model and signal error. Following the same procedure as illustrated for eq9, we construct a table showing the variation in closed loop poles for different perturbed plant matrices. Table 6.9 shows the results. No appreciable degradation in performance is found. The real part of the feedback root changes by as much as 35% from the nominal closed loop value of $Re(\gamma) = -140$, but this is insufficient to degrade response time much below 10 ms. Since a response time of 20 ms with less than 50% overshoot comprise the target performance criteria, the system is extremely robust to this degree of error.

One control aspect which must be verified is the ability of the power supplies to provide the necessary responses. The delay time and slew rate are embodied in the power supply "lag" model. However, the voltage limits have not been built into the models. These limits are highly nonlinear, so we must check *a posteriori* whether the control system resulting from our design procedure will saturate at a

lower voltage than needed for some reasonable plasma displacement. We assume a 1 cm vertical displacement, using the shape state interpreter row reflecting this displacement. We then calculate the voltage demand resulting from that vector of sensor measurements due to the final optimized eq10 control law. For a 1 cm displacement with zero velocity, the demand is ±370 V to EFCU/L, OH2U, and OH2L. This is quite acceptable for EFCU/L, with a power supply limit of ±500 V, but not quite attainable by the OH2 supplies, with fully-loaded limits of ±100 V. Response time will therefore be somewhat more sluggish than the ideal case, but since the EFC driving signal dominates the system response, this effect should not be sufficient to reduce the response time below 20 ms (note the small effect on time constant in the second gain sweep plot).

It is of interest to ask whether the eq10 control law provides satisfactory control for other equilibria. If so, the task of the control designer is substantially eased, and the likelihood that satisfactory control will not extend between operating point equilibria during a shot is much diminished. To explore this question, we apply the eq10 control law to the eq9 case, with the same EF coil/circuit configuration as that used in the eq10 design. This results in eq9 being driven unstable, with a closed loop fastest growth rate of greater than 1000 sec^{-1}. This is likely the result of the difference in state interpretation embodied in the SVD implementation of the PDOO feedback law calculated for eq10. The state interpreter is calculated for the eq10 plasma, with magnetic axis offset from the midplane by 2 cm, more highly elongated than eq9, with entirely different decay index and modal response. The magnetic axis of equilibrium eq9 is on the machine midplane, Z=0. In order to accomodate the high passive growth rate of eq10, the control system must provide a high gain, and thus a higher effective phase shift in coil driving signal than that required to stabilize eq9.

Despite the fact that these two equilibria both have 3 MA plasma currents, similar magnetic axis radii and internal inductances, the same control law calculated

for one of them cannot be used to stabilize the other.

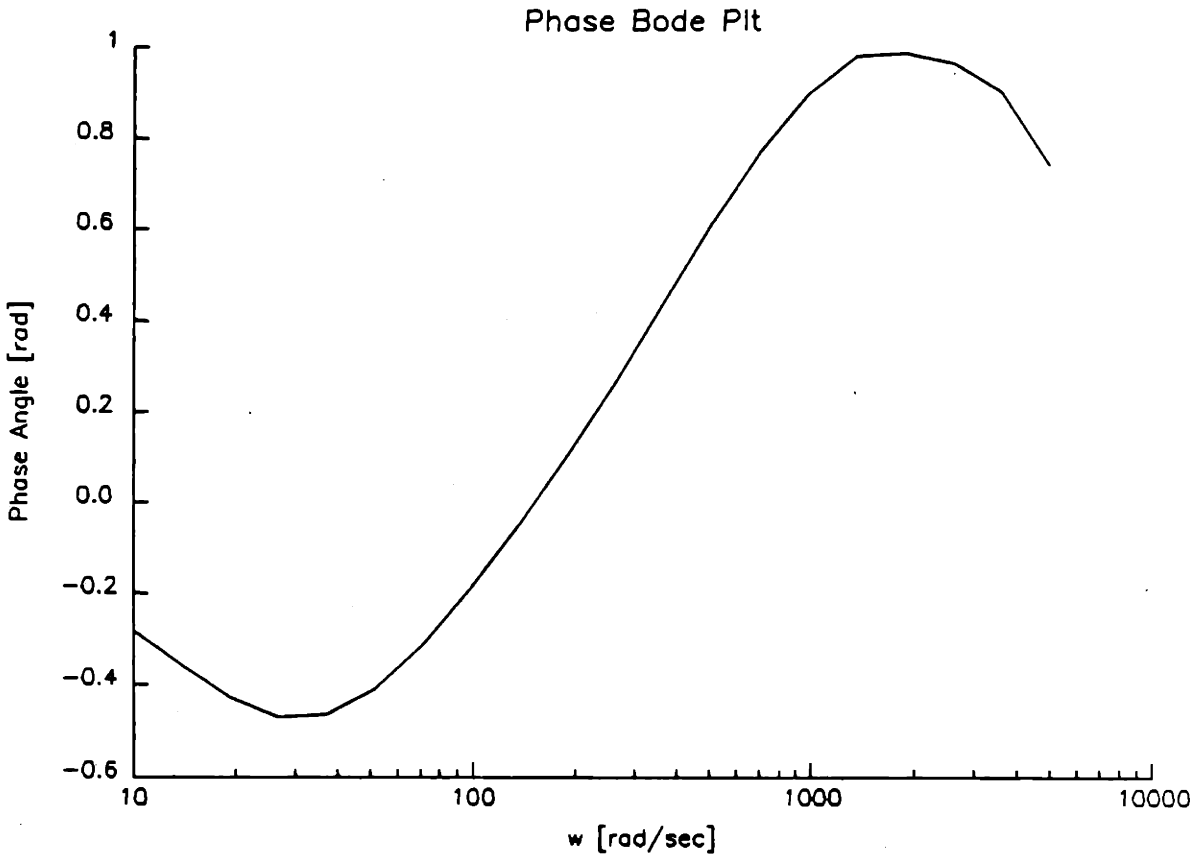

Figure 6.15: Phase Bode plot for eq9 with EFCU/L control using multipole moment state interpreter improved by addition of EFC current predictor.

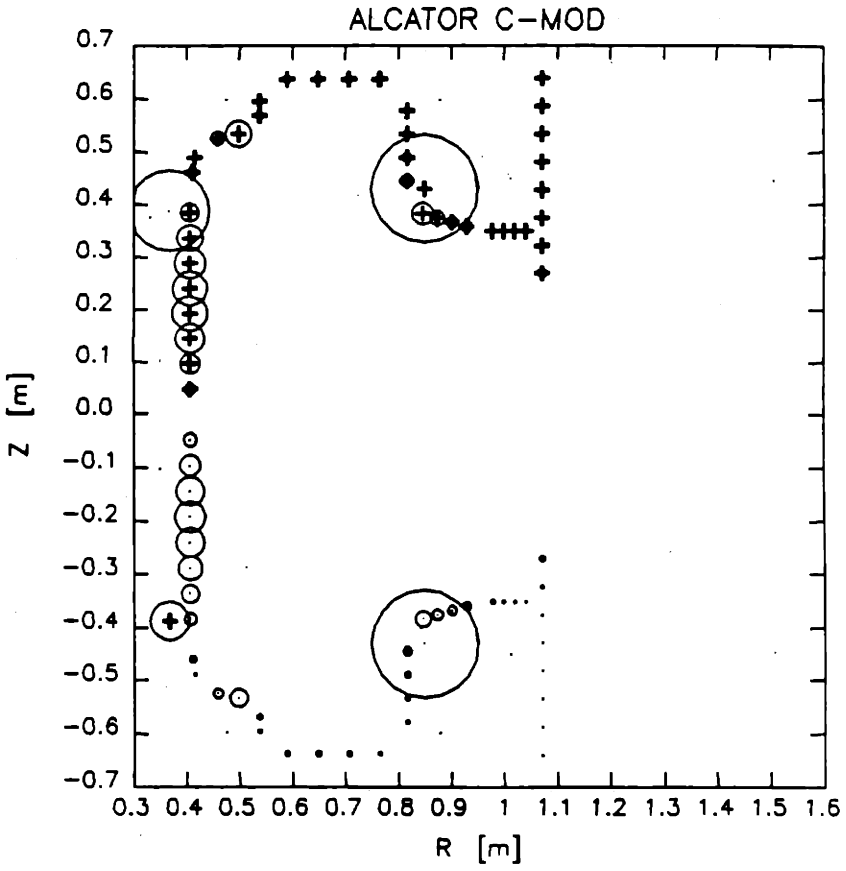

Figure 6.16: Current mode for eq10 passive unstable mode in presence of EFCU/L, OH2U, and OH2L as stabilizing EF coils.

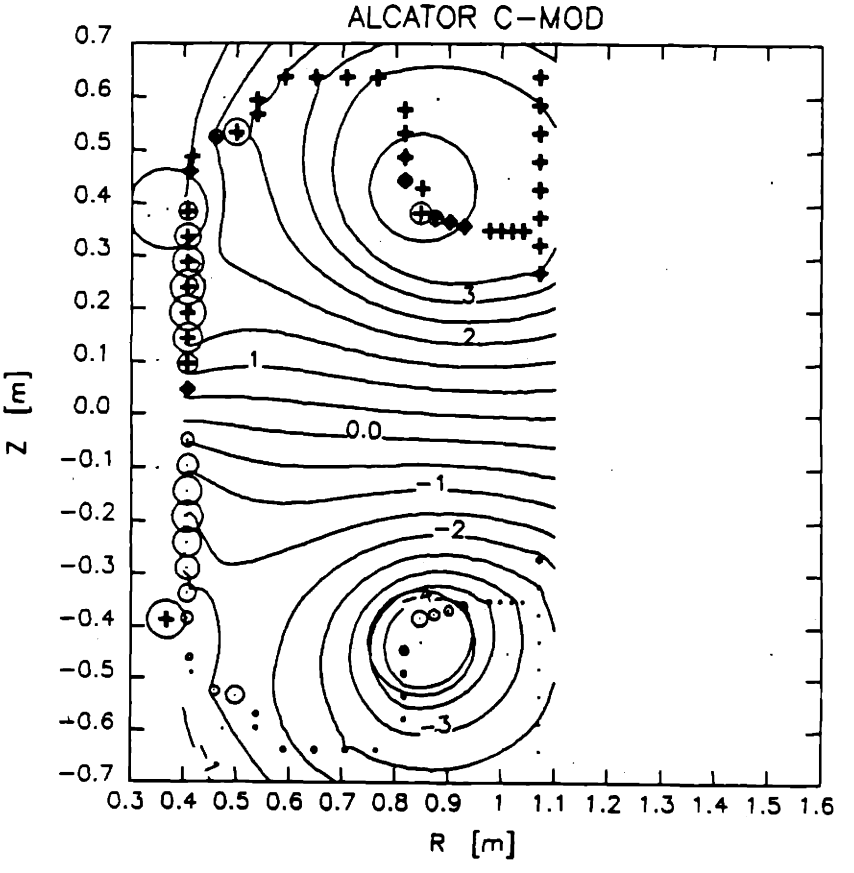

Figure 6.17: Current mode and flux contours for eq10 passive unstable mode in presence of EFCU/L, OH2U, and OH2L as stabilizing EF coils.

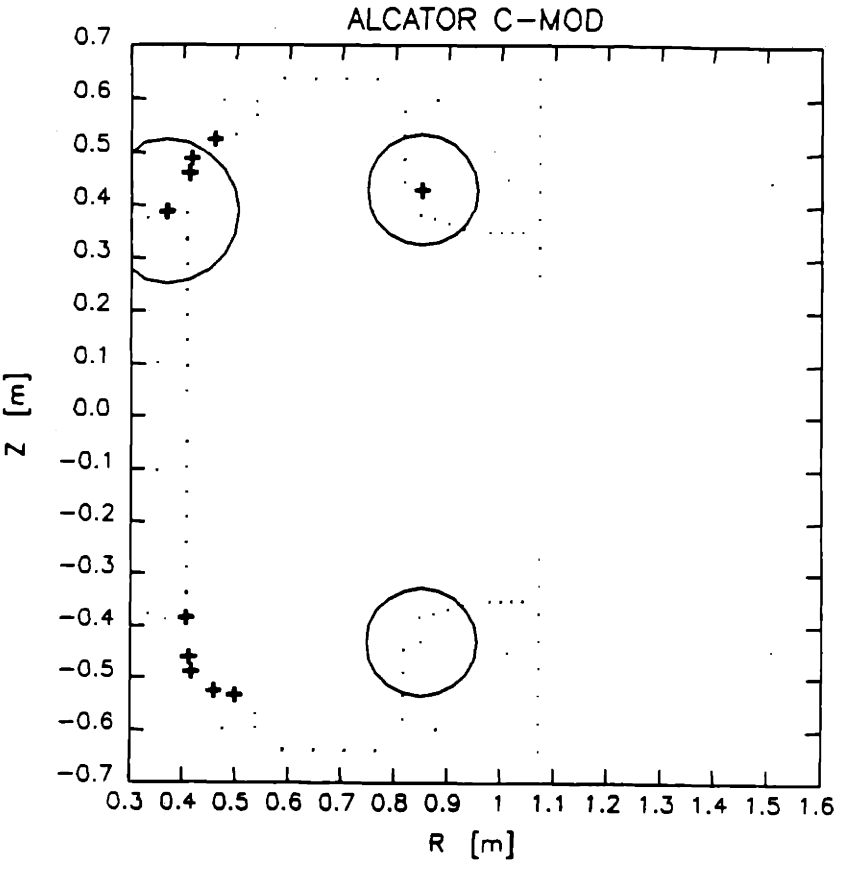

Figure 6.18: Current mode plot for passive stable mode numbered "2" in table of eq10 passive modes ($\gamma = -5.6$).

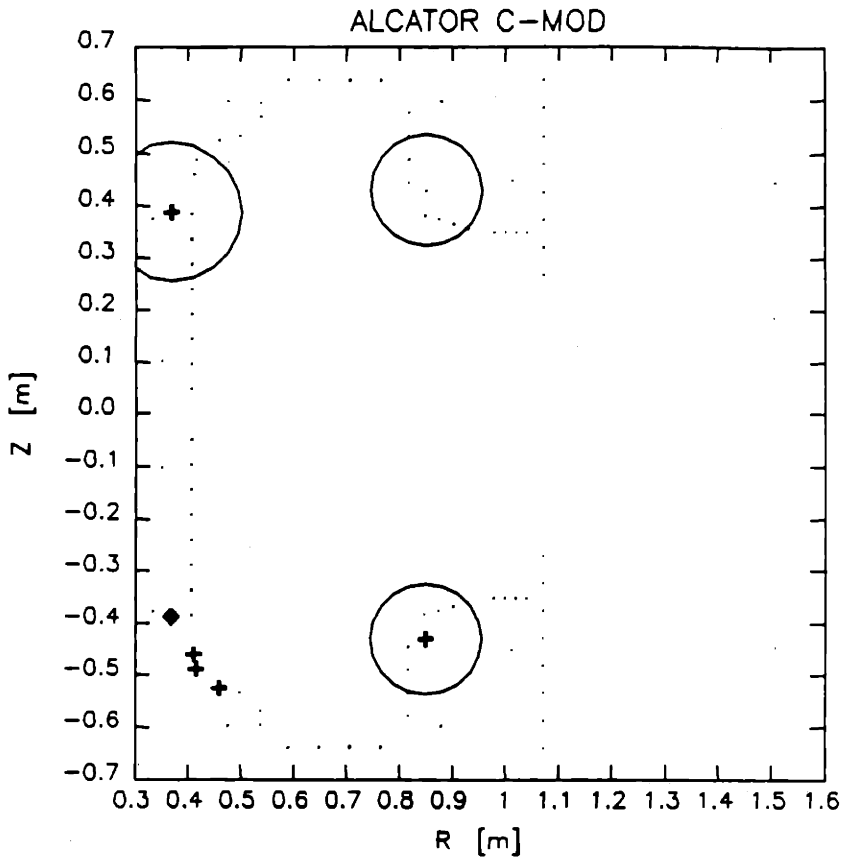

Figure 6.19: Current mode plot for passive stable mode numbered "3" in table of eq10 passive modes ($\gamma = -7$).

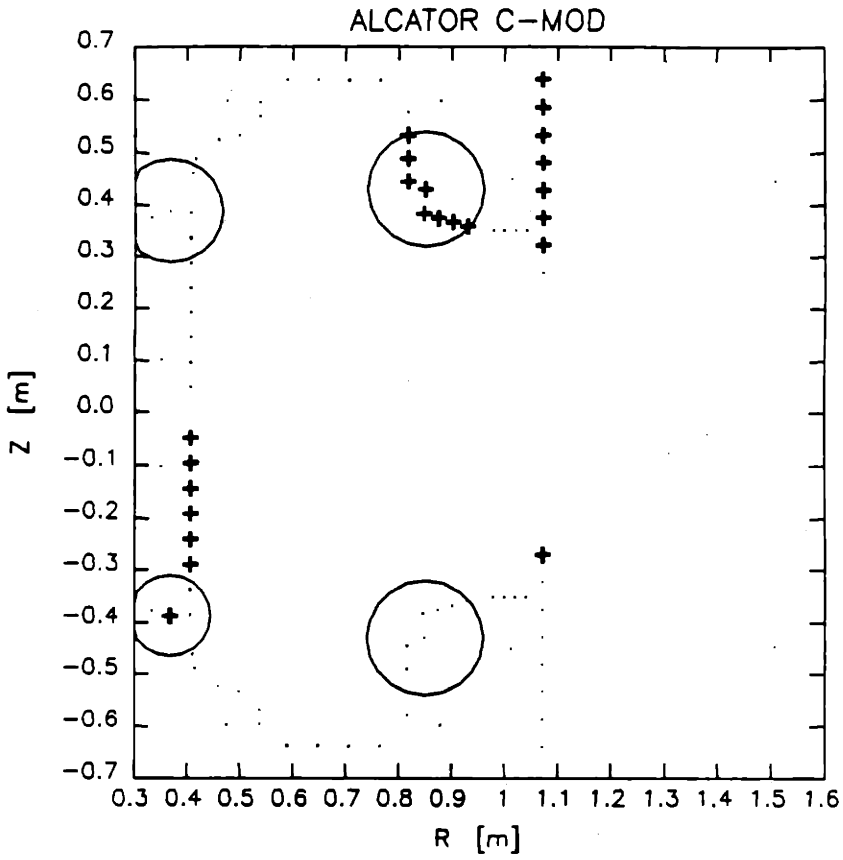

Figure 6.20: Current mode plot for passive stable mode numbered "4" in table of eq10 passive modes ($\gamma = -22$).

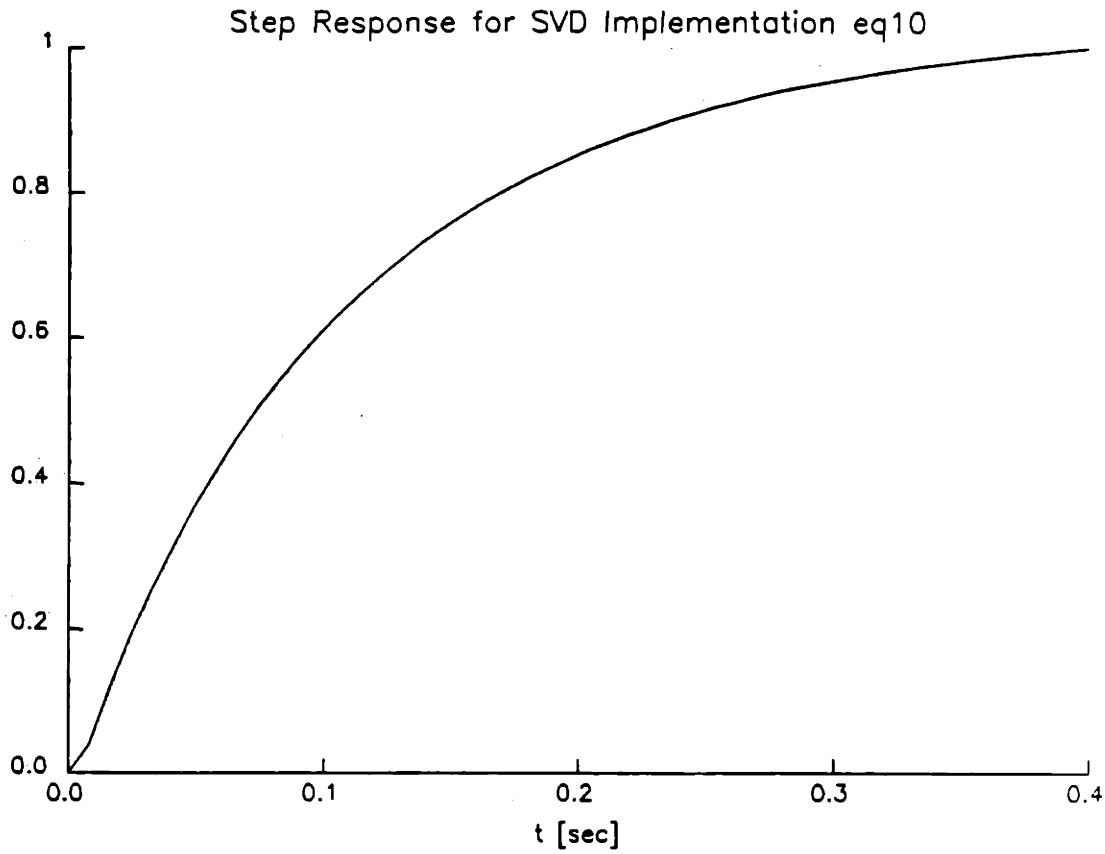

Figure 6.21: Step response for the direct SVD implementation of PDOO FB for eq10 with only the unstable pole placed.

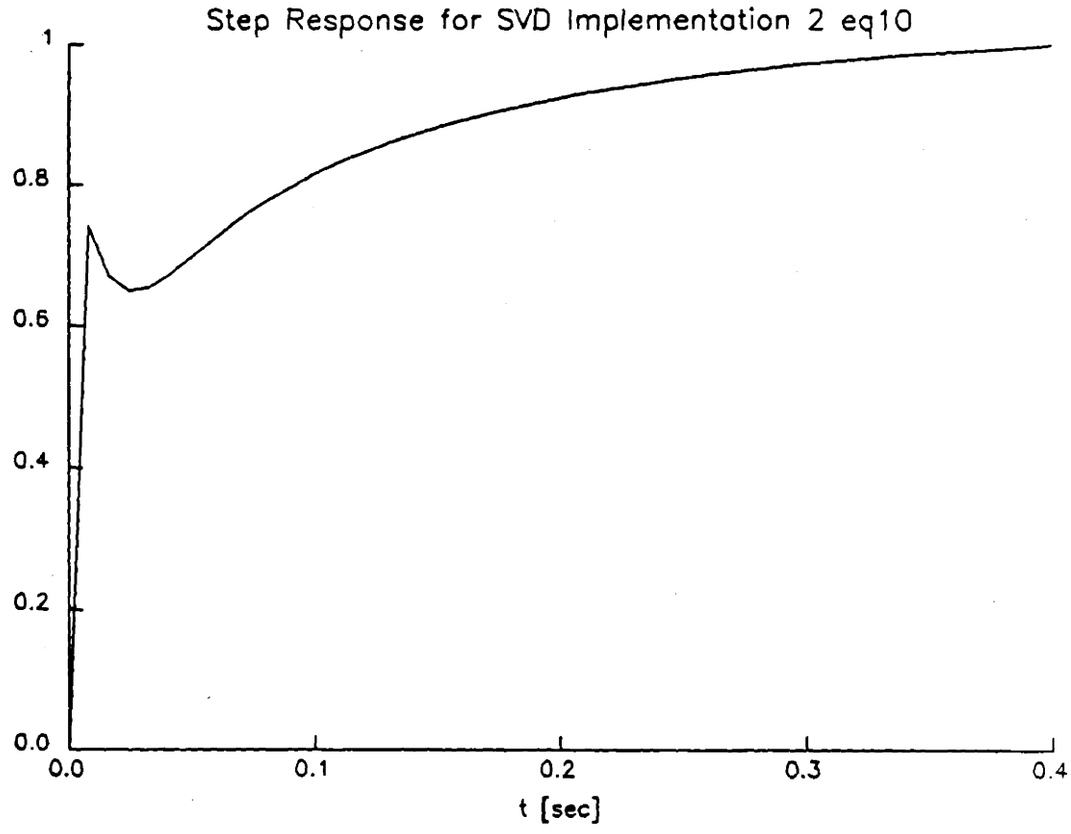

Figure 6.22: Step response for the direct SVD implementation of PDOO FB for eq10 with both $\gamma = -5$ and unstable pole placed.

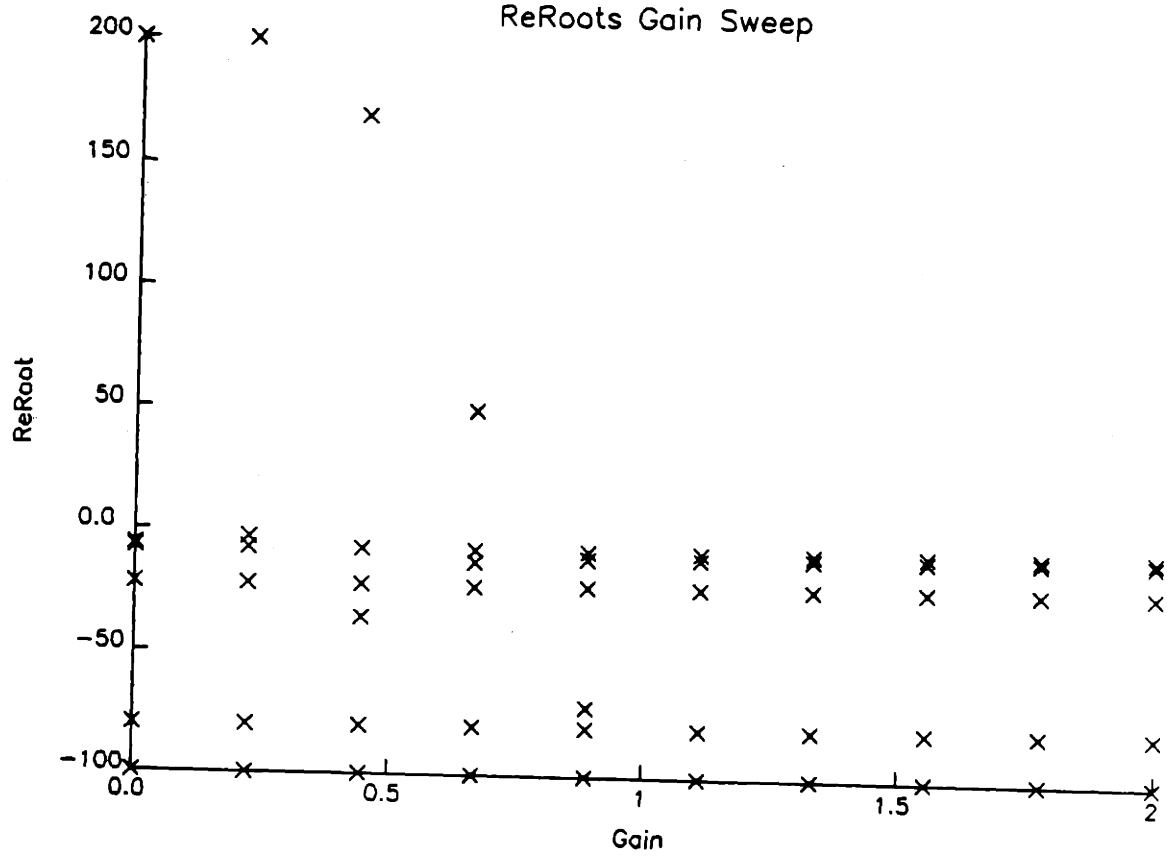

Figure 6.23: Gain sweep of largest singular value in Gp and Gd matrices to search for optimum gain value.

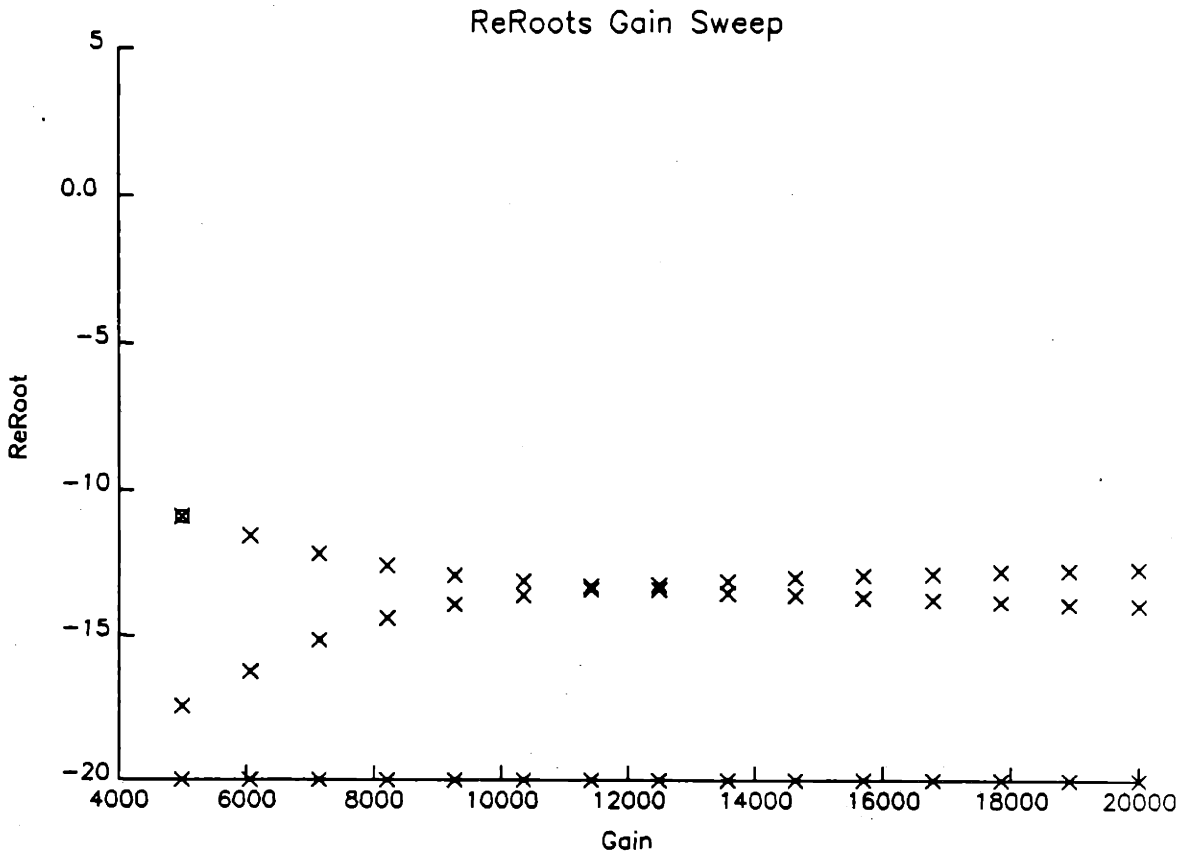

Figure 6.24: Gain sweep of second singular value in Gp and Gd matrices to search for optimum gain value.

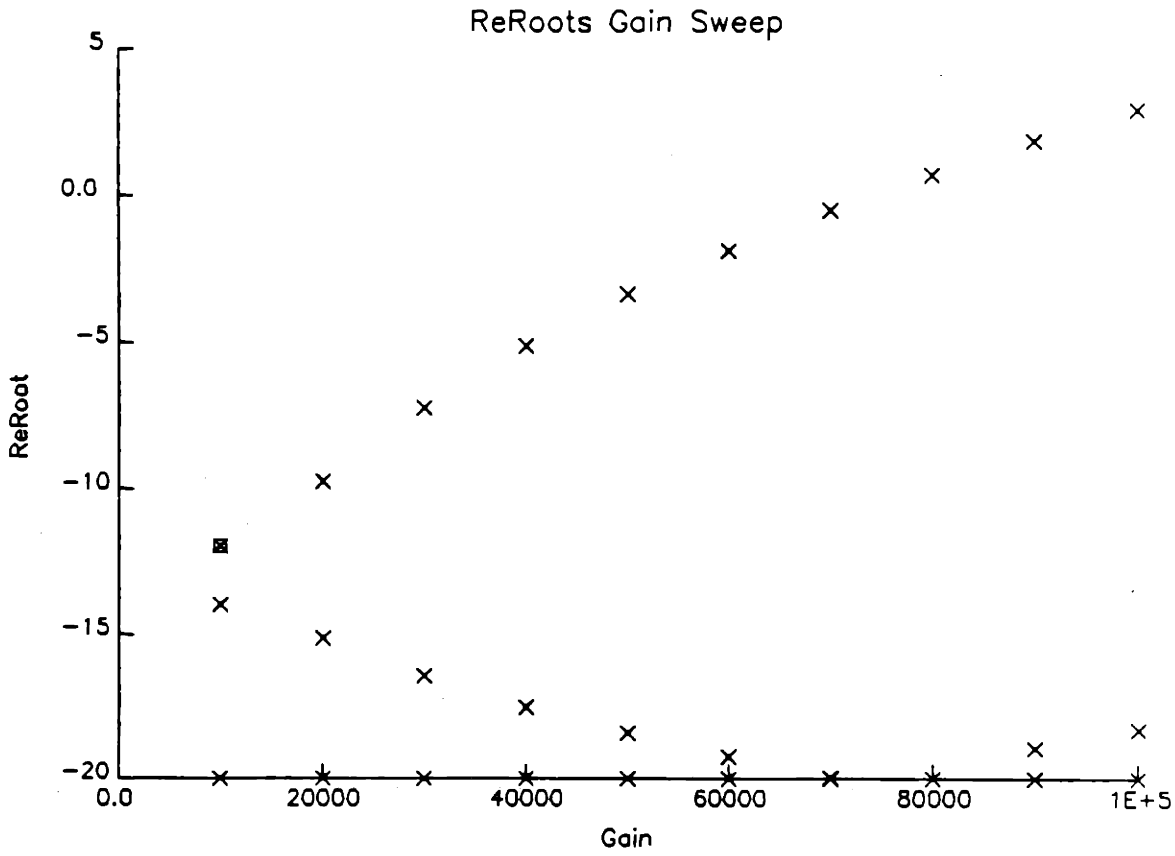

Figure 6.25: Gain sweep of third singular value in Gp and Gd matrices to search for optimum gain value.

6.9 Discussion

This chapter has addressed the problem of actual feedback law design for the tokamak axisymmetric control problem. Although exhaustive gain searches can result in satisfactory control laws for systems with one or two control circuits, such an approach becomes intractable for systems with more degrees of freedom. To allow analysis of truly multivariable systems, a pole placement algorithm was introduced for nominal control law calculation, and an observer design appropriate for the computational constraints was derived. This approach was shown to be useful even for a single control degree of freedom, as well as extremely powerful for the design of a control law involving several coils.

The Alcator C–MOD analog-digital hybrid control architecture was described and the general pole placement and observer approach was generalized to accomodate that system. An algorithm for directly implementing the PD output observer on the hybrid system was derived, and examples of pole placement using this method were given. The eq9 equilibrium was used to illustrate the application of various control design tools as they were described.

The use of state interpreters was discussed, and a variety of candidate interpreters was considered. The multipole moment plasma state predictor was shown to perform the best among these, in particular when used to calculate and incorporate a predictor for driven coil current. It was demonstrated that performance could be limited by the presence of slow decay modes, primarily involving large currents in the low resistance driven EF coils. Performance was improved by both attempting to place such poles at more well-damped locations, and by including a predictor for driven coil current in the state interpretation matrix.

Control performance was analyzed by addressing both time domain, frequency domain, and explicit experimental robustness criteria. Time domain quantities were calculated using the response of the system to step voltage demands to the

driven coil power supplies. Frequency performance was examined by calculating the frequency response of individual decoupled signal loops passing through the system. Robustness to plant model was investigated by perturbing the individual matrices describing various physical aspects of the plant model. Robustness to signal error was evaluated by eliminating certain sensors or groups of sensors and calculating the effect on closed loop eigenvalues.

Finally, a complete control design for 3 driven EF circuits was shown for the eq10 equilibrium. This design demonstrated that the presence of other EF coils can limit performance even further than the EFCU/L circuit alone. In particular, the OH2U/L coils each have L/R times of 213 ms, significantly longer than the L/R time of each EFC coil, 89 ms. The 12-phase OH2 power supplies are also much slower than the chopped EFC power supply. These two factors make it very difficult to improve performance to the nominal target of a 20 ms response time, and to provide sufficient robustness to tolerate 5% error in plant model or loss of individual flux loops. However, using a combination of pole placement and gain space searching, an overall response time under 10 ms was achieved. This value roughly characterizes both rise and settling time with no overshoot. Error robustness calculations showed that this final control law was extremely robust to model error.

Unfortunately, the optimized control law derived for eq10 was found to drive the eq9 equilibrium highly unstable. This is what one would expect, given that the passive growth rate being stabilized in eq10 is much higher than that of eq9, resulting in a higher required feedback gain as well in the eq10 case. Furthermore, the SVD implementation is necessarily very equilibrium-specific, since the "state interpreter" implicit in the SVD formulation consists of the particular principal vectors needed to implement PDOO control for eq10. Control laws calculated for one equilibrium using the PDOO algorithm and direct SVD hybrid implementation are therefore not generally applicable to other equilibria.

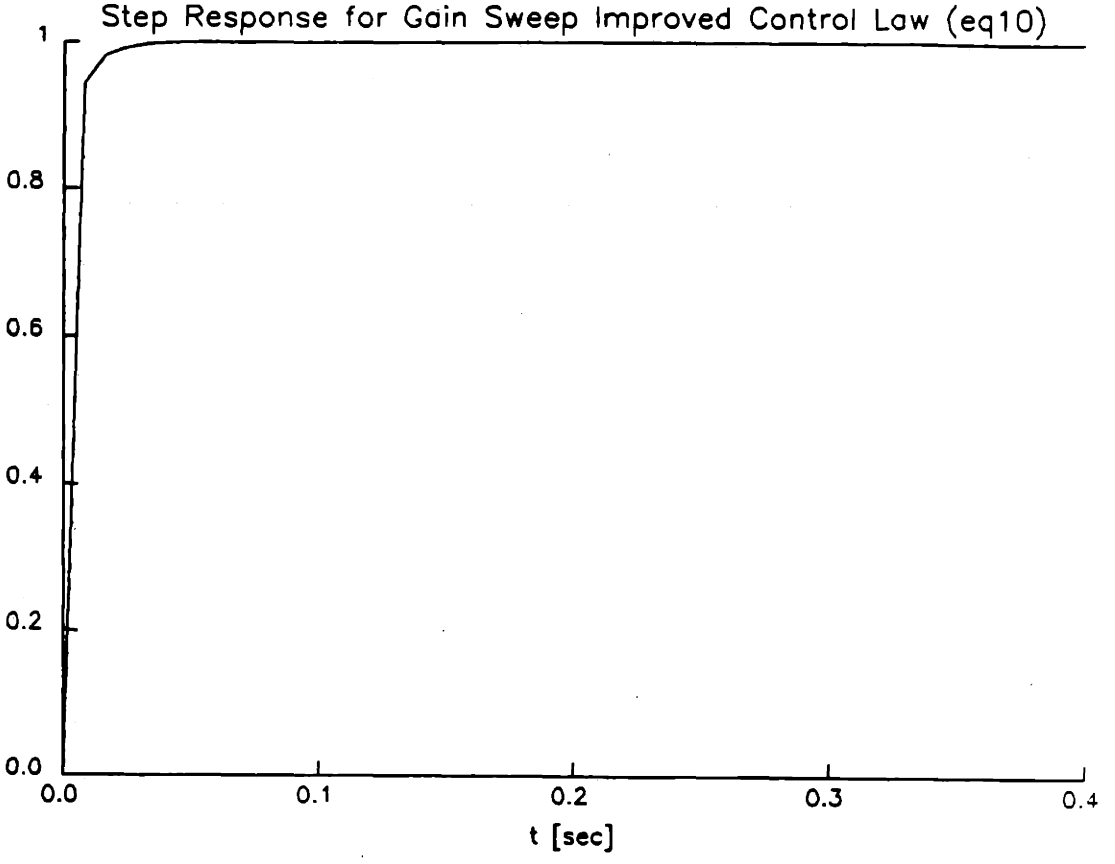

Figure 6.26: Step response for the gain sweep-improved SVD implementation of PDOO FB for eq10 with both $\gamma = -5$ and unstable pole placed.

Chapter 7

Summary and Conclusions

This work has explored various methods of analysis and design of axisymmetric control systems for tokamaks, with an emphasis on vertical stability control. The nature and use of the rigid vertical plasma model was discussed and both passive and control design results were presented. A novel linearized, flux conserving, perturbed equilibrium plasma stability model was also derived, and applied to the problem of passive and active stability analysis. This model was then used in extensive control design calculations. The use of pole placement algorithms in solving the axisymmetric plasma stability control problem was described, and appropriate state observers were derived. The pole placement and output observer algorithms were then reformulated to be implemented using the Alcator C-MOD digital-analog hybrid control system. Finally, examples of applications of these formulations were presented. These algorithms were discovered to yield satisfactorily high performance and robustness control laws, but not to be generally applicable from one equilibrium to another very different equilibrium.

7.1 Rigid Plasma Models

Rigid models are generally simple to use and easy to understand. They provide a quick estimation of relative plasma vertical stability, and allow rough design of control systems. Control laws arising from such models have been shown by other researchers to provide adequate performance to stabilize equilibria with vacuum field curvature approaching the critical decay index [ref][LandL]. Rigid models exhibit much of the essential physics of the vertical instability. Qualitative results such as the form of the conductor current distribution due to the unstable mode and the need for vertical velocity feedback are predicted fairly well using a rigid plasma. However, quantitative vertical stability results appear to be quite sensitive to plasma model, and can be poorly predicted with a rigid model.

In the present work, certain aspects of rigid modeling were analyzed and discussed. Basic difficulties concerning single filament plasma models were addressed, including the problem of filament location and calculation of the proper destabilizing force acting on the filament. The variation in and convergence of calculated growth rates as a function of number of filaments was studied. It was found that for typical C–MOD equilibria, a relatively small number of filaments, on the order of 5-10, was necessary to come within 10% of the converged growth rate. Only about 20 filaments were required to reach 1% of the converged value. Single filament models were found to yield low passive growth rates compared to those calculated with multifilament models, giving rise to more optimistic predictions regarding controllability and power supply limits.

Multifilament rigid plasma model results proved sufficiently restrictive and compelling in the case of certain C–MOD control coil configuration analyses to cause a major redesign of the vacuum vessel and creation of a special fast power supply-driven pair of control coils.

However, rigid models do not generally treat the plasma as flux conserving or

account properly for the nonrigid degrees of freedom in a physical plasma. As a result, the quantitative results of stability analysis, such as passive growth rates, proper modal observers, and actual control law requirements, are predicted inaccurately. The importance of this degree of inaccuracy varies greatly with equilibrium characteristics. Satisfactory stabilization of equilibria which approach the limits of machine performance will of course demand the most accuracy in modeling.

7.2 Perturbed Equilibrium Plasma Model

The present work has determined that even a simple nonrigid plasma model with approximate flux conservation can result in passive growth rates which are significantly different from those calculated using a rigid model. Passive growth rates differing by as much as a factor of 2 from the rigid values were calculated using the perturbed equilibrium approach. Since passive growth rates were shown to be related to the maximum tolerable delay time, such an error can result in a large reduction in actual power supply response time safety margin.

Because the Alcator C–MOD vacuum vessel contributes very strongly to vertical stabilization, vessel currents must be included in the plasma response model in order to be able to analyze this machine correctly. To estimate the influence of vessel currents on the plasma, a mapping function was calculated which expands vessel current modes in effectively equivalent EF coil current modes. This approximation was demonstrated to be very good for the vessel modes possessed of low order variation in poloidal angle, which are the important modes in the problem. Furthermore, the intrinsic number of degrees of freedom in the nonrigid plasma model was investigated using singular value decomposition methods. The actual dimensionality of the plasma response subspace was found to be about 4-5, since the space of vectors of flux at the vessel due to plasma variations can be spanned to an accuracy of better than 0.1% by a basis set of only 4-5 principal vectors. This

indicates that the 13 degrees of freedom arising from the EF coil current and equilibrium perturbation is likely to be sufficient to characterize the significant plasma response coupling to the conductor array.

Using this vessel mapping with the flux conserving perturbed equilibrium plasma model results in vertical modes which are qualitatively similar in form to those calculated using a rigid model. However, the nonrigid model growth rates differ significantly from the rigid model growth rates, and the plasma response, conductor currents, and vacuum flux due to these modes are somewhat different, reflecting the extra degrees of freedom available to the model.

The passive growth rate prediction for a standard C–MOD equilibrium was compared to that derived from a similar equilibrium calculated using the Tokamak Simulation Code (TSC). Although certain aspects of the simulations differed somewhat, including details of the vacuum vessel model and plasma profiles, the predicted growth rates differed by about 50%. By contrast, the TSC prediction was greater than the corresponding rigid result by a factor of 3.

7.3 Active Control Analysis

Active studies using the rigid model exhibited the need for velocity feedback, a phenomenon which was demonstrated to arise as a result of the relative degree of inductive coupling in the plasma-vessel and plasma-driven coil systems. A single pole "lag" power supply model was used with single variable direct feedback on actual plasma vertical position and velocity to explore delay tolerance. For the two equilibria studied with this power supply delay model, the maximum tolerable "lag" time constant was roughly equal to the inverse of the passive growth rate. Among the rigid equilibria studied, the most unstable had an elongation of $\kappa_{sep} = 2$ and an unstable growth rate of 1 ms, and could tolerate a maximum power supply delay

of 1 ms as well. This was deemed to be the most unstable growth rate to be safely attainable with the final EFC control coil design and fast power supply chosen. This power supply has a response time of 200 μsec, providing a safety margin of a factor of 5 over the tolerable delay time.

By contrast, using the perturbed equilibrium plasma model, approximately the same growth rate was found to occur in a standard C–MOD equilibrium with $\kappa_{sep} = 1.85$. This suggests that a $\kappa_{sep} = 2$ equilibrium may not be attainable with as large a safety margin as indicated by the rigid calculation, but that an elongation of at least $\kappa_{sep} = 1.85$ can be attained with that margin of safety. Actual control design further substantiated the satisfactory performance of such an equilibrium.

7.4 Axisymmetric Control Design

General multivariable control system design was discussed, and the use of pole placement algorithms described. A full state feedback approach coupled with a PD output observer was derived for the case of feedback unconstrained by architecture. The PD output observer solution was designed to be calculable using only linear methods, avoiding the complexity and time demands of a nonlinear Ricatti solution. The linear observer was demonstrated to provide satisfactory reconstruction of conductor modes when flux loops alone constitute the sensor array, and excellent reconstruction when B_p coils are used in addition to flux loops.

The C–MOD analog-digital hybrid control system was then described, and the PD output feedback algorithm implemented using that architectural constraint. Intermediate state interpreters were derived which could provide information to system operators, facilitating between-shot manual refinement of control performance. A direct SVD implementation of the exact PD output control law was also demonstrated, and later tested for the case of the most demanding equilibrium pre-

sented here. Use of the different state interpreters was illustrated using a standard $\kappa_{95} = 1.6$, $\kappa_{sep} = 1.7$ C–MOD equilibrium (eq9), controlled only by the EFCU/L coils and power supply. This equilibrium was shown to be satisfactorily controlled using a toroidal multipole moment state interpreter. The system performance was then improved by the inclusion of an explicit predictor for control coil current in the state interpreter. The final, improved control system exhibited a rise time of about 10 ms, settling time of less than 50 ms, and zero overshoot. These parameters were shown to compare favorably with performance characteristics for actual shots in currently operating machines. The final control law was also demonstrated to be robust enough to model error to provide satisfactory performance even when the resistance, mutual inductance, and plasma response matrices were each independently perturbed by $\pm 5\%$.

Various performance testing approaches were described, including time domain (step response), frequency domain (multivariable Bode plot), and systematic error effect calculations. In addition, the use of gain sweeping (gain space searching) and frequency sweeping (Bode plot construction), taking advantage of the form of the hybrid architecture, was described for control law refinement purposes.

A $\kappa_{95} = 1.7$, $\kappa_{sep} = 1.85$ equilibrium (eq10) was used to illustrate the general design strategy, including determination of a nominal control law, and testing and refinement of system performance. The nominal control law for this case was chosen to be the direct implementation of the SVD of the PD output observer. This case, in which the OH2U and OH2L coils were used along with the EFCU/L control circuit to stabilize the plasma, resulted in a nominal rise time of greater than 20 ms with zero overshoot, but an extremely long settling time greater than 140 ms. After improvement by gain space searching, the rise time was reduced to less than 10 ms with no overshoot, and the settling time to also about 10 ms.

7.5 Conclusions

Rigid plasma models, although easy to use and often sufficient to allow derivation of satisfactory control algorithms, in general make significantly more optimistic predictions than more accurate nonrigid plasma models. The flux conserving perturbed equilibrium approach derived here, for example, predicts a passive growth time of 1 ms for eq10 passively stabilized by EFCU/L, OH2U, and OH2L. The corresponding rigid prediction was 1.7 ms. This latter is the characteristic delay time of a 12-phase power supply. If one were to use the growth time as an estimate of maximum tolerable delay time, such a difference could lead designers using a rigid model to choose an inadequate supply to stabilize this case.

When discretized models of the stabilizing conductors are used, it is very natural and powerful to use a state space representation to analyze and design for stability. This formalism allows the application of multivariable system analysis techniques, which have been demonstrated here to be extremely useful in the design of control laws. The full state feedback pole placement approach coupled with output observers enables designers to establish stable nominal control laws even for many-variable systems. The performance and refinement methods we have described allow further improvement to extract the maximum performance from the control system.

The analog-digital hybrid control system architecture of both Alcator C–MOD and TCV has been demonstrated to be sufficient to allow implementation of the control laws derived using multivariable pole placement, as well as allowing operator refinement between shots. A choice of implementations and forms of state interpreters was described. It was demonstrated that the multipole moment state interpreter provided the best control for eq9, using an EFC current predictor to improve performance. Using an explicit state interpreter allows an operator to refine the control algorithm in a straightforward way between shots, since the variables of

interest can be made available to the operator, and are intermediate elements of the control loop. The operator can thus modify gains explicitly affecting the stability of the variable in need of improvement between shots. A state interpreter approach is generally preferable to a more equilibrium-specific approach such as the direct SVD implementation if sufficient robustness and performance can be demonstrated for the final design, since greater operator flexibility is usually desirable.

However, if high performance is required, a direct SVD implementation refined with gain sweeping and Bode plot performance testing will likely result in the maximum performance for a specific equilibrium. Extremely demanding equilibria with passive growth rates approaching the safe limits of power supply response may require an SVD implementation which is more specifically adjusted to fit that particular case. Such specific control laws would best be reserved for the final, relatively time invariant state of a highly elongated plasma during flattop, using appropriate state interpreters for the rapidly changing plasmas during the rampup and evolution preceding the final flattop state.

Finally, the present study using the flux conserving perturbed equilibrium model indicates that equilibria having separatrix elongations of at least 1.85 can be stabilized robustly with the present C–MOD control architecture and conductor/sensor configurations. Thus, the the nominal design specification for plasma shaping can be met.

7.6 Suggestions for Further Study

There is a great deal of continuing work to be done along the lines of this study. To a large extent, the designs analyzed here have been illustrative, but not complete. Various aspects of the models have been simplified to facilitate explanation and illustration of the approach. In order to apply these techniques in actual C–MOD

shots, more explicitly detailed cases will have to be analyzed.

The machine model itself must be expanded in detail. For example, the effects of cooling on the vacuum vessel and EF coils will have to be studied in some detail to achieve the correct maximally efficient control laws. This can best be done when some data have been amassed regarding the actual thermal behavior of the machine, including such information as cool-down times between shots and temperature variation of the vacuum vessel during a day of operation. The EF coil set which is actually present in the machine includes at least two more coil pairs which contribute to vertical stability. These are EF1U/L and EF2U/L, the upper and lower coils in each pair driven independently of their mates on the other side of the midplane. These were not modeled in this work in order to simplify illustration as well as to take a conservative approach to stabilizability. Their presence is expected to somewhat reduce passive growth rates, and create more performance-limiting slow decay modes. The reduction in passive growth rate should be less than about 25%, since the effect of the better plasma-coupled OH2 and EFC pairs was to cause about this degree of change.

Extensions of the plasma model would also be very interesting to undertake. In particular, allowing pressure to vary in the perturbed equilibrium approach would allow approximate modeling of adiabatic compression and the effects of phenomena such as sawteeth which affect the pressure profile.

Another extremely important next step is to properly benchmark the perturbed equilibrium plasma model predictions with a more accurate stability code. Of interest in this regard would be both comparison with marginal wall position stability boundaries predicted by an ideal MHD code, and comparison with a previously benchmarked, more accurate, resistive wall stability code.

Essentially the only tokamak studies previous to this work which have employed state space methods have focused on optimal control analysis. Optimal

control theory has many promising features, although it suffers from the limitations mentioned earlier. However, it would be of great interest to compare the performance of control laws obtained using various cost functionals to the performance of control laws resulting from the pole placement and refinement algorithms presented here.

Finally, the ultimate test of an analysis and resulting control law design is the performance resulting when implemented on actual machines. It is hoped that much of the preceding analysis will be used directly on Alcator C–MOD, very likely revealing the important physics aspects which must be modified in the model. A large part of the mission of Alcator C–MOD involves the study of shaped plasmas and the general problem of axisymmetric control. The perturbed equilibrium plasma model will also be applied to analysis of JT–60 Upgrade, and similar control designs will hopefully be tested on that machine as well. Actual machine implementation provides the final arbitration of control quality, and will inevitably lead to better understanding of the axisymmetric control problem.

Bibliography

[1] Freidberg, J. P., Ideal Magnetohydrodynamics, Plenum Press, (1987)

[2] Parker, R. R., Sheffield, J., Nucl. Fus. **29** (1989), 489

[3] Wesson, J. A., Nucl. Fus. **18** (1978), 87

[4] Rebut, P., Bartlett, D., et al, Tenth Internat'l Conf. on Plasma Physics and Contr. Nucl. Fusion Research, London, (1984) (IAEA Rept. # IAEA-CN-44/A-I-1)

[5] Jardin, S., Larrabee, D., Nucl. Fus. **29** (1989), 1095

[6] Thome, R., Pillsbury, R., et al, Passive and Active Circuits for Vertical Plasma Stabilization, PFC Rept. PFC/RR-83-32, Mass. Inst. of Tech., Cambridge, (1983)

[7] Neilson, G., Dyer., G. R., et al, Nucl. Fus. **24** (1984), 1291

[8] Hutchinson, I. H., Nucl. Fus. **29** (1989), 2107

[9] Bertolini, E., Mondino, P. L., et al, Fus. Tech. **11** (1987), 71

[10] Lackner, K., McMahon, A., Nucl. Fus. **14** (1974), 575

[11] Rebhan, E., Salat, A., Nucl. Fus. **16** (1976), 805

[12] Haas, F., Nucl. Fus. **15** (1975), 407

[13] Lazarus, E. A., Lister, J. B., et al, Nucl. Fus. **30** (1990), 1107

[14] Solano, E. R., Neilson, G. H., et al, Nucl. Fus. **30** (1990), 1107

[15] Humphreys, D. A., Hutchinson, I. H., Filament-Circuit Model Analysis of Alcator C-MOD Vertical Stability, PFC Rept. PFC/JA-89-28, Mass. Inst. of Tech., Cambridge, (1989)

[16] Haney, S. W., Methods for the Design and Optimization of Shaped Tokamaks, PFC Rept. PFC/RR-88-12, Mass. Inst. of Tech., Cambridge, (1988)

[17] Albanese, R., Coccorese, E., et al, Nucl. Fus. **29** (1989), 1013

[18] Hoffmann, F., Marcus, F. B., et al, Plasma Phys. and Contr. Nucl. Fusion **28** (1986), 705

[19] Jardin, S. C., Pomphrey, N., et al, J. of Computational Physics **66** (1986), 481

[20] Khayrutdinov, R., Plasma Equilibrium and Transport in a Tokamak Fusion Device Using the Inverse Variable Technique, to be submitted to J. of Computational Physics.

[21] Ramos, J. J., TSC Simulations of Alcator C-MOD Discharges III: Study of Axisymmetric Stability, PFC Rept. PFC/RR-90-9, Mass. Inst. of Tech., Cambridge, (1990)

[22] Hutchinson, I. H., Becker, H., et al, Physics and Engineering of Alcator C-MOD, PFC Rept. PFC/RR-88-11, Mass. Inst. of Tech., Cambridge, (1988)

[23] Johnson, J. L., Dalhed, H. E., J. of Computational Physics **32** (1979), 212

[24] Wolfe, S., priv. comm.

[25] Press, W. H., Flannery, B. P., Numerical Recipes, Cambridge University Press, Cambridge, England, (1986)

[26] Bernard, L. C., Berger, D., et al, Nucl. Fus. **18** (1978), 1331

[27] Ramos, J. J., priv. comm.

[28] Friedland, B., Control System Design, McGraw-Hill, New York, (1986)

[29] Patel, R., Munro, N., Multivariable System Theory and Design, Pergamon Press, Oxford, England, (1982)

[30] Roberge, J. K., Operational Amplifiers, John Wiley and Sons, New York, (1986)

[31] Marcus, F. B., Hofmann, F., et al, Nucl. Fus. **30** (1990), 1511

[32] Van Milligen, B., Nucl. Fus. **30** (1990), 157

[33] Alladio, F., Crisanti, F., Nucl. Fus. **26** (1986), 1143

[34] Chen, C-T., Analysis and Synthesis of Linear Control Systems, Pond Woods Press, Stonybrook, New York, (1978)

[35] Wesson, J., Tokamaks, Clarendon Press, Oxford, England, (1987)

[36] Greenwald, M., Gwinn, D., et al, Plasma Phys. and Contr. Nucl. Fusion Research (Proc. Tenth Internat'l Conf., London), IAEA Vienna (1984), vol. 1, 45

[37] Greenwald, M., Besen, M., et al, Plasma Phys. and Contr. Nucl. Fusion Research (Proc. Eleventh Internat'l Conf., Kyoto), IAEA Vienna (1986), vol. 1, 139

[38] Pribyl, P. A., Plasma Position Control on Alcator C, PFC Rept. PFC/RR-81-21, Mass. Inst. of Tech., Cambridge, (1981)

[39] Lister, J. B., Lazarus, E. A., Nucl. Fus. **30** (1990), 2349